Alma Mater Studiorum – Università di Bologna

DOTTORATO DI RICERCA IN

Meccanica e Scienze Avanzate dell'ingegneria

Ciclo XXXI

Settore Concorsuale di afferenza: 09/A3

Settore Scientifico disciplinare: ING-IND/21

INNOVATIVE AL ALLOYS FOR HIGH PERFORMANCE AUTOMOTIVE PISTONS: ENHANCEMENT OF SPECIFIC STRENGTH AT HIGH TEMPERATURE AND RESISTANCE TO KNOCK DAMAGE

Presentata da
Dott.ssa Eleonora Balducci

Coordinatore Dottorato
Prof. Marco Carricato

Relatore
Prof.ssa Lorella Ceschini

Correlatore
Prof. Nicolò Cavina

Esame finale anno 2019

Abstract

The increasingly strict regulations on greenhouse gas emissions make the fuel economy a pressing factor for automotive manufacturers. Lightweighting and engine downsizing are two strategies pursued to achieve the target. In this context, materials play a key role since these limit the engine efficiency and components weight, due to their acceptable thermo-mechanical loads.

Piston is one of the most stressed engine components and it is traditionally made of Al alloys, whose weakness is to maintain adequate mechanical properties at high temperature due to overaging and softening. The enhancement in strength-to-weight ratio at high temperature of Al alloys had been investigated through two approaches: increase of strength at high temperature or reduction of the alloy density. Several conventional and high performance Al-Si and Al-Cu alloys have been characterized from a microstructural and mechanical point of view, investigating the effects of chemical composition, addition of transition elements and heat treatment optimization, in the specific temperature range for pistons operations. Among the Al-Cu alloys, the research outlines the potentialities of two innovative Al-Cu-Li(-Ag) alloys, typically adopted for structural aerospace components.

Moreover, due to the increased probability of abnormal combustions in high performance spark-ignition engines, the second part of the dissertation deals with the study of knocking damages on Al pistons. Thanks to the cooperation with Ferrari S.p.A. and Fluid Machinery Research Group- Unibo, several bench tests have been carried out under controlled knocking conditions. Knocking damage mechanisms were investigated through failure analyses techniques, starting from visual analysis up to detailed SEM investigations. These activities allowed to relate piston knocking damage to engine parameters, with the final aim to develop an on-board knocking controller able to increase engine efficiency, without compromising engine functionality. Finally, attempts have been made to quantify the knock-induced damages, to provide a numerical relation with engine working conditions.

List of symbols and abbreviations

ICE: Internal Combustion Engine

R: material strength

ρ: material density

p(ϑ): in-chamber pressure

ϑ: crank angle

p_0: crankcase pressure

D: diameter

F_G: combustion gas force acting on piston

TDC: top dead center

BDC: bottom dead center

F_i: inertia load acting on piston

F_N: normal force (F_G + F_i) acting on piston

rpm: revolutions per minute (engine crankshaft)

s_{pist}: mean piston speed

F_L: lateral force acting on piston

F_C: con-rod reaction

DI: direct injection

PFI: port fuel injection

SA: spark advance

T: temperature

α: thermal expansion coefficient

D: diffusion coefficient

D_0: diffusion constant (depending by the diffusing species)

Q: activation energy for diffusion

R: gas constant

J: diffusion flux

C: concentration of a certain substance

R: average precipitate size

σ: precipitate-matrix interfacial free energy

$C_{eq}^{(\alpha/\beta)}$: equilibrium solubility of the solute in the matrix/precipitate phase

γ_{SFE}: stacking fault energy

f_v: fraction volume of precipitates or dispersoids

γ_{GB}: energy of precipitates or dispersoids interfaces

M: generic metal

TM: transition metal

RE: rare earth

RS: rapid solidification

HTT curves: hardness-time-temperature curves

$Rp_{0.2}$: proof strength

UTS: ultimate tensile strength

E%, A_t%: elongation to failure

σ_p: true plastic stress

ε_p: true plastic strain

K: strength coefficient (Hollomon's law)

n: strain hardening exponent (Hollomon's law)

PFZ: precipitate free zone

RT: room temperature

MAPO: Maximum Amplitude Pressure Oscillation

Index

General Introduction

The constantly growing concerns on global environmental protection and climate change determine increasingly strict regulations on pollutant and greenhouse gas emissions, which form the golden thread of this Ph.D. thesis. As the European Environment Agency reports, the transport field (in particular road transportation) was responsible of almost a quarter of greenhouse gas emissions in 2016 [1] (Fig.i). These numerical data further strengthen the importance of the so called "low-emission mobility" among the objectives of the European Climate Action [2].

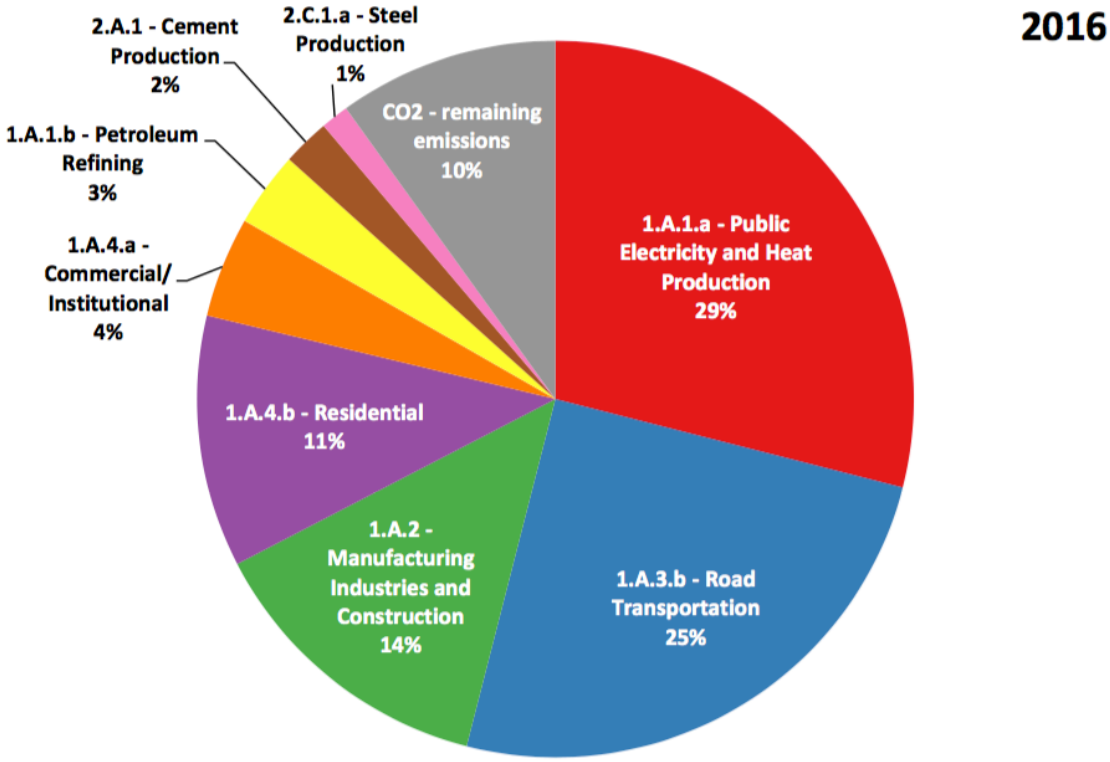

Fig.i: Share of the largest key source of CO_2 emissions in 2016 for EU-28 and Iceland [1].

Since carbon dioxide (CO_2) plays the major role among the greenhouse gas emissions, EU legislation mainly focuses on mandatory reduction of CO_2 emissions for new cars, vans and heavy-duty vehicles. Focusing on passenger cars, emission limits are specifically set according to the vehicle mass (heavier cars are allowed higher emissions than lighter cars), and only the fleet average is regulated, which means that manufacturers are still allowed to sell vehicles with emissions above the limits, provided these are balanced by vehicles with lower emissions. In particular, as graphically explained in Fig.ii, the latest EU regulation No 253/2014 [3] requires that

the fleet average to be achieved by new cars in 2020 is 95 grams of CO_2 per kilometre, while the 2025 target is supposed to be roughly equal to 70g/km [4].

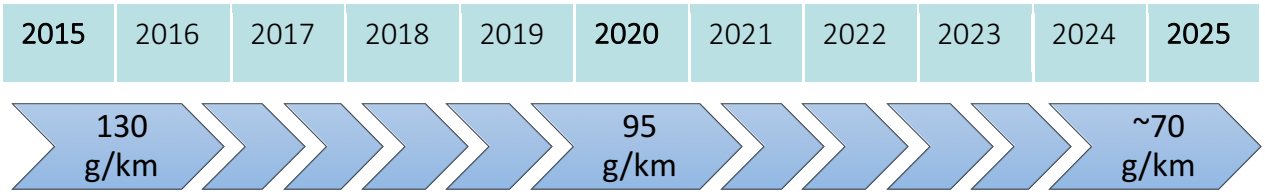

Fig.ii: Temporal overview of CO_2 requirements up to 2025. Up to date, the threshold limit for 2025 is only estimated, since EU needs to evaluate numerical data on more recent CO_2 emissions in order to set ambitious yet realistically achievable targets.

In case the average CO_2 emissions of a manufacturer's fleet exceed the allowed limit, the manufacturer has to pay an excess emissions premium for each car registered, which amounts to: (i) €5 for the first g/km of exceedance, (ii) €15 for the second g/km, (iii) €25 for the third g/km, (iv) €95 for each subsequent g/km; starting from 2019, the cost will be €95 from the first gram of exceedance onwards.

As a consequence, the financial penalties are extensively driving innovation in the automotive field, making the improvements of fuel economy one of the most pressing factor for automotive manufacturers [5]. As stated in [2], in order to fulfil CO_2 requirements it is fundamental to "*speed up the deployment of low-emission alternative energy for transport, such as advanced biofuels, electricity, hydrogen […]*", but "*further improvements to the internal combustion engine will be* [also] *needed*". Due to the lack of today infrastructures to meet the global requirements, in fact, hybrid or electric vehicles are considered long-term alternatives [6,7]; moreover, the optimal solution should also take into account the CO_2 emissions associated with the generation of energy supplied to vehicles, such as electricity and alternative fuels, ensuring that the upstream emissions do not erode the benefits related to alternative fuels/energy.

In the short-term, in order to boost the fuel economy of internal combustion engines (ICEs), two main strategies should be implemented:

1. Vehicle lightweighting. Even if this trend started many years ago as for intensive aluminium use for car body structures [8], research in this field is still active, as also confirmed by the year by year conference organised by Global Automotive Lightweight Materials [http://www.global-automotive-lightweight-materials-europe.com] since 2012. In this context, Al alloys continue to play a key role, given their great potential in terms of mass savings due to high strength-to-weight ratio, combined with good corrosion resistance, good castability and formability. Currently, Al alloys are massively used both for structural components in the car body (e.g. space-frame and bumpers [8,9]), and for critical

components forming the combustion chamber, such as cylinder heads and pistons, where Al high thermal conductivity is beneficial. Moreover, the adoption of Al pistons also enhances secondary mass savings, such as that of con-rods and crankshafts. This is the main reason behind the adoption of Al alloys in the major part of all passenger cars pistons, cylinder heads, crankcases. Nevertheless, the main limit of aluminium alloys is to maintain adequate mechanical properties at temperatures exceeding around 200°C, due to overaging (precipitates coarsening) which negatively affects the alloy hardness and strength. Specifically focusing on pistons, the decay of mechanical properties places significant limits to pistons operating temperatures and/or mechanical loads at the specific temperature, feeding at the same time an active research aimed to increase or somehow stabilise Al mechanical properties up to 300°C.

Generally speaking, to further promote mass savings, it is necessary to increase the strength-to-weight ratio (R/ρ) of Al alloys at high temperature, which requires: (i) an increase of Al alloys resistance at high T and/or (ii) a reduction in alloy density.

2. Increased engine efficiency. The mere mass saving cannot meet the requirements on CO_2 emissions, but a parallel, never-ending research aimed to increase the ICEs efficiency is needed. Besides hybridisation and the reduction of both friction losses and aerodynamic drag, significant improvements could be reached through the increase of combustion efficiency. Focusing on spark-ignition engines, among the most promising strategies there is engine downsizing, which implies a higher specific power thanks to the adoption of turbochargers [6,10]. As a drawback, these higher efficiency engines are characterised by drastically increased temperature and pressure conditions inside the combustion chamber, which lead to:
    - Higher thermo-mechanical stresses on pistons and cylinders under normal combustions
    - More likely occurrence of knocking combustions: it is in fact necessary to accept light knock in order to reap the full benefits of turbocharging. Due to its pressure oscillation and local heating, knock further increases the thermo-mechanical stresses of pistons and combustion chamber components in general.

Both these factors further emphasize the need of Al alloys with enhanced mechanical properties at high temperature for pistons production; in addition, their resistance to knock

should be assessed, in order to determine the acceptable knocking thresholds, which allow to reach the operating points of maximum efficiency, without compromising engine (and in particular pistons) functionality.

On this basis, it is evident how *material properties themselves contribute in setting the lower limit of fuel consumption*. Light and heat resistant Al alloys for automotive pistons, with increased R/ρ ratio at high temperature, able to both produce secondary mass savings and to withstand light knocking combustions, might be considered a key factor in order to move forward in the path of "zero-emissions vehicles".
During the Ph.D. activities, many research efforts have been done towards these interconnected aspects, as highlighted in Fig.iii:

- The first part of the Ph.D. thesis deals with both conventional Al alloys, currently adopted for pistons production, and innovative Al alloys which are indeed considered to be promising in this field. Most of the research activities about the conventional alloys consists of chemical modifications, heat treatments optimization and tensile testing at room and high temperature, all of which accompanied by in-depth microstructural characterization. In particular, most of the alloys object of the activities have been provided by Duraldur S.p.A. and Ducati S.p.A., and part of the in-depth TEM and STEM characterization has been conducted in cooperation with the Norwegian University of Science and Technology (NTNU), Dept. of Physics and Dept. of Materials Science and Engineering and Dept. of Physics.
- The second part of the Ph.D. thesis collects all the experimental activities dealing with the study of knocking damage on Al automotive pistons, carried out in cooperation with Ferrari Auto S.p.A. and Fluid Machinery Research Group – Unibo. Several bench tests have been carried out on the 3.9 liter bi-turbo V8 GDI turbocharged engine equipping the Ferrari California T model (412 kW; 560 Hp at 7500 rpm and 755 Nm torque at 4750 rpm). The spark advance of each single cylinder was separately controlled by imposing a targeted MAPO 99.5% or 98%; the max test duration was set to 20h. Pistons consist of the commercial Al-Si alloy M142P, provided by Mahle GmbH.

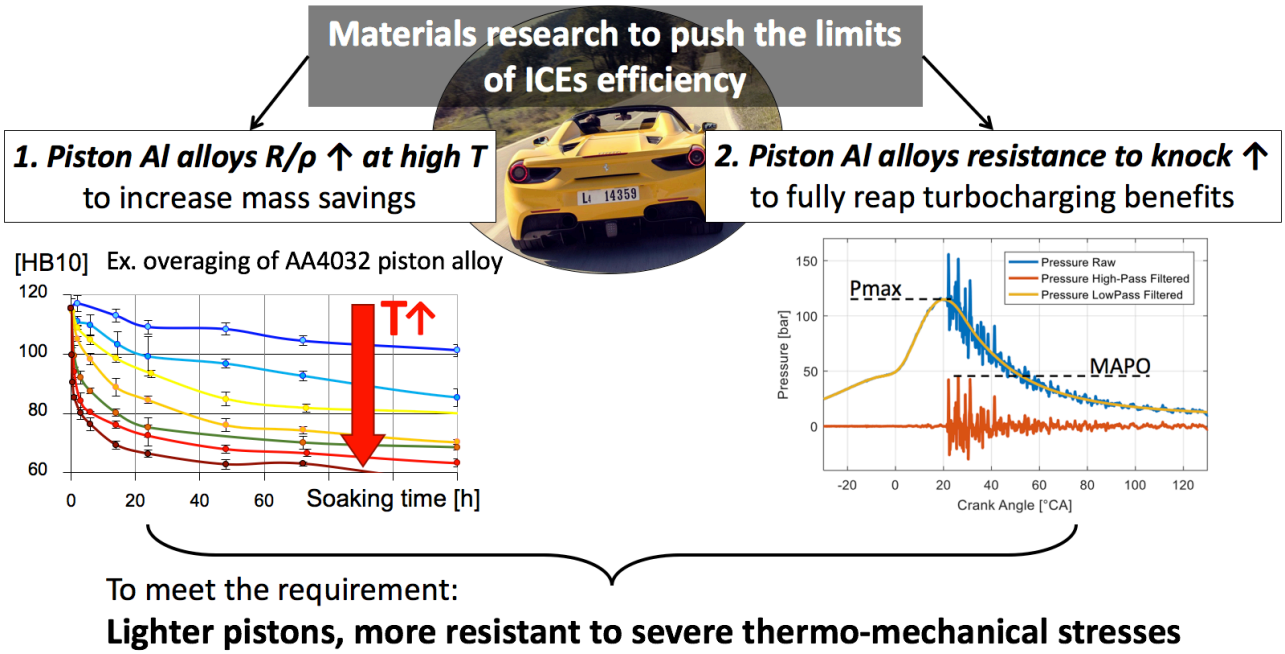

Fig.iii: Two main research issues of the Ph.D. thesis, given the golden thread of internal combustion engines efficiency / CO_2 reduction.

Bibliography

[1] European Environment Agency, Annual European Union greenhouse gas inventory 1990–2016 and inventory report 2018, 2018. https://www.eea.europa.eu/publications/european-union-greenhouse-gas-inventory-2018.

[2] Reducing CO2 emissions from passengers cars, (2017). https://ec.europa.eu/clima/policies/transport/vehicles/cars_en (accessed September 1, 2018).

[3] REGULATION (EU) No 253/2014 OF THE EUROPEAN PARLIAMENT AND OF THE COUNCIL of 26 February 2014, 2014.

[4] G. Archer, 2025 CO2 Regulation- The next step to trackling transport emissions, Transp. Environ. (2015) 2–5.

[5] J.J. Michalek, P.Y. Papalambros, S.J. Skerlos, A Study of Fuel Efficiency and Emission Policy Impact on Optimal Vehicle Design Decisions, Trans. ASME. 126 (2004) 1062–1070. doi:10.1115/1.1804195.

[6] H. Vafamehr, A. Cairns, O. Sampson, M.M. Koupaie, The competing chemical and physical effects of transient fuel enrichment on heavy knock in an optical spark ignition engine, Appl. Energy. 179 (2016) 687–697. doi:10.1016/j.apenergy.2016.07.038.

[7] J. Mutzke, B. Scott, R. Stone, J. Williams, The Effect of Combustion Knock on the Instantaneous Heat Flux in Spark Ignition Engines, SAE Int. (2016). doi:10.4271/2016-01-0700.Copyright.

[8] E.A.A. European Aluminium Association, Applications- Car body- Body structures, in: Alum. Automot. Man., 2013.

[9] W.S. Miller, L. Zhuang, J. Bottema, A.J. Wittebrood, P. De Smet, Recent development in aluminium alloys for the automotive industry, Mater. Sci. Eng. A. 280 (2000) 37–49.

[10] Y. Qi, Z. Wang, J. Wang, X. He, Effects of thermodynamic conditions on the end gas combustion mode associated with engine knock, Combust. Flame. 162 (2014) 4119–4128. doi:10.1016/j.combustflame.2015.08.016.

PART A
AL ALLOYS FOR AUTOMOTIVE PISTONS

As highlighted in the General Introduction Sect., vehicle lightweighting is a key issue in order to fulfil the stringent EU regulations in terms of CO_2 and harmful emissions. The growing demand for weight reduction in the transport field fosters the use of aluminum alloys also for crucial engine components, such as engine head, crankcase and pistons, which operate at high temperature. The main limit of Al alloys is, however, to maintain high values of strength-to-weight ratio (R/ρ) at temperatures exceeding 200°C, due to:

i. the continuous decrease of mechanical properties induced by overaging, which consists in a diffusion-controlled coarsening of strengthening precipitates, depending both on temperature and time of exposure;
ii. the alloy softening, connected to the higher mobility of dislocations.

In particular, among engine components, pistons are the most critical for both design and alloy development, due to the continuous high temperature exposure and the consistent thermo-mechanical stresses induced by combustions. Moreover, piston weight is determining for secondary mass savings, such as that of con-rods and crankshafts.

After a brief overview on piston working conditions and the consequent requirements for piston alloys (Chapter 1), followed by an outlook to the mechanisms which affect Al alloys softening at high temperature (Chapter 2), Part A of this Ph.D. thesis collects the experimental activities carried out on two groups of typical Al alloys for pistons, with the aim to study a possible increase in the alloys resistance at high temperature and/or to evaluate the potential reduction in the alloy density: Al-Si alloys in Chapter 3 and Al-Cu in Chapter 4.

THEORETICAL BACKGROUND

Chapter 1:

Automotive pistons

1.1 Piston functions and working conditions

Piston is one of the most complex and crucial component of automotive engines, demonstrated by the fact that the research on new geometries, materials and coatings for pistons has always been extremely active. Basically, its fundamental functions are [1–4]:

- To transmit the combustion power: piston transfers, via piston pin and connecting rod, the combustion pressure to the crankshaft for producing rotation.
- To form the combustion chamber, together with cylinder head and cylinder wall which guides the moving piston, as clearly visible in Fig.1.1:
    - in conjunction with the piston rings, piston help sealing the cylinder, in order to prevent the escape of combustion gases;
    - Piston is involved in dissipating the absorbed combustion heat to the cylinder liner and the cooling oil.

These functions determine the severe mechanical and thermal stresses of pistons, which are separately taken into account in the following paragraphs.

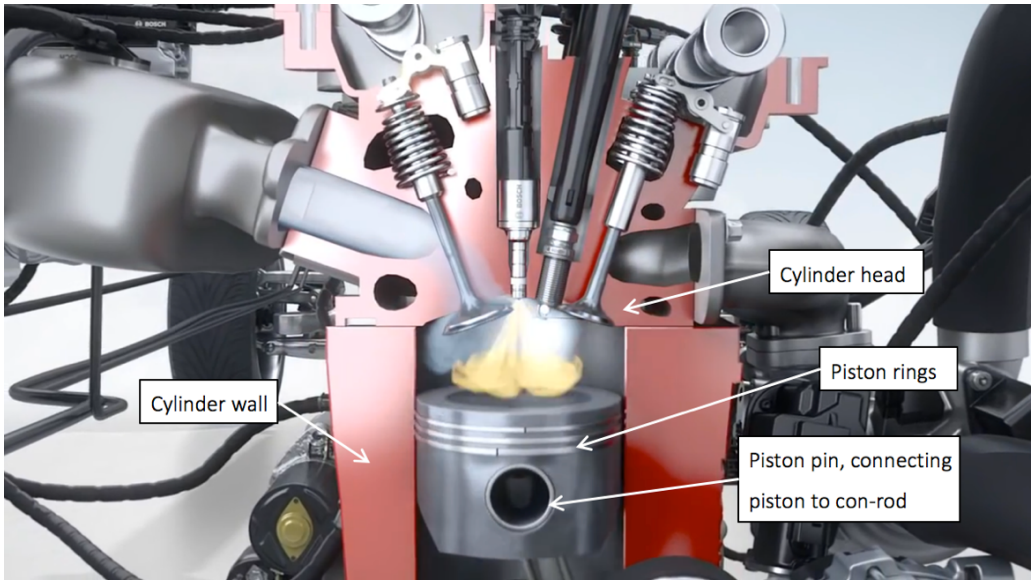

Fig.1.1:Section of direct-injection spark ignition engine, showing the piston working conditions (from [5]*).*

1.1.1 Piston mechanical loads

Part of piston mechanical loads are due to the fact that piston directly receives the combustion pressure, which is converted into rotation of the crankshaft and therefore into brake power. The today spark ignition engines reach up to 200bar as peak combustion pressure [2].
The resulting force F_G produced by gas is axial and not constant over the combustion cycle. In particular, as can be highlighted by any in-chamber pressure signal (Fig.1.2), gas pressure p is function of the crank angle (ϑ) and it achieves its maximum value during the combustion phase.

$$F_G = [p(\vartheta) - p_0] \cdot \frac{\pi D^2}{4}$$

where:

- p(ϑ)= in-chamber pressure (function of crank angle ϑ)
- p_0 = crankcase pressure
- D = piston diameter

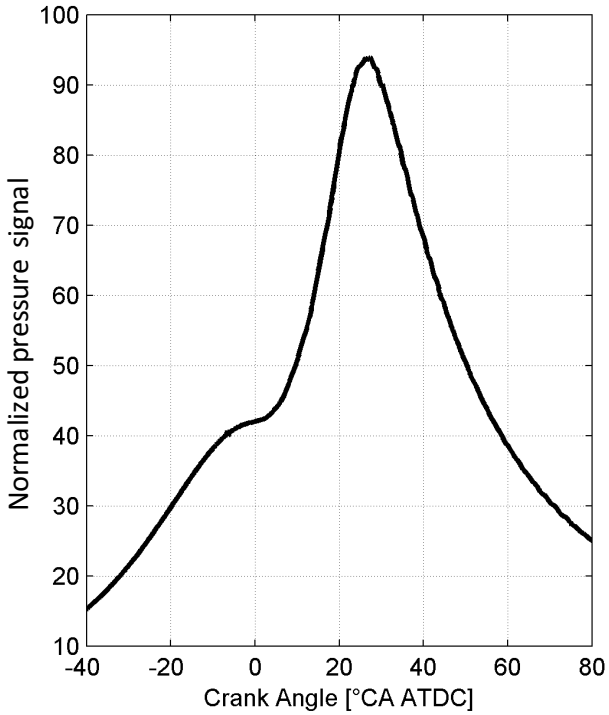

Fig.1.2: Mathematical expression of the axial force due to in-chamber gas pressure p(ϑ) and its variation during a combustion cycle.

Not to be neglected also the inertia load F_i, which is axially directed and it is therefore superimposed to the combustion gas force F_G. The inertial effects are due to the acceleration produced by piston reciprocating motion, which determines a variable piston speed during its stroke. As reported in [6,7] and shown in Fig.1.3, piston speed is null in correspondence of top dead center (TDC) and bottom dead center (BDC), while piston acceleration here reaches its maximum values. Piston inertia load is clearly proportional to piston acceleration, reported in its mathematical formula in Fig.1.3b.

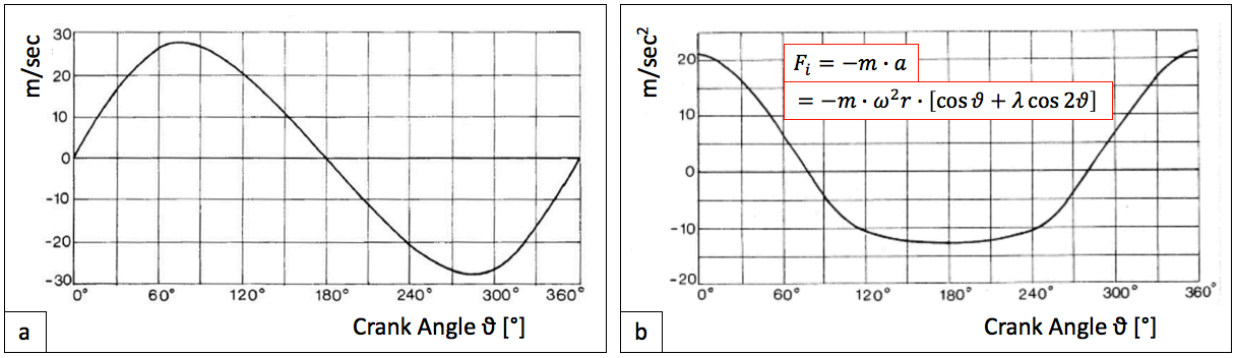

Fig.1.3: Piston speed (a) and acceleration (b) as a function of crank angle [7]. *Numerical data are calculated considering piston stroke = 2r = 85mm, (Crank radius)-to-(con-rod length) = λ = 0,24, rpm=6000.*

Approximatively, the absolute value of inertia load is directly related to mean piston speed [6,8,9]. The mean piston speed can be calculated as a function of the engine rotation speed and piston stroke; Eq.1.1 reports the mathematical formula for mean piston speed and the numerical value of Ducati Superbike 1299 Panigale, which reaches the maximum power at 10'500 rpm:

$$\widetilde{s_{pist}} = 2 \cdot \frac{rpm}{60\ s/min} \cdot stroke \xrightarrow{Ducati\ SB\ 1299\ Panigale} 2 \cdot \frac{10500\ rpm}{60\ s/min} \cdot \frac{60{,}8\ mm}{1000\ mm/m}$$
$$= 21{,}3\ m/s$$

Eq.1.1: Calculation of mean piston speed in Ducati SuperBike 1299 Panigale.

This value indicates that Ducati is a high performance engine, since the typical mean piston speed for 4 stroke motorcycle pistons is in the range 15-18 m/s, while it might reach 10-20 m/s for passenger cars pistons [8]. It should be stressed that mean piston speed (and therefore inertia load) is directly related to piston stroke, besides engine rotation speed which usually reaches high values in racing engines. Together with piston diameter, the stroke determines engine displacement and thus significantly contribute to setting the engine max power. In order to maintain high engine performance, both high engine displacement and low inertia loads should be pursued. In addition to piston lightweight, the stroke is thus usually kept as low as possible, the low displacement being compensated by high piston diameter and giving origin to square or over-square engines.

The abovementioned axial forces F_G and F_i approximately reach the same order of magnitude and both contribute to the normal force F_N, as shown in Fig.1.4. The F_N load is sustained by the con-rod reaction, which forms an angle with respect to pin axis. Due to this redirection, a lateral force F_L arises in addition to the normal force F_N. Hence piston sides are differentiated into

(major) thrust side and anti-thrust side, in case the side is loaded during the power event or during the compression event respectively.

Since the cylinder wall guides the reciprocating piston motion, it withstands the lateral force F_L which produces high friction losses. It is in fact reported in literature that pistons are responsible for 30-40% of the overall friction loss in an engine [10]. Aiming to reduce friction (and dissipate heat), cylinder walls are usually invested by oil and almost all today cylinder liners are honed, in order to produce a texture able to retain the lubricant; moreover, piston skirt has usually an anti-friction coating [1].

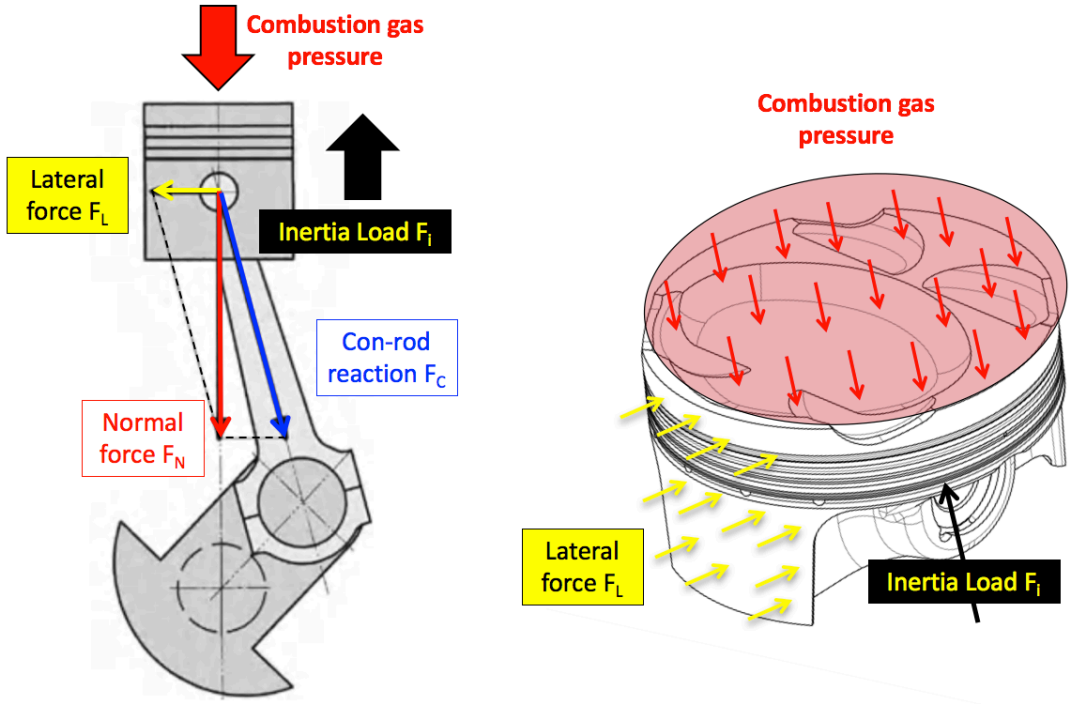

Fig.1.4: Piston mechanical loads due to combustion gas pressure.

As well as the axial force F_N, also the lateral force F_L produces fatigue stress on pistons: as reported in Fig.1.5, the contact pressure between cylinder bore and piston skirt changes direction several times during the combustion cycle [3,11,12], depending on piston tilting, piston lateral motion and bore distortion.

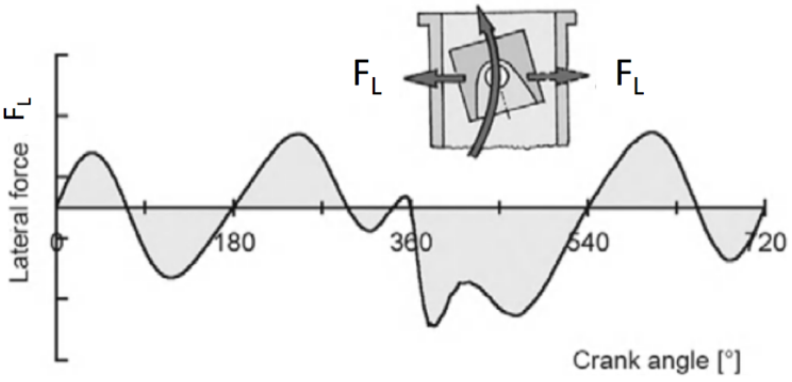

Fig.1.5: Non-constant lateral force F_L acting on pistons [3].

1.1.2 Piston thermal loads

Thermal loading substantially derives from the fact that pistons are directly in contact with the mixture of fuel and air burnt inside the combustion chamber, which can reach peak temperatures in excess of 2000°C [1–3,12]. Together with heat dissipation to the walls and coolants, the fresh intake air or mixture lowers piston temperature; the intake gas temperature reaches its maximum values in turbocharged engines, where it can reach 40-70°C or even exceed 200°C in case the intercoolers are not adopted. Due to material thermal inertia, however, piston head does not exactly follow these temperature fluctuations, but vary of just a few °C [3].
Generally speaking, the temperature levels and distributions in an automotive piston depend on several parameters:

- Engine characteristics: gasoline or diesel engines, turbocharged or not, direct injection (DI) or port fuel injection (PFI)
- Engine operating point: temperatures generally increase with increasing rpm and load
- Engine calibration: spark advance (SA), air/fuel ratio
- Combustion chamber geometry: piston geometry, material and amount of heat dissipated through cylinder and cylinder head cooling channels
- Piston cooling system (in case it exists): in high performance engines, oil squirters/nozzles are secured to the block and hit the underside of the piston through pressurized oil at intake and exhaust side [13]. In this case, piston temperature field also depends on the number of squirters, their location and the oil mass flow. The other parts of the piston underside area are usually simply invested by the oil centrifuged by the crankshaft rotation.

Pistons might also have an internal cooling channel (usually characterizing diesel applications).

The order of magnitude of the influence of each single parameter on pistons temperature at the 1st ring groove is highlighted in Table 1.1. It should be pointed out that, a part from the presence of piston cooling and the coolant temperature, the in-chamber pressure plays a relevant role. This characteristic will be in depth discussed in Part B of this Ph.D. thesis.

Table 1.1: Effects of various operating parameters on the temperature in the 1st piston ring groove (from [3]*).*

Operating parameters	Change in engine conditions	Change in temperature in the 1st piston ring groove
Coolant temperature	10°C	4–6°C
Water cooling	50% antifreeze	5°C
Lubricating oil temperature (without piston cooling)	10°C	1–2°C
Charge air temperature	10°C	1.5–3°C
Piston cooling with oil	Spray nozzle at conrod big end	–8°C to –15°C on one side
	Stationary nozzle	–10°C to –30°C
	Salt-core cooling channel	–25°C to –50°C
	Cooled ring carrier	–50°C (additional reduction in temperature, relative to the salt-core cooling channel)
Cooling oil temperature	10°C	4–7°C
Brake mean effective pressure p_{me} (n = const.)	1 bar	4–8°C
Speed n (p_{me} = const.)	100 rpm	2–4°C
Ignition angle, injection timing	1°CA	1.5–3°C
Air/fuel ratio λ	Range of variation λ = 0.8–1.0	< 10°C

The temperature field reported in Fig.1.6 can be considered representative of a piston equipping a turbocharged gasoline engine, with oil cooling system hitting piston bottom [3]. The peak temperature (around 300°C) is reached at piston crown [3,12]; beneath the 1st ring groove, the temperature considerably decreases due to the heat transferred from piston to its rings and finally to cylinder wall and lubricant; the average temperature in correspondence of piston pin boss and piston skirt is usually lower than 200°C.

As reported later in Part B of this Ph.D. thesis, piston temperature field plays an active role in favoring abnormal combustions in gasoline engines and it significantly influences engine

calibration strategy and fuel consumption as a consequence. Even regardless of material strength at high temperature (which has a substantial impact on the choice of piston materials), it is desirable to have low temperatures at piston crown.

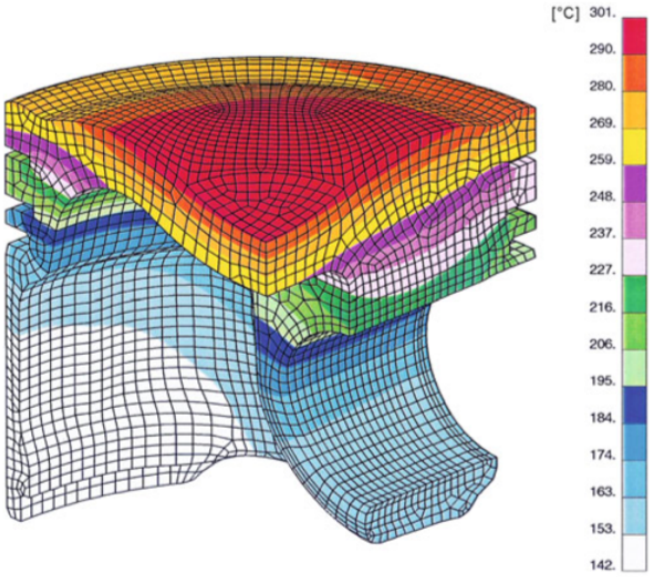

Fig.1.6: Temperature distribution in a gasoline engine piston [3].

1.1.3 Requirements for piston materials

The aforementioned piston functions and subsequent working conditions, directly turn into requirements which help guiding the choice of materials for this component [1,2,4], as below highlighted.

1. Piston transmits the combustion power and it withstands severe thermo-mechanical stresses:
    - Piston material should necessary retain an adequate resistance at high temperature, in particular at piston crown where T around 300°C can be reached)
    - Piston material should exhibit a high thermal conductivity, to promote a uniform T at piston head and limit peak T, which contributes in avoiding abnormal combustions.
    - Piston mass should be kept as low as possible in order to limit the F_i generated by its alternating motion and to emphasize secondary mass savings (mainly con-rod, crankshaft). It is worth pointing out that the requested lightweight design increases stresses on piston material due to the narrower sections supporting the external forces: a high R/ρ ratio is therefore necessary.

- Due to the lateral force F_L and the consequent high contact pressure between piston and cylinder bore, piston skirt material should be wear and scuffing resistant and the two tribo-elements (piston and cylinder liner) should exhibit low friction coefficient.

2. Piston forms the combustion chamber and it helps sealing combustion gases:
   - In order to lower the power loss connected to blow-by (combustion gases entering into the crankcase) even during engine warm-up, the clearance of piston skirt to cylinder wall is kept as low as possible (≈25÷100μm). As a consequence, piston should maintain a low thermal expansion.
   - Due to the high combustion pressure on rings, piston should be wear resistant at ring grooves and have a low chemical compatibility with rings material, in order to avoid micro-welding which significantly penalize rings functionality.
3. Piston for passenger cars should be mass produced: material should be not expensive and have a high machinability and formability.

These basic requirements are summarized in Fig.1.7 with reference to specific piston areas.

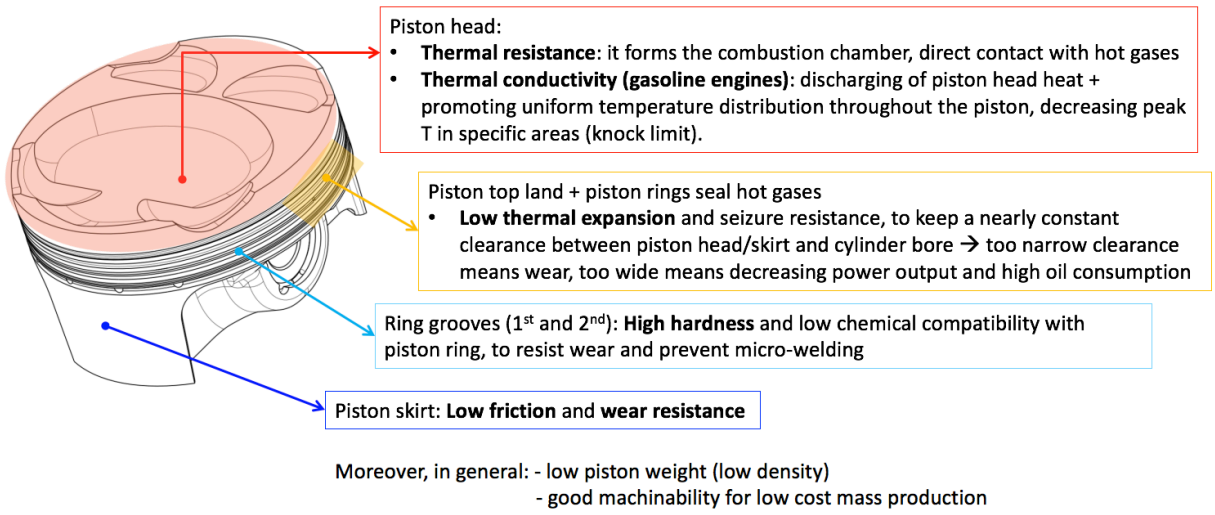

Fig.1.7: Summary of basic requirements for piston materials.

1.2 Typical materials for pistons

1.2.1 Bulk materials

In addition to literature survey, the wide range of products supplied by one of the most famous pistons producer (Mahle [3]) was mainly considered for the determination of the most common piston materials. The main categories competing as piston materials are:

- Al alloys, which cover the majority of gasoline pistons;
- Steels (or cast irons), traditionally adopted in case the strength at high temperature or wear resistance of Al alloys is not sufficient to meet the loads. This regards in particular diesel applications, which operate at higher in-chamber pressure and do not suffer from knocking phenomena (tolerating therefore the lower thermal conductivity and higher mean temperature of steel/cast iron pistons);
- Other materials, such as powder metallurgy components (even Al-based) and ceramics, which are usually niche products for racing prototypes.

Since the whole thesis deals with Al pistons, the principal Al alloys for pistons are following described. Besides many promising characteristics of Al alloys as regards the abovementioned requirements for piston materials, one of their main and very limiting drawbacks is the drop of properties at high temperature. The latter issue will not be considered in this chapter, since it deserves an in-depth examination and it is the core of Chapter 2. The criticality of Al strength at high temperature should be always taken into account since it guides the research for Al piston alloys.

Al-Si piston alloys

Traditionally, pistons are produced from cast or forged Al-Si alloys [1–3]. Apart from their low resistance at high temperature, these in fact exhibit many desirable characteristics for pistons:

- Low density compared to steel (ρ = 2.7 g/cm^3 VS 7.8 g/cm^3) and high R/ρ; Si additions further contribute in lowering piston weight.
- High thermal conductivity, in the range 140-160 W/mK at 20°C for eutectic Al-Si12 alloys (compared to 80 W/mK for spheroidal cast iron and 50 W/mK for steel).
- Low thermal expansion coefficient. Steel exhibits a lower thermal expansion coefficient (α_{steel} = 12 x 10^{-6} °C^{-1}) with respect to pure Al (α_{Al} = 23.5 x 10^{-6} °C^{-1}), however Si additions

significantly lower the thermal expansion coefficient of pure Al, and the reduction depends on the amount of Si (Table 1.2).

Table 1.2: Variation of Al-Si thermal expansion coefficient as a function of Si content (wt%) [3].

Alloy (Si wt%)	Al-Si (12)	Al-Si (18)	Al-Si (23)
Thermal exp [$°C^{-1}$] (range 20-100°C)	19.6 x 10^{-6}	18.6 x 10^{-6}	18.3 x 10^{-6}

Considering Al-Si phase diagram, three different microstructures can be obtained depending on the Si content: hypoeutectic, eutectic (12.6 wt% Si), hypereutectic (Fig.1.8).
Coarse primary Si crystals form first in hypereutectic alloys, usually in polygonal shape; due to their hardness, they favor the wear resistance of hypereutectic Al-Si alloys, but their brittle nature and sharp edges penalize the alloy ductility. The use of such alloys is usually confined to diesel engine pistons.

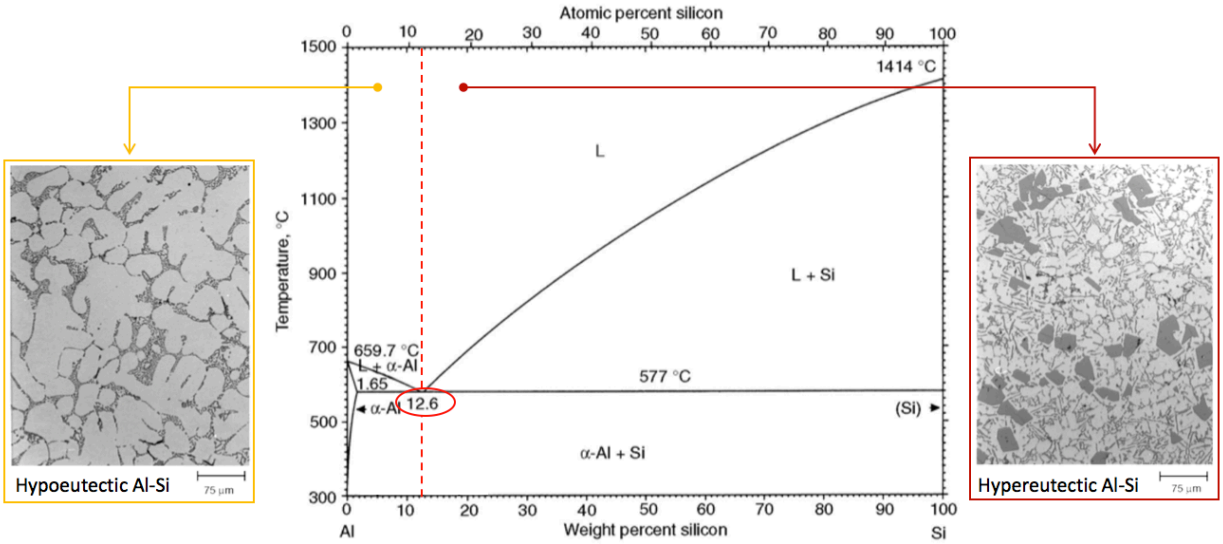

Fig.1.8: Al-Si phase diagram and optical micrographs representative of hypoeutectic and hypereutectic microstructures (from [14]*).*

It is indeed widespread the adoption of eutectic Al-Si alloys, similar to the commercial Mahle® M124 (for standard pistons) or M142 (for high performance pistons), whose chemical composition limits and mechanical properties are shown in Table 1.3 [3]. These alloys were in-depth studied during the Ph.D. activities, as reported in Chapter 3. In the eutectic Al-Si alloys, Si solidifies with a plate-like morphology, known to penalize fatigue resistance and ductility, so that

the morphology of eutectic Si particles are traditionally spheroidized thanks to the addition of small amount of Na or Sr (ppm) [1,15,16].

Compared to M124 (later referred to as AlSi12 alloy or AA4032), M142 (later referred to as AlSi12CuNiMg alloy or AA4032+Cu+Ni) contains the same amount of Si, but increased amount of Cu and Ni, which are known to enhance the thermal stability of Al alloys [17,18,27,28,19–26]. This is due to the fact that Cu and Ni form intermetallic phases (Al_7Cu_4Ni, Al_9FeNi, Al_3Ni_2, Al_3Ni, AlNiCuFeSi- based, AlCuNiSi-based) which are intrinsically more stable than the Al matrix at high temperature and provide an effective load transfer. The higher presence of intermetallics in AlSi12CuNiMg alloy is clearly visible by comparing Fig.1.9a and Fig.1.9b, while Fig.1.9c shows the nature of these secondary phases.

Table 1.3: Chemical composition and mechanical properties of Al-Si piston alloys M124 and M142 (produced by Mahle®), both in the cast and forged condition [3].

Alloys / El. [wt%]	M124	M142
Si	11.0 – 13.0	11.0 – 13.0
Cu	0.8 – 1.5	2.5 – 4.0
Mg	0.8 – 1.3	0.5 – 1.2
Ni	0.8 – 1.3	1.75 – 3.0
Fe	max 0.7	max 0.7
Mn	max 0.3	max 0.3
Ti	max 0.2	max 0.2
Zn	max 0.3	max 0.3
Cr	max 0.05	max 0.05
Zr	/	max 0.2
V	/	max. 0.18
Al	balance	balance

Cast alloys		M124	M142
Hardness HB10	20°C	90–130	100–140
Tensile strength R_m [MPa]	20°C	200–250	200–280
	150°C	180–200	180–240
	250°C	90–110	100–120
	350°C	35–55	45–65
Yield strength $R_{p0.2}$ [MPa]	20°C	190–230	190–260
	150°C	170–210	170–220
	250°C	70–100	80–110
	350°C	20–30	35–60
Elongation at fracture A_5 [%]	20°C	<1	<1
	150°C	1	<1
	250°C	3	1.5–2
	350°C	10	7–9
Fatigue strength σ_{bw} [MPa]	20°C	90–110	100–110
	150°C	75–85	80–90
	250°C	45–50	50–55
	350°C	20–25	35–40
Young's modulus E [MPa]	20°C	80,000	84,000–85,000
	150°C	77,000	79,000–80,000
	250°C	72,000	75,000–76,000
	350°C	65,000	70,000–71,000
Thermal conductivity λ [W/mK]	20°C	145	130–135
	350°C	155	140–145
Thermal expansion α [10^{-6} m/mK]	20–100°C	19.6	18.5–19.5
	20–200°C	20.6	19.5–20.5
	20–300°C	21.4	20.5–21.2
	20–400°C	22.1	21.0–21.8
Density ρ [g/cm³]	20°C	2.68	2.75–2.79
Relative wear rate		1	0.85–0,9

Forged alloys		M124P	M142P
Hardness HB10	20°C	100–125	100–140
Tensile strength R_m [MPa]	20°C	300–370	300–370
	150°C	250–300	270–310
	250°C	80–140	100–140
	300°C	50–100	60–100
Yield strength $R_{p0.2}$ [MPa]	20°C	280–340	280–340
	150°C	220–280	230–280
	250°C	60–120	70–120
	300°C	30–70	45–70
Elongation at fracture A_5 [%]	20°C	<1	1
	150°C	4	2
	250°C	20	6
	300°C	30	20
Fatigue strength σ_{bw} [MPa]	20°C	110–140	110–140
	150°C	90–120	100–125
	250°C	45–55	50–60
	300°C	30–40	40–50
Young's modulus E [MPa]	20°C	80,000	84,000
	150°C	77,000	79,000
	250°C	72,000	75,000
	300°C	69,000	73,000
Thermal conductivity λ [W/mK]	20°C	155	140
	150°C		
	300°C	165	150
Thermal expansion α [10^{-6} m/mK]	20–100°C	19.6	19.2
	20–200°C	20.6	20.5
	20–300°C	21.4	21.1
Density ρ [g/cm³]	20°C	2.68	2.77
Relative wear rate		1	0.9

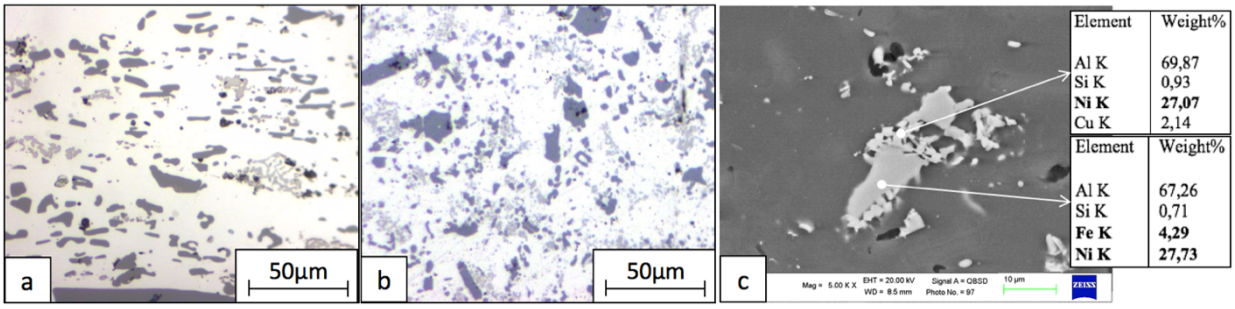

Fig.1. 9: OM micrographs of AlSi12 (a) and AlSi12CuNiMg piston alloy (b) in the peak-aged condition; (c) SEM micrographs highlighting Cu-Ni-Fe based intermetallic compounds in AlSi12 alloy.

Both alloys can be produced by casting or forging techniques. Due to the high castability of AlSi alloys (excellent fluidity and feedability) and the low cost of this technology, the majority of pistons for mass applications are produced by gravity die casting [1,3]. Hot forged pistons, however, show higher strength at relatively low temperatures (Table 1.3), thanks to their finer and more uniform microstructure; the more homogeneous mechanical properties also allow to reduce the safety factor for piston design. As a consequence, one of the main gains is the possibility to produce a lower wall thickness at pin boss area, enhancing lightweight [2,3].

The advantages of forged Al-Si alloys over cast ones vanish above 250°C, due to the fragmented nature of eutectic Si particles in forgings compared to the three dimensional and interconnected eutectic Si network embedded in the ductile α-Al matrix in castings [20,21,29]; this concept can be applied to any intermetallic compound in general. The degree of interconnectivity of these rigid phases can result in an extra increase of load transfer from the matrix to the reinforcement, particularly important at high temperature since the matrix is getting softer in a larger proportion than the reinforcement.

Al-Cu piston alloys

Al-Cu piston alloys are less widespread in the automotive scenario and used exclusively for forged pistons [3]. Considering the data provided by Mahle® for M-SP25 piston alloy and reported in Table 1.4, the benefits of this Al-Cu alloy over both the previously analyzed Al-Si piston alloys are evident in terms of R/ρ, while the alloy thermal expansion coefficient is higher for Al-Cu alloy (penalized by the negligible Si content). Due to the more expensive production route but high potential in terms of high temperature resistance, Al-Cu piston alloys are typically used for racing applications.

The commercial Mahle® M-SP25 Al-Cu alloy corresponds to the AA2618 alloy, in-depth investigated in [30] and studied during Ph.D. activities, as reported in Chapter 4. The alloy takes advantage of Fe and Ni, both present in quantities around 1wt% and forming high-temperature resistant secondary phases together with Cu [31,32], as reported in Fig.1.10. Moreover, the alloy might also contain low amount of Zr, element which is extensively used for its anti-recrystallization effects and it also induces the formation of high temperature resistant Al_3Zr precipitates [33,34].

Table 1.4: Chemical composition and mechanical properties of Al-Cu alloy M-SP25 (produced by Mahle®), in the forged condition [3].

Alloy / El. [wt%]	M-SP25
Si	max 0.25
Cu	1.8-2.7
Mg	1.2-1.8
Ni	0.8 – 1.4
Fe	0.9-1.4
Mn	max 0.2
Ti	max 0.2
Zn	max 0.1
Cr	/
Zr	/
V	/
Al	balance

Forged alloy		M-SP25
Hardness HB10	20°C	120–150
Tensile strength R_m [MPa]	20°C	350–450
	150°C	350–400
	250°C	130–240
	300°C	75–150
Yield strength $R_{p0,2}$ [MPa]	20°C	320–400
	150°C	280–340
	250°C	90–230
	300°C	50–90
Elongation at fracture A_5 [%]	20°C	8
	150°C	9
	250°C	12
	300°C	12
Fatigue strength σ_{bw} [MPa]	20°C	120–150
	150°C	110–135
	250°C	55–75
	300°C	40–60
Young's modulus E [MPa]	20°C	73,500
	150°C	68,500
	250°C	64,000
	300°C	62,000
Thermal conductivity λ [W/mK]	20°C	140
	150°C	
	300°C	170
Thermal expansion α [10^{-6} m/mK]	20–100°C	22.4
	20–200°C	24
	20–300°C	24.9
Density ρ [g/cm^3]	20°C	2.77
Relative wear rate		1.3

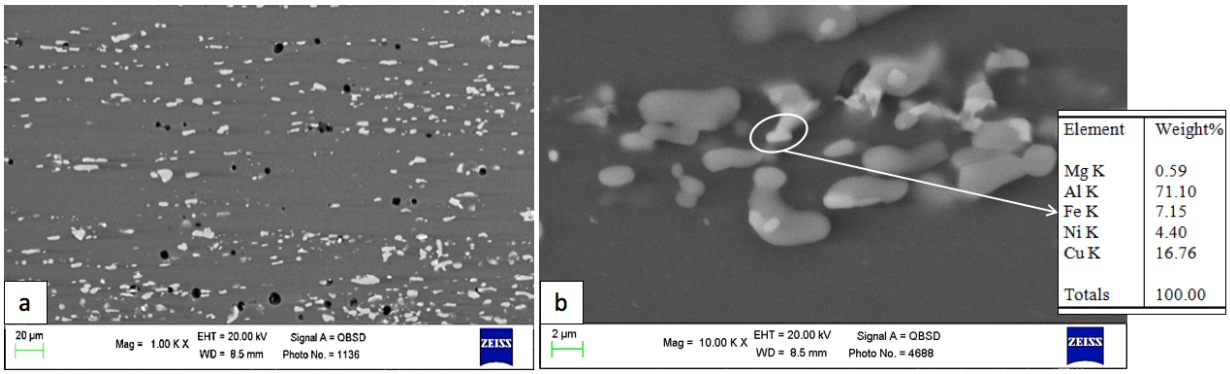

Fig.1.10: SEM micrographs of AA2618 piston alloy in the peak-aged condition at a) low magnification (1000X) and b) high magnification (10'000X).

Among Al-Cu alloys, also the less common belonging to Al-Cu-Li group are considered promising for pistons production: Li significantly contributes to a density reduction of the alloy [35] (it exhibits the lowest density among metals, equal to 0.534 g/cm^3), moreover it increases the Young's elastic modulus of the alloy (around 6% increase due to 1wt% Li addition [36]). Due to the importance of low mass in the reciprocating parts of engines, several experimental activities have been carried out during the Ph.D. [37–39] with the aim to evaluate AA2099 and AA2055 Al-Cu-Li

alloys resistance after thermal exposure and mechanical properties at high temperature (see Chapter 4 for the in-depth characterization).

Up to now, none of the available researches in literature show the adoption of these innovative alloys for pistons production nor any high temperature application. The enhancements in specific strength and stiffness have made indeed Al-Li alloys a competitive alternative to more conventional aluminum alloys (such as those of the 6XXX and 7XXX series) for structural applications in the aerospace field [40–44].

1.2.2 Hints to Al pistons coatings

Al pistons skirt typically exhibits a coating whose aim is to prevent piston seizure or even local welding between the piston and the cylinder in case of insufficient lubricant supply or reduced lubricant functionality due to excessively high temperatures. Grafal [2,3] is the standard coating for gasoline engines pistons produced by Mahle® and interacting with cast iron or steel cylinder surface + Nikasil coating. Grafal consists in a roughly 20µm thick polymeric matrix with graphite particles embedded, exhibiting self-lubricating properties, good wear resistance and able to withstand temperatures up to 250°C. The same concepts are applied to coatings based on heat resistant resins + embedded molybdenum disulphide (MoS_2), which exhibits anti-scuffing properties as well, and a mixture of embedded graphite and molybdenum disulphide can also be employed [45].

Phosphate, TiO_2 and DLC coatings on the whole pistons are less widespread, the latter typically adopted for both pistons skirt and cylinder liner to substantially reduce frictions in racing applications. Also electroless Ni coatings might be employed, mainly on pistons crown, in order to enhance a uniform temperature distribution and reduce the possibility of abnormal combustions (peaks temperature and hot spots might cause knocking combustions, as discussed in Part B). From the opposite side, ceramic thermal barrier coatings (TBCs) might be applied to pistons crown in order to favor an adiabatic combustion chamber [46], but these are not of interest for spark-ignition engines since their efficiency is more likely penalized by abnormal combustion modes.

In addition to piston skirt, also the 1st ring groove is normally coated, with the aim to prevent an anomalous wear of Al and 1st ring micro-welding or even sticking due to elevated combustion pressures and temperatures. Typically, Al pistons 1st ring groove is hard anodized, with a coating thickness of about 15-20µm. Thicker layers (up to around 30µm) can be adopted in case

of expected high wear of the anodized layer, in order to avoid direct contact between piston and its ring during the whole expected piston life.

In case of excessively high in-chamber pressure (and consequently elevated temperatures), hard anodizing might be no longer sufficient since it consists of a hard layer supported by a softened Al substrate, leading to the so called “ice-on-mud” effect) and a ring carrier might be required. The ring carrier is an external reinforcement method, and it frequently consists in a cast iron annular ring cast into Al pistons and positioned in the top-ring groove area [1]. Before the casting process, the insert is typically coated with Al, which acts as a binder and it helps forming a sound metallurgical bonding. It is indeed more difficult to adopt the co-forging process for ring carriers, in case the forging route is preferred for pistons.

Fig.1.11 shows an example of coatings adopted for high performance motorbike pistons. The same strategies are adopted for the analyzed Ferrari pistons, as reported in Sect.6.1 of this Ph.D. thesis which fully describe pistons objective of Unibo bench tests.

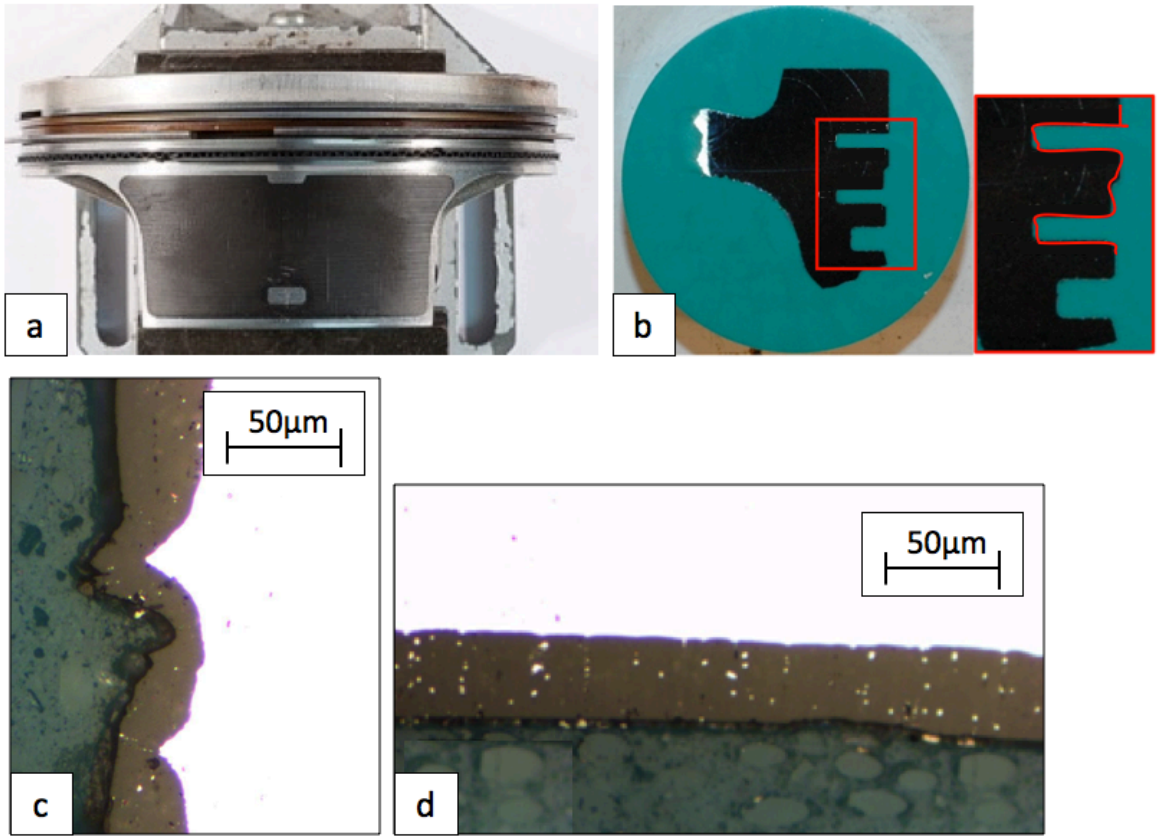

Fig.1.11: Images of piston equipping Ducati Multistrada 1200 engine: a) piston macrograph, revealing the presence of piston skirt coating; b) OM metallographic section of piston lands, where hard anodizing covers both 1st and 2nd ring groove as highlighted in red; c) and d) OM micrographs showing the presence of thick anodizing layer (≈25µm).

Chapter 2:

Thermal stability of Al alloys

2.1 Mechanisms affecting Al alloy properties at high temperature

2.1.1 Principles of diffusion

When dealing with heat resistance, diffusion plays the major role since it underlies all softening mechanisms occurring at high temperature. It is therefore essential to briefly discuss on the basis of diffusion before focusing in specific on Al alloys resistance at high temperature. From an atomic perspective, diffusion consists in the migration of atoms from a lattice site to another one. Different kind of diffusion can be identified, with respect to the diffusion paths [47,48]:

- *Vacancy diffusion*. In most metals and alloys, diffusion occurs by vacancies movement. This requires an empty adjacent site (vacancy), moreover the atom must reach the sufficient energy to both break bonds with its neighbor atoms and to cause the lattice distortion connected to the movement itself.
- *Interstitial diffusion.* If the solute atom is sufficiently small, however, it will locate in an interstice between the larger solvent atoms, forming an interstitial solid solution. Diffusion of interstitial atoms usually occurs by atoms jumping from an interstitial site to another.
- *Grain boundary diffusion.* Finally, atomic migration may also occur along the core of dislocations, grain boundaries or at secondary phases interfaces. Experimental studies have shown that this kind of diffusion is more rapid than diffusion through the interior of a crystal, given the higher amount of energy stored in proximity of microstructural discontinuities.

At room temperature, just a small fraction of atoms is capable of diffusive motion by virtue of their vibrational energy, but this fraction significantly increases with rising temperature, as well as the

vacancies density and atoms mobility. This is confirmed by the main mathematical law governing diffusion in solids [47,48]:

- Diffusion coefficient D [m^2/s], which indicates the rate at which atoms diffuse, increases with increasing temperature, following an Arrhenius-type equation (Eq.2.1):

$$D = D_0 e^{-\frac{Q}{RT}}$$

Where
- D_0 = constant (depending on the diffusing species) [m^2/s]
- Q =activation energy for diffusion (depending by the diffusing species and associated with the requirement that the atom must vibrate with sufficient amplitude to break the nearest neighbouring bonds to move to the new locations) [J/mol]
- R = gas constant =8.314 J/(mol K)
- T = absolute temperature [K]

Eq.2.1: Diffusion coefficient D.

- Fick's 1st and 2nd law for steady and non-steady state diffusion (reported in Eq.2.2 for one-dimensional diffusion in x direction) represent the mathematical relations that connect the concentration of the diffusing species with distance.

[1st] Steady state:

$$J = -D\frac{dC}{dx}$$

Where
- J = diffusion flux [mol/ m^2 s]
- D = diffusion coefficient (constant at a certain T) [m^2/s]
- C = concentration of a certain substance [mol/m^3]

[2nd] Non-steady state:

$$\frac{\partial C}{\partial t} = D\frac{\partial^2 C}{\partial x^2}$$

Where the effect of time t is incorporated with respect to the previous formula

Eq.2.2: Fick's laws for diffusion.

2.1.2 Heat treatment of Al alloys (T6, T7) and overaging

Due to the essential requirement of high specific strength, crucial components in the automotive field are usually made of *heat treated* Al alloys, which take advantage of precipitation strengthening in order to considerably increase their mechanical properties. As reported in [48–50], the basic requirements for Al alloys able to undergo precipitation strengthening is to have alloying elements with: (i) high equilibrium solid solubility at elevated temperatures, (ii) low solubility at room and moderate temperatures, (iii) the capability to form precipitates that strain

the lattice. The aforementioned requirements are necessary to fulfil the typical phases of the T6 heat treatment of Al alloys, which consists of solution, quench and subsequent aging to reach peak hardness. Each single phase and its critical issues are following described.

- *Solution* consists in holding the Al samples at high temperature (usually at T ≥ 500°C), with the aim to take into solid solution the maximum practical amounts of the soluble hardening elements in the alloy and to dissolve most of the coarse intermetallic particles, forming a homogeneous solid solution between Al matrix and alloying elements. Moreover, the chemical segregation which intrinsically accompanies dendrites formation is reduced. The whole solution phase relies on the phenomenon of diffusion, therefore it is a time-temperature dependent process [47].

  Due to the huge presence of diverse alloying elements in high performance Al alloys, secondary phases usually show different dissolution temperature and eutectic or low temperature melting phases are often encountered. In order to avoid incipient melting during heat treatment, which would lead to inhomogeneous microstructure and consistent decrease of mechanical properties, it is fundamental not to exceed the melting temperature of these eutectic phases. If appreciable eutectic melting occurs as a result of overheating, in fact, properties such as tensile strength, ductility, and fracture toughness may be degraded [48].

  Since lower solution temperatures expand the heat treatment time (and time of furnace employment as well, penalizing both the productivity and the cost-per-part), a two-step solution heat treatment is often carried out to overcome the incipient melting issue: the 1^{st} stage of the solution treatment is performed at temperature below the eutectic phase melting and it lasts until its complete dissolution; higher temperatures characterize the 2^{nd} stage, which is aimed to complete the solution process, making all solute atoms available for the subsequent precipitation hardening. Compared to a single-step solution treatment, which would be characterized by a lower temperature due to incipient melting of eutectic phases, the two-step solution is able to considerably shorten the treatment time.

- *Quench* is a rapid cooling from the solution temperature up to that of the quench medium (usually hot water at T ≈ 50°C). The cooling rate is one of the most critical issue of T6 heat treatment, since a high cooling rate is necessary to retain alloying elements in solid solution. In fact, given the difference in solid solubility at solution vs quench temperature (one of the aforementioned fundamental requirements for Al alloys to be suitable for heat treatment), a supersaturated, metastable solid solution is obtained, which tends to evolve towards an

equilibrium re-arrangements of atoms. The objective of quench is not only to retain solute atoms in solution, but also to maintain a certain minimum number of vacant lattice sites to assist in promoting the low-temperature diffusion required for precipitates formation [48].

- *Artificial aging* is the final stage: starting from a supersaturated solid solution, it is aimed to promote the formation of evenly spaced and coherent strengthening precipitates, in order to achieve the peak hardness (in case of T6 heat treatment). Temperatures in the range 150°C-200°C are usually involved to enhance and accelerate the formation of strengthening precipitates (compared to natural aging which consists in holding at room temperature for several days). Different steps of microstructural evolution might be covered during the aging thermal exposure:
    - at first, the formation of Guinier-Preston (GP) zones occurs, which consist in solute atoms collected into a cluster which still has the same crystal structure as the solvent phase;
    - then, prolonging thermal exposure, GP zones usually turn into coherent precipitates, which provide the maximum strengthening effects as subsequently explained;
    - finally, coherent but metastable precipitates tend to coarsen into semi-coherent and eventually equilibrium incoherent phases.

Since the amount of strengthening by precipitation hardening depends on the lattice distortion of Al matrix, the aforementioned microstructural evolution is responsible of the variation of alloy hardness and mechanical properties, as visually reported in Fig.2.1a and referring to Al-Cu alloys. In particular, due to mismatch in size between matrix and precipitates, the strain field surrounding the coherent particles (Fig.2.1b) provides the highest strength by obstructing and retarding the movement of dislocations; the maximum hardness does not correspond to the formation of the equilibrium ϑ phase (Al_2Cu), but to the metastable, transition phases ϑ'', which form in a considerably finer distribution than does ϑ. In particular, simple hardness tests are able to keep track of the microstructural changes induced by aging, from which tensile properties can be determined thanks to the nearly linear relationship existing between alloy hardness and strength (as reported in [30,37,38,51] for Al-Cu and Al-Si alloys).

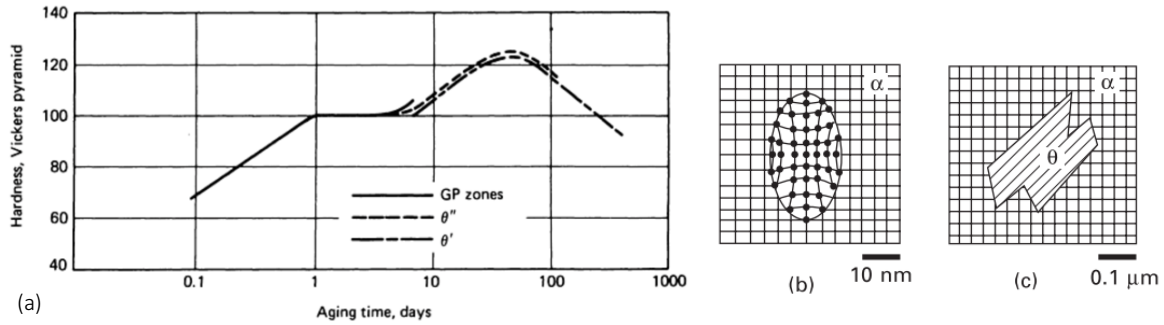

Fig.2.1: (a) Hardness curve for an Al-4Cu alloy showing the relationship between the various precipitates formed and the hardness on aging at 130 °C [48,52]*; (b) Strengthening coherent precipitate ϑ'', which distorts lattice structure* [1]*; (c) Coarsening of ϑ precipitates up to the loss of coherency, which provides lower lattice mismatch* [1].

As a matter of fact, the *aging curves* (temperature-time-hardness curves at different soaking temperature) are the most common tool adopted to optimize both time and temperature of aging. An example of aging curves is offered by Fig.2.2, which focuses on the heat treatment of AA2618 piston alloy [30]. It can be highlighted that, due to the diffusion-controlled nature of the aging process, the formation of strengthening precipitates (connected to hardness increase) is faster at higher temperature but very slow at temperature as low as 50°C, at which a hardness of 120HB cannot be reached even after 50h soaking. Peak hardness (around 140HB for the alloy at issue) is reached after roughly 4h of soaking at 220°C, 6h at 210°C, 20h at 200°C and 25-30h at 190°C. It has also to be noted that a hardness higher than 140HB is only achieved by heat treatments at 190°C or 200°C, and that a rapid decrease of hardness (and tensile properties) is observed while prolonging the soaking after peak hardness.

The observed results depend on the fact that higher precipitation temperatures are usually associated with a lower nucleation rate and thus a coarser precipitates distribution. Also, as the aging temperature approaches the solvus, the amount of precipitates decreases (vanishing at the solvus) [48]. However, the higher the temperature, the higher the rate of precipitation, and hence the maximum strengthening is attained in less time. It has also to be pointed out that the duration and temperature of solution and aging stages mainly depends on the diffusivity of alloying elements forming strengthening precipitates, while the microstructure before heat treatment plays a minor role (it affects the diffusion distance).

Contrarily to T6 heat treated Al alloys, aged with the aim to reach the peak hardness, alloys in T7 tempers are overaged, which means that some degree of strength has been sacrificed to improve dimensional stability, particularly in products intended for service at elevated

temperatures (T7 is frequently applied to cast or forged engine parts such as pistons). Aging temperatures used to produce T7 temper are generally higher than those used to produce T6 temper in the same alloys [53], in order to reduce the treatment time (see the aging curves reported in Fig.2.2).

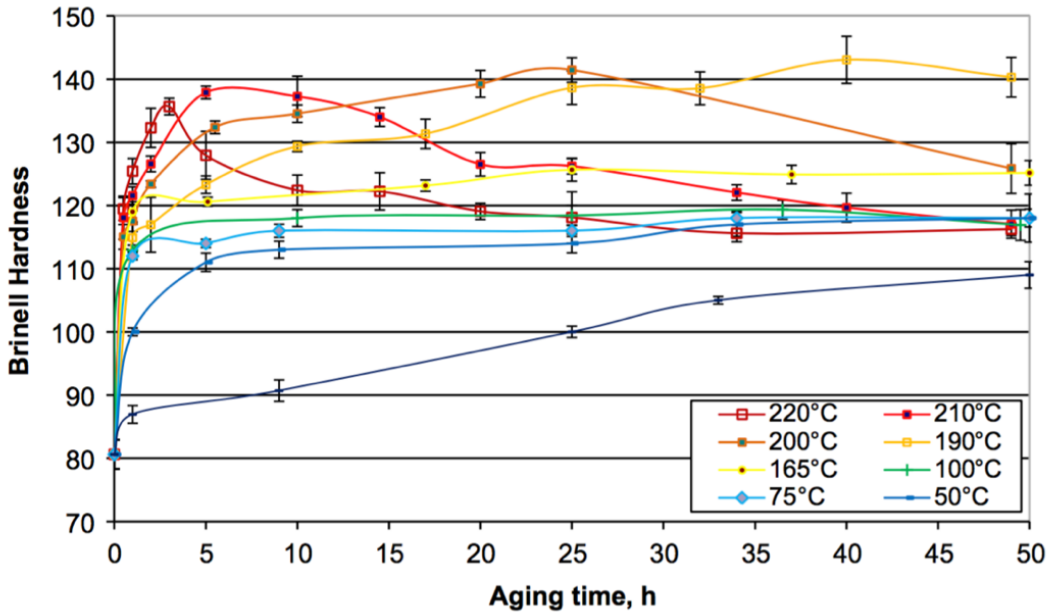

Fig.2.2: Aging curves of AA2618 piston alloy at different temperatures in the range 50°C-220°C, from [30].

As well as aging, also *overaging* is a diffusion driven phenomenon. Overaging consists in a rapid coarsening of strengthening precipitates, which finally lose their coherency with Al matrix and significantly reduce their strengthening effect. In view of what reported above, due to the metastable condition of coherent precipitates, overaging affects all the heat treated Al alloys. The alloy softening might be the result of a prolonged artificial aging, over the reach of peak hardness, or it might be provoked by a whatsoever thermal exposure at temperatures as high as 200°C or above. Once the formation of coherent precipitates has been attained, then further change in the precipitates is caused by the tendency for the system to reduce the precipitate/matrix interfacial area [48]. Thus, with time at a given aging temperature, the smaller precipitates dissolve, with the solute diffusing through the matrix and contributing to the growth of the larger particles. This results in a microstructure containing larger, but fewer, precipitates, which offer a lower contribution to alloy strengthening [48]. The evolution of precipitates is graphically shown in Fig.2.3 [48]; it should be noticed that precipitates coarsening usually starts from grain boundaries, due to the favored diffusion in these sites.

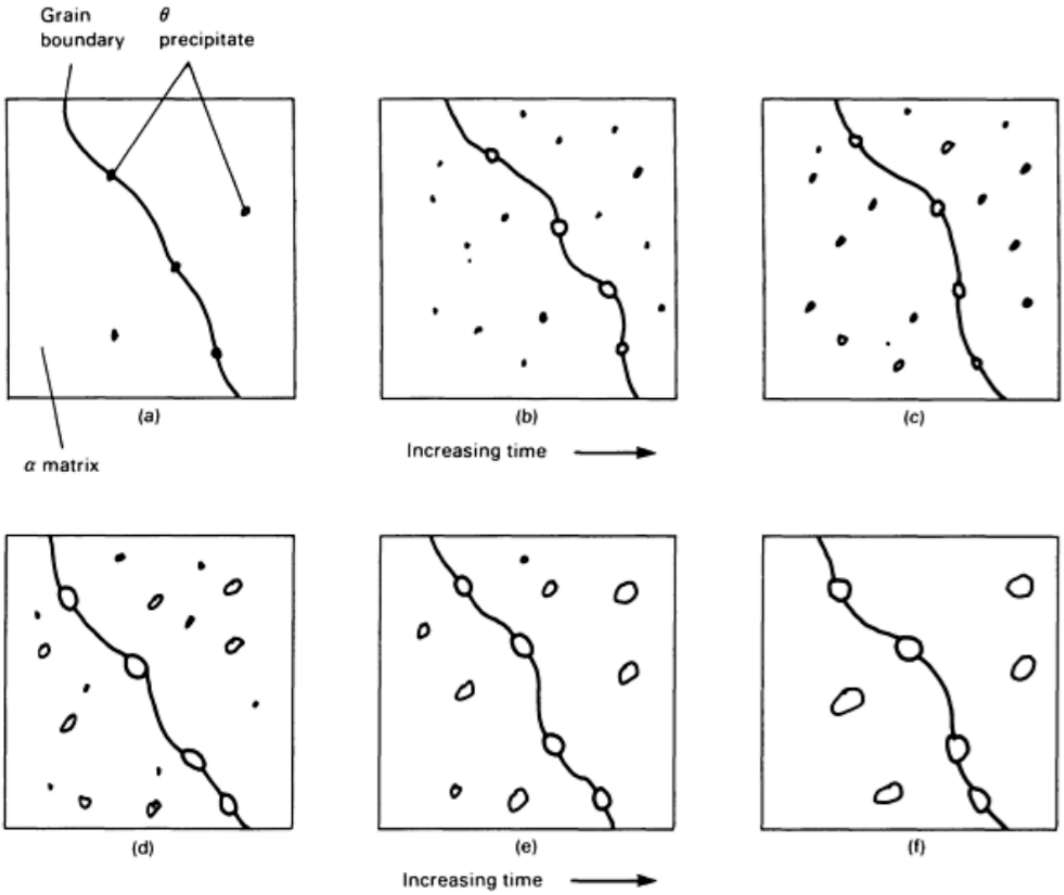

Fig.2.3: Schematic illustration of formation of ϑ precipitates in the α matrix (a and b) and their coarsening (c to f) [48].

The coarsening of strengthening precipitates is governed by Ostwald ripening. Generally speaking, this is a thermodynamically-driven spontaneous process, occurring during the latest stage of precipitation, and consisting in the growth of larger precipitates at the expenses of smaller ones. The phenomenon is based on the fact that large particles are more energetically favored and their coarsening minimizes the interfacial free energy [54]. Liftshitz et al. [55] and Wagner [56] showed that the average precipitate size R increases with time t according to Eq.2.3:

$$[R(t)]^3 - [R(t=0)]^3 = kt, \quad k \propto \frac{D\sigma}{\left({C_{equilibrium}}^{\beta} - {C_{equilibrium}}^{\alpha}\right)^2}$$

Eq.2.3: Coarsening rate of precipitates.

where:

- D = diffusivity of the rate-controlling solute
- σ = precipitate-matrix interfacial free energy
- C_{eq}^{β} is the equilibrium solubility of the solute in the precipitate phase
- C_{eq}^{α} is the equilibrium solubility of the solute in the matrix phase

In analogy to the aging curves, the so-called overaging curves (temperature-time-hardness curves) are able to keep track of the precipitates evolution. The rate of hardness decrease at a specific temperature and the minimum plateau of hardness are function of the thermal stability of the precipitates which strengthen Al matrix. An example of that is offered by Fig.2.4 [57], which compares the overaging curves of two different piston alloys, namely AA4032 Al-Si alloy and AA2618 Al-Cu alloy, which will be in depth discussed in Chapter 3 and Chapter 4.

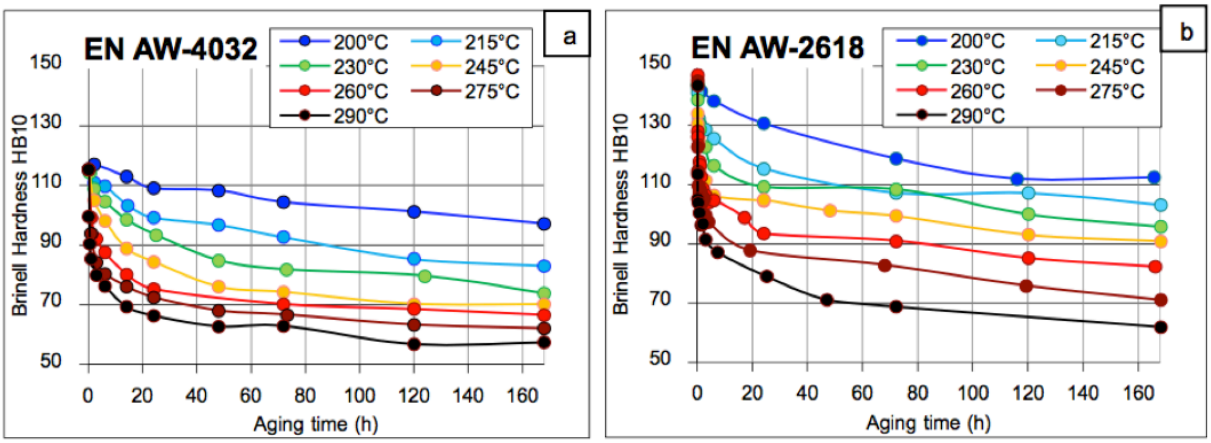

Fig.2.4: Overaging curves of a) EN AW-4032 and b) EN-AW 2618 alloys, in the range 200÷290°C [57].

2.1.3 High temperature phenomena: mobility of atoms, vacancies, dislocations and creep damage

Overaging, which is activated by high temperature exposure, continues affecting alloy properties also at room temperature, since it consists of phases and precipitates evolution and it strongly affects the strain field in Al matrix, as reported in the previous paragraph.

In addition to the metallurgical changes induced by overaging, however, high temperature is also responsible of a higher vibrational energy of atoms and a subsequent increased diffusion mobility. Favored by heat, diffusion is responsible of:

- A greater mobility of dislocations: dislocations climb is activated, in addition to dislocations glide which governs plastic deformation at room temperature. Work hardening cannot be therefore employed to strengthen materials at high temperature, due to the fact that dislocations are no more effective in preventing the movement of other dislocations. This is particularly true for Al alloys, which show a high value of stacking fault energy γ_{SFE}, which is directly proportional to dislocation mobility [58]. Moreover, recrystallization processes

are induced at high temperature, undermining the strengthening produced by the saturation of dislocations.

- An increased amount of vacancies, which considerably favors diffusion phenomena.
- The so-called "grain boundary sliding" [59]: grains are moving freely along their borders, giving origin to cavities and holes and promoting creep damage. Contrarily to material strengthening at room temperature, grain size reduction cannot be therefore employed under creep regime, due to grain boundary sliding.

In particular, creep occurs in any metal or alloy at a temperature where atoms become sufficiently mobile to allow time-dependent rearrangement of the structure [60]. As a consequence, even under a constant load well below the material yield stress, a permanent continuous deformation occurs, which might lead to component failure. Generally speaking, creep effects are visible at temperatures exceeding about 0.5 of the melting point of the material [K], which for Al alloys means at T≥200°C. Unfortunately, 200°C can be considered the lower temperature bound for some engine components, such as pistons, which means that high temperature mobility of atoms and creep should be taken into account.

Constant load creep curves usually consist of different stages, as displayed in Fig.2.5 [61]:

- An initial rapid elongation ε_0
- Primary creep: the creep rate rapidly decreases with time. The competing process of strain hardening and recovery eventually leads to a somewhat stable dislocation configuration.
- Secondary creep: it is also referred to as steady-state creep, since strain rate becomes nearly constant.
- Tertiary creep: the strain rate significantly increases, due to coalescence of voids or internal cracks which reduce the component cross section and permanently change its shape.

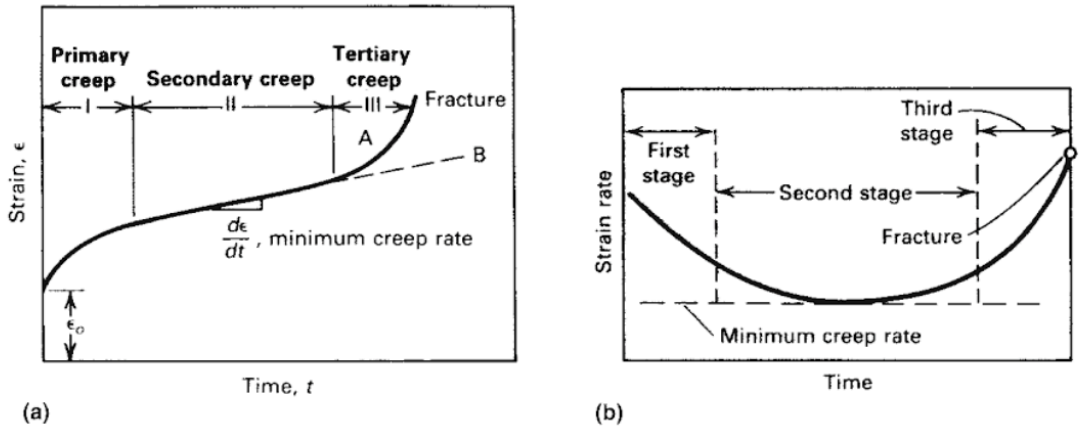

Fig.2.5: Typical shape of creep curves: (a) Creep strain; (b) Creep strain rate [61].

In conclusion, a creep-resistant material should satisfy the following requirements:

- to have a high melting temperature;
- to have a coarse grain structure: the less are grain boundaries, the less important or even negligible is grain sliding ([59,62]);
- To exhibit a high amount of thermally stable precipitates or secondary phases, able to pin grain boundaries (so-called pinning effect) and obstruct deformation ([59,62]).

The last point is considered the most effective contrast method against creep [59], and at the same time stable and close-spaced precipitates could assure strength even at high temperature. These guidelines have to be taken into account when considering Al alloys for pistons production, given the creep regime temperatures involved for these engine components.

2.2 Increasing resistance at high temperature

All the aforementioned issues which penalize Al alloys performance at high temperature, namely overaging, increased amount of vacancies, higher mobility of dislocations and creep damage, are connected to diffusion. In order to increase the resistance of materials under diffusion regime (considerably activated above 200°C for Al alloys), the main strategy is to put obstacles to the easy movement of lattice defects (dislocations), which is responsible of plastic deformation.
Generally speaking, dislocation mobility can be reduced by making dislocation interact with stress fields, created by other dislocation cells, sub-boundaries and grain boundaries or solute atoms, precipitates and dispersoids [63]. As mentioned in the previous paragraph, all obstacles become increasingly transparent to dislocation motion at elevated temperature, due to the dislocations climb or cross-slip activation. The effectiveness of dislocations cells or grain boundaries as obstacles is substantial just at low temperature. Strengthening at high temperature should be therefore directed towards slowing down the diffusional and thermally activated processes [63]. In the following paragraphs, each effective strategy would be separately taken into account, with a specific focus on Al alloys.

2.2.1 Solid solution strengthening

The strengthening mechanism provided by solid solution is due to the fact that solute atoms (both in substitutional or interstitial position in the matrix) impose a lattice strain on the surrounding host atoms [47], reducing dislocation movements and creating obstacles to their rearrangement. A high density of dislocations is therefore needed for the plastic deformation to proceed. For those elements that form solid solution, the strengthening effect increases with increasing difference in the atomic radii of the solvent [64]. Some alloying elements segregate to dislocations and form dragging obstacles [63].

Nevertheless, solid solution strengthening is not deeply effective in Al alloys in general, both at low and high temperature, because the matrix cannot dissolve any solute in significant quantities [54,58], if conventional production routes are considered.

2.2.2 Precipitation strengthening

Alloying to precipitate a second phase is perhaps the most effective and successful strengthening route [63]. Basically, two mechanisms control particles interaction with dislocations, depending on the coherency between the precipitates and the matrix, and in both cases the strength of interaction between dislocations and second phase particles is determined by the particle size and volume fraction and by the nature of the particles themselves.

In case of *not coherent* particles, there is a strong difference between matrix and precipitates deformation; in order to "accommodate" the deformation, dislocations will be stored in the matrix, next to the precipitates [58]. According to Orowan mechanism, successive dislocation loops are formed around precipitates during deformation, as shown in Fig.2.6; the smaller the precipitate radius, the smaller the precipitate spacing and the higher the precipitate volume fraction, the higher will be the resulting hardening effect. The stress τ required for dislocations movement is, in fact, inversely proportional to the distance L between the precipitates, as reported in Eq.2.4.

During Orowan looping, the material work hardens rapidly with strain due to dislocation foresting, and develops strength with deformation. The associated deformation is usually homogeneous [63].

$$\tau \propto \frac{G}{L}, where\ G\ is\ the\ shear\ modulus$$

Eq.2.4: Stress τ required for dislocation movements over coarsened precipitates.

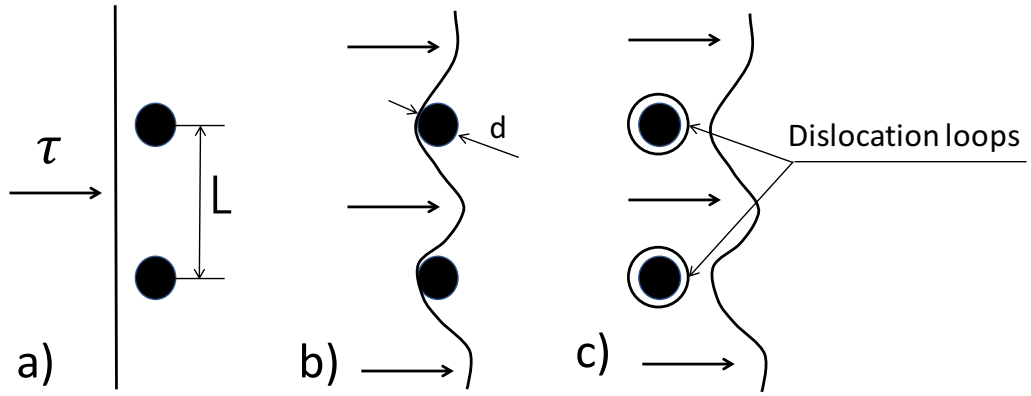

Fig.2.6: Orowan mechanism for not coherent precipitates (e.g. overaged precipitates). Dislocation passage occurs leaving dislocation loops around precipitates.

Coherent precipitates are indeed more effective in obstructing dislocations movement and pinning grain boundaries [65], because they require more energy for the dislocations to move past them: during the movement, in fact, the particles generally lose their coherence and high-energy, incoherent interfaces are built. The strengthening of alloys by lattice misfit occurs by virtue of the interaction between the dislocation and the stress field around the coherent particles. The possible interactions between coherent particles and high angle grain boundaries are described in Fig.2.7, where the latter is the well known Ashby mechanism, consisting in dislocation cutting through the particle.

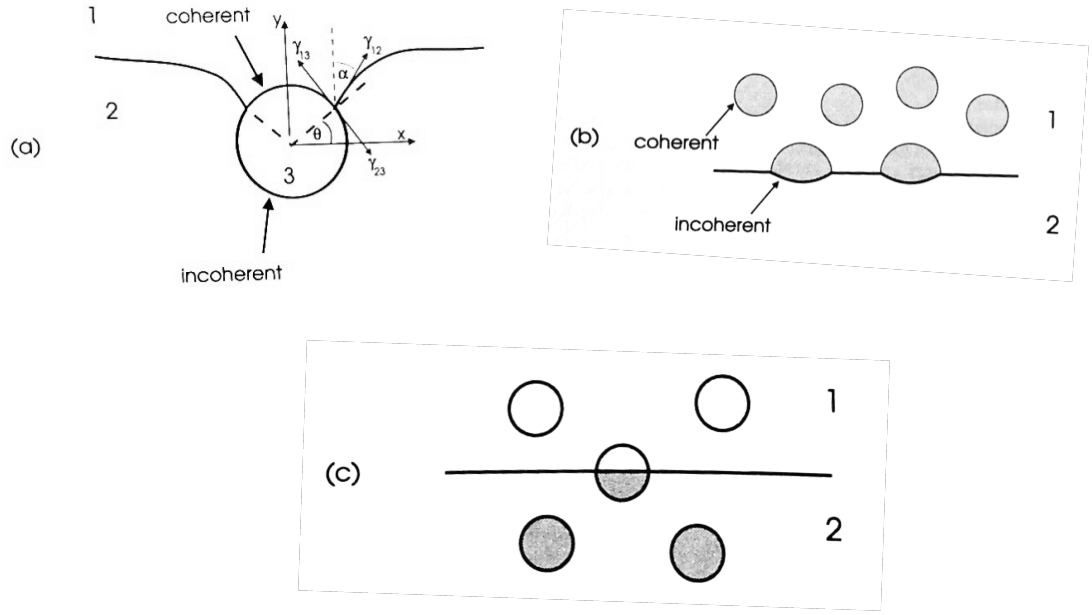

Fig.2.7: Coherent particles create different obstacles to high angle boundary movements: (a) the boundary by-passes the particle; (b) the boundary stops at the particle, (c) the boundary cuts through the particle [65].

As regards the effect of all coherent particles, secondary phases or dispersoids [65]:

- Due to the high stored energy and the severe strain field which is created around them, large particles can be preferential sites for nucleation of new, recrystallized grains
- Closely-spaced particles can exert a significant pinning effect on grain boundaries [58]. In particular, as described by Eq.2.5 for Zener pinning effect, their hardening effect is directly proportional to their fraction volume (f_v) and the energy of their interfaces (γ_{GB}), while inversely proportional to precipitates radii r.

$$P_{Z(average\ pinning\ pressure-\ dispersoids)} = \frac{3\, f_{(vol.fraction)}\, \gamma_{GB(boundary\ energy\ )}}{4\, r_{(average\ radius\ of\ the\ dispersoid)}}$$

Eq.2.5: Zener pinning effect [65,66].

Zener pinning equation confirms that two fundamental parameters should be taken into account to provide an effective strengthening, that is particle size and interparticle spacing. By varying both the particle size and spacing, acceleration or retardation of recrystallization could be produced [65]. As a matter of fact, there is a maximum interparticle distance below which the subgrains are blocked before they migrate sufficiently in order to transform themselves into high energy boundaries with high mobility [58], necessary for starting recrystallization.

Besides the abovementioned characteristics, particle shape has the slightest influence; it should be however underlined that dislocation re-arrangements and nucleation occur preferably next to non-equiaxial particles [58].

2.3 Suitable alloying elements for heat resistant precipitates

In Sect.2.2, precipitation strengthening was identified as the major strengthening mechanism able to enhance high temperature resistance of Al alloys. Among all the requirements, both precipitates spacing and size play a key role since they significantly influence the interaction with dislocations. The main target for heat resistant Al alloys is therefore to achieve a sufficiently small spacing of finely dispersed thermally stable particles, resistant to coarsening, with a high volume fraction. The critical issues in achieving the objective are analyzed in the following paragraphs, with a specific focus on conventionally castable Al alloys. Just a few hints are made in the last paragraph to the potentiality of the rapidly solidified Al alloys.

2.3.1 General criteria – Ni superalloys VS Al alloys

Aiming to draw up the main criteria in developing heat resistant Al alloys, yet castable through conventional metallurgy processes, a brief outlook to Ni superalloys was presented by Knipling et al. in their review [54]. The Ni-based superalloys are in fact the most successfully engineered high-temperature alloys developed to date. Their extraordinary creep resistance is achieved primarily thanks to the Ni_3Al precipitates, with $L1_2$ structure, isomorphous and coherent with the fcc Ni-rich matrix. Al shows a significant solubility in Ni, thus a large volume fraction of precipitates is easily achievable, without the need of specific casting techniques.

On the contrary, just a few elements show an appreciable solubility (>1 at%) in Al alloys, considering conventional solidification processes. This characteristic unfortunately leads to an intrinsically lower precipitation fraction in Al-based alloys, so it becomes crucial to get small dispersed phases (of the order of 10nm or less, according to Knipling et al. [54]) to provide an effective strengthening. Clearly, these phases should also be very coarsening-resistant during thermal exposure, in order to keep their fine structure and thus their efficacy in hindering dislocations motion. This marks the major difference between Ni and Al heat-resistant alloys: for Ni alloys, the size of precipitates is not a limitation thanks to the higher volume fraction. A visual explanation of this phenomenon is provided by Fig.2.8 [54], which compares the shear stress required for a dislocation to loop around a precipitate (Orowan stress) in both Ni and Al alloys characterized by different size and volume fraction f of precipitates. This is of course an approximation: even if dislocation looping is the main strengthening mechanisms in case of

overaged and coarsened precipitates, in neither Ni or Al system is deformation at elevated temperature governed directly by the only Orowan mechanism.

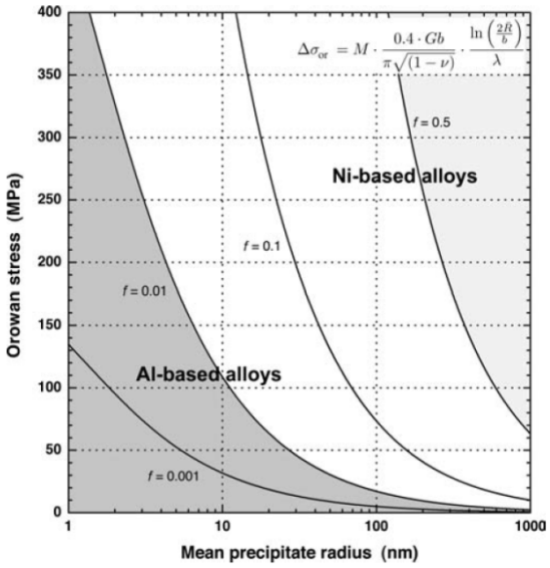

Fig.2.8: Comparison between Ni and Al-based alloys, in terms of Orowan stress as a function of mean precipitate radius "R" for various volume fractions "f" of the dispersed phase. It provides an explanation of the importance of small precipitates dimensions in Al-based alloys [54].

Extending the analogy further, it is possible to identify another fundamental characteristic of Ni superalloys which is applicable to Al alloys as well: it is desirable that the strengthening compounds have the cubic $L1_2$ structure, chemically and structurally analogous to Ni_3Al in the Ni-based superalloys [54]. The importance of such phases is due to the fact that they can maintain their coherency with the matrix at elevated temperatures [67], improving this way the high-temperature behavior of the alloy. In fact, the similarity in crystal structure between the matrix (fcc structure for both Al and Ni alloys) and precipitated phases allows for a coherent interface and small lattice parameter mismatch, which is essential for minimizing the interfacial free energy driving Ostwald ripening (see Sect. 2.1.2, Eq.2.3) and therefore precipitates coarsening [54].

2.3.2 The key role of trialuminides Al_3M with $L1_2$ structure

Despite the abovementioned poor solubility of all alloying elements and the consequent low volume fraction of precipitates, some alloying elements have been found adequate to enhance Al heat resistance. Intermetallic compounds are the most promising candidates for strengthening of heat resistant Al alloys, due to their excellent thermal stability [18,54,68–73]. According to

Knipling et al. [54], among all intermetallics, those with the stoichiometric formula Al_3M (where M stands for an element of the transition metals, lanthanide or actinide series) are particularly attractive and are analogous in terms of chemistry to the precipitates Ni_3Al, reinforcing Ni super alloys. In Fig.2.9 [54], all the elements able to form trialuminides (and their equilibrium structure) are highlighted.

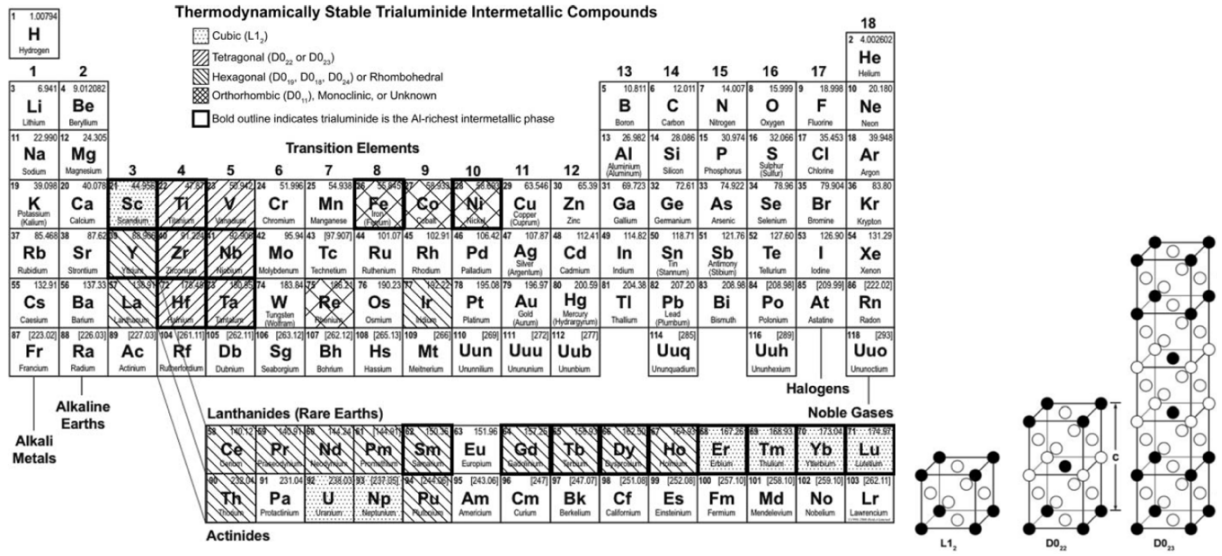

Fig.2.9: a) Highlighted the elements which form thermodynamically stable trialuminide (Al_3M) intermetallic compounds, with the equilibrium structure indicated by the legend, b) Comparison between cubic $L1_2$ and tetragonal DO_{22}/ DO_{23} structures [54].

Before separately analyzing the most promising candidates forming Al_3M intermetallic compounds, a few remarks are required to correctly guide the choice of alloying elements able to strengthen Al alloys at high temperature:

- It is desirable that such compounds have a $L1_2$ structure: tetragonal structures are less strengthening and less resistant to coarsening [74], due to the higher mismatch with the matrix.
- A large solubility at the solution temperature is fundamental for dissolving a high amount of alloying elements in the single phase α-Al solid solution, prior to aging. At the same time, a high gradient of solubility with temperature is desired in order to produce a large amount of finely dispersed trialuminides [54].
- Primary precipitation is undesirable due to two main reasons:
    i. it produces a decrease of solute retained in α-Al solid solution, thus limiting the potential strengthening (mainly connected to precipitates formed upon aging) [54,75].

ii. since the dispersoids precipitate directly from the as-cast state, they are inhomogeneously distributed and readily nucleate and growth into coarse particles. In particular, a very poor resistance to recrystallization is achieved in regions next to grain boundaries, where large primary particles are known to encourage recrystallization during annealing and to provide some preferential sites for nucleation [33,76], promoting a refined microstructure.

The key role in enhancing thermal resistance is connected to the precipitates formed after solution+quench+aging: these are in fact characterized by a higher volume fraction and above all finer dimensions than the primary ones, producing an increased strain energy in the matrix around them and being more effective in hindering dislocation motion (see Zener pinning effect in Sect. 2.2.2, Eq.2.5).

- Those elements with a terminal peritectic phase equilibrium with Al are prone to primary precipitation, exhibiting therefore a strong tendency to lose significant amount of solute [54]. In specific, in case the alloy contains solute beyond the minimum liquid solubility, the first solid to form under equilibrium conditions is the properitectic, or primary, Al_3M ordered phase [76]. Primary precipitation also promotes grain refining (see for ex. the study by Wong et al. [77], with 0.3 wt% Zr additions to 6XXX Al alloy).

  Among the terminal peritectic elements are Zr, Cr, Hf, Mo, Nb, Ta, Ti, V, W [58]. In order to suppress the formation of solute-rich primary (or properitectic) Al_3M phases, a minimum undercooling is necessary to reach the metastable liquidus of α–Al solid solution; from the other side, for a given solidification rate, there is a corresponding critical solute concentration below which primary precipitation of Al_3M will not occur. The phenomenon has been studied in detail for the Al-Zr system over a wide range of solidification rates and Zr concentration by Ohashi et al. [78] and Hori et al. [79], and their results are clearly shown in Fig.2.10. Few precautions are therefore required to adequately cast Al alloys, in order to fully reap the benefits offered by additions of peritectic elements.

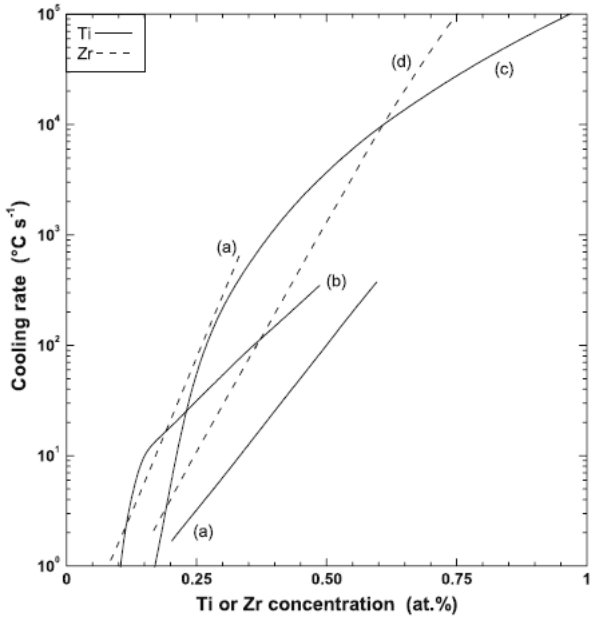

Fig.2.10: Critical cooling rate for suppressing primary AlTi or Al_3Zr, solid line and dashed line respectively; results found by Ohashi and Ichikawa (a) and Hori et al. (d) [76].

Addition of transition elements to form trialuminides

Among intermetallic compounds, the trialuminides formed with transition metals are of interest because of their low density, high melting point, good oxidation resistance and potentially useful high-temperature strength for aerospace and automotive applications [80]. As graphically reported in Fig.2.9, however, except for Sc which crystallize into the equilibrium, high symmetric structure $L1_2$, all transition elements are thermodynamically stable in the $D0_{22}$ or $D0_{23}$ tetragonal structures, characterized by low symmetric shape and intrinsically brittle. Among them, there are the widely adopted Ti, Zr, Hf, V, which are characterized by considerably low diffusion coefficient in Al [54] and are therefore promising for thermally stable precipitates.

Many researches show the potentiality of Sc in combination with other transition elements [34,75,80,81]:

- Several transition elements can be incorporated substitutionally in Al_3Sc, forming $(Al, X)_3Sc$ with the desired $L1_2$ structure.
- Sc has a relatively high diffusivity in α-Al [54], and the coarsening resistance of its trialuminides is considerably enhanced through the additions of transition elements with lower diffusion coefficient.

In particular, a pronounced synergistic effect in increasing high temperature resistance is observed when both Sc and Zr are present [33,34,75,76,82–85]:

- Much of its effectiveness is attributed to the formation of Zr-enriched outer shells onto the Al_3Sc precipitates [75,83], which were found to further stabilize Sc trialuminides at high temperature.
- Since Sc shows a terminal eutectic with Al, while Zr a terminal peritectic, their combination is particularly efficient: due to microsegregation, the dendrites are enriched in Zr and depleted in Sc, while the opposite is observed in the interdendirtic regions [75]. This means that no precipitates free areas are produced after the heat treatment.
- Sc was also reported to favor the decomposition of supersaturated Al-Zr solution and a homogeneous $Al_3(Sc,Zr)$ distribution: Jia et al. [86] highlighted that the distribution of strengthening precipitates becomes more homogeneous when Sc content is increased, and at least a minimum amount of Sc is necessary to promote a homogeneous microstructure.

However, due to its prohibitively price for industrial applications, Sc additions have not been performed nor considered during the Ph.D. activities.

As regards the addition of transition elements without Sc, several studies have been focused on single Zr, Ti or V additions [68,75–77,87,88]. A few criticalities have to be overcome:

- All of them have peritectic phase equilibrium, which means that:
  i. the alloy should not contain solute in excess with respect to minimum liquid solid solubility in order to avoid primary precipitation under normal cooling conditions. Many studies dealing with these elements additions involve high cooling rates (≈20°C/s in [68,89]) to avoid primary precipitation.
  ii. the variation in solute concentration might be substantial between the outer and inner dendritic regions [58], in particular in the latter areas the solute concentration might be significantly greater than the bulk composition (see for ex. Zr variation measured by quantitative electron-probe microanalysis -EPMA- across multiple dendritic cells in [75]). In cast Al–Zr alloys, the initial distribution of Zr solute atoms is highly non-uniform [88,90], leading to precipitate-free interdedritic channels that have a deleterious effect even on room temperature strength.
- For Zr, Ti and V, the equilibrium structure of Al_3M is tetragonal ($D0_{22}$ or $D0_{23}$), but under certain conditions primary trialuminides may solidify from the melt with the metastable

cubic $L1_2$ structure [54,78]. Many efforts have been made to stabilize $L1_2$ structure of Zr/Ti trialuminides or better to enhance the formation of such structured precipitates. In particular Mn and Cr have been found to help stabilizing $L1_2$ structured Al_3Ti [91,92], while elements such as Cr, Mn, Fe, Cu, Zn are known to promote $L1_2$ Al_3Zr formation [91–95].

- The heat treatment of these modified alloys is significantly different from that of the conventional alloys, since Al_3M trialuminides precipitate from the solid solution at relatively high temperature (350-500°C) compared to the classical Al-based precipitates (around 150-200°C, as confirmed by the heat treatment proposed in the following Chapters 3-4). This is essentially due to the low diffusion coefficient of the transition elements into Al matrix and it also indicates the trialuminides thermal stability. A specific heat treatment has to be developed.

Addition of rare earth elements to form trialuminides

Fig.2.9 shows that, among the rare earth elements (RE), Er, Tm, Yb, Lu exhibit a structure progressively more cubic with decreasing their atomic radius, and are therefore stable in $L1_2$ structure. Their considerably low solid solubility [54] makes however the supersaturation of solute impossible to achieve under the moderate cooling rates characterizing conventional solidification processes, while primary precipitation is most likely [96]. As well as transition elements, also rare earth elements can substitute for Sc in $L1_2$ ordered $Al_3(Sc,RE)$ [96,97] and show promising results in terms of high temperature resistance [98,99].

2.3.3 Advantages of Zr additions and heat treatment

As already mentioned, owing the sluggish diffusivity of Zr in Al ($1.20 \times 10^{-20} m^2 s^{-1}$ at 400°C), Al_3Zr trialuminides can maintain a high strength at aging temperature as high as 400°C [75,96,97]. Moreover, Al-Zr master alloys are not expensive and Zr is usually present in small amount in each Al alloy for forged products, for its enhancement in recrystallization resistance. Due to these promising characteristics for industrial applications, this element deserves particular attention.

Precipitation of Al_3Zr

According to Knipling et al. [76,88] who deeply investigated a simple Al-0.1at%Zr alloy in order to study the precipitation sequence of Zr, $D0_{23}$ equilibrium precipitates are not nucleated

directly from the supersaturated α-Al solid solution during aging. These coarser phases are rather formed during dissolution and overaging at T>450°C of nearby pre-existing $L1_2$ precipitates, which are indeed produced by prior aging. As confirmed by TEM and SEM investigations on Al-0.1Zr at% alloy [88], the $L1_2$ → $D0_{23}$ structural transformation occurs at approximately 500°C: overaging causes the dissolution of the small, high-number-density Al_3Zr ($L1_2$) precipitates within the dendritic cells, that re-precipitate heterogeneously on grain boundaries or (most likely) dislocation cuttings, leaving behind a deleterious precipitate-free zone. The phases of overaging are reported in Fig.2.11, where the ultimate step marks the formation of the heterogeneously nucleated, disk-shape, equilibrium precipitates $D0_{23}$.

It should be however pointed out that the temperature marking the transformation from $L1_2$ to $D0_{23}$ structure is sensitive to:

- Chemical composition. As well as increasing the aging temperature, also decreasing the supersaturation reduces the chemical driving force for nucleation, driving to larger precipitates and a reduced equilibrium volume fraction of precipitated phases (true for any precipitation reaction) [88].
- Dislocation density, since it influences the kinetics of diffusion. The higher the dislocation density, the lower the aging temperature which leads to the formation of $D0_{23}$ precipitates (e.g. Zedalis and Fine [74] observed transformation to the equilibrium $D0_{23}$ structure in Al-0.24Zr at% aged at 450°C, previously cold rolled).

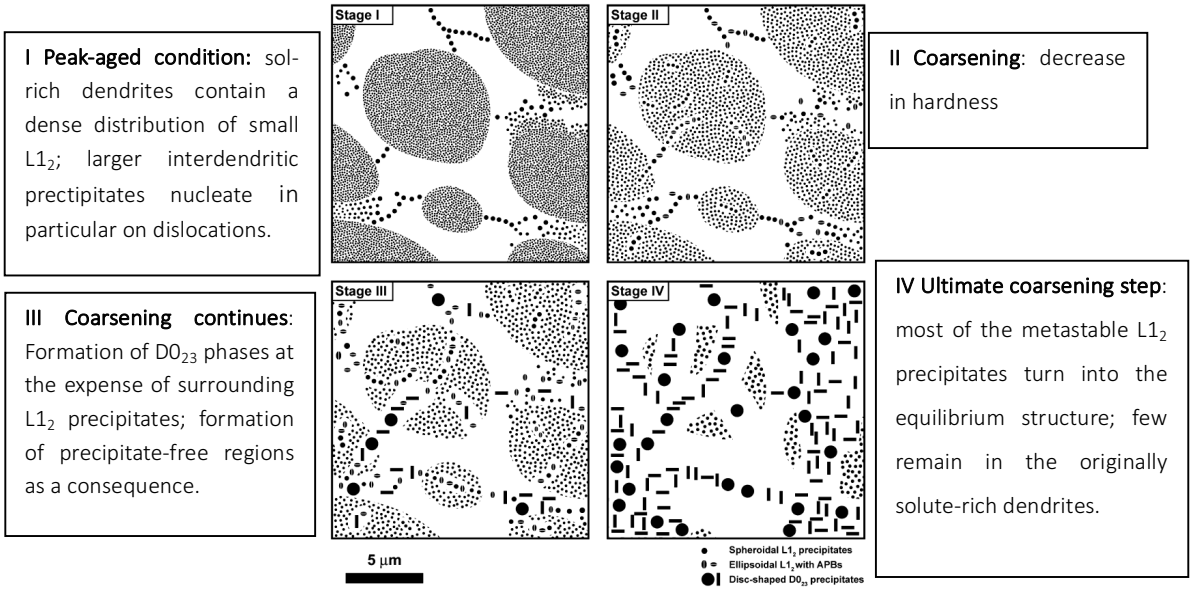

Fig.2.11: Representation of Al_3Zr coarsening during overaging [88].

Heat treatment to stimulate the formation of $L1_2$ Al_3Zr

Due to this criticality, alloys containing Zr cannot be homogenized at T around 500°C (as usually prescribed for Al alloys) without first precipitating Al_3Zr in coarse $D0_{23}$ structure and thus resulting in minimal precipitation hardening during subsequent aging.

Different heat treatments are proposed in literature:

- Knipling et al. in [75,88] tested an isochronal aging, consisting in 25°C increments, each lasting 3h, beginning at 200°C; this slow ramp heating, though not directly applicable in an industrial context due to an extended treatment time, stimulates the precipitation of very fine-structured compounds, due to the great supersaturation and chemical driving force at the lower possible temperatures. The isochronal aging showed that in a simple binary Al-Zr alloy, precipitation of spheroidal nanometer-scale Al_3Zr commences between 400-425°C [75] and can be detected by a pronounced hardening response; the hardness starts decreasing above 500°C, due to the transformation of metastable $L1_2$ structures into their equilibrium $D0_{23}$ structures. Ramping can also be important so slow diffusing elements like Zr get the necessary time to form the appropriate dispersoids [100].
- According to Knipling et al., Al-0.19at%Zr achieves peak strength upon 24h isothermal aging at 375°C [76].
- The study carried out by Booth-Morrison et al. [97] on Al-Zr-Sc-Er alloy confirms that Zr is essentially immobile in Al at 300°C and at least soaking at T ≥ 400 °C should be employed to stimulate Al_3Zr formation.
- As reported by Robson et al. [101–103], which carried out experimental activities on 7XXX Al alloys with Zr additions, usually the solution treatment for Al alloys is aimed to dissolve the max number of unwanted intermetallic compounds and eutectic phases and homogenize the solute distribution. In case of Zr containing Al alloys, however, the solution step might be tailored to increase the effectiveness of Zr based dispersoids, which usually precipitate inhomogeneously from the as-cast state, leaving precipitate-free interdendritic channels.

  In order to minimize the inhomogeneity into the dendrites, which are mainly due to Al-Zr terminal peritectic, multi-step annealing procedures can be adopted [101,102]. The position and width of the dispersoid free regions depends on the temperature of homogenization: at higher Zr levels (inner of the dendrites), the nucleation rate is large and many particles form, each of which is only able to grow to a small size before exhausting

the supersaturated Zr; at lower Zr level (interdendritic channels), the nucleation rate falls, and each particle can grow to a larger size before exhausting the supersaturated Zr [101]. This implies that the heat treatment giving the best dispersoids distribution in Zr enriched regions is not the same as the optimum heat treatment conditions for dispersoid precipitation in the low Zr regions. Ramp heating at a sufficiently slow rate, combined with holding at 2 different homogenization temperatures, are expected to stimulate the formation of Zr dispersoids at different Zr levels. In particular Robson et al. [102] suggest a slow ramp heating (20°C/h) up to 88% of the homogenization temperature (T_{hom}), holding 5h at this $0.88T_{hom}$, then again slow ramp heating (20°C/h) up to the T_{hom} and holding for 24h.

- The effectiveness of ramp heating proposed by Robson [101–103] is further confirmed by Zhao et al. [104], who carried out TEM studies on an Al-Cu alloy with Zr-Ti-V additions, heat treated according to different heating rates (300°C/h and 50°C/h). The higher heating rate was reported to produce trialuminides with a larger mean size, with preferential nucleation sites in the dendrite edges. Finer and more uniformly distributed precipitates are promoted by lower heating rate.

All of these studies have been following taken into account when defining the heat treatment cycle for Al alloys with Zr additions.

2.3.4 Focus on Mo additions in Al-Si alloys

Besides the promising studies reported by Colombo et al. [98,99] on the beneficial effects of Er and Zr additions on the high temperature properties of AlSi7Mg A356 alloy, which are mainly attributed to the presence of Al_3Er, Al_3Zr and Al_3(Er, Zr), it is reported in literature that Si has a negative influence in the Al-Si-TM system (where TM stands for transition metal), since it lowers the peritectic/eutectic temperature and the solid solubility of the alloying elements in the Al matrix, further decreasing their ability to form dispersoids [105,106]. Moreover, Si has a so called "poisoning effect": apart from the enhancement in stimulating the heterogeneous nucleation of trialuminides, Si is reported to incorporate in their structure, hence decreasing their coarsening resistance [96,105].

Farkoosh et al. [105,107] propose the addition of up to 0.3wt% Mo to stimulate the formation of Al-(Fe, Mo)-Si dispersoids in the conventionally cast Al-Si-Cu-Mg alloys, with an average content of

0.1wt% Fe and around 7wt% Si. As well as the abovementioned transition elements, Mo exhibits a sluggish diffusivity in Al (5.52 x 10^{-23} m^2s^{-1} at 400°C [54]), even if it is not reported by Knipling et al. [54] to form the desirable and thermally stable $L1_2$ trialuminides.

Nanometric dispersoids in Al-Si-Cu-Mg-Mo alloys have been observed through TEM analyses after a solution treatment consisting in two steps: (i) 4h at 500°C + (ii) 1h-10h at 540°C. The micro-hardness evolution during the whole solution treatment was evaluated in [105] and reported in Fig.2.12: compared to 500°C, soaking at 540°C induces a higher mobility of the Mo solutes enabling the precipitation of the dispersoids. In particular, the maximum hardness value was detected after 1h soaking at 540°C.

After the usual aging treatment (5h at 200°C to achieve a T7 condition), a moderately higher hardness was exhibited by Mo containing alloy, coupled with a consistent improvement of tensile properties at 300°C [105]. The number of dispersoids further increases in case of Mn additions up to 0.5wt% [107], since this element might substitute for Fe in Al-(Fe, Mo)-Si dispersoids.

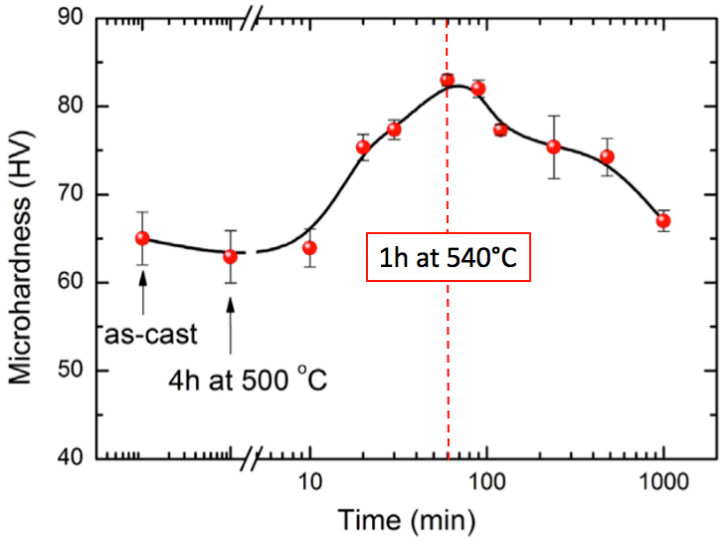

Fig.2.12 :Micro-hardness evolution of Mo modified Al-Si-Cu-Mg alloy, from [105].

2.3.5 Hints to the potentialities of Rapidly Solidified Al alloys

The term Rapid Solidification (RS) has been traditionally attributed to such processes such as atomization, melt spinning, splat quenching, spray deposition, cold spray, plasma spray, laser melting, ball milling and cryomilling, where cooling rates exceed 10^3°C/s. The product resulting from these techniques is really expensive and it is hardly a shaped casting [108]; both the

characteristics make (to now) RS techniques absolutely not applicable to mass production of powertrain components (pistons in specific), which are the main objective of this Ph.D. thesis. It is however worth mentioning these techniques since they allowed and continue allowing to reach substantial results in terms of thermal stability of Al alloys.

Since the conventional casting of Al alloys containing dispersoid elements above their saturation limit usually results in the formation of undesirable, coarse, primary intermetallics [109], penalizing the alloy mechanical properties, the traditional approach is to add dispersoid-forming elements below the saturation limit, which is considerably restrictive for both TM and RE elements, as highlighted in Sect.2.3.1-2.3.2. The main advantage of all RS processes is the possibility to overcome the limitation of the low solid solubility of most of the alloying elements in Al, extending further the supersaturation of such elements and effectively refining primary intermetallic compounds, which act as dispersoids and provide an effective strengthening [110]. Through rapid chill methods, in fact, almost complete precipitation of solute occurs on cooling and precipitation hardening during post solidification aging is not necessary [111]. Limited enhancement in thermal resistance was also reported in literature for high pressure die casting (HPDC) methods [112].

The interest in RS approximately started in the '80s, as confirmed by the Symposium sponsored by ASTM in 1984 [113]. According to the review by Knipling et al. [54], the rapidly solidified alloys based on the eutectic Al-Fe system represent one of the most heat resistant Al alloys, taking advantage of both solid solution strengthening and Al-Fe dispersoids, and are covered by few patents [114,115]. More recent patents by Pandey [111,116–118] interchangeably deal with Al-Fe, Al-Ni, Al-Mg eutectic system as a basis, taking advantage of transition elements (Sc, Zr, Ti, Hf, Nb) and rare earth elements (Er, Yb, Y, Gd) additions, with the aim to stimulate the formation of $L1_2$-structured trialuminides (Al_3M). In fact, as explained by Pandey in [111] and confirmed by Knipling et al. in [54], the intrinsic advantage of $L1_2$-structured trialuminides is the low mismatch with Al matrix, resulting in lattice coherency between precipitate-matrix, low driving force for particle growth and subsequent coarsening resistance.

EXPERIMENTAL ACTIVITIES

Chapter 3:

Al-Si alloys for pistons

Due to the widespread use of Al-Si alloys for automotive pistons, the first part of Ph.D. activities was focused on these alloys. Chapter 3 is divided as follows:

- Sect. 3.1 focuses on the standard eutectic Al-Si piston alloy, containing small amounts of Cu and Ni (chemical composition in the range of the abovementioned Mahle® alloy M124 - Sect.1.2). This alloy is considered as a starting point for further improvements in thermal stability.

  The whole section is taken from the published paper *"EN AW-4032 T6 Piston Alloy After High-Temperature Exposure: Residual Strength and Microstructural Features", E.Balducci, L.Ceschini, Al.Morri, An.Morri, Journal of Materials Engineering and Performance, Vol.26(8), pp.3802-3812, 2017.* The study reports the effects of thermal exposure on AA4032 piston alloy, assessed through hardness and room temperature tensile tests on peak-aged and overaged samples, coupled with microstructural and fractographic investigations
- Sect. 3.2 focuses on a similar eutectic Al-Si piston alloy (chemical composition in the range of the abovementioned Mahle® alloy M142- Sect.1.2), containing higher amounts of Cu with respect to AA4032. According to what reported in literature, the alloy should mark a step towards improving the high temperature performance of AA4032. The alloy was supplied by Duraldur S.p.A., which is specialized in the production of gravity cast and forged pistons for gasoline and diesel engines, both for passengers cars and heavy duty applications. The alloy heat treatment was optimized and the effects of thermal exposure on the alloy were evaluated through overaging curves.
- Sect.3.3 reports the results of small additions of transition elements with the aim to further reduce the consequences of overaging on AA4032+Cu+Ni. In particular, the experimental activities focus on Mo additions.

3.1 EN AW-4032 T6 Piston Alloy After High-Temperature Exposure: Residual Strength and Microstructural Features

[The whole Sect. is taken from the published paper whose title is shown below, made available by Springer Nature License Number 4522580963137].

JMEPEG (2017) 26:3802–3812
DOI: 10.1007/s11665-017-2835-z

1059-9495/$19.00

EN AW-4032 T6 Piston Alloy After High-Temperature Exposure: Residual Strength and Microstructural Features

Eleonora Balducci, Lorella Ceschini, Alessandro Morri, and Andrea Morri

(Submitted February 10, 2017; in revised form May 27, 2017; published online July 24, 2017)

Keywords: Aluminum; Automotive and Transportation; Electron Microscopy; Optical Metallography Microscopy; Static Mechanical

Abstract

This study aims to evaluate the effects of prolonged thermal exposure on both microstructural evolution and mechanical properties of the EN AW-4032 T6 piston alloy. For the purpose, the experimental activities have been carried out on samples machined from forged and heat treated automotive pistons. The effects of overaging have been investigated in the temperature range 140÷290°C, firstly by evaluating the time-temperature-hardness curves and then by carrying out room temperature tensile tests on overaged samples. The material softening was substantial and extremely rapid when the soaking temperature exceeded 250°C. During overaging, both the tensile strength and the residual hardness considerably decreased, and a relationship between these parameters has been established. The alloy behavior in the plastic field has been modelled according to the Hollomon's equation, showing that both the strain hardening exponent and the strength coefficient are a function of the residual hardness. The results were finally related to the corresponding microstructural changes: OM and FEG-SEM metallographic and fractographic analyses on overaged samples gave evidence of coarsened precipitates along the grain boundaries.

3.1.1 Introduction

For many years, eutectic Al-Si12 alloys have been widely used in critical automotive components, such as engine blocks or pistons, due to their good castability, low thermal expansion coefficient, high thermal conductivity, combined with good wear and corrosion resistance [18,19,106]. The increasingly tighter regulations on greenhouse gas emissions recently led automotive manufacturer to consider both significant weight reduction and higher fuel efficiency as guidelines for materials research and development. Together with new alloys or surface modification treatments to reduce friction loss and vehicle weight, the engine downsizing and the re-introduction of turbochargers have been implemented in newly developed cars, in order to boost fuel economy and engine efficiency, without affecting engine performance. As a drawback, all the recent strategies aimed to optimize engine efficiency, turbochargers in particular, increase temperature and pressure in the combustion chamber, resulting in the need for piston, cylinder and engine block materials to withstand more severe thermo-mechanical stresses [19,57,119].

The thermal stresses are significantly high at piston crown [13], which is directly in contact with exhaust gases and which is part itself of the combustion chamber; literature data report that the piston crown might reach [120] or even exceed 300°C [1,29], for prolonged time. Since the operating temperature of aluminum pistons usually exceeds the aging temperature [121], heat treatable aluminum alloys inevitably undergo in-service overaging, which consists in a diffusion-controlled coarsening of the strengthening precipitates formed by the heat treatment [30]. As a consequence, the lattice distortions provided by the precipitates are considerably reduced, their lower capability to hinder dislocation motion causing a significant decrease in the alloy strength.
Modern gasoline engine pistons typically consist of Al-Si12 alloys, which allow the recommended mass savings for the high-speed reciprocating engines; the production route might select either casting or forging processes [3,29], the last one being the typical choice when a consistent weight reduction is required. However, high temperature strength is still one of the main challenges of piston alloys, due to the following considerations:

- The higher the material strength is, the thinner the piston sections are, allowing both primary and secondary mass savings (lower inertia forces lead to reduced stresses on both connecting-rod and crankshaft, resulting in a greater weight reduction). Secondary mass savings are a key tool for maximizing vehicle fuel economy, their great importance being highlighted by recently developed simulations aimed to predict their potential [122,123].

- Pistons have to be exploited under extreme temperature and pressure conditions to gain the maximum engine efficiency, which is therefore strictly connected to the high temperature material strength.

As reported in [121], EN AW-4032 is a eutectic Al-Si alloy widely used for engine pistons production; the alloy contains significant quantities of Cu, Ni, Mg (around 1wt%), in order to increase thermal stability, while Fe content is maintained below 0.3wt%. It is well known that several factors affect the alloy mechanical properties at high temperature: (i) the chemical composition (since alloying elements provide solid solution and precipitation strengthening); (ii) the thermal stability of the strengthening precipitates produced by aging treatment; (iii) other microstructural features, such as the shape and morphology of eutectic Si and other intermetallics, that are usually thermally stable up to the temperature of the solution treatment- about 500°C.
EN AW-4032 alloy is usually subjected to T6 or T7 heat treatment, which promotes the formation of Cu, Mg and Si based precipitates (Mg_2Si, Al_2Cu, Al_2CuMg, etc. according to [25,121,124,125]. Unfortunately, all these precipitates are prone to coarsening during high temperature exposure. Differential scanning calorimetric (DSC) studies by Biroli et al. [124] reported that the main strengthening precipitate, the coherent β''-Mg_2Si phase, turns into the incoherent, equilibrium β phase around 285°C, with an imposed heating rate of 20°C/min. Similarly, the ϑ''-Al_2Cu phases rapidly lose their coherency with the matrix, turning into a mixture of stable ϑ precipitates or rod-shaped Q-$Al_5Cu_2Mg_8Si_6$ phases after overaging for 100h at 250°C [26], or even completely forming the Q-$Al_5Cu_2Mg_8Si_6$ phases after overaging for 1000h at 350°C [18,19]; the latter phases are considered too coarse to effectively strengthen the matrix. Cu also forms several aluminides when combined with Ni addition, like Al_3CuNi, Al_7Cu_4Ni [26]; both the thermal stability and the fine size of these compounds make Ni an important alloying element for improving high temperature resistance of EN AW-4032 piston alloy [25,29], even if its high prize has recently guided some researchers to evaluate the minimum Ni content to withstand pistons requirements [26,126].
In addition to that, the formation of Fe-based intermetallic compounds is inevitable even if Fe is present at low concentration, due to the negligible solubility of this element in the α-Al solid solution; usually Fe is added (at low concentration) in order to enhance the alloy properties at high temperature. The volume fraction of Fe-based intermetallics is strictly connected to its content: the so-called T-Al_9FeNi phase was present in 5 vol% in a similar AlSi12Ni alloy with Fe=0.69wt% [21]; the measured volume fraction decreases under 3.74% in an AlSi12Cu1Ni1Mg1 alloy with

Fe=0.6wt% [19], while the 2.13vol% of T phase was predicted by Thermo-Calc simulations in an AlSi12Cu1Ni1 alloy with Fe=0.40wt% [26].

Even if the use of EN AW-4032 for high performance automotive pistons is widespread, still there is a lack of literature data aimed to quantify and model the decrease of the alloy mechanical properties during high temperature exposure. The in-service decay of piston alloy properties determines the limits of the maximum temperatures and pressures in the combustion chamber and therefore it also limits the engine efficiency. This study provides reliable data about the residual mechanical properties of the EN AW-4032 alloy after high temperature exposure and it aims to relate the mechanical behavior of this alloy to the corresponding microstructural changes.

3.1.2 Material and methods

Material

The experimental activities were carried out on samples machined from forged and T6 heat treated pistons, made of the EN AW-4032 alloy. Spectrometric chemical analyses, by glow discharge optical emission spectroscopy (GDOES), were carried out on samples machined from the forged pistons and the average results are reported in Table 3.1.

The alloy heat treatment consists of solution, water quench and aging, according to the parameters reported in Table 3.2 and chosen by the supplier.

Table 3.1: Chemical composition (wt%) of the EN AW-4032 alloy determined by GDOES measurements.

Element	Si	Fe	Cu	Mn	Mg	Zn	Ti	Ni	Al
Wt %	11.56	0.219	0.992	0.005	1.04	0.029	0.044	1.02	bal.

Table 3.2: Parameters of the industrial T6 heat treatment of EN AW-4032 alloy.

Solution		Quench in water		Aging	
T [°C]	t [h]	T [°C]	t [s]	T [°C]	t [h]
525 ± 5	8	50÷70	35	200 ± 5	20

Hardness-time-temperature curves

In order to assess the thermal stability of the alloy, several samples (12x6x4 mm^3 in size) were machined from the heat-treated forged pistons. The specimens were subsequently overaged in the temperature range 140÷290°C, from 10min up to 168h. This temperature range was selected within the range of interest to assess pistons resistance in the in-service conditions and it

was investigated through 30°C steps up to 200°C and through finer 15°C steps up to 290°C. Brinell hardness tests were carried out according to the ASTM E 10-08 standard (hardened steel ball indenter with 2.5mm diameter and 62.5kg load applied). For each time-temperature condition, 6 hardness measurements (performed on 2 different specimens) were carried out in order to reduce the possible influence of inhomogeneous microstructure. The corresponding hardness-time-temperature (HTT) curves were therefore obtained.

Tensile tests

In order to further investigate the effect of thermal exposure on the T6 heat treated EN AW-4032 piston alloy, tensile tests were carried out at room temperature on overaged samples. 5 classes of specimens, each one characterized by different time-temperature of exposure, were used. Fig.3.1 shows the geometry of flat tensile specimens machined from the piston crowns (Fig.3.2) according to ISO 6892-1:2009 standard. Tensile tests were carried out on a screw tensile testing machine, according to EN ISO 6892-1:2009, at a strain rate of $3.3 \times 10^{-3} s^{-1}$. Proof strength ($Rp_{0.2}$), ultimate tensile strength (UTS) and elongation to failure (E%) were evaluated. Finally, the behavior of the alloy in the plastic field was modelled through the Hollomon's law [127], reported in Eq.3.1, where σ_p is the true plastic stress, ε_p the true plastic strain, K is the strength coefficient and n the strain hardening coefficient. The strength coefficient (K) and the strain hardening exponent (n) have been calculated according to ISO 10275:2007 standard. The tensile properties have been finally related to the residual hardness of the alloy after soaking.

$$\boldsymbol{\sigma_p = K\varepsilon_p^{\,n}}$$

Eq.3.1: Hollomon's law [127].

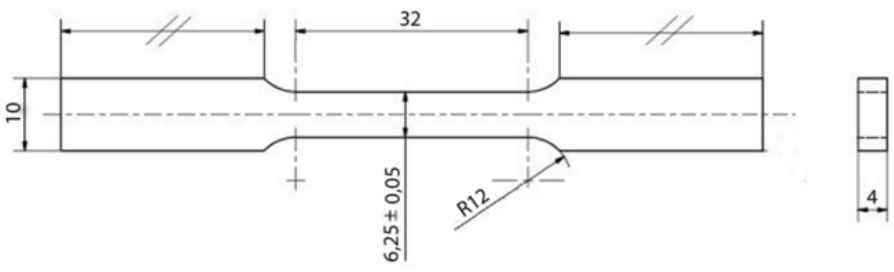

Fig.3.1: Geometry and dimensions [mm] of flat tensile specimens.

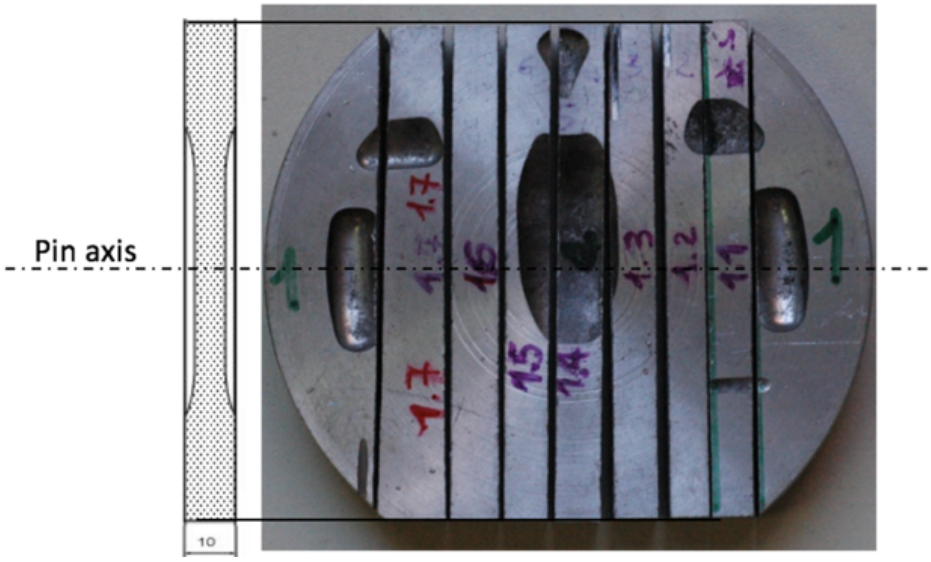

Fig.3.2: Scheme of tensile specimens, machined from pistons crown.

Microstructural and fractographic characterization

To study the alloy microstructure and to relate its mechanical behavior to the microstructural changes caused by thermal exposure, microstructural analyses were carried out by optical microscopy (OM), scanning electron microscopy (SEM), equipped with energy dispersive X-ray spectroscopy (EDS), and field emission gun scanning electron microscopy (FEG-SEM). Samples for microstructural characterization have been cut from the tensile specimens, close to the fracture surfaces, then cold embedded in resin, ground and polished according to ASTM E3 standard. OM investigations were carried out on both chemically etched and simply polished samples, through a Zeiss Axio® Image Analizer. According to ASTM E407 standard, two different etching treatments were used: immersion for 15s in the Keller's reagent for grain size measurement and immersion for 2min in H3PO4 at 50°C. Unetched samples were analyzed through both Zeiss LEO® 1530 SEM-FEG and Zeiss EVO® MA 50 SEM for microstructural investigations. In addition, fractographic analyses were carried out aiming to highlight the differences in the fracture pattern at different residual hardness values, related to the induced microstructural changes. To get accurate SEM-EDS analyses, fracture surfaces have been therefore subjected to ultrasonic cleaning in acetone for 30s.

3.1.3 Results and discussion

Hardness-time-temperature curves (HTT)

The determination of the HTT curves is the first step to evaluate the thermal stability of an alloy, because they offer an immediate overview of its mechanical response to thermal exposure. Moreover, such experimental data are useful for validating the simulations of piston temperature distribution. In fact, thanks to HTT data, by knowing the test endurance and the local hardness value it is possible to evaluate the local working temperature.

As clearly shown in Fig.3.3, the overaged EN AW-4032 T6 alloy exhibits a fork of properties within 115÷118HB (peak-aging condition) and 57HB (hardness plateau). The latter is reached after 5 days of exposure at 290°C and can be considered the lower hardness threshold for the EN AW-4032 T6 alloy, since further thermal exposure does not result in any further alloy softening.

By considering the thermal response at the lower temperatures, namely 140÷200°C, a slight hardness increase is perceivable: the starting material, characterized by 115HB, reaches 118HB after soaking at 140°C for 5 days (or less at higher temperatures). This means that the output of the industrial heat treatment (whose parameters are reported in Table 3.2) is a slightly under-aged temper condition. This aspect immediately underlines a significant margin of improvement in the industrial practice, since piston alloys are usually T7 heat treated (stabilized) [1] to enhance dimensional stability. Moreover, for the investigated soaking times, the alloy maintains the peak-aged hardness values (115-118HB) when exposed at temperatures lower than 170°C. Since the hardness response of the heat-treated aluminum alloys mainly depends on nature, size and distribution of the strengthening precipitates formed during aging, the almost constant values of alloy hardness after 1week of exposure at 170°C confirm the thermal stability of the reinforcing precipitates up to this temperature.

By considering the behavior at higher temperatures, it is clear that, when temperature exceeds 200°C, the higher the temperature, the faster the loss of mechanical properties. This phenomenon gives evidence of the temperature dependent, diffusion-controlled mechanisms characterizing the overaging process. The hardness loss starts to get considerably rapid when temperature exceeds 245°C, as revealed by the close-spaced HTT curves in the range 260÷290°C. This behavior is typical of heat treated aluminum alloys, as confirmed by similar studies by the authors [30,57] and it is related to the activation of stable phases precipitation.

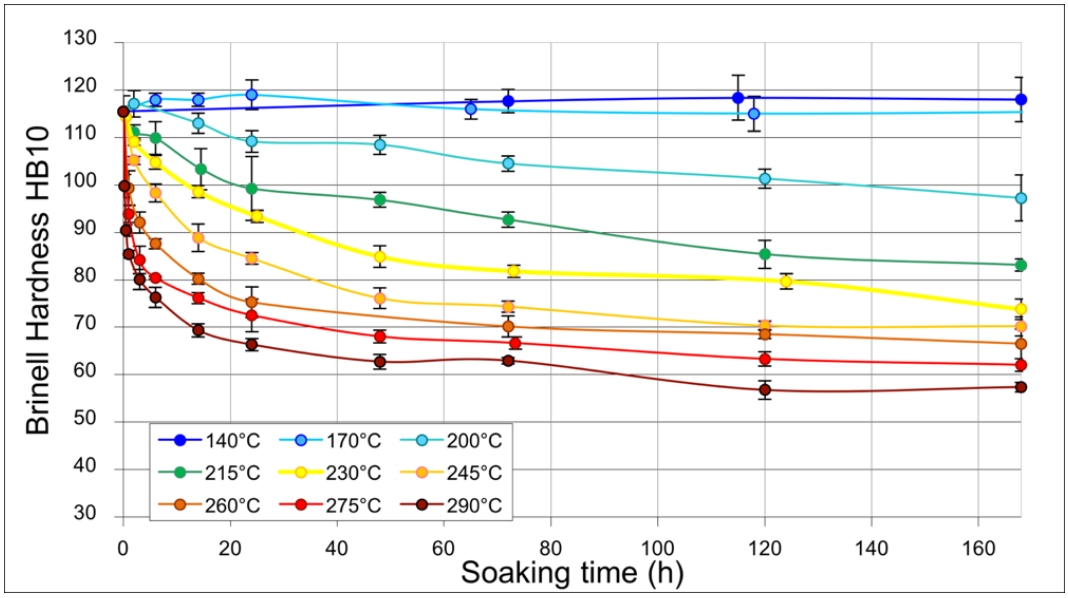

Fig.3.3: Hardness-time-temperature (HTT) curves of the EN AW-4032 alloy, after forging and T6 heat treatment. Each data point represents the average of 6 measurements, while error bars represent ± 2σ (corresponding to 95% confidence level.

Tensile tests

Tensile tests were carried out at room temperature on 5 classes of specimens (Table 3.3), each one characterized by a residual hardness in the range 118HB-57HB after thermal exposure. Table 3.3 gives evidence of the slight difference among the target and the achieved hardness values of the different classes. Time and temperature of exposure were chosen by means of the HTT curves (Fig.3.3).

Table 3.3: Classes of specimens characterized by different residual hardness, due to different thermal exposure.

Class HB10	Thermal exposure	HB10 (Average)	HB10 (St. Dev.)
Peak-aged	None	117	0.6
105	6 h at 230°C	101	0.9
90	33 h at 230°C	88	0.5
75	72 h at 290°C	73	0.2
60	120 h at 290°C	60	0.3

The actual residual hardness was then related to the Proof Strength ($Rp_{0.2}$), Ultimate Tensile Strength (UTS) and Elongation to failure (E%) evaluated with the tensile tests, whose results are reported in Table 3.4. As expected, strength (as well as residual hardness) decreases with increasing time and/or temperature of thermal exposure, while elongation to failure significantly increases. In particular, the set of specimens with a residual hardness of 60HB shows an average

hardness reduction of 49% if compared to the peak aged class, a reduction of 69% and 46% in $Rp_{0.2}$ and UTS respectively, but an increase of E% around 344%.

Table 3.4: Average values of Proof Strength, Ultimate Tensile Strength and elongation to failure with their respective standard deviation, for each investigated hardness class.

Class HB10	$Rp_{0.2}$ [MPa] (Av. ± St. Dev.)	UTS [MPa] (Av. ± St. Dev.)	E% [%] (Av. ± St. Dev.)
Peak-aged	263 ± 2.5	304 ± 4.0	1,8 ± 0.6
105	216 ± 2.1	268 ± 4.2	2,7 ± 0.4
90	178 ± 2.3	238 ± 4.6	3,6 ± 0.3
75	120 ± 5.7	201 ± 2.1	5,7 ± 0.9
60	82 ± 3.1	165 ± 2.7	8,0 ± 0.4

The correlation between mechanical properties and thermal exposure (quantified by the corresponding residual hardness) is reported in Fig.3.4 and Fig.3.5: a linear regression well fits both $Rp_{0.2}$ and UTS data, while a logarithmic equation was chosen to model the elongation to failure trend. The relationships among residual hardness and mechanical properties of the alloy are in agreement with those reported by the authors [30] for the alloy EN AW-2618.

In order to have a complete overview of the mechanical behavior of this piston alloy, the Hollomon's equation [127] (Eq.3.1) was used to model the relationship between true stress and true strain in the plastic field. As reported in Fig.3.6a, the strain hardening exponent n follows a power law, exhibiting a continuous increase with decreasing residual hardness. Fig.3.6b instead shows that a positive slope linear regression well fits the relationship between the strength coefficient K and the residual hardness.

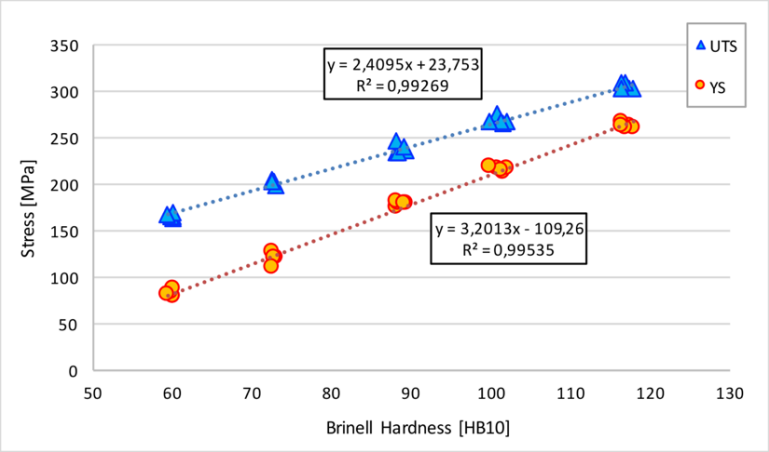

Fig.3.4: Linear correlation between proof strength / ultimate tensile strength and residual hardness of EN AW-4032 T6. Different hardness values were obtained after different thermal exposure, as reported in Table 3.3.

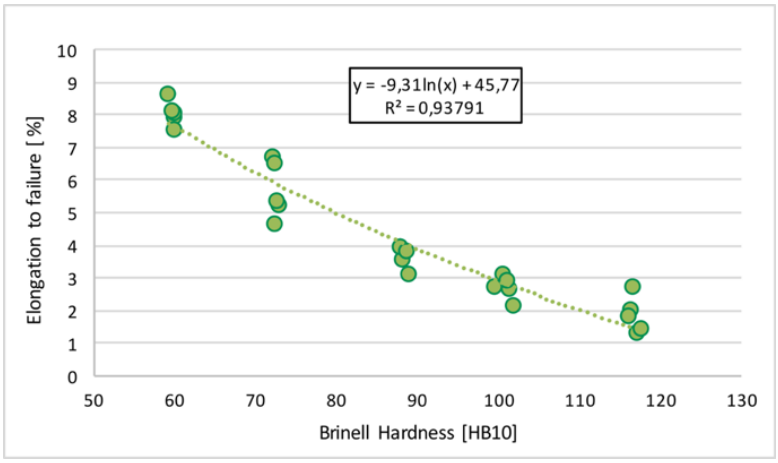

Fig.3.5: Correlation between total elongation to failure and residual hardness values for the EN AW-4032 alloy. Different hardness values were obtained after different thermal exposure, as reported in Table 3.3.

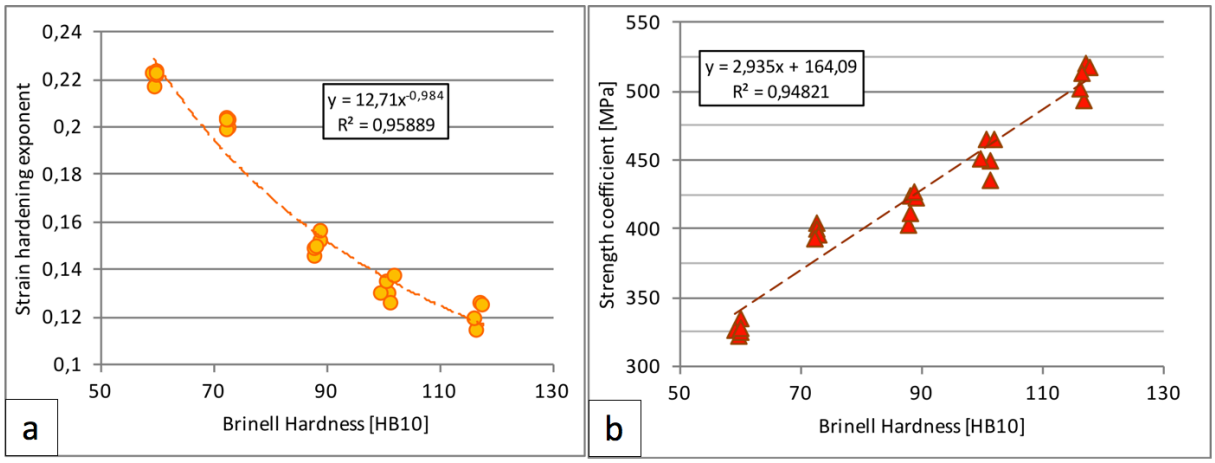

Fig.3.6: Correlation between residual hardness and: (a) strain hardening exponent n; (b) strength coefficient K. Different hardness values were obtained after different thermal exposure, as reported in Table 3.3.

The opposite trend of n and K parameters (Fig.3.6) is related to the different strengthening mechanisms able to hinder the dislocations movement at peak-aged (higher hardness) or overaged (lower hardness) conditions.

The main strengthening mechanism in the peak-aged alloy is precipitation hardening, which is offered by the elastic distortion of the crystal structure due to the presence of very fine, coherent and shearable precipitates; the elastic distortions act as considerably efficient obstacles to dislocations motion. This is clearly shown in Fig.3.4 and Fig.3.6b, which show that the higher the residual hardness is (peak-aging condition), the higher the values of the strength coefficients K and proof strength $Rp_{0.2}$ are. However, once the coherent precipitates (characterizing the peak-aged alloy) are cut by dislocations, according to Ashby mechanism [128], dislocations are allowed to

move freely, without significant interaction with each other or with other fine phases, therefore with negligible strain hardening. This explains the low values of the strain hardening exponent n (Fig.3.6a), related to the higher residual hardness values.

On the contrary, the strengthening mechanism in the overaged alloy is chiefly related to the presence of coarsened, not coherent and not shearable precipitates. The interaction between coarse particles and dislocations switches from Ashby to Orowan mechanism [128,129]: dislocations can easily by-pass the coarse particles, leaving dislocation rings around them. This firstly leads to low values of proof strength and strength coefficient. If further stress is imposed, the interaction between dislocations themselves creates obstacles to further dislocations movement, which means that a significant strain hardening is produced, or better, a higher stress is required for the deformation process to proceed. This explains the significant increase in the strain hardening exponent n for the considerably overaged conditions.

By combining the empirical expression of K and n in Hollomon's law (Eq.3.1), Eq.3.2 is obtained, able to model the true stress-true strain relationship for the tested alloy in the plastic field:

$$\sigma_{true} = (2.935 \cdot HB + 164.09) \cdot \varepsilon_{true}^{(12.71 \cdot HB^{-0.984})}$$

Eq.3.2: Model for the true stress-true strain relationship for the tested alloy in the plastic field.

Eq.3.2 was implemented to compare the modelled curves to the actual data in the plastic field. The comparison is reported in Fig.3.7: the dashed lines refer to the modelled behavior and they are limited to stresses exceeding $Rp_{0.2}$, while the solid lines are representative of the actual alloy behavior and they therefore cover both elastic and plastic fields. By considering the data reported in Fig.3.7, it seems that Eq.3.2 is more suitable to describe the plastic behavior of the alloy (i) at lower residual hardness and (ii) at low levels of plastic deformation. This can be related to the fact that: (i) the strain hardening mechanism (well described by the Hollomon's law) is mainly active in the overaged alloy, characterized by the presence of incoherent but close-spaced precipitates with dislocation loops; (ii) the cracking of Si particles, which occurs during plastic deformation, prevents the alloy from significant hardening.

However, it has to be noted that the model is extremely accurate, providing therefore an effective instrument for FEM calculations in the field of interest.

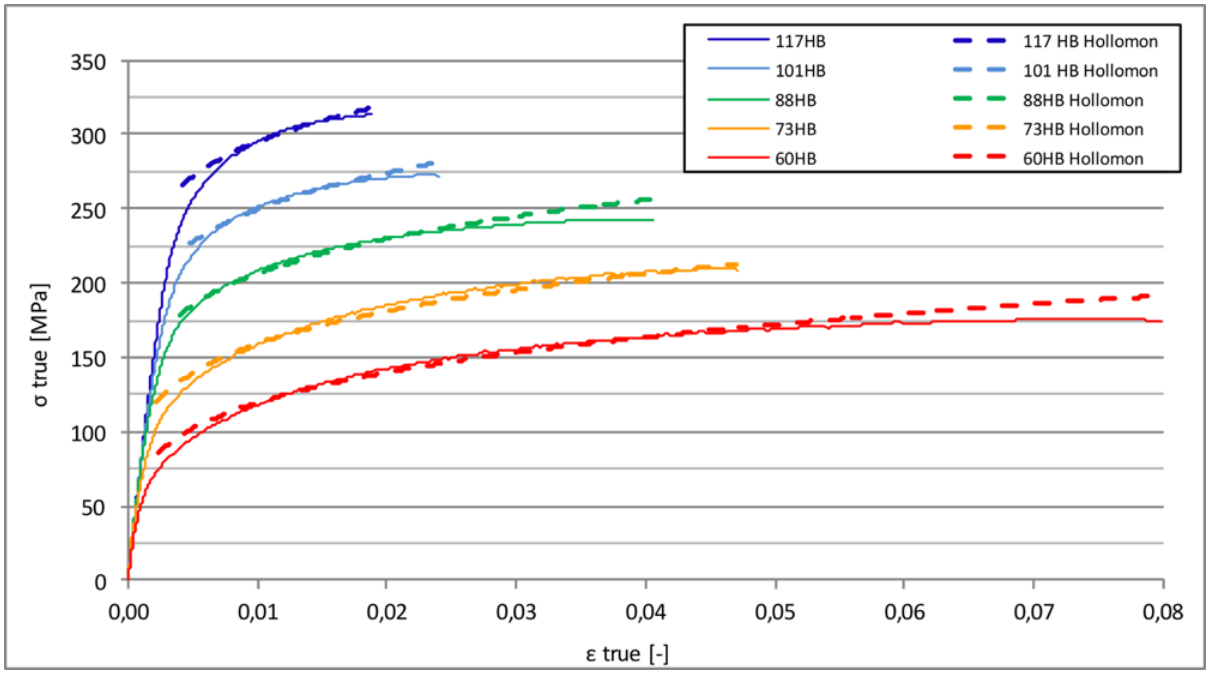

Fig.3.7: Comparison between representative true stress-true strain curves (solid lines) of the EN AW-4032 T6 alloy after thermal exposure and the plastic behavior (dashed lines) of the same alloy modelled according to Eq.3.2.

Microstructural analyses

OM and SEM-EDS analyses were carried out to relate the mechanical properties and microstructural features of the EN AW-4032 T6 alloy. Fig.3.8 reports representative SEM and OM micrographs of the alloy after the forging process and subsequent heat treatment. In Fig.3.8a the presence of coarse (primary and eutectic) Si particles, not homogeneous in size (consistent with the forging process as also reported in [29]), is clearly visible (grey in figure), as well as other lighter and finer compounds, probably Ni-Cu-Mg-Fe based intermetallics. Moreover, intermetallic compounds and Si particles are aligned along the plastic flow direction. The presence of plastic flow bands is also evident in Fig.3.8b which shows the microstructure of the alloy after Keller's chemical etching: the plastic deformation process fragments part of Si crystals and leads to fine and slightly elongated grains with an average size of 7µm.

Backscattered electron SEM micrographs and EDS analyses of some representative intermetallics are reported in Fig.3.9. In particular, Fig.3.9a shows fine Cu-Ni rich compounds clustered next to coarser Fe-Ni based phases which seem to initiate their nucleation. A similar morphology can be observed in Fig.3.9b, in which coarser Mg-Si rich intermetallic compounds are surrounded by finer and bright Cu-Ni-Fe rich intermetallics.

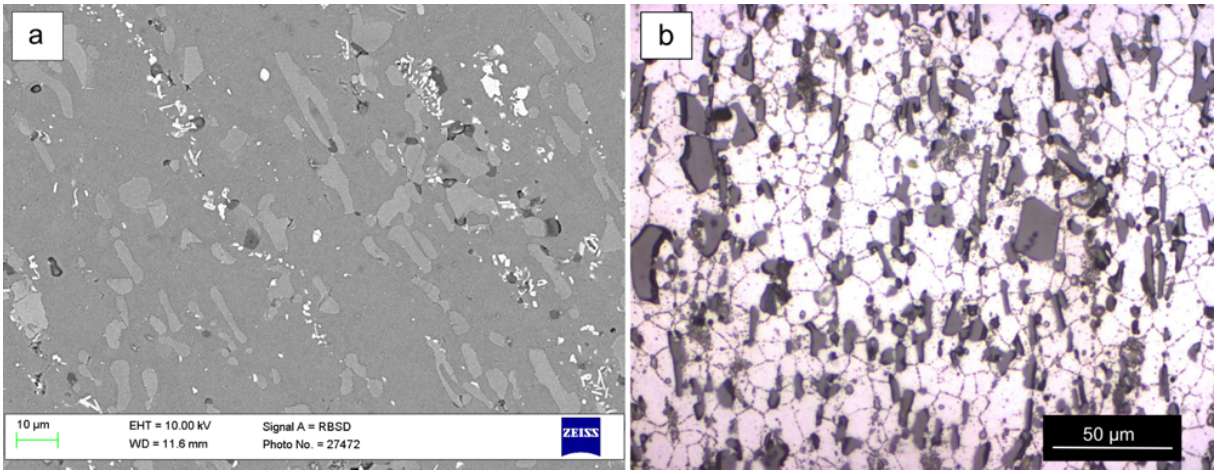

Fig.3.8: SEM micrograph of polished (a) and OM optical micrograph of chemical etched (b) samples of the EN AW-4032 T6 alloy.

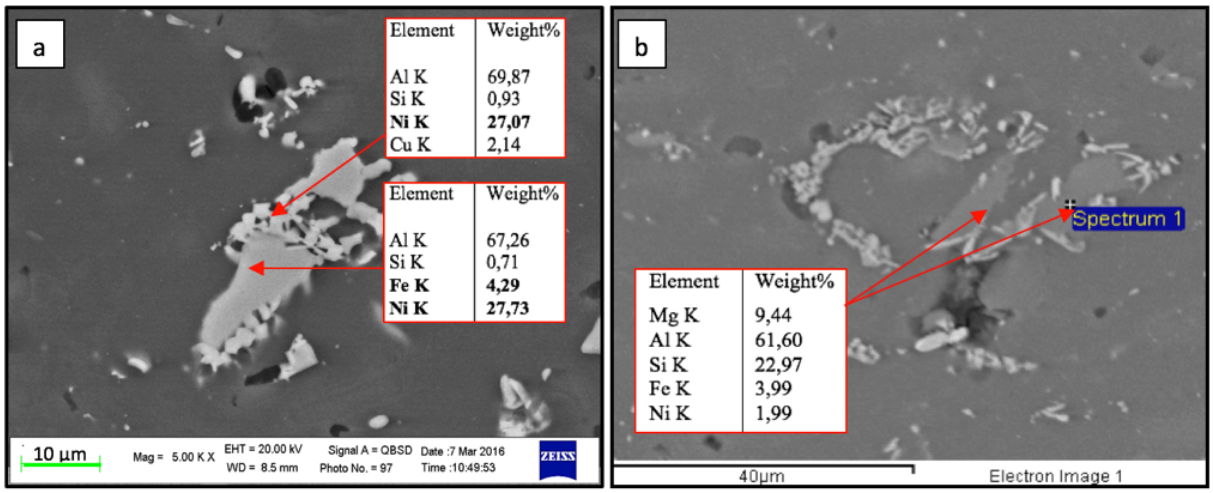

Fig.3.9: Backscattered electrons SEM micrographs of the forged and T6 heat treated EN AW-4032 alloy: (a) coarse Fe-Ni rich intermetallics surrounded by Al-Ni-Cu compounds and corresponding semi-quantitative EDS spectra; (b) Al-Si-Mg-Fe-Ni intermetallics, enclosed by finer and presumably Ni-Cu-Fe based compounds.

Fig.3.10 shows OM micrographs of H_3PO_4 etched samples, extracted close to the fracture surfaces of the tensile specimens. In particular, Fig.3.10a highlights the presence of some intergranular cracks in the peak-aged specimen. Chemical etching does not highlight any precipitation, that instead clearly appears in the thermally exposed specimens (Fig.3.10b and Fig.3.11). The latter, softened down to60 HB, shows small intermetallic compounds precipitating at grain boundaries but no cracks are evident along these boundaries. The coarsening of precipitates, in fact, leads to a significant depletion of strengthening precipitates at grain boundaries, which subsequently gives origin to precipitation free zones (PFZs [30,130]). Due to the very small grain size, an extended volume fraction of grains becomes free from precipitates, resulting in high dislocation mobility. This is the reason why, as reported in Fig.3.4, Fig.3.5, Fig.3.6,

Fig.3.7, the higher the thermal exposure, the lower the tensile properties and the higher the elongation to failure of the material.

SEM-FEG micrographs reported in Fig.3.11 show, at higher magnifications, the microstructure of thermally exposed alloy. Consistently with the performed EDS analyses (Fig.3.9) and literature data [25,26,29], coarse eutectic Si particles (dark grey) and bright Al-Ni-Cu-Fe based compounds (larger than 1µm) are visible. A fine network of precipitates coarsened due to thermal exposure (yet smaller than 1µm), decorates grain boundaries. The extremely small size of the precipitates does not allow EDS analyses to reveal their chemical compositions. However, since the EN AW-4032 alloy is subjected to T6 heat treatment, which promotes the precipitation of precursor phases of stable Mg_2Si, Al_2Cu, Al_2CuMg, etc. [25,121,124,125], the incoherent precipitates observed at grain boundaries are thought to belong to these families.

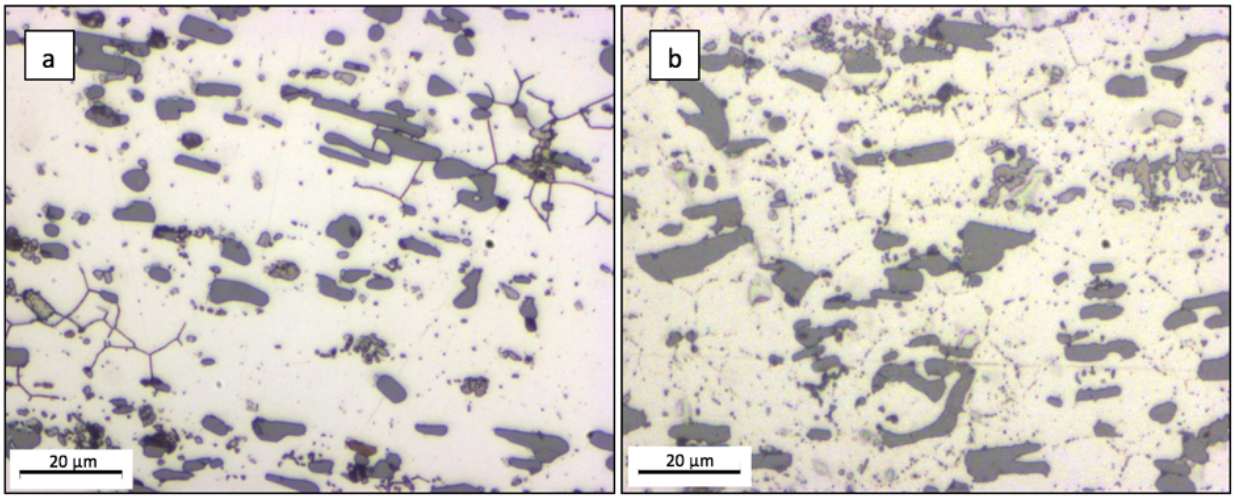

Fig.3.10: OM micrographs of EN AW-4032 samples machined from tensile specimens, after etching with H_3PO_4: (a) cracked Si particles, decohesion of Si and intermetallics with intergranular cracks on peak aged sample; (b) formation of fine inchoerent precipitation of strengthening phases at grain boundaries, in thermally exposed samples - 120h at 290°C.

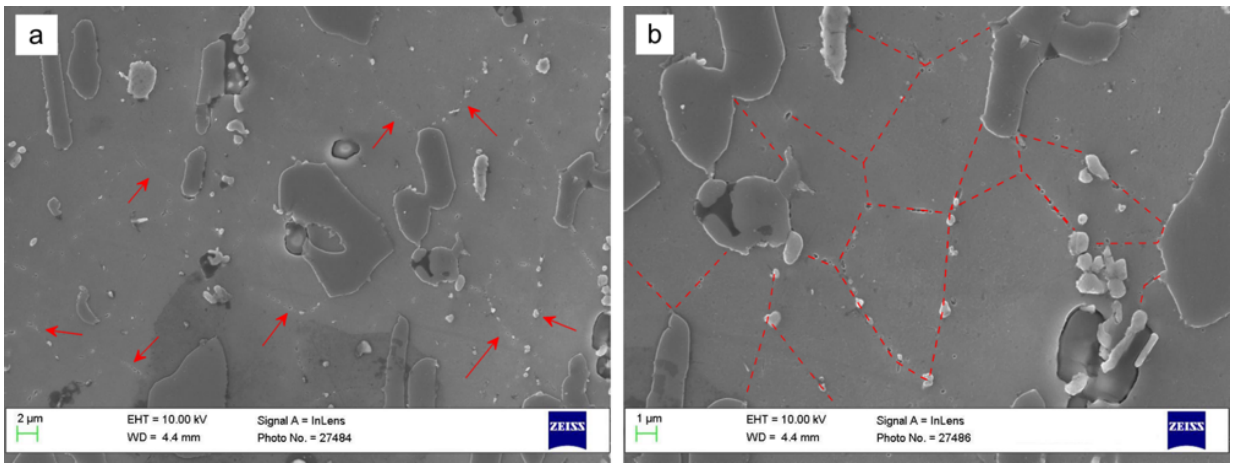

Fig.3.11: FEG-SEM micrographs of EN AW-4032 samples machined from tensile specimens subjected to 120h at 290°C. Precipitation at grain boundaries is pointed out by arrows (a) and dashed lines (b).

Fractographic analyses

SEM investigations of the fracture surfaces are useful to assess the effects of microstructural evolution, due to thermal exposure, on the fracture pattern. It is also worth to point out how the different fracture patterns are consistent with the slight elongation to failure of the peak-aged specimens respect to that measured on the overaged ones (Table 3.4). Fig.3.12 shows the SEM micrographs referring to the peak-aged and highly overaged tensile specimens.

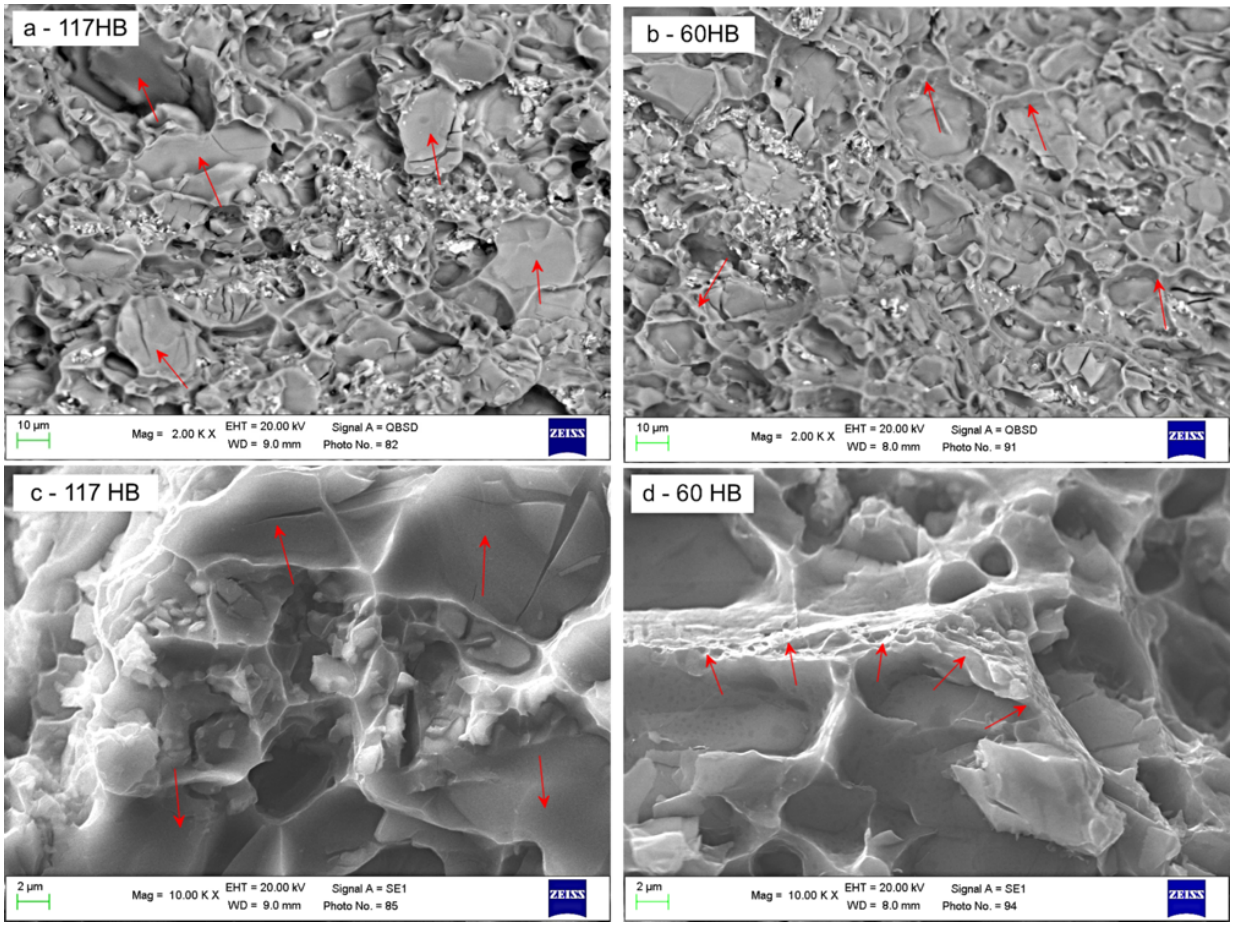

Fig.3.12: Different magnitude SEM micrographs of the fracture surfaces of peak aged (a,c) and overaged (b,d) tensile samples. In the labels the residual hardness of the specimens is reported.

Low magnification backscattered electron micrographs (Fig.3.12a and Fig.3.12b) clearly show similar fractographic features but with some differences. The peak aged specimen (Fig.3.12a) shows a higher fraction of brittle, fractured, coarse Si crystals (indicated by the arrows) together with a higher amount of fine Cu-Fe-Ni intermetallic compounds (brighter phases in the micrographs). Otherwise, the overaged specimen (Fig.3.12b) seems to show a larger plastic deformation of the matrix (pointed out by the arrows). These observations are in accordance with the literature [29,131], stating that mechanical stresses usually lead to cracking or decohesion of

large particles, which initiate the failure. However, it is possible to define two different failure mechanisms:

- for peak-aged specimens, cracks nucleate at large Si particles and finally involve the decohesion and fracture of finer intermetallic compounds, with further propagation along grain boundaries (Fig.3.10a)
- for the over-aged specimens, Si particles cracking is followed by severe plastic deformation of the surrounding matrix, which leads to fracture. The latter behavior can be explained by considering that thermal exposure causes the softening of the matrix due to the coarsening of precipitation phases (Fig.3.10b and Fig.3.11).

The presence of two different fracture patterns is further confirmed by the SEM micrographs at higher magnification, reported in Fig.3.12c and Fig3.12d. Peak aged sample (Fig.3.12c) clearly shows cleavage fracture of Si crystal (pointed out by the arrows), surrounding mixed intergranular and ductile fracture zones in correspondence of finer intermetallic compounds. On the contrary, fractured Si crystals in the overaged samples (Fig.3.12d) are surrounded by extended plastic areas, on which very small dimples (probably associated to coarse precipitates inner to the grains [30]) are clearly visible.

3.1.4 Conclusions

The present study was focused on the effect of thermal exposure on EN AW-4032 piston alloy; the analyses consisted of hardness and room temperature tensile tests on peak-aged and overaged samples, coupled with microstructural and fractographic investigations. A complete characterization of the strengthening mechanisms of the alloy during in-service operations has been provided, together with an effective model of the mechanical behavior of the material. The results of the study can be summarized as follows:

- The time-temperature-hardness curves of the EN AW-4032 T6 alloy have been investigated in the temperature range of interest for pistons, 140-290°C. The alloy exhibits a fork of properties within 118HB (peak-aging) and 57HB (overaging).
- The T6 heat treated alloy exhibits a considerable decrease of mechanical properties when subjected to thermal exposure. The higher the time or temperature of exposure, the lower the strength of the alloy and higher its ductility.

- The plastic behavior of the alloy at room temperature can be modelled through Hollomon's equation, as a function of residual hardness, with higher accuracy for low residual hardness and low plastic deformation conditions.
- Tensile specimens machined from forged and heat treated pistons reveal a fine but inhomogeneous microstructure, consisting of coarse primary Si crystals and intermetallics bands (Cu-Ni-Fe, Mg-Si and Cu-Ni based compounds) due to the extrusion process undergone by the alloy. This inhomogeneity does not significantly affect the repeatability of the tensile tests, always resulting in moderate standard deviations.
- The coarsening of strengthening precipitates due to thermal exposure is responsible for larger elongation to failure and lower tensile strength. OM as well as FEG-SEM analyses clearly show several networks of coarsened precipitates decorating grain boundaries after prolonged overaging.
- Fracture patterns of tensile specimens in different overaging conditions confirm the microstructural changes caused by thermal exposure.

3.2 AA4032 with higher amount of Cu: Heat Treatment Optimization

3.2.1 Introduction

The research on the AlSi12CuNi piston alloy here reported has not been published yet. As already mentioned, with respect to AA4032, this alloy exhibits higher amounts of Cu and almost comparable or slightly superior Ni, which significantly enhance its resistance to thermal exposure [17,18,27,28,19–26]. This is due to the fact that both Cu and Ni form intermetallic phases (Al_7Cu_4Ni, Al_9FeNi, Al_3Ni_2, Al_3Ni, AlNiCuFeSi- based, AlCuNiSi-based) which are intrinsically more stable than the Al matrix at high temperature and provide an effective load transfer.

Several researches [18,19,29,126,132–135] dealing with similar Al-Si alloys have been taken into account in order to optimize the heat treatment for this specific alloy, both the solution and the subsequent artificial aging treatment. In particular, different options have been analyzed:

- Cho et al. [18] studied some nearly eutectic Al-Si alloys with different content of Cu and Ni, proposing a T6 heat treatment consisting of solution treatment at 510°C for 2h, quench and artificial aging at 210°C for 5h; a peak-aged hardness of 140-120HB was obtained.
- A lower solution temperature of 495°C, maintained for 8h, was selected by Mohamed et al. [132] followed by quench and artificial aging at 155°C, 180°C, 200°C, 220°C, 240°C for 5h (T6 and T7 tempers). Also in this case, different amounts of Cu in Al-Si alloy have been considered. According to the authors, the aging heat treatment consisting in 5h soaking at 180°C offers the peak aged condition for the alloy similar to that studied in this Sect.
- Dealing with AlSi12Ni alloys, Stadler et al. [126,135] and once again propose a solution heat treatment consisting in 8h soaking at 495°C, confirming the solution treatment reported in [132].
- An artificial aging of 5h at 210°C was carried out in [19] by Cho et al., while Konečna et al. [29] carried out a T7 heat treatment at 215°C for 9h on a similar eutectic AlSi12CuNi alloy.

These researches, coupled with DTA analyses and hardness data collected during the experimental activities, were the basis for the heat treatment optimization. It should be also taken into account that this alloy is employed for pistons production, which means that a T7 temper is preferable to T6 due to the higher dimensional stability. This aspect would be following considered.

3.2.2 Material and methods

The AlSi12CuNiMg was supplied in the form of large cast ingots by Duraldur S.p.A.

In order to provide a finer microstructure and a more homogeneous solidification rate, the ingots have been re-melted at Metallurgy Dept. through an induction furnace (TopCast®) up to 800°C; the alloy was then poured in a permanent mold containing approximately 1kg of material for each casting, whose cylindrical geometry is shown in Fig.3.13. In order to prevent Al sticking to the mold, a homogeneous, thin layer of Boron Nitride or Graphite-based spray was adopted.

The melting procedure consisted of:

i. Cutting the supplied ingots into small pieces (roughly 3 x 3 x 6cm) to reach the approximate weight of 1kg
ii. Cutting the master alloy Al-10wt%Sr for the addition of 300ppm Sr, in order to correctly modify the morphology of eutectic Si (3g of master alloy per 1kg of whole casting)
iii. Putting all pieces into the furnace and starting the actual melting by imposing a temperature of 800°C in a protective Ar atmosphere.
iv. Starting the pouring cycle after complete melting and holding to reach a homogeneous temperature, in the mold pre-heated to 200°C.

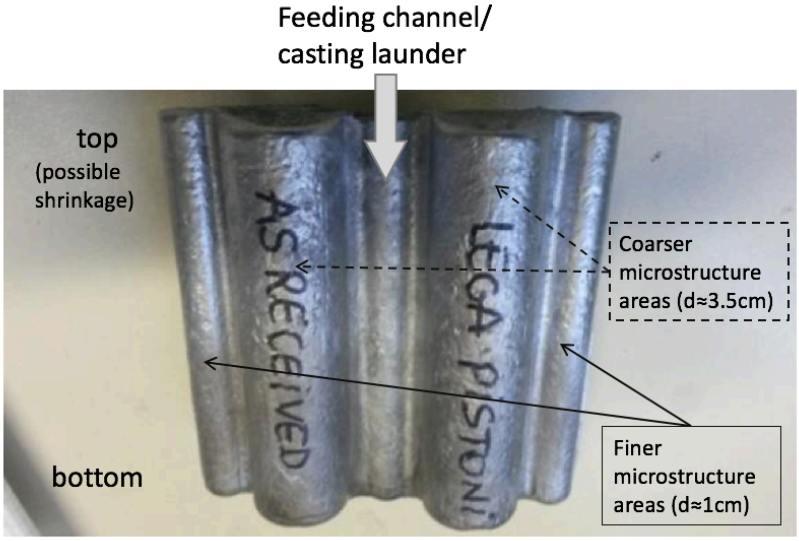

Fig.3.13: Casting of approximately 1kg weight, starting from the supplied ingots of AlSi12CuNiMg.

Spectrometric chemical analyses, by glow discharge optical emission spectroscopy (GDOES), were carried out on samples taken from the top and the bottom of the castings, in order to gain data about the macro-scale segregation of the alloying elements. The analyses did not show

anomalies, just a negligible Cu and Ni variation (up to 0.1wt%) was detected due to the higher specific weight of these elements. The average results are reported in Table 3.5.

Table 3.5: Average chemical composition of the AlSi12CuNiMg castings.

Elements [wt%]	Si	Mg	Mn	Fe	Ni	Cu	Al
Mean	10.6	1.03	0.25	0.26	0.77	3.50	Bal.

The heat treatment was subsequently optimized taking advantage of:

- Differential Thermal Analysis (DTA), which is able to detect both exothermic or endothermic changes in the samples and it allows to determine the melting temperature of the possible eutectic phase. As reported in Sect.2.1.2, in fact, a two-step solution heat treatment is often carried out to overcome the incipient melting issue: the 1st stage of the solution treatment is performed at temperature below the eutectic phase melting and it lasts until its complete dissolution; higher temperatures characterize the 2nd stage, which is aimed to complete the solution process, making all solute atoms available for the subsequent precipitation hardening. DTA analyses were carried out on samples of 30mg weight, put in alumina crucible, following a heating rate of 10°C/min from 30°C up to 700°C, in constant Ar flux (30mL/min).
- Brinell hardness measurements, carried out on samples grinded up to 600 grit size (at least), using a hardened steel ball indenter with d=2.5mm and 62.5kg weight.

The optimized heat treatment for the base alloy would be following referred to as T7-base.

OM and SEM microstructural investigations were also carried out at each step of the experimental activities. It should be pointed out that cast material coming from the lateral areas with finer microstructure (Fig.3.13), in particular from the bottom of the casting, was preferentially selected for all the analyses in order to avoid the scattering of results related to porosity or incomplete feeding and/or different microstructure size.

3.2.3 Results and discussion

The as cast microstructure is reported in Fig.3.14. It can be noted the presence of several polygonal-shaped blocks of primary Si and acicular-shaped eutectic Si phases (both dark grey). A large amount of Cu and Ni phases is also visible as light grey colored phases. Limited porosity is perceivable al low magnification.

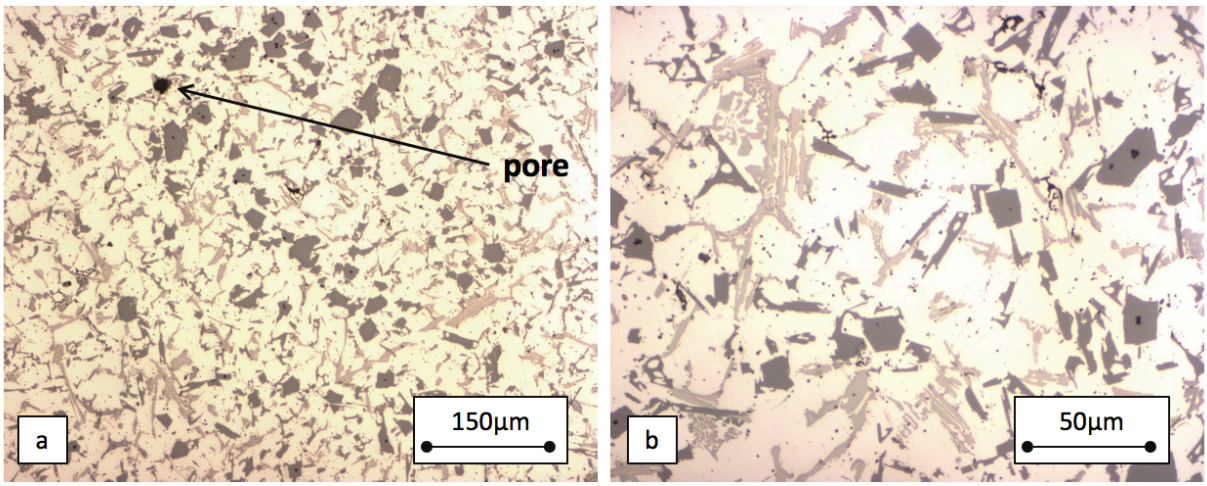

Fig.3.14: OM micrographs of the as-cast AlSi12CuNiMg alloy, respectively at low and high magnification.

Optimization of the solution phase

DTA analysis has been at first carried out on the as cast alloy (Fig.3.15a) to determine the best combination of soaking time and temperature for the solution heat treatment. A limited endothermic peak with an onset temperature around 508°C can be noticed, before reaching the huge peak of heat flow associated to the whole alloy melting. In view of this and of the aforementioned bibliographic references, which suggested a prolonged solution treatment at 495°C [126,132,135], 495°C was the temperature selected for the first step of the solution treatment. DTA analyses were then repeated after 1h (Fig.3.15b), 2h (Fig.3.15c), 3h, 4h soaking at 495°C. It can be clearly noticed that the endothermic peak at 508°C disappears after 2h soaking, and the same was of course observed after 3h and 4h soaking (DTA graphs here not reported). The observation is also confirmed by the trend of the heat flow derivative of the as cast sample compared to that subjected to 2h soaking, reported in Fig.3.15d. It can be therefore inferred that 2h soaking at 495°C is sufficient to avoid the incipient melting which would have been encountered around 508°C.

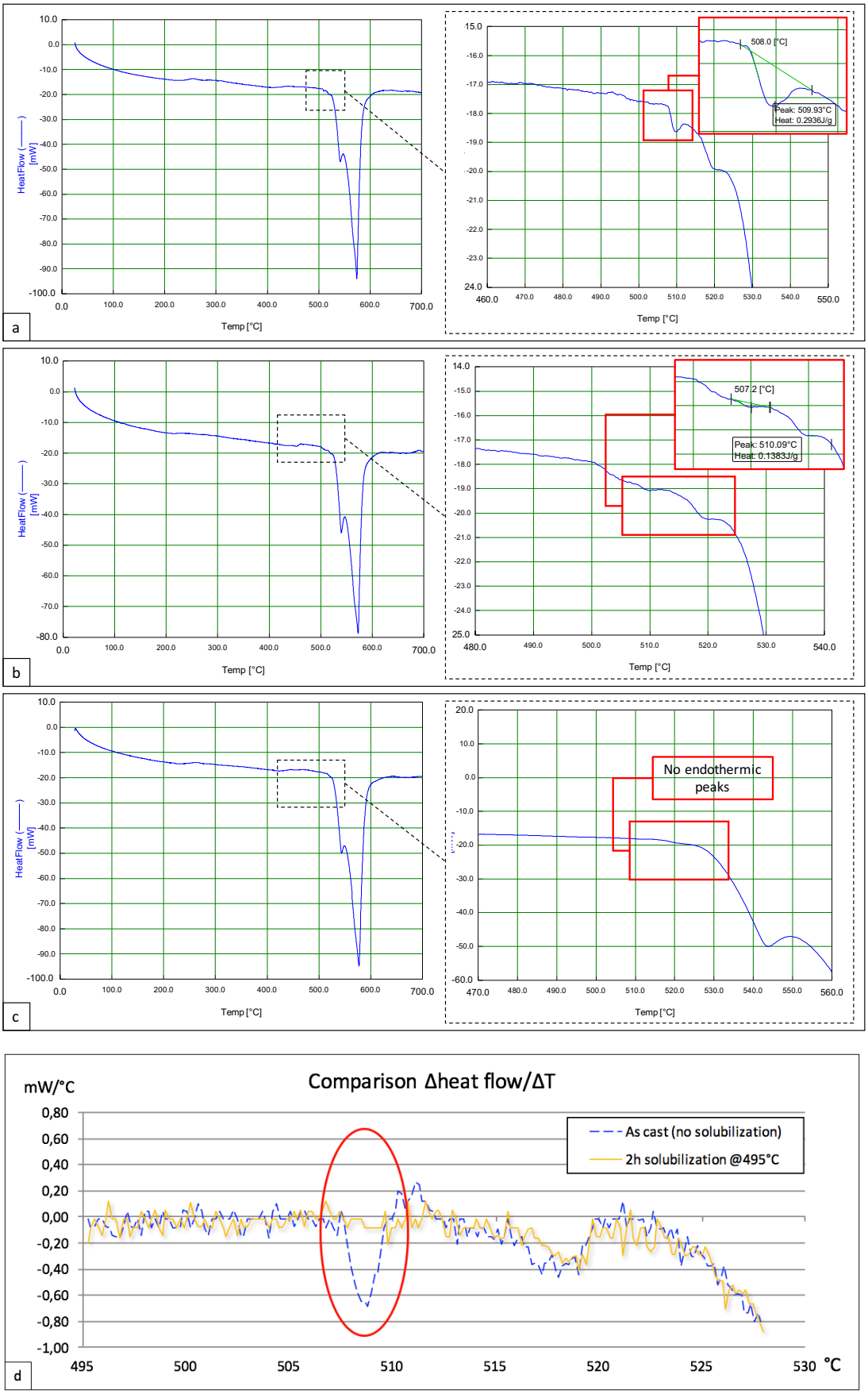

Fig.3.15: DTA analyses on the AlSi12CuNi alloy in the following conditions: a) as cast; b) after 1h soaking at 495°C; c) after 2h soaking at 495°C; d) trend of the derivative ΔHeat Flow/ΔT of as cast and 2h-solutioned samples, showing the lack of discontinuity at 508°C after 2h soaking at 495°C.

The temperature of the 2nd step of the solution treatment was then determined by observing Fig.3.15c and/or the solid line in Fig.3.15d, representative of the alloy condition after the 1st step of solution. The onset of the subsequent consistent phase transformation is observed around 525°C: a lower temperature was therefore selected, equal to 515°C, and maintained for 2h, 3h, 4h, 5h. Soaking time was not further extended, considering the 8h solution treatment at 495°C proposed by [126,132,135] and even just 2h at 510°C carried out by Cho et al. [18].

Aiming to determine the optimal duration of the 2nd step of solution treatment, Brinell hardness tests after different solution time + aging for 5h at 215°C were selected as a valid instrument. As reported in Sect. 2.1.2, in fact, the objective of the solution treatment is to make all solute atoms available for the subsequent precipitation hardening; the optimal solution treatment would therefore exhibit the higher hardness after the aging treatment. The hardness data are reported in Fig.3.16. It can be noticed that a hardness increase of approximately 10HB is achieved between 2h and 4h soaking at 515°C, with no appreciable differences between 2h and 3h soaking. Even if a 2nd step of solution treatment consisting of 4h holding at 515°C appears the optimum choice for this alloy, 2h soaking at 515°C was considered the best compromise costs/benefits. This is further supported by the solution treatment proposed by Cho et al. in [18], which consisted in a single step of just 2h soaking at 510°C.

The final solution treatment selected for the alloy therefore consisted in holding for 2h at 495°C + holding for 2h at 515°C.

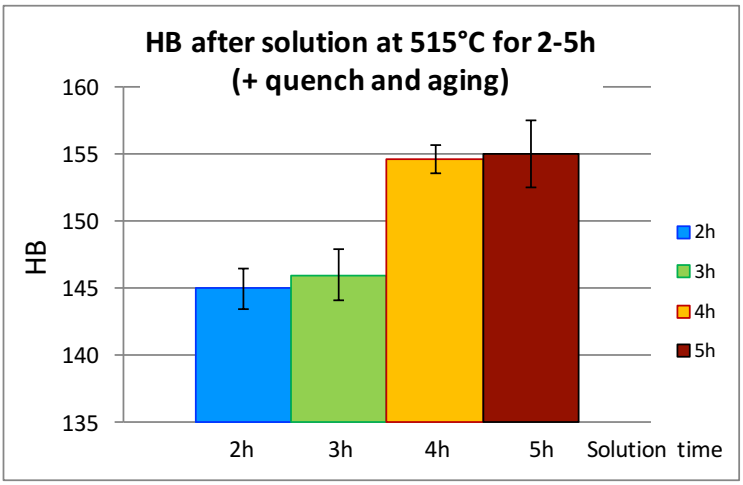

Fig.3.16: Hardness measurements after solution treatments characterized by different duration (+ quench + aging 5h at 215°C).

Optimization of the artificial aging

The artificial aging step was once again optimized taking advantage of Brinell hardness measurements, this time after the selected solution treatment + quench + different aging conditions. According to the aforementioned references for similar AlSi12CuNi alloys, Cho et al. [18,19] propose an artificial aging at 210°C for 5h, while Mohamed et al. [132] consider 5h soaking at 180°C to achieve a peak hardness; finally, Konečná et al. [29], who worked in particular on an AlSi12 *piston* alloy, carried out a T7 heat treatment at 215°C for 9h. A temperature range between 180°C-215°C was therefore selected to evaluate the optimal artificial aging. Since this alloy is employed for pistons production, a T7 temper would be preferable, in agreement with Konečná et al. [29].

The different aging curves are reported in Fig.3.17. It can be noted that soaking as long as 5h produce an overaged T7 temper both at 200°C and 215°C, while holding at 185°C approximately maintains the peak hardness even after 9h. Since the variation of the alloy hardness is narrow comparing the results of 5h and 9h soaking at 215°C (5HB, negligible if considering the standard deviation), the first option was considered the optimal combination of costs/benefits for the aging step.

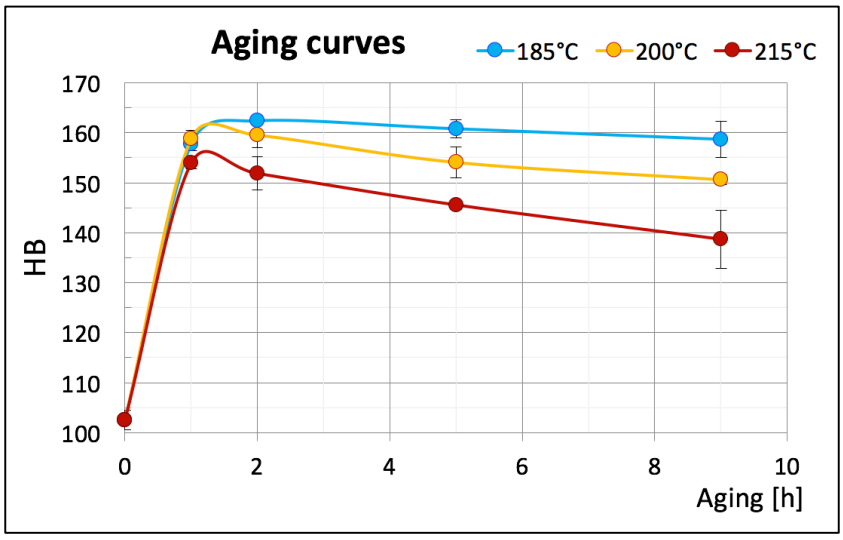

Fig.3.17: Aging curves of the AlSi12CuNi alloy at 185°C-200°C-215°C up to 9h, after solution (2h at 495°C + 2h at 515°C) and quench. The starting point (≈100HB) is representative of the alloy hardness after solution + quench.

The OM micrographs after the optimized T7 heat treatment for the base alloy, consisting in solution for 2h at 495°C + 2h at 515°C, quenching, and artificial aging for 5h at 215°C (later reported as T7-base) are shown in Fig.3.18. By comparing these with the OM micrographs of the

as cast condition (Fig.3.14), a lower amount of light grey, secondary phases, even finer, is perceivable, as well as a rounder shape of primary Si crystals.

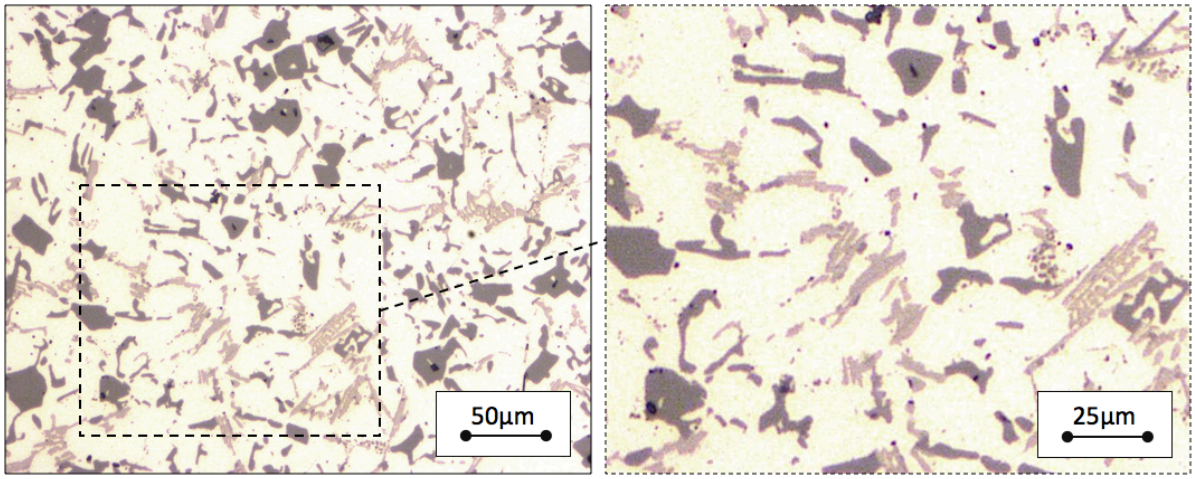

Fig.3.18: OM micrographs of the AlSi12CuNiMg alloy after T7-base temper.

SEM-EDS analyses (Fig.3.19) highlight the presence of:

- Dark grey Al(MgCu)Si phases, which might correspond to the blocky Q phase ($Al_5Mg_8Si_6Cu_2$)
- Light grey AlCuNi phases, usually characterized by acicular shape (fine rounded white phases are more seldom encountered, but visible in Fig.3.19b)
- A few light grey, skeleton like, AlCuNiFeMnSi phases are also observed (here not reported)
- Primary Si crystals, dark and barely detectable in the Al matrix.

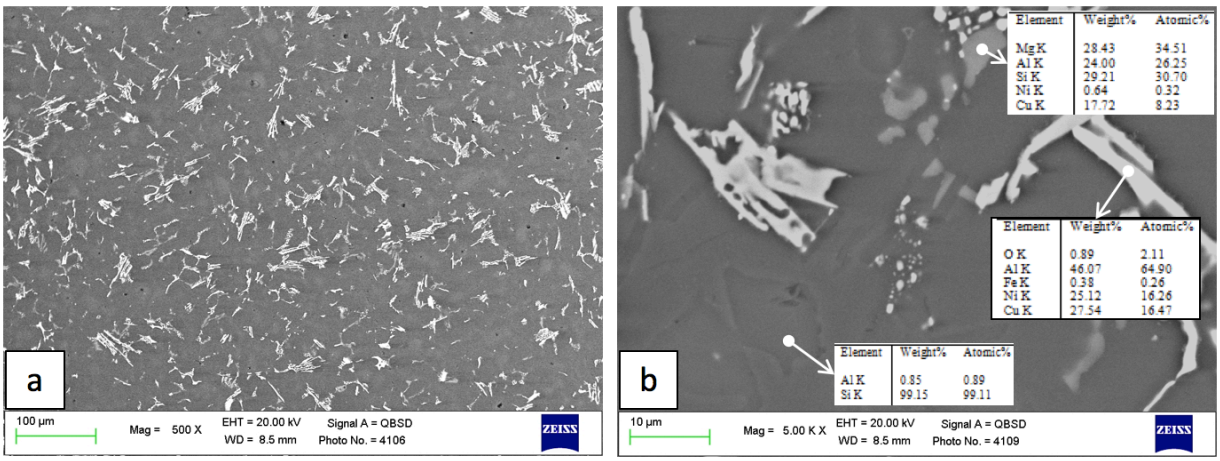

Fig.3.19: SEM-EDS analyses of the AlSi12CuNiMg alloy after T7-base temper at a) low, b) high magnification. Images acquired through backscattered electrons.

3.3 AA4032 with higher amount of Cu: effects of Mo additions after overaging at 250°C

3.3.1 Introduction

The research on the AlSi12CuNi piston alloy + Mo additions here reported has not been published yet. As already mentioned in Sect. 2.3.4, the presence of Si in Al alloys is reported to disturb the formation of thermally stable trialuminides. Aiming to enhance the high temperature properties of this eutectic Al-Si alloy, containing high amount of Cu and Ni, Mo additions have been tested. For these experimental activities, the promising results by Farkoosh et al. [105,107] on Al-Si-Cu-Mg alloy have been taken into account. In order to get the full benefits of Mo additions, given the already good mechanical properties at high temperature of the base alloy, up to 0.3 wt% Mo was added to the base alloy; this is in fact the maximum amount of Mo which can be retained in Al solid solution without incurring in primary precipitation during solidification, for any conventional casting techniques.

As regards the heat treatment, Farkoosh et al. [105,107] proposed a solution treatment consisting in 2 homogenization steps in order to promote the formation of Al-(Fe,Mo)-Si dispersoids: (i) 4h at 500°C + (ii) 1h at 540°C to achieve the peak hardness. After that, quench and the more suitable aging treatment for the specific Al-Si alloy can be applied without affecting Mo dispersoids, due to the relatively low temperature involved.

3.3.2 Material and methods

As already reported in Sect. 3.2.2 for the base material, also the modified alloy was re-melted through an induction furnace (TopCast®), with the same permanent mold geometry shown in Fig.3.13 and containing around 1kg of material for each casting. The casting steps were slightly different due to the addition of specific amounts of the master alloy Al-10wt%Mo and the need to enhance Mo diffusion. In particular, the following (iv- vi) steps have been added:

i. Cutting the supplied ingots into small pieces (roughly 3 x 3 x 6cm) to reach the approximate weight of 1kg

ii. Cutting the master alloy Al-10wt%Sr for the addition of 300ppm Sr, in order to correctly modify the morphology of eutectic Si (3g of master alloy per 1kg of whole casting)
iii. Putting all pieces into the furnace and starting the actual melting by imposing a temperature of 800°C in a protective Ar atmosphere
iv. Cutting the master alloy Al-10wt%Mo (≈30g) to reach the targeted 0.3wt% Mo and putting all pieces into the furnace, always working in a protective Ar atmosphere to limit oxidation
v. Increasing the furnace temperature up to 900°C for at least 30minutes to stimulate homogenization and master alloy dissolution
vi. Slowly cooling from 900°C to 800°C
vii. Starting the pouring cycle, in the mould pre-heated to 200°C.

GDOES analyses were then carried out on samples taken both from the top and the bottom of the castings, to gain data about the macro-scale segregation of the alloying elements and to have the confirmation of the actual Mo addition. The analyses did not show anomalies, and the average results are reported in Table 3.6.

Table 3.6: Average chemical composition of the AlSi12CuNiMg castings + Mo additions.

Elements [wt%]	Si	Mg	Mn	Fe	Ni	Cu	Mo	Al
Mean	11.3	0.95	0.24	0.23	0.72	3.25	0.29	Bal.

To optimize the heat treatment for Mo containing alloy, especially as regards the solution step which is aimed in this case to enhance the formation of Mo dispersoids, DTA analyses were not repeated. The alloy was in fact slightly modified with tiny additions of a low diffusivity element, which is supposed not to produce low melting phases. Brinell hardness tests were indeed performed on samples grinded up to at least 600 grit size, using a hardened steel ball indenter with d=2.5mm and 62.5kg weight, with the aim to detect the best compromise of solution temperature/holding time by evaluating the average hardness after solution. The hardness after solution is in fact mainly connected to matrix supersaturation and eventually Mo precipitation.
Then, the aging heat treatment already optimized for the base alloy (Sect. 3.2.3) was also applied to the Mo enriched alloy, in order to stimulate the formation of conventional Cu, Mg, Si and Ni based precipitates. The so defined optimized heat treatment, consisting in solution to enhance the formation of Mo dispersoids + quench + conventional aging, would be hereafter referred to as T7-Mo.

Finally, to evaluate the effectiveness of Mo additions for high temperature resistance and/or the effectiveness of different heat treatments (T7-base and T7-Mo) in stimulating Mo-based dispersoids, overaging heat treatments have been performed at 250°C for both base and Mo containing alloy, heat treated according to both T7-base and T7-Mo temper conditions.
OM and SEM microstructural investigations were carried out at each step of the experimental activities.

3.3.3 Results and discussion

The as cast microstructure is reported in Fig.3.20. It can be noted the presence of polygonal-shaped blocks of primary Si and acicular-shaped eutectic Si phases (both dark grey). A large amount of Cu and Ni secondary phases is also visible as light grey colored phases. Several porosities are visible and the microstructure seem coarser than that of the base alloy reported in Fig.3.14.

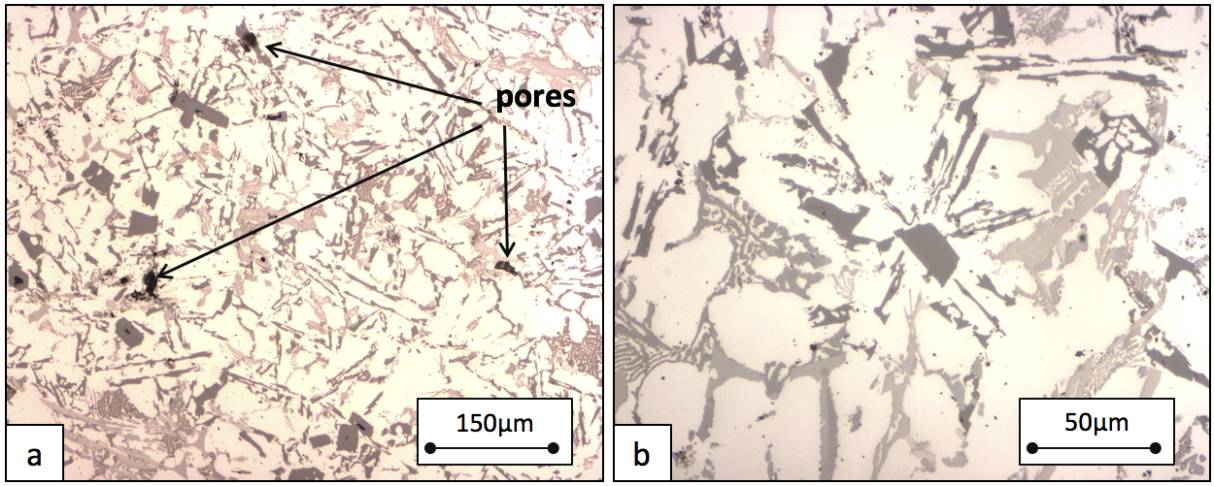

Fig.3.20: OM micrographs of the as-cast AlSi12CuNiMg alloy + Mo additions, respectively at low and high magnification.

Optimization of the solution phase

Due to the presence of a low melting phase revealed by DTA analysis in the as cast base alloy (see the endothermic peak with an onset T≈508°C in Fig.3.15a), the 1st step of solution consisting in 2h soaking at T=495°C was also applied to the Mo enriched alloy. DTA analyses on the base alloy also highlighted the presence of a peak associated to the complete melting, with an onset T≈525°C (Fig.3.15c); as a consequence, in order to avoid incipient melting also for Mo enriched alloy, most of the attempts to optimize the solution treatment did not exceed this temperature but rather took advantage of more prolonged soaking time. The formation of Mo

dispersoids is in fact governed by diffusional phenomena, so that an increase of holding time would have a similar effect to an increase in holding temperature. In a single attempt, an additional soaking at 540°C for 1h was introduced, in order to determine the influence of higher T in boosting the formation of Mo-based dispersoids as suggested by Farkoosh et al. [105], though with the awareness of a possible partial melting. In specific, the following time/temperature combinations have been tested to optimize the solution phase for Mo containing alloy:

- 2h at 495°C + 2h at 515°C (the same solution step carried out in T7-base)
- 2h at 495°C + 3h at 515°C
- 2h at 495°C + 4h at 515°C
- 2h at 495°C + 4h at 515°C + 1h at 540°C.

The hardness data after all abovementioned solution conditions + quench on Mo enriched alloy are reported in Fig.3.21. It should be pointed out that a negligible increase in hardness is promoted by additional holding 1h at 540°C, so that this additional step was discarded. It is indeed evident that a higher hardness is offered by a 2nd step consisting in 4h holding at 515°C. The optimized solution step of the T7-Mo heat treatment therefore consisted of 2h holding at 495°C + 4h at 515°C + quench.

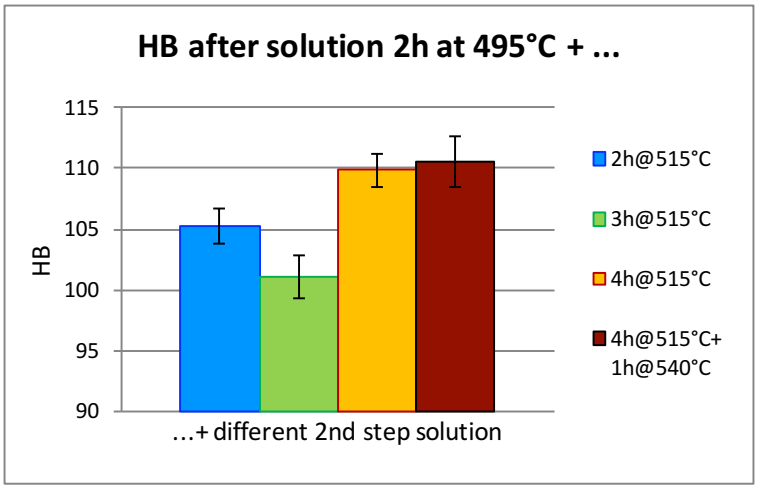

Fig.3.21: Hardness measurements after solution treatment characterized by 2h soaking at 495°C + a 2nd step consisting in different combinations of time/temperature of soaking + quench.

To complete the T7-Mo heat treatment, the aging step of 5h at 215°C was applied to the alloy. The results of both T7-base and T7-Mo heat treatment, on base and Mo enriched alloys are compared in Fig.3.22. Under both temper conditions, the base alloy shows a slightly superior hardness.

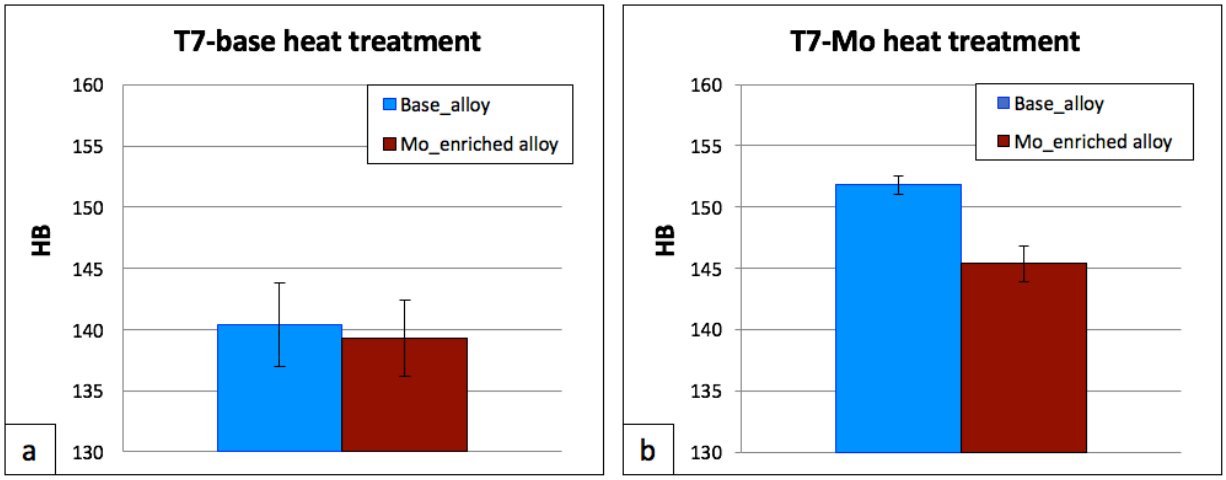

Fig.3.22: Hardness values for both base and Mo enriched alloy, in a) T7-base (2h at 495°C + 2h at 515°C; quench; 5h at 215°C) and b) T7-Mo (2h at 495°C +4h at 515°C; quench; 5h at 215°C) temper conditions.

The OM micrographs of Mo enriched alloy after the T7-base treatment, comparable for magnification and heat treatment with Fig.3.18, are reported in Fig.3.23. With respect to the base alloy, a higher amount of skeleton-like secondary phases is observed. SEM-EDS results, shown in Fig.3.24, highlight that these mainly consist of Al-Ni-Cu based phases. The results might partially explain the lower hardness of the Mo enriched alloy after aging: it can be inferred that Mo alters the supersaturation of Ni and Cu, so that Al matrix is depleted and less amounts of these elements are available to form strengthening precipitates. Moreover, coarse secondary particles containing high amount of Mo and Si were highlighted.

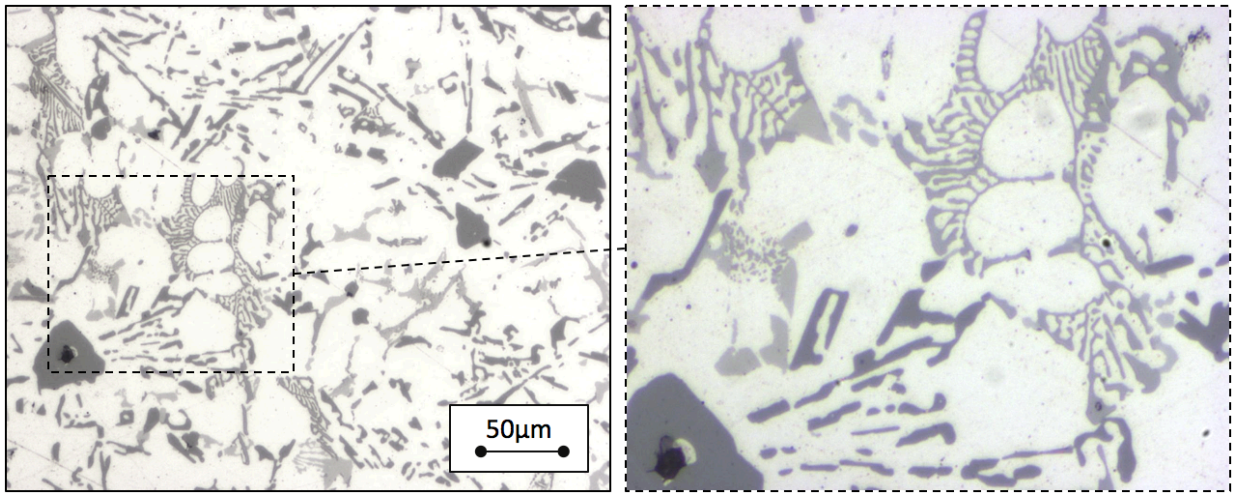

Fig.3.23: OM micrographs of the AlSi12CuNiMg + Mo alloy after T7-base temper.

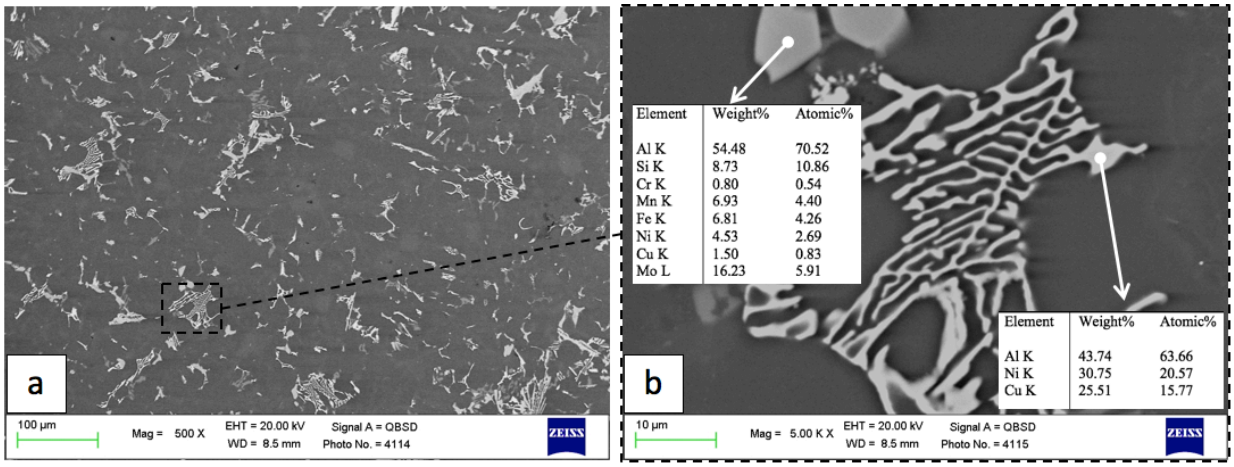

Fig.3.24: SEM-EDS analyses of the AlSi12CuNiMg + Mo alloy after T7-base temper at a) low, b) high magnification. Images acquired through backscattered electrons.

The microstructural features of Mo enriched alloy after T7-Mo treatment are totally comparable to what observed after T7-base treatment. SEM micrographs are reported in Fig.3.25: a huge interdentdritic shrinkage can be easily recognized (Fig.3.25a), as well as the presence of both Al-Cu-Ni skeleton-like secondary phases, and Mo-Si enriched blocky secondary phases, with an analogous morphology of those observed in Fig.3.24b at higher magnification. The high amount of casting defects and porosities characterizing the Mo containing alloy further explains the lower hardness detected after heat treatment.

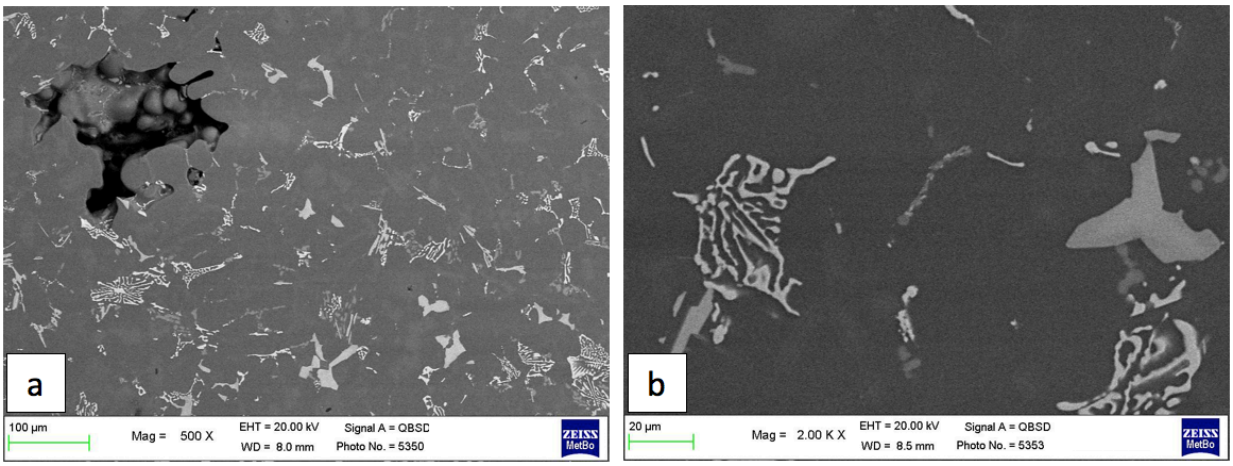

Fig.3.25: SEM-EDS analyses of the AlSi12CuNiMg + Mo alloy after T7-Mo temper at a) low, b) high magnification. Images acquired through backscattered electrons.

Overaging at 250°C

Both alloys, under both temper conditions, have been subjected to overaging at 250°C up to 1week. The results are reported in Fig.3.26. A separate discussion should be made for the Mo

containing alloy heat treated according to T7-Mo treatment, whose samples were characterized by several casting defects and are not well representative of the overaging behavior of the alloy. Excluding this curve, no differences in terms of residual hardness are detected due to heat treatment nor chemical composition.

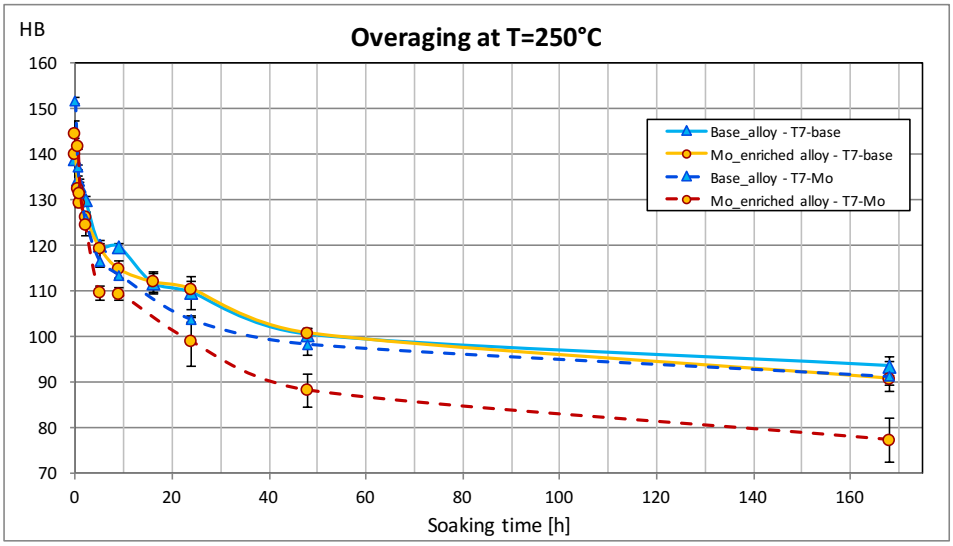

Fig.3. 26: Overaging data at T=250°C of AlSi12CuNiMg base and Mo enriched alloy, in T7-base and T7-Mo conditions.

Due to these unsatisfying results, Mo additions were not further investigated in this alloy. Besides the increased amount of casting defects in Mo enriched alloy, the comparable values of residual hardness of the alloys after overaging have been mainly related to the exceptionally high performance of the starting AlSi12CuNiMg alloy. The base alloy, in fact, takes advantage of substantial amounts of Cu (≈3.5wt%), Mg (≈1.0wt%), and Ni (≈0.8wt%) to enhance thermal resistance and it might be not affected by limited (thus negligible) Mo additions (≈0.3wt%).

To confirm this hypothesis, the same amount of Mo, equal to 0.3wt%, has been added to the less heat resistant A356 casting Al alloy (AlSi7Mg0.3), which does not contain Cu nor Ni. Since this alloy is not object of the present Ph.D. thesis, results are just briefly reported. The conventional solution phase of the T6 treatment on A356 alloy, proposed in literature in [136], consists in 4.5h soaking at 535°C. The Mo enriched alloy was indeed subjected to the heat treatment suggested by Farkoosh et al. [105], consisting in 4h at 500°C + an additional step at 540°C. The hardness data after solution + quench are reported in Fig.3.27a and a substantial increase in hardness during the soaking at 540°C can be noticed. The subsequent conventional aging treatment was then carried

out on Mo containing alloy (4.5h at 160°C, according to [136]). The overaging data at 250°C (Fig.3.27b) show a superior performance of Mo enriched alloy, with an average residual hardness higher of about 5HB (≈13% compared to the starting material) at the hardness plateau reached after 24h soaking.

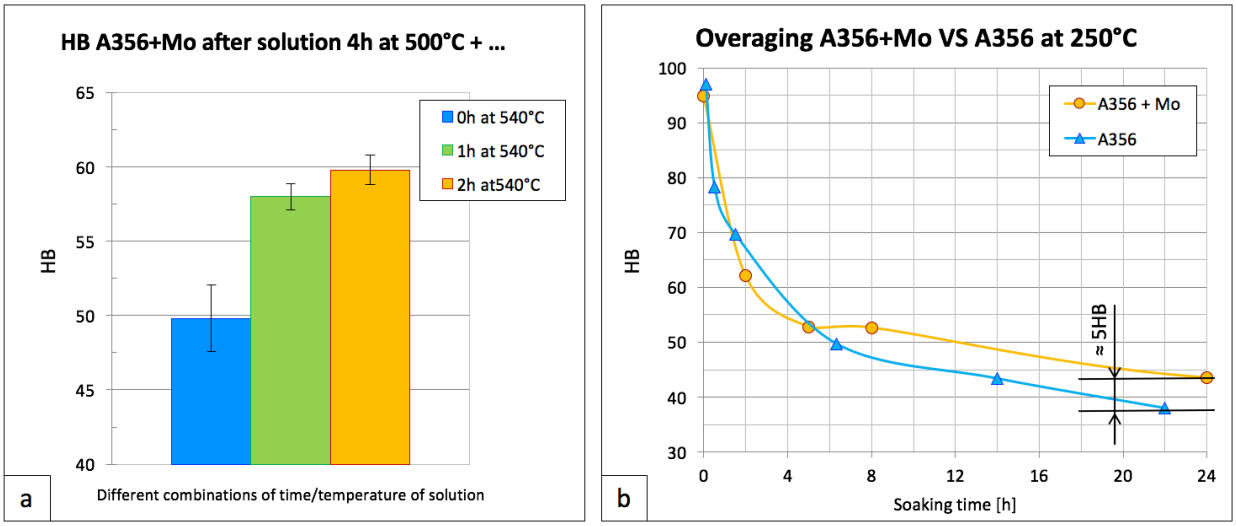

Fig.3.27: (a) Hardness measurements of A356+0.3wt%Mo after different solution treatments + quench; (b) Overaging data at T=250°C of base A356 and A356+0.3wt%Mo under T6 temper conditions.

Chapter 4:

Al-Cu alloys for pistons

As already mentioned in Sect.1.2, Al-Cu alloys for pistons are typically dedicated to hot forged components for racing applications. Compared to Al-Si alloys, these exhibit in fact a higher potential in terms of high temperature resistance and they deserve an in-depth study. Chapter 4 is divided as follows:

- Sect. 4.1 focuses on the comparison between Al-Si EN-AW4032 piston alloy (widely investigated in Sect. 3.1) and the high performance Al-Cu EN AW-2618 piston alloy, which has a chemical composition in the range of the abovementioned Mahle® alloy M SP25 (Sect. 1.2). To now, EN AW-2618 is considered as the most promising conventional Al alloy for pistons.

  This section consists in selected parts of the published paper *"Effect of thermal exposure on mechanical properties of EN AW-2618 and EN AW-4032 piston alloys", E.Balducci, L.Ceschini, Al.Morri, An.Morri, La Metallurgia Italiana, Vol.6, pp.89-92, 2016.* The study compares the effects of thermal exposure on the most widely adopted Al-Si and Al-Cu piston alloys, assessed through hardness and room temperature tensile tests on peak-aged and overaged samples, coupled with microstructural and fractographic investigations
- Sect. 4.2 reports the results of small additions of Zr to EN AW-2618 alloy, with the aim to further increase its thermal stability. The base material was supplied by Duraldur S.p.A. in the form of extruded bars. Part of the activities (dealing with SEM-FEG and TEM microstructural characterization) have been carried out in cooperation with Prof. Marisa di Sabatino Lundberg and Prof. Yanjun Li, Dept. of Materials Science and Engineering, Norwegian University of Science and Technology (NTNU), Trondheim. The main results of this research were published in the following papers:
  - *"High Temperature Behavior of the EN AW-2618A Piston Alloy Containing 0.12wt% Zr: Influence of Heat Treatment", E.Balducci, L.Ceschini, Al.Morri, An.Morri, M.Di Sabatino, L.Arnberg, Y.Li, Materials Today: Proceedings, Vol.2, Issue 10, pp. 5037-5044, 2015.*

- *Effect of Zr Addition on Overaging and Tensile Behavior of 2618 Aluminium Alloy", S.Toschi, E.Balducci, L.Ceschini, E.A.Mørtsell, A.Morri, M.Di Sabatino, Metals 2019, 9, 130, 2019.*

- Sect. 4.3, 4.4, 4.5 deal with two innovative Al-Cu-Li alloys, AA2099 and AA2055, widely adopted for structural aerospace applications thanks to their considerably low specific weight and high elastic modulus, characteristics with turn into high specific strength at room temperature. Al_3Li was not considered in the previous Sect. 2.3 while discussing thermally stable trialuminides, since it is in fact metastable and it cannot fulfil the criterion of high temperature stability. The alloys were however considered interesting due to their considerably low density.

  Starting from no data available in literature, mechanical properties of Al-Cu-Li alloys after overaging and at high temperature have been assessed in the temperature range 200°C-300°C, showing promising results in terms of specific strength. The comparison with AA2618 properties confirms the high performance of these alloys, which are finally declared to be suitable for powertrain components operating at temperature up to 250°C. SEM-EDS and STEM analyses were carried out to study the microstructural features of the alloys both in the T83 temper condition (as received) and overaged condition, in order to precisely link the microstructural evolution to the decay of properties. STEM characterization was conducted in cooperation with Prof. Randi Holmestad and Ph.D. Sigurd Wenner, Dept. of Physics, Norwegian University of Science and Technology (NTNU), Trondheim.

  The whole Sect. 4.3, 4.4, 4.5 are taken from the published papers dealing with Al-Cu-Li alloys:

  - *"Thermal stability of the lightweight 2099 Al-Cu-Li alloy: tensile tests and microstructural investigations after overaging", E.Balducci, L.Ceschini, S. Messieri, S.Wenner, R.Holmestad, Materials & Design, Vol.119, pp.54-64, 2017*
  - *"Effects of overaging on microstructure and tensile properties of the 2055 Al-Cu-Li-Ag alloy", E.Balducci, L.Ceschini, S.Messieri, S.Wenner, R.Holmestad, Materials Science & Engineering A, Vol.707, pp.221-231, 2017*
  - *"High Temperature Tensile Tests of the Lightweight 2099 and 2055 Al-Cu-Li Alloy: A Comparison", E.Balducci, L.Ceschini, S.Messieri, The Journal of The Minerals, Metals & Materials Society (TMS), Vol.70, Issue 11, pp.2716-2725, 2018.*

4.1 Effect of thermal exposure on mechanical properties of EN AW-2618 and EN AW-4032 piston alloys

[The whole Sect. is an extract from the published paper whose title is shown below. ©2016. This manuscript version is made available under the CC-BY-NC-ND 4.0 licence].

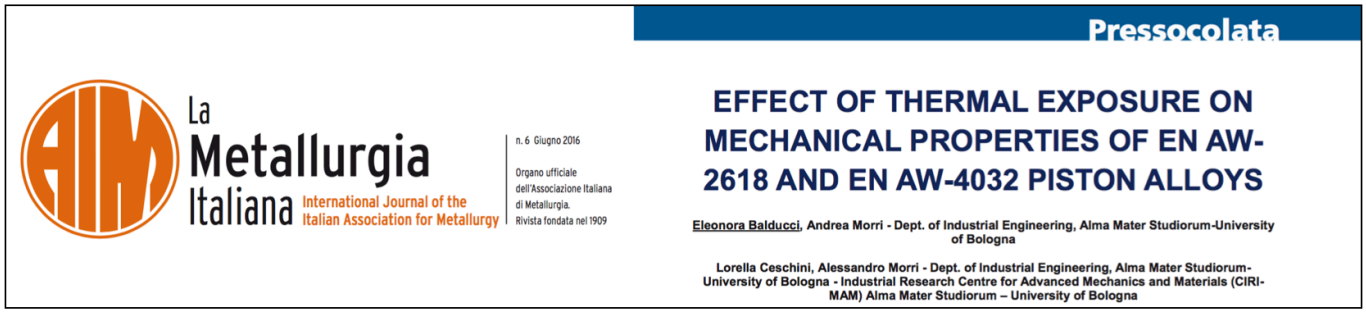

Keywords: Piston Alloy; Thermal Exposure; Tensile Properties; Microstructure

4.1.1 Introduction

The present study focuses on two Al alloys, widely used for high performance forged pistons: EN AW-2618 and EN AW-4032. Their thermal resistance was assessed in the range 200÷290°C, up to 168h, through hardness-time-temperature curves and tensile tests. In both cases, a decrease in hardness and tensile strength was observed, but EN AW-2618 performed better thanks to the lower coarsening rate of Cu-based strengthening precipitates. The different tensile behaviour was related to their microstructures and strengthening mechanisms, that led to different fracture mechanisms as evidenced by fractographic analyses.

The aim of this study was to put the basis for a further optimization of these high performance Al alloys, considering industrial applicability.

4.1.2 Material and methods

Material

The experimental activities were carried out on samples machined from the crown of 10 forged and T6 heat treated pistons, 5 of them made of EN AW-2618, the remainders made of EN

AW-4032 alloy. GD-OES chemical analyses were carried out on specific samples; results are reported in Table 4.1.

Table 4.1 : Average chemical composition [wt%] of the EN AW-2618 and EN AW-4032 alloys

EN AW-2618 [wt%]					
Cu	Mg	Ni	Fe	Zr	Al
2.13	1.43	1.03	0.89	0.14	bal.

EN AW-4032 [wt%]					
Si	Fe	Cu	Mg	Ni	Al
11.56	0.22	0.99	1.04	1.02	bal.

After the forging process (carried out at 400°C), both alloys were T6 heat-treated, according to different combinations of temperature and time during solution and aging, as reported in Table 4.2.

Table 4. 2: Parameters of the industrial T6 heat treatment of EN AW-2618 and EN AW-4032 alloy

Solution 2618		Quench		Aging 2618	
T [°C]	t [h]	T [°C]	t [s]	T [°C]	t [h]
525 ± 5	8	50÷70	35	200 ± 5	20

Solution 4032		Quench		Aging 4032	
T [°C]	t [h]	T [°C]	t [s]	T [°C]	t [h]
500 ± 5	8	50÷70	35	200 ± 5	9

Overaging curves

In order to determine the alloys thermal stability, several samples with average dimension (12x6x4) mm^3 were machined from T6 treated forged pistons. The specimens were then subjected to overaging, according to different conditions of temperature, in the range 200-290°C, and soaking time, from 10min up to 168h. Temperatures were selected within the range of interest to assess pistons resistance, since modern piston crowns constantly withstand T≥200°C during service, but also peaks of 300°C can be easily reached [119].

Tensile tests

To further investigate the effect of thermal exposure on the T6 heat-treated EN AW-4032 and EN AW-2618 piston alloys, room temperature tensile tests were carried out on overaged samples. Flat dog bone tensile specimens, machined from T6 heat-treated piston crowns, were used, with 32mm gauge length, 6mm gauge width and 3mm gauge thickness. Before test, specimens were subjected to thermal exposure according to different combinations of time/temperature, in order to reach the same residual hardness values for the comparison. The investigated residual hardness values are reported in Table 4.3 for both alloys. To have a complete characterization, SEM analyses of representative fracture surfaces have been also carried out.

Table 4.3: Overaging heat treatment to reach comparable residual hardness values of EN AW-4032 and EN-AW 2618.

EN AW-4032		EN AW-2618	
Residual hardness [HB]	Overaging treatment	Residual hardness [HB]	Overaging treatment
Peak-aged: 115	/	115	10h at 230°C
105	6h at 230°C	105	120h at 230°C
90	33h at 230°C	90	3.5h at 290°C
70	7h at 290°C	70	50h at 290°C

4.1.3 Results and discussion

Overaging curves

The overaging curves (Fig.4.1) clearly show the superior performance of the EN AW-2618 alloy, for all the investigated conditions. After thermal exposure for 168h in the range 200-260°C (temperature usually reached in high performance piston crown [119]), samples of EN AW-2618 show an average residual hardness value 20HB higher. This difference is significantly reduced to 9HB and 5HB, respectively, for 168h thermal exposure at 275°C and 290°C. It is also worth noting that the decrease of hardness after 48h of thermal exposure is less pronounced for EN AW-4032 alloy (Fig.4.1a), at all the investigated temperatures. This behaviour can be related to a faster kinetics of both nucleation and subsequent coarsening of strengthening precipitates of EN AW-4032 alloy, if compared to EN AW-2618 alloy. The main strengthening phase in 4032 alloy consists of β-Mg_2Si, while in 2618 it consists of S-Al_2CuMg. Differential scanning calorimetric (DSC) studies carried out on the solutioned and quenched alloys, subsequently heated at 20°C/min, showed that the formation of coherent β phase occurs at 250°C in the 4032 alloy [124], while the exothermic peak linked to coherent S formation in 2618 alloy is shifted at temperature higher than 280°C [137]. Different precipitation kinetics are also highlighted by the considerably different time to achieve the peak-aging conditions at 200°C (see the parameters reported in Table 4.2): 20h for EN AW-2618 alloy, just 9h for EN AW-4032 one.

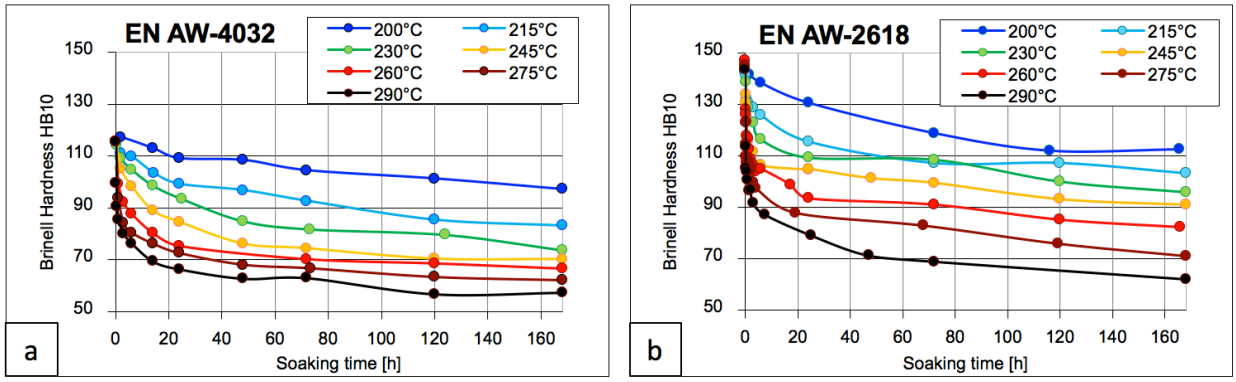

Fig.4.1: Overaging curves of a) EN AW-4032 and b) EN-AW 2618 alloys, in the range 200÷290°C.

Tensile tests

The tensile test results of both alloys, compared at the same level of residual hardness, are reported in the flow curves of Fig. 4.2. The curves referring to 2618 alloy are taken from a previous study by the authors [30]. Even if 0,2%proof strength shows similar values and seems to be simply related to the residual hardness and precipitation strengthening, it can be easily noted the higher elongation to failure of EN AW-2618, and its more pronounced tendency to dislocation hardening. SEM analyses of the tensile fracture surfaces (Fig. 4.3) clearly confirm that the difference in ductility is linked to different microstructural features that characterize the two alloys. The Al matrix of EN AW-2618 exhibits a significant presence of fine intermetallics, some microns in size, homogeneously distributed (see Fig. 4.3a); according to literature data [31,131] these particles mainly belong to the Al_9FeNi T-phase, but also to Al_2Cu, Al_7Cu_4Ni, $Al_7Cu_2(Fe,Ni)$. On the contrary, EN AW-4032, due to the eutectic composition, reveals a substantial presence of large eutectic Si particles that contribute to the overall alloy brittleness: cracks on large Si crystals are highlighted by red arrows in Fig. 4.3b.

The different mechanisms of load transfer between intermetallics and matrix can be recognized at higher magnification and for lower residual hardness (Fig. 4.3c-d). The homogeneously distributed fine intermetallics, present in the EN AW-2618 alloy (Fig. 4.3c), allow an optimal load transfer, causing a significant and visible plastic deformation of the matrix. Even at 90HB residual hardness, plastic deformation of the matrix is slightly visible in EN AW-4032 samples, highlighted by green arrows in Fig. 4.3d; given the substantial presence of Si crystals, the fracture mechanism is governed by brittle failure of larger Si particles, while little load is supported by the matrix, before fracture.

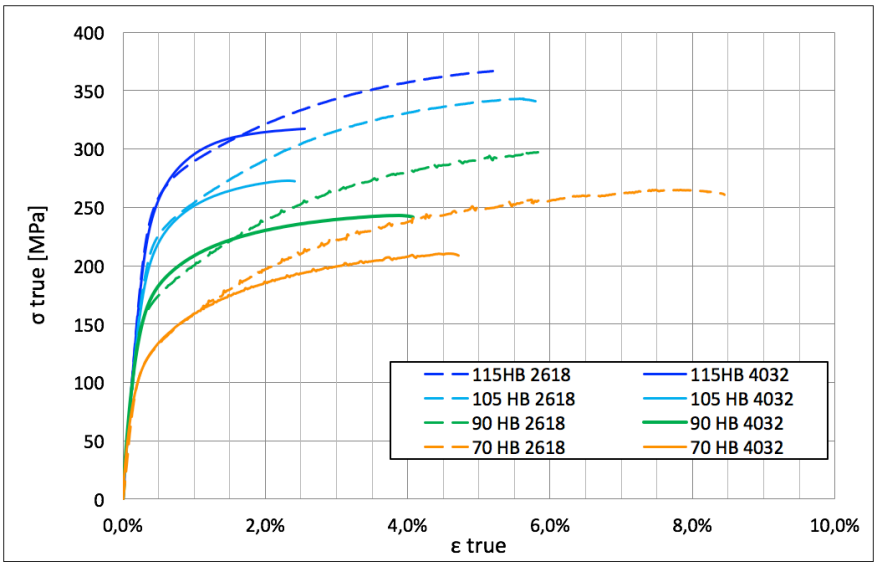

Fig.4.2: True stress and true strain curves of EN AW-2618 (dotted line) [30] *and EN AW-4032 alloy (solid line), compared at the same level of residual hardness.*

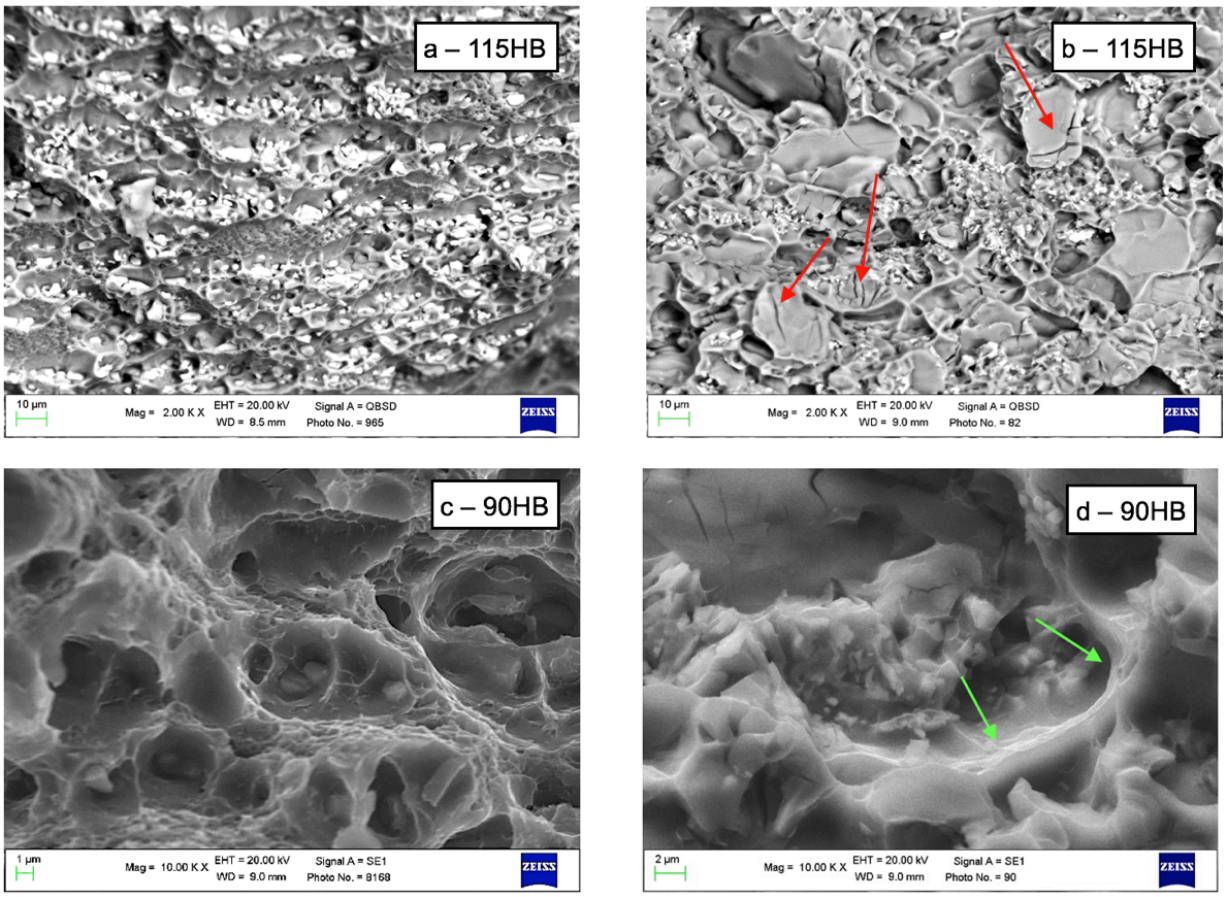

Fig.4.3: a) SEM backscattered electrons micrographs at low mag. of EN AW-2618 - 115HB, b) EN AW-4032 - 115HB; c) SEM secondary electrons micrographs at high mag. of EN AW-2618 - 90HB, d) EN AW-4032 - 90HB.

4.1.4 Conclusions

The overaging curves in the range 200÷290°C highlighted the superior thermal stability of the EN AW-2618 alloy with respect to EN AW-4032; this was related to higher volume fraction of Cu-based strengthening precipitates, characterized by lower coarsening rate. Tensile tests of both alloys, comparing the same residual hardness conditions, gave also evidence of the higher elongation to failure and tendency to dislocation hardening of EN AW-2618; this is due to the homogeneous dispersion of fine, thermally stable intermetallics which effectively hinder dislocation movement, without compromising alloy ductility as coarse Si particles do in the eutectic EN AW-4032 alloy.

4.2 Effects of Zr additions on EN AW-2618 Al-Cu piston alloy after overaging at 250°C-300°C

4.2.1 Introduction

EN AW-2618 aluminum alloy is generally used for high performance pistons produced by hot forging. Apart from a considerable quantity of Cu and Mg, EN AW-2618 contains an equal amount of Fe and Ni (around 1wt%), whose aim is to enhance the formation of thermally stable secondary phases with the stoichiometric formula Al_9FeNi (T-phase), which significantly increase the high temperature resistance of the alloy [31,32]. Nevertheless, the decrease of mechanical properties during soaking at high temperature is still significant in the T6 temper conditions, as highlighted by Ceschini et al. in [30].

As already discussed in Chapter 2, it is proved that dislocation movements at high temperature can be hindered by a dense distribution of fine and thermally stable precipitates, able to limit recovery and recrystallization processes. In this section, the effects of limited Zr additions on the high performance EN AW-2618 alloy have been assessed with the aim to enhance the base alloy heat resistance. Zr is extensively used for its anti-recrystallization effects and it also induces the formation of coarsening resistant Al_3Zr precipitates, which are reported to be thermally stable in the desirable $L1_2$ structure up to 500°C [76,88,101,102]. It should be pointed out that (see Table 4.4) the base alloy already contained up to 0.11wt%Zr, but the aim of this work was to reap the full benefits of Zr additions, by:

- increasing Zr content up to the maximum amount which is retainable in solid solution during conventional casting, while avoiding the pro-peritectic precipitation of primary trialuminides → Zr was therefore increased up to 0.25wt%
- tailoring the heat treatment (in particular the solution step) to stimulate an optimal size, shape and distribution of strengthening $L1_2$-structured trialuminides → besides the conventional industrial practice, a second heat treatment based on the research by Robson et al. [101–103] was tested.

The theoretical background reported in Sect.2.3 (particularly in Sect 2.3.3) lays the basis of the experimental activities hereafter discussed.

4.2.2 Material and methods

The high performance piston alloy EN AW-2618 was provided in the form of extruded bars with 100mm diameter by Duraldur S.p.A. The bars were re-melted through an induction furnace (TopCast®) to make base and Zr enriched castings of approximately 1kg weight, with the same permanent mold geometry shown in the previous Fig.3.13. The steps for the casting process are the same as those reported in Sect.3.2 and Sect.3.3, where steps iii-v are limited to Zr enriched alloy:

i. Cutting the supplied bars of base material into small pieces (roughly 3 x 3 x 6cm) to reach the approximate weight of 1kg
ii. Putting all pieces into the furnace and starting the actual melting by imposing a temperature of 800°C in a protective Ar atmosphere
iii. Cutting the master alloy Al-10wt%Zr into small pieces to reach the targeted 0.25wt% Zr and putting all pieces into the furnace, always working in a protective Ar atmosphere in order to limit oxidation
iv. Increasing the furnace temperature up to 900°C for at least 30minutes to stimulate homogenization and master alloy dissolution
v. Slowly cooling from 900°C to 800°C
vi. Starting the pouring cycle, in the mold pre-heated to 200°C.

GDOES analyses were then carried out on samples taken both from the top and the bottom of the castings, to gain data about the macro-scale segregation of the alloying elements and to have the confirmation of the actual Zr addition. The analyses did not show any anomaly, and the average results for base and Zr enriched alloy respectively are reported in Table 4.4 and Table 4.5.

Table 4.4: Average chemical composition of the base EN AW-2618 alloy.

Elements [wt%]	Cu	Mg	Ni	Fe	Zr	Si	Ti	Al
Mean	2.13	1.26	1.09	0.90	0.11	0.10	0.10	Bal.

Table 4.5: Average chemical composition of the EN AW-2618 alloy with Zr additions.

Elements [wt%]	Cu	Mg	Ni	Fe	Zr	Si	Ti	Al
Mean	2.11	1.25	1.09	0.87	0.26	0.11	0.10	Bal.

Both alloys have been then heat treated to the T6 temper conditions, testing two different routes whose schemes are reported in Fig.4.4:

- *Industrial route*, which consists in 8h soaking at 525°C + quench + 20h aging at 200°C (as reported in [30] and in Sect.4.1.2); this heat treatment would be following referred to as IHT (Industrial Heat Treatment).
- *Robson's route*, which led to substantial changes to the solution step. Due to the peritectic nature of Zr (see Sect 2.3.3 for further details), its concentration significantly changes towards the dendrites and the temperature stimulating Zr precipitation in the inner dendritic areas, (enriched in Zr) is different from the optimal temperature for interdendritic areas (which contain a lower amount of Zr). Robson [101–103] thus proposes a two-step homogenization treatment, where the lower temperature is equal to 88% of the final homogenization temperature, and it is aimed to boost the number of dispersoids, avoiding precipitates free interdendritic channels. Moreover, a slow ramp heating to reach both the intermediate and the final solution temperature is supposed to play a relevant role; Robson [102] suggests this equal to 20°C/h: if the ramping is too fast, large cubic dispersoids with a heterogeneously distribution tend to form [100].

  Taking into account the researches by Knipling et al. [76,88], who found that Al_3Zr transformation from $L1_2$ to $D0_{23}$ structure occurs at approximately 500°C, a maximum temperature of 490°C was chosen for the solution step. The intermediate temperature was therefore imposed equal to 0.88 x 490 ≈ 430°C. In order to make the modified heat treatment applicable to industrial practice, several phases have been shortened with respect to Robson's suggestion: ramp heating was not applied to reach the intermediate solution temperature, and soaking time was reduced with the aim to keep the solution process duration below 24h. This heat treatment would be following referred to as RHT (Robson Heat Treatment)

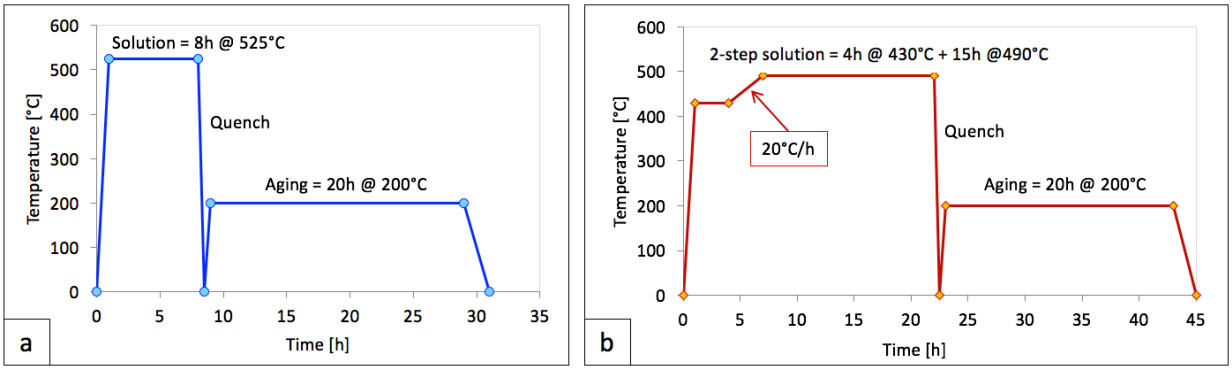

Fig.4.4: (a) Schematic of conventional IHT; (b) schematic of modified RHT. Both heat treatments have been applied to both base and Zr enriched alloys.

To evaluate the efficacy of the chemical modifications/heat treatments in enhancing the alloy thermal resistance, overaging data were acquired both at 250°C and 300°C, up to 192h soaking. Brinell hardness tests were performed on samples grinded up to at least 600 grit size, using a hardened steel ball indenter with d=2.5mm and 62.5kg weight.

OM, SEM-EDS and TEM microstructural investigations have been carried out to complete the alloys characterization. OM and SEM analyses have been carried out on specimens embedded in resin, mechanically ground with SiC papers up to 4000 grit and finally polished up to 0.05µm colloidal silica. Samples for TEM analyses were prepared by grinding the material to 100 µm thin foils, which were punched to 3mm discs. The discs were then electropolished using a Struers TenuPol-5 unit and an electrolyte containing 1/3 HNO_3 and 2/3 CH_3OH, cooled down to −25°C during electropolishing. The applied voltage was 20V. All TEM images were acquired on a cold-feg TEM-2100F microscope, operated at 200kV. Samples were imaged in $<110>_{Al}$ directions.

Finally, tensile tests at room temperature and at 250°C have been carried out on selected samples using a screw tensile testing machine. In particular, both alloys in RHT and IHT condition + 48h soaking at 250°C (middle overaged condition) have been tested, at least 3 specimens for each condition, in order to assess the influence of Zr additions.

4.2.3 Results and discussion

Starting material

In the as-cast condition, higher amounts of intermetallic phases are observed in the Zr enriched alloy. Both castings show an average SDAS ≈ 30µm.

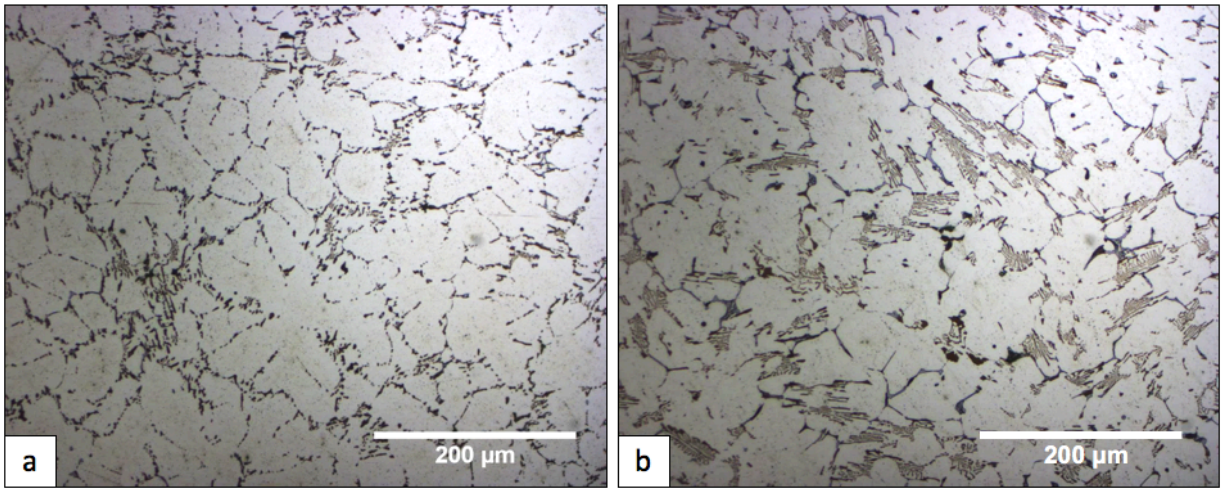

Fig.4.5: OM micrographs in the as-cast condition of (a) base alloy (b) Zr enriched alloy at the same magnification.

Heat treatment: comparison between IHT and RHT

The purpose of the solution step for EN AW-2618 alloy is to dissolve possible clusters of Cu-Mg, in particular of Al_2CuMg and Al_2Cu, which could form fine and uniformly distributed precipitates during the subsequent aging. According to literature data [31,32], 8h soaking at 480°C respectively results in a complete/partial dissolution of Al_2CuMg/Al_2Cu; on the contrary, 5h soaking at 530°C succeed in dissolving all Al_2CuMg and Al_2Cu phases, but a few Al_7Cu_4Ni still remain. The peculiar T-phase characterizing EN AW-2618 alloy and providing a high heat resistance cannot be indeed completely dissolved even at temperature as high as 600°C [32], so that soaking at 530°C simply results in T-phases fragmentation and spheroidization.

Once again, high magnification OM micrographs acquired after the solution heat treatment (Fig.4.6), both according to the IHT and RHT specifications, reveal the higher presence of intermetallics in Zr enriched alloy. In particular, numerous skeleton-like secondary phases are highlighted in Fig.4.6c,d, while the same phases appear more fragmented in the base alloy.

SEM-EDS analyses on solutioned samples (Fig.4.7) are in complete agreement with literature data [31,32]: the presence of Al_9FeNi, Al_7Cu_4Ni on the alloys after both IHT and RHT solution step is revealed, while Al_2Cu phases is dissolved. In both base and Zr enriched alloys, RHT leaves a higher content of undissolved Cu and Ni based secondary phases (appearing in white color through backscattered electrons and encircled in red in Fig.4.7b and Fig.4.7d). This is mainly linked to the fact that RHT involves a lower solution temperature compared to IHT, so that a lower amount of Cu and Ni containing secondary phases (in particular Al_7Cu_4Ni) is dissolved.

The higher matrix supersaturation obtained through IHT solution is confirmed by the hardness variations monitored during several steps of IHT and RHT treatments (Fig.4.8):

- both the base and Zr enriched alloy exhibit higher hardness values after the conventional solution step IHT compared to the innovative solution step RHT;
- both the base and Zr enriched alloy exhibit higher hardness values in the T6 temper condition after the whole IHT treatment compared to RHT.

It should be also pointed out that no variation of hardness is associated to the different chemical compositions: limited additions of 0.14wt% Zr seems to have a negligible effect in terms of hardness in the solution + quench or peak-aged conditions.

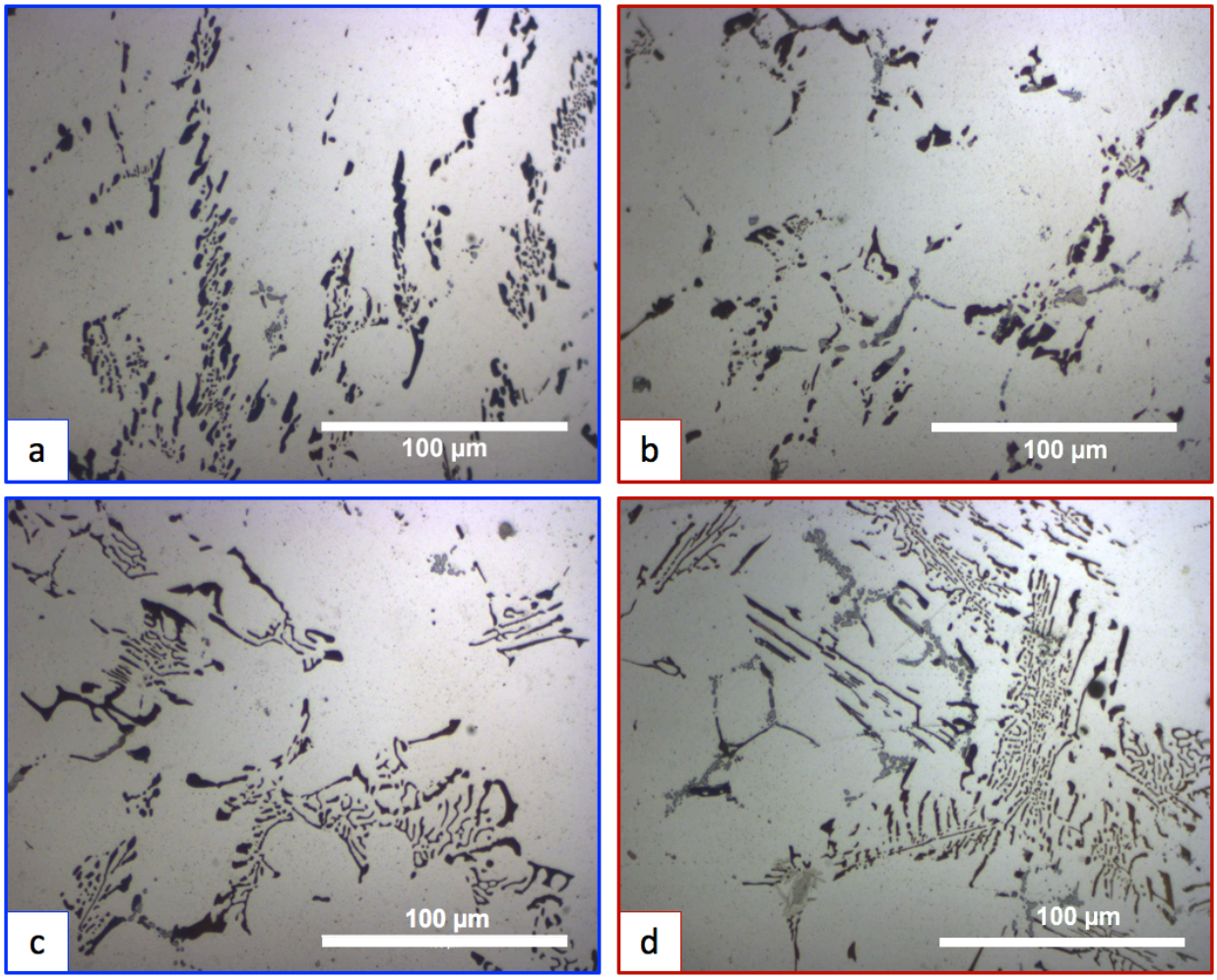

Fig.4.6: Optical micrographs after solution + quench of (a), (b) base alloy (c), (d) Zr enriched alloy at the same magnification; blue encircled images (a), (c) refer to the conventional IHT solution step, red encircled images refer to the modified RHT solution step (see the specifications of both heat treatment in Fig.4.4).

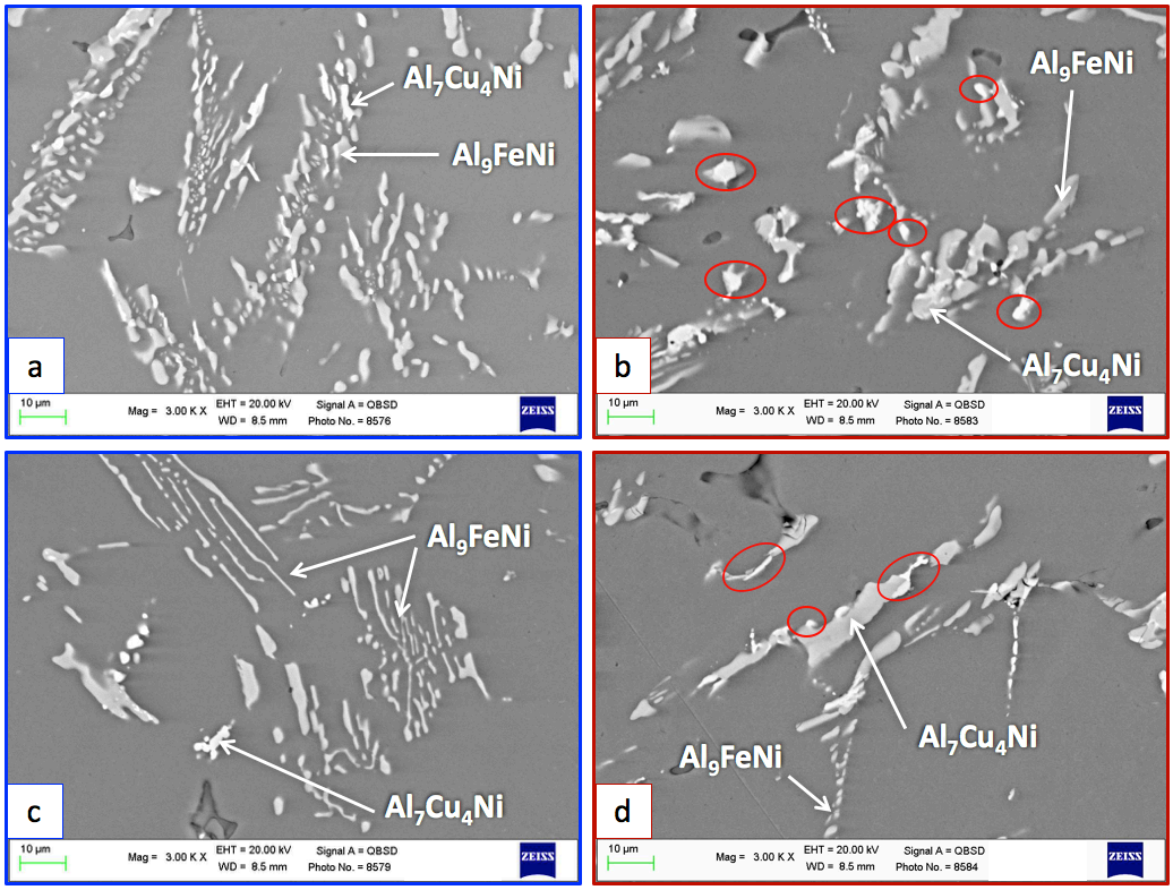

Fig.4.7: SEM micrographs after solution + quench of (a), (b) base alloy (c), (d) Zr enriched alloy at the same magnification; blue encircled images (a), (c) refer to the conventional IHT solution step, red encircled images refer to the modified RHT solution step (see the specifications of both heat treatment in Fig.4.4). Images are acquired through backscattered electrons.

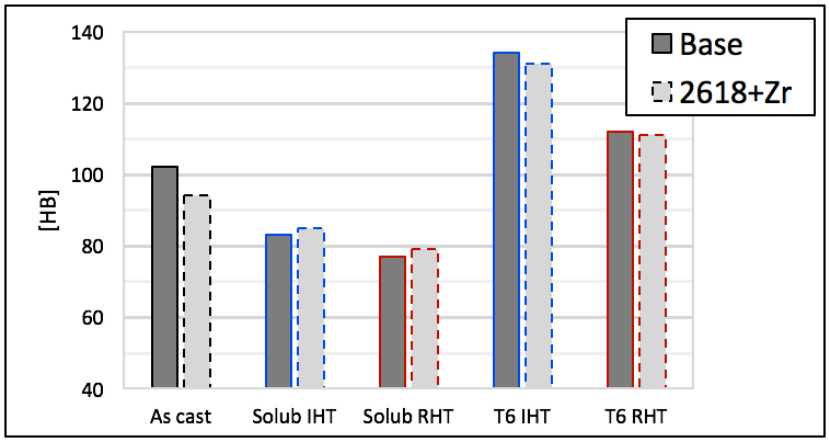

Fig.4.8: Brinell hardness evolution of base and Zr enriched alloy during IHT and RHT steps.

Overaging at 250°C and 300°C

Overaging curves of both alloys and after both heat treatments are reported in Fig.4.9. Once again, it can be inferred that the same behavior is exhibited by the alloys and that IHT treatment leads to more valuable or comparable results in terms of residual hardness.

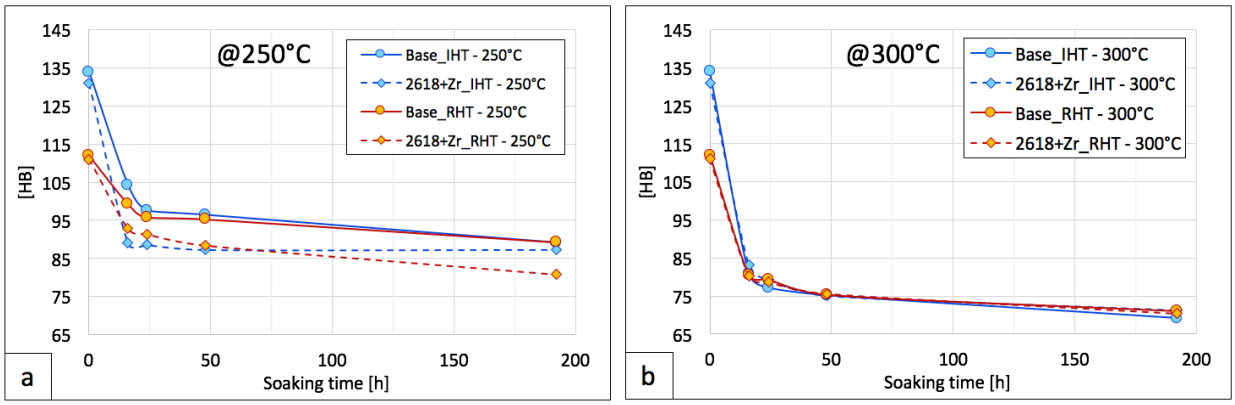

Fig.4.9:Overaging data (a) at T=250°C and (b) at 300°C of base and Zr enriched alloy, after IHT and RHT heat treatment.

Even if overaging results were not promising, microstructural characterization through both SEM-FEG and TEM was carried out on samples in the fully overaged condition (192h at 300°C) in order to evaluate the presence of thermally stable precipitates. It should be pointed out that, in this overaged condition, all combinations of alloy/heat treatment exhibit the same residual hardness (Fig.4.9b). IHT treated alloys have been however studied with particular attention since this heat treatment represents the best compromise in terms of residual hardness and industrial applicability, compared to RHT.

High magnification SEM-FEG micrographs reveal the substantial presence of coarsened precipitates in Al matrix; Fig.4.10 reports images collected from the IHT treated samples.

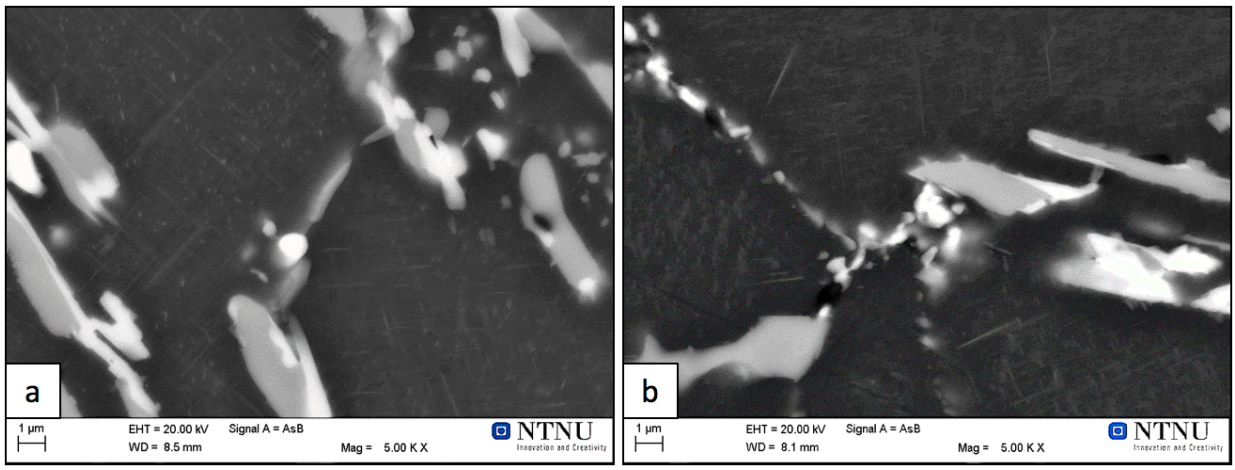

Fig.4.10: High magnification SEM-FEG micrographs showing the substantial presence of coarsened precipitates in Al matrix after 192h soaking at 300°C: (a) base alloy - IHT, (b) 2618+Zr - IHT.

Aiming to verify the presence of Zr based precipitates and to assess possible differences in their size and distribution due to heat treatment, TEM analyses have been also carried out on IHT

base alloy (which is the starting point of the experimental activity) and both IHT and RHT Zr enriched alloy, in the fully overaged condition.

TEM analyses on IHT base alloy after 192h soaking at 300°C are reported in Fig.4.11. The lower magnification images (Fig.4.11a-b) show that the base alloy matrix is packed with relatively large needles, which tend to grow in the <001>Al direction and probably consist of coarsened Al_2CuMg phases. This precipitation is typical for nucleation and growth of needles along dislocation lines and usually produces precipitates with a lower hardening potential. Many grain boundary particles, mainly consisting of Al-Fe-Ni based secondary phases, can be also noticed. By observing the micrograph at higher magnification (Fig.4.11c), it can be inferred that these coarsened precipitates still exert their pinning effect on dislocations.

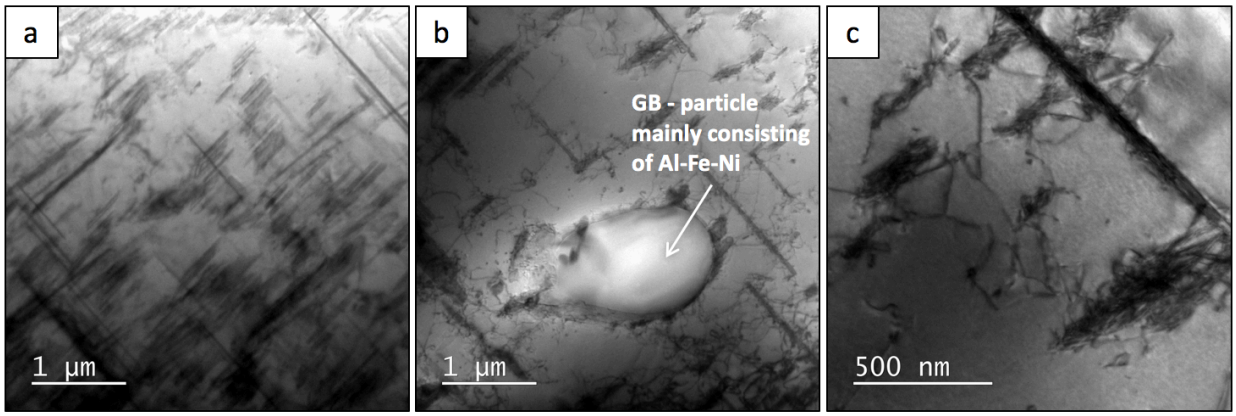

Fig.4.11: TEM images of the IHT base alloy after 192h soaking at 300°C, all acquired along the <110>Al direction. The lower magnification images show (a) large precipitate needles consisting in coarsened Al_2CuMg phases, (b) a grain-boundary coarse particle. At higher magnification, it is possible to observe dislocations pinned by the aforementioned needle-like precipitates. Images (a) (c) have been recently published in [138].

TEM analyses on IHT Zr enriched alloy after 192h soaking at 300°C are reported in Fig.4.12. The images at high magnification (Fig.4.12a) show that the microstructure mainly consists of coarsened needle-like precipitates (probably with the Al_2CuMg), whose length is ranging from 50nm to more than 1µm. However, in this case, precipitates have a higher number density and they are more homogeneously distributed compared to IHT base alloy (compare Fig.4.11a to Fig.4.12a), exhibiting at the same time a lower size (compare Fig.4.11c to Fig.4.12b). In addition to that, several nanometric-sized and spherical Al_3Zr dispersoids are observed, as also confirmed by Selected Area Electron Diffraction (SAED) from particle encircled in Fig.4.12c.

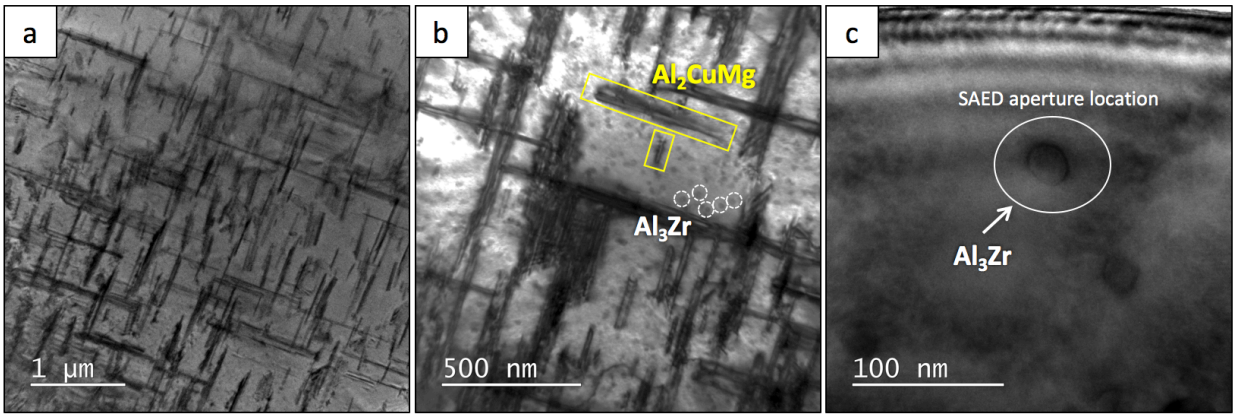

Fig.4.12: TEM images of the IHT Zr enriched alloy after 192h soaking at 300°C, all acquired along the <110>Al direction. The lower magnification image (a) shows once again the huge amount of coarsened Al_2CuMg phases. At higher magnification(b) several nanometric-sized spherical trialuminides can be noticed. Selected Area Electron Diffraction (SAED) from particle encircled in (c) confirms that it consists of Al_3Zr dispersoids. Images (a) (b) have been recently published in [138].

TEM analyses on RHT Zr enriched alloy after 192h soaking at 300°C are reported in Fig.4.13. The images at low magnification show the huge presence of the needle-like coarsened precipitates already highlighted in the previous alloys. These are more uniformly distributed than what observed in the IHT base alloy (compare Fig.4.11a to Fig.4.13a), yet they are characterized by a coarser size than what reported for the IHT Zr enriched alloy (compare Fig.4.12b to Fig.4.13b). HR-TEM also shows several cuboidal phases with an average size of 10nm, one of them reported in Fig.4.13c. Both EDS and diffraction confirm that these particles contain Zr and they must be Al_3Zr dispersoids.

In summary, TEM analyses on the fully overaged samples reveal that:

- Regardless of the heat treatment, Zr enriched alloy has a more uniform distribution of the coarsened needle-like precipitates, which are supposed to be the Al_2CuMg S-phases. In particular, the IHT Zr enriched alloy exhibit finer and more homogeneous precipitates compared to the RHT alloy.
- A high amount of nanometric Zr based dispersoids dominate the microstructure of Zr enriched alloys, both IHT and RHT; these maintain nanometric size (≈10nm) in the fully overaged condition.

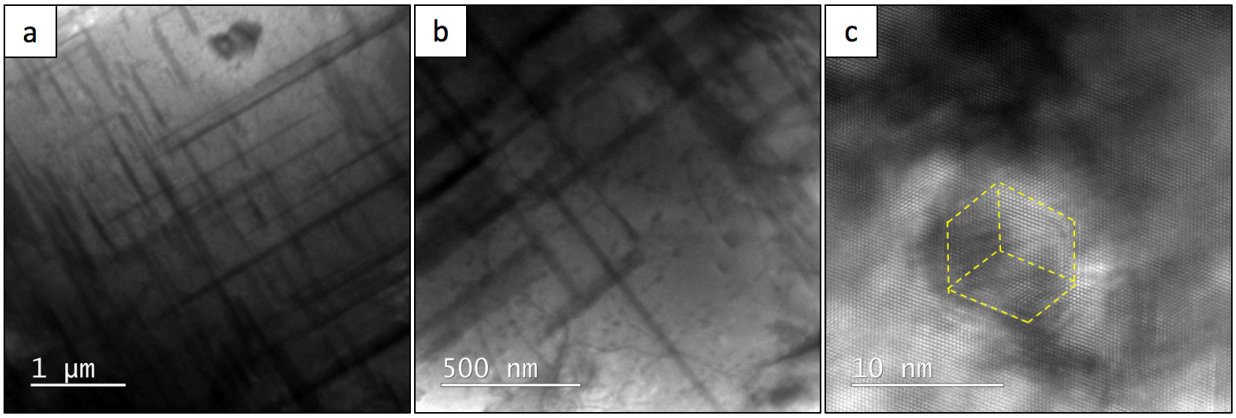

Fig.4. 13: TEM images of the RHT Zr enriched alloy after 192h soaking at 300°C, all acquired along the <110>Al direction. The lower magnification image (a) shows once again the huge amount of coarsened Al_2CuMg phases. (b) At higher magnification, several nanometric-sized spherical trialuminides can be noticed in between needle-like precipitates. (c) HR-TEM image of a cuboidal phase with an average dimension of 10nm, which is supposed to be an Al_3Zr dispersoid.

Tensile tests at RT and 250°C

Aiming to evaluate the effectiveness of Zr additions, tensile tests have been conducted at both room and high temperature on RHT and IHT alloys. In order to partially reduce the effects of conventional Al-Cu-Mg based precipitates, which typically strengthen this alloy after the T6 heat treatment but are prone to coarsening at T>200°C [30], the middle overaged condition produced by 48h soaking at 250°C was considered. The results are reported in Fig.4.14 and confirm a slight improvement of tensile properties due to Zr additions, under both heat treatment, even if the overaging curves of base and Zr enriched alloys at 250°C are almost superimposed (Fig.4.9a). It should be however pointed out that, regardless of Zr content, IHT samples always exhibited a superior performance, both at room temperature and at 250°C.

Some additional tensile tests are ongoing in order to completely characterize, even from a mechanical point of view, the potential of Zr enrichment on the present alloy. In particular, in sight of the TEM analyses, the IHT Zr enriched alloy in the fully overaged condition (192h at 300°C) is expected to distinctly show the benefits of (though) small Zr additions.

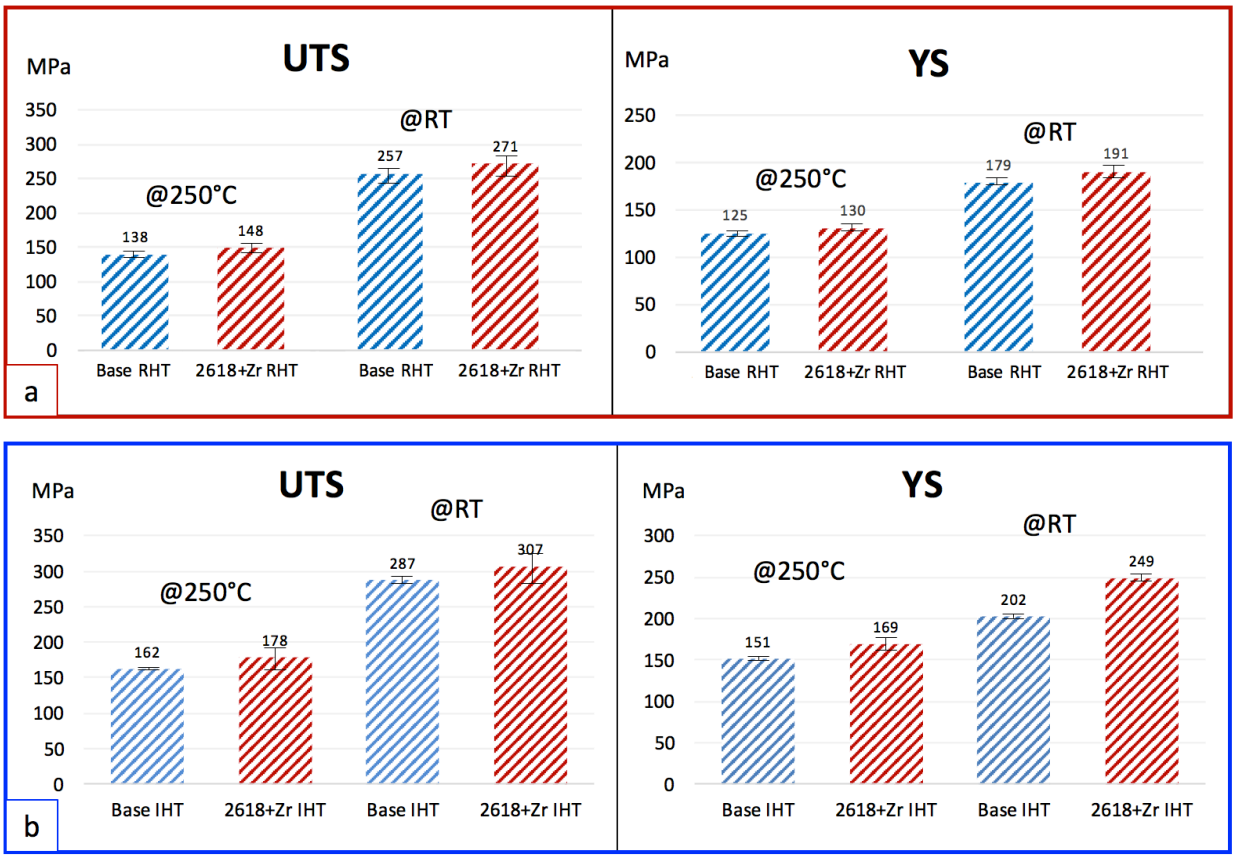

Fig.4.14: Results of tensile tests conducted at RT and 250°C on base and Zr enriched alloys, respectively RHT (a) and IHT (b) heat treated and additionally overaged for 48h at 250°C.

4.2.4 Conclusions

The effects of small Zr additions (in order to reach up to 0.25wt% Zr) to the base EN AW-2618 piston alloy (containing 0.11wt% Zr) and the influence of heat treatment variations (RHT) with respect to the conventional industrial practice (IHT) have been evaluated in terms of enhancement of material performance at high temperature. In particular, overaging curves have been collected at 250°C-300°C, while the microstructural features induced by Zr enrichment and heat treatments after soaking at 300°C have been evaluated through in depth TEM analyses.

The innovative RHT heat treatment, whose aim is to stimulate the formation of fine and homogeneously distributed Zr trialuminides, seems not to achieve the target after overaging in terms of improved residual hardness (always worse than IHT treated alloys) as well as coarsening resistance of precipitates (qualitatively evaluated through TEM analyses). However, tensile tests of RHT treated alloys confirmed the positive influence of Zr dispersoids: at both RT and 250°C, RHT Zr enriched alloy shows superior mechanical properties than RHT base alloy.

Due to the absence of evident advantages of RTH treatment, and considering its extended duration with respect to the conventional IHT (which makes it hardly applicable to an industrial field), no additional experimental activities on RHT treated alloys are scheduled.

As regards IHT treated samples, Zr enrichment (+0.14wt%) results in hardness comparable to the base alloy after thermal exposure. Nevertheless, TEM analyses in the fully overaged condition at 300°C show important benefits related to an increased Zr content:

- a huge presence of nanometric-sized, spherical Al_3Zr dispersoids, which have not been highlighted in the base IHT alloy;
- a much more homogeneous distribution of finer (though coarsened) needle like strengthening phases, which are supposed to be Al_2CuMg.

The promising microstructural features after overaging, are confirmed by the superior performance of Zr enriched alloy after tensile tests, both at RT and 250°C.

4.3 Thermal stability of the lightweight 2099 Al-Cu-Li alloy: tensile tests and microstructural investigations after overaging

[The whole Sect. is taken from the published paper whose title is shown below. ©2017. This manuscript version is made available under the CC-BY-NC-ND 4.0 licence].


Contents lists available at ScienceDirect

Materials and Design

journal homepage: www.elsevier.com/locate/matdes

Thermal stability of the lightweight 2099 Al-Cu-Li alloy: Tensile tests and microstructural investigations after overaging

E. Balducci [a,*], L. Ceschini [a], S. Messieri [b], S. Wenner [c], R. Holmestad [c]

[a] Dept. of Industrial Engineering, Alma Mater Studiorum University of Bologna, viale del Risorgimento 4, Bologna, Italy
[b] Ducati Motor Holding, Bologna, Italy
[c] Dept. of Physics, Norwegian University of Science and Technology, Høgskoleringen 5, Realfagbygget D4-153, Trondheim, Norway

HIGHLIGHTS

- Lightweight AA2099 exhibits thermal stability comparable or even higher than Al-Cu alloys specifically developed for high T
- Overaged AA2099 showed high residual tensile strength, suggesting potential use in high T yet lighter automotive components
- STEM investigations revealed the superior thermal stability of T_1 phase (typical of Al-Cu-Li alloys) compared to ϑ and S

GRAPHICAL ABSTRACT

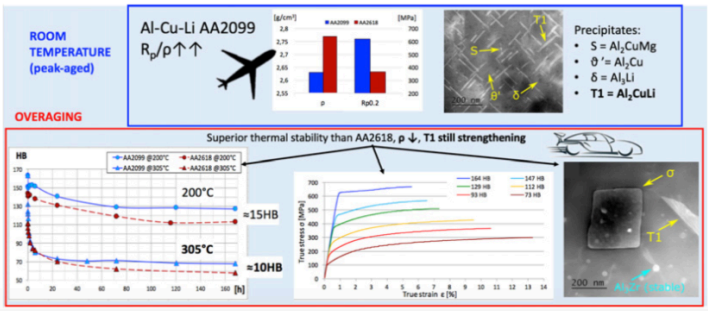

Keywords

Al-Cu-Li alloy; Thermal effect; Hardness test; Tensile test; Microstructure; STEM.

Abstract

The thermal stability of the lightweight, T83 heat treated 2099 Al-Cu-Li alloy was assessed in the temperature range 200-305°C, through both hardness and tensile tests after overaging. After prolonged thermal exposure, the alloy exhibited a better performance compared to aluminum alloys specifically developed for high temperature applications, with the advantage of a considerable lower density. The tensile behavior was modelled through Hollomon's equation as a function of residual hardness. The changes in the alloy performance were explained through both

SEM and STEM investigations. Microstructural analyses gave evidence of Ostwald ripening, while fractographic analyses revealed a transition from an intergranular to a ductile fracture mechanism in the overaged alloy. STEM investigations highlighted the superior thermal stability of the T_1 phase compared to ϑ and S strengthening phases, which dissolved during overaging at 245°C. The study underlines the need to enhance the formation of T_1 precipitates when high temperature strength is required. The results of the present study suggest that the 2099 alloy is a very promising candidate for automotive engine components, which are extremely demanding in terms of both thermal resistance and lightweight.

4.3.1 Introduction

The 2099 Al alloy belongs to the third generation of Al-Li alloys, which are high performance and lightweight materials. Lithium exhibits the lowest density among metals, equal to 0.534 g/cm^3, hence it significantly contributes to a density reduction of the alloy. The substantial influence of Li addition in density reduction was at first underlined by Peel et al. [35] in the empirical formula to calculate Al alloy densities (Eq. 4.1).

$$\rho\ (g/cm^3) = 2.71 + 0.024Cu + 0.018Zn + 0.022Mn - 0.01Mg - 0.004Si - \mathbf{0.079Li}$$

Eq.4.1: Empirical formula to evaluate the density of Al alloys; atomic symbols represent the concentration of the element in wt%. The benefit of Li addition is clearly visible [35].

Another relevant aspect is that Li increases the Young's elastic modulus of the alloy (around 6% increase due to 1wt% Li addition [36]). Combined with the possibility to use conventional production processes, the enhancements in specific strength and stiffness have made Al-Li alloys a competitive alternative to more conventional aluminum alloys (such as those of the 6XXX and 7XXX series) for structural applications in the aerospace field [40–44], due to the consistent improvements in payload and fuel efficiency.

Rioja et al. [36,139] offered a comprehensive review on the microstructural and technical issues which finally lead to the development of the complex third generation of Al-Li alloys. Starting from the first generation, a significant enhancement in fracture toughness has been achieved thanks to both a specific balance in chemical composition and a simultaneous optimization of the thermo-mechanical processing. To obtain the maximum benefits in terms of mechanical properties, Al-Li alloys need to be processed to the T8 condition (solution, quench, cold stretch,

artificial aging), the key point being the generation of the desired texture and sub-structure to make the precipitation more effective and uniform [140,141]. Cold deformation, in fact, induces a dislocation network which acts as nucleation site for co-precipitation of strengthening intermetallics (mainly Cu and Li based); the result is, therefore, both a refinement of precipitates microstructure and a reduction in precipitation at grain boundaries, which is deleterious in terms of toughness [36,142]. Together with an increased Cu/Li ratio, T8 heat treatment promotes the formation of the T_1 (Al_2CuLi) phase at the expenses of δ' (Al_3Li) precipitates [36,143–147], which offers the maximum strengthening effect and is more thermally stable. In addition to these strengthening phases, the relevant presence of Cu and Mg in Al(-Cu)-Li alloys leads to the formation of ϑ' (Al_2Cu), S' (Al_2CuMg) and σ ($Al_5Cu_6Mg_2$) phases. Mg is also known to promote the nucleation of T_1 precipitates at the expenses of ϑ' [148].

Usually, Zr and Mn are also added in low quantities; these elements are known to form Al_3Zr (spherical) and $Al_{20}CuMn_3$ (rod-like shaped) dispersoids, essential to control texture, to pin grain and sub-grain migration and to inhibit recrystallization, enhancing fracture toughness [36,142,149–151]. Given the opposite microsegregation patterns of Mn and Zr in Al, the joint addition of these elements is thought to produce a more uniform dispersion coverage, even if recent studies highlighted a reduction in recrystallization resistance [150].

An overview of the microstructural features of the 2099 Al-Cu-Li alloy is offered by Rioja et al. in [36], whose schematic is reported in Fig.4.15. Further in-depth microstructural investigations are present in literature, which confirm the abovementioned features and characteristics of both strengthening precipitates and dispersoids [142,152,153].

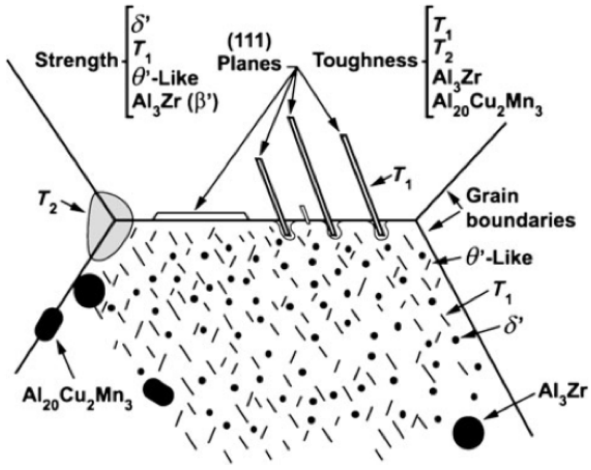

Fig.4.15: Schematic of Al-Cu-Li 2099 alloy microstructural features, focusing on precipitates and dispersoids [36]. *Reprinted under Springer permission.*

Since the '80s, several studies have been carried out on T8 heat treated AA2099, due to its interesting properties for aerospace applications, however there is a substantial lack of studies focusing on the thermal stability of this alloy. Very few studies, whose aim is mainly linked to the design of the aging treatment, deal with thermal exposure of AA2099 at medium-high temperature (that is below 200°C), but little attention has been given to microstructural features [146,152,154,155].

Jabra et al. [156] firstly evaluated the response of AA2099 to prolonged thermal exposure at elevated temperatures (180°C, 230°C, 290°C), in order to replicate a range of possible thermal environments. For all the investigated temperatures, a decrease of tensile properties was found, coupled with an increase of the elongation to failure. Even if the decay of tensile properties showed a good correlation with residual hardness data, no systematic relationship was determined. Moreover, up to date, there is a total lack of microstructural investigations on the high temperature overaging of the AA2099 alloy, which still raises open questions about the thermal stability of its precipitates, or about which type of precipitates are needed during the aging treatment in case of high temperature applications.

Further studies are therefore required in order to completely characterize the alloy strengthening mechanisms and, above all, to evaluate the maximum service temperature the alloy is able to withstand without a significant strength loss. The study falls within a wider context: the huge benefits of AA2099 in terms of mass savings make it a potential candidate not only for structural components in the aerospace field, but also for automotive applications, even for engine components. The increasingly topical race to boost fuel economy, which today involves car manufacturers, has not to be neglected. Since automotive applications are extremely challenging in terms of both specific strength and service temperature, the aim of this study is to evaluate the possibility to expand the 2099 temperature range of applications. Time-Temperature-Hardness curves, tensile tests at room and high temperature on peak-aged and overaged samples, and microstructural investigations through both Scanning and Transmission Electron Microscopy have been carried out, in order to outline the microstructural modifications which mainly affect the mechanical behavior of the alloy.

4.3.2 Material and methods

The material used in the present study was a 2099 Al-Cu-Li alloy, provided by Alcoa in the form of extruded bars with 85mm diameter. The alloy was industrially heat treated according to the T83 condition (which consists of solution treatment, quench, 3% stretching at room temperature followed by artificial aging). The chemical composition limits of AA2099, provided by the supplier, are reported in Table 4.6.

Table 4.6: Chemical composition limits [wt%] of AA2099.

Cu	Li	Zn	Mn	Mg	Ti	Zr	Fe	Al
2.4-3.0	1.6-2.0	0.4-1.0	0.10-0.50	0.10-0.50	0.10	0.05-0.12	0.07	Bal.

In order to assess the thermal stability of the alloy, several specimens (10x15x6) mm^3 in size, were cut from the T83 extruded bar. The samples were then subjected to different overaging heat treatments in the temperature range 200-305°C, the soaking time ranging from 2min up to 168h. Additional overaging curves at lower temperatures (155-185°C) were added to the analyses, aiming to determine the maximum temperature the alloy is able to withstand without any loss of properties; for this purpose, the soaking time was reduced to 24h. During the heat treatments, the temperature of the samples was controlled by a K-type thermocouple, allowing ± 2°C variation of the targeted temperature. For each time-temperature condition, the residual hardness of the alloy was determined as the average of 6 hardness measurements, performed on 2 different samples. Brinell hardness tests were carried out according to the ASTM E 10-08 standard, the indenter being a hardened steel ball, 2.5mm in diameter, and the applied load being equal to 62.5kg.

The microstructural characterization of T83 and overaged alloy was carried out on samples mechanically ground with SiC papers to 4000 grit and finally polished up to 0.05µm colloidal silica. Chemical etching through Keller's reagent (95mL H_2O, 2.5mL HNO_3, 1.5mL HCl, 1mL HF) was then carried out in order to perform Optical Microscopy (OM) analyses, while Scanning Electron Microscopy (SEM) analyses and Energy Dispersive Spectroscopy (EDS) investigations were carried out on not-etched samples.

Once the minimum residual Brinell hardness of the alloy has been determined through overaging curves, the interval between the maximum hardness value (characterizing the T83 condition) and the minimum value was divided into 6 equally spaced hardness classes, in order to study the variation of tensile properties due to thermal exposure. It is in fact widely accepted that mechanical properties of Al alloys deteriorate during thermal exposure, and a nearly-linear

relationship exists between the softening of the alloy and the decrease of its tensile properties [30]. With the aim to reach the targeted residual hardness for each class, specific overaging heat treatments were performed on tensile specimens, the time-temperature parameters being selected according to the previous overaging results. Room temperature tensile tests were then carried out on both T83 and overaged samples, using a screw tensile testing machine. Test parameters and geometry of samples were defined according to EN ISO 6892-1: 2009 standard; the strain rate was set equal to 3.3×10^{-3} s^{-1}; the specific dimensions of the tensile samples are reported in Fig.4.16.

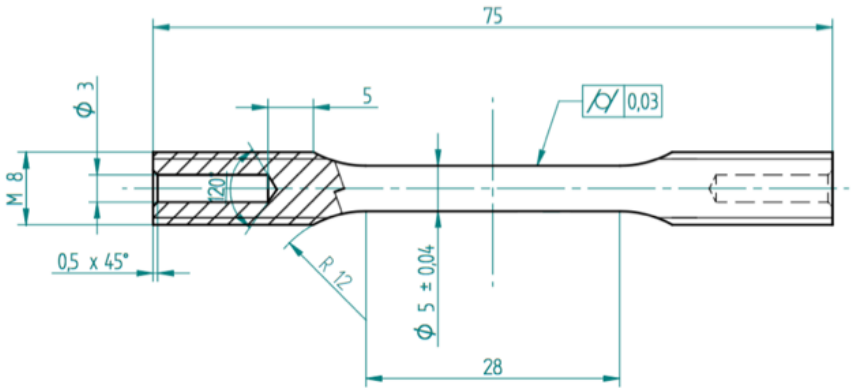

Fig.4.16: Geometry and dimensions [mm] of tensile specimens

Proof strength ($Rp_{0.2}$), ultimate tensile strength (UTS) and elongation to failure (A_t%) were evaluated according to EN ISO 6892-1: 2009 standard; the representativeness of the results was assured by testing 3 specimens for each class of residual Brinell hardness. To accurately establish the relationship between the average values of UTS, $Rp_{0.2}$, A_t% and residual hardness, the targeted residual hardness was confirmed by Brinell hardness tests, performed on grip areas of tensile samples after testing.

In order to completely describe the flow behavior at room temperature, the true stress–true strain (σ-ε) curves referring to different overaging conditions have been also modelled according to Hollomon's equation [127]:

$$\boldsymbol{\sigma = K\varepsilon^{n}}$$

Eq.4.2: Hollomon's law, representative of the behaviour of the alloy in the plastic field, when deformation occurs at room temperature.

The strength coefficient K and the hardening coefficient n were evaluated according to ISO 10275:2007 standard, taking into account true stress-true strain data between 2% plastic strain and

the percentage plastic extension at maximum force (A_g). Since the purpose was to outline the changes in the alloy behavior due to thermal exposure, K and n values have been modelled as a function of the residual hardness of tensile samples.

In order to relate experimental results with microstructural changes, SEM analyses of the fracture surfaces were carried out, using both secondary and backscattered electrons. Finally, to investigate how the density, size and type of precipitates evolve during overaging, annular dark-field scanning transmission electron microscopy (ADF-STEM) studies were conducted. Samples were prepared by grinding the material to 100 μm thin foils, which were punched to 3mm discs. The discs were electropolished using a TenuPol-5 unit and an electrolyte containing 1/3 HNO_3 and 2/3 CH_3OH, cooled down to −25 °C. The applied voltage was 20V. The ADF-STEM images were acquired on a JEOL JEM-2100F microscope, operated at 200kV. Samples were imaged both in $<001>_{Al}$ and $<112>_{Al}$ directions for identification of all the phases present, with small tilts away from the zone axes to minimize the influence of diffraction effects on the image contrast.

4.3.3 Results and discussion

Starting material

The as-received alloy was characterized both by OM and SEM-EDS investigations. Representative OM micrographs, both in the longitudinal and transverse directions, are reported in Fig.4.17, and reveal the typical unrecrystallized microstructure of T8 Al-Cu-Li alloys [36,40,142,157,158], with grains elongated along the extrusion direction.

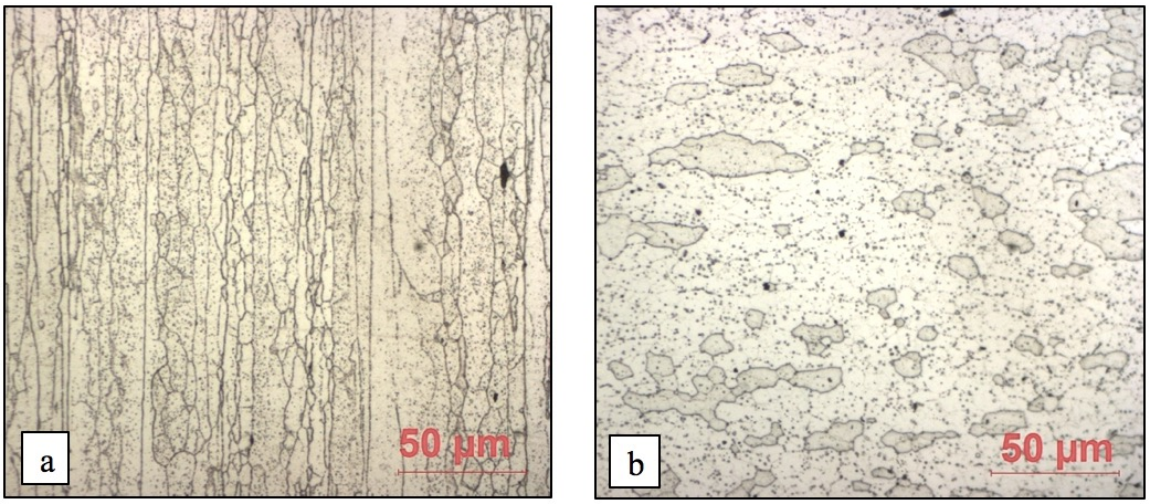

Fig.4.17: OM micrographs of the T83 AA2099, after chemical etching by Keller's reagent: (a) longitudinal and (b) transverse directions.

This morphology is confirmed by SEM investigations on T83 alloy (Fig.4.18a), which show secondary phases aligned towards the extrusion direction. Consistent with observations by Ma et al. [142], EDS analyses reveal that the secondary phases mainly consist of Al-Mn-Fe-Cu, and that brighter areas are richer in Cu (Fig.4.18b). Due to the very fine size of coherent precipitates and dispersoids, characterizing the 2099 alloy in the T83 condition, SEM investigations were not able to resolve other microstructural features.

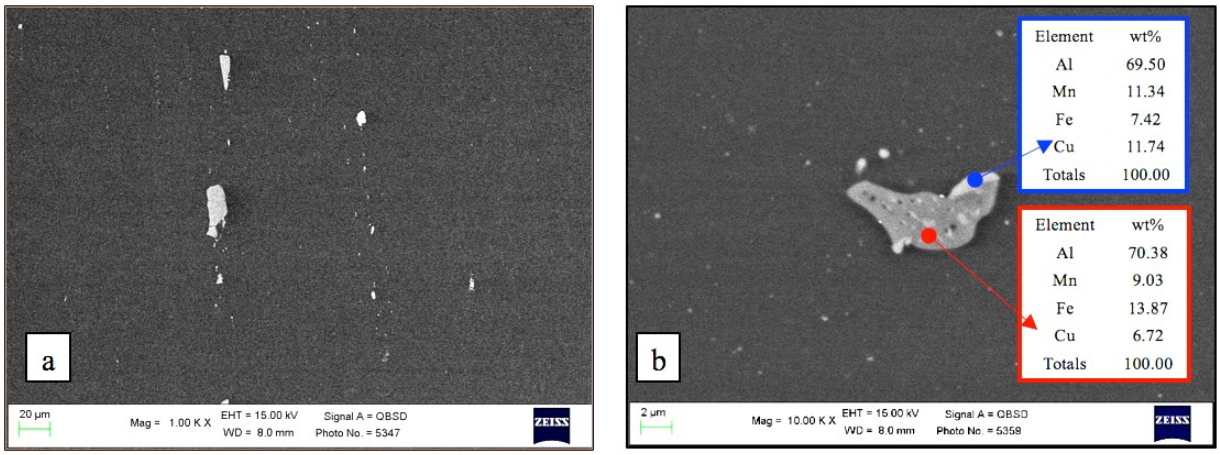

Fig.4.18: SEM-EDS analyses of AA2099 in the T83 condition at (a) low and (b) high magnification, with focus on Al-Mn-Fe-Cu secondary phases.

Time – Temperature – Hardness curves

The complete overaging curves, obtained in the range 200–305°C for soaking time up to 168h, are reported in Fig.4.19a. Lower temperatures (155–185°C) were also investigated for shorter soaking time, up to 24h, and the results are reported in Fig.4.19b. To have a more effective

comparison with curves at higher temperatures, also the curve at 200°C was here reported in solid line.

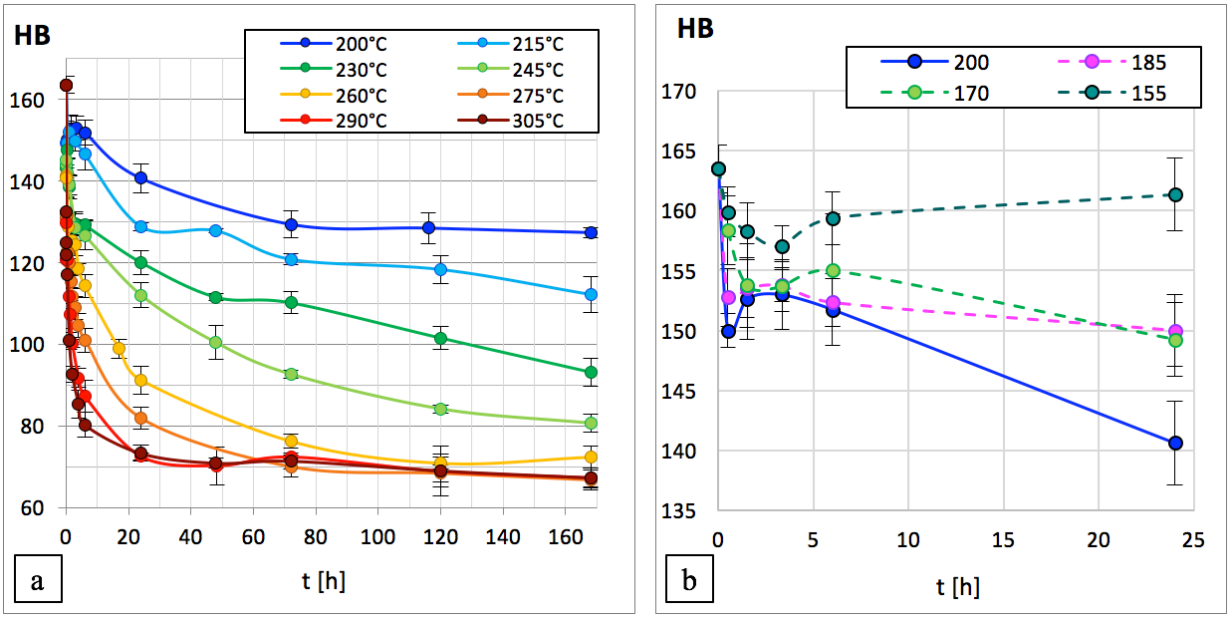

Fig.4.19: Overaging curves referring to AA2099; each point is obtained as the average of 6 Brinell hardness values; error bars are representative of 95% confidence interval (+/-2σ). (a) Overaging curves in the range of interest (200-305°C) to assess the thermal stability of the alloy. (b) Overaging curves in the range 155-180°C with a reduced soaking time, aimed to determine the maximum temperature which does not produce softening; part of 200°C overaging curve (solid line) is also reported, to make an effective comparison with the additional overaging curves at 155-185°C (dashed lines).

Since the softening of the alloy consists of a diffusion-controlled mechanism, the strength loss is more pronounced and it occurs faster at higher temperatures. Fig.4.19b, however, reveals that the thermal stability of the alloy is compromised even at temperatures which are usually considered relatively low in the automotive field; in fact, the high hardness value characterizing the T83 condition, equal to 164HB, is immediately lost after only 30 min of exposure at 200°C.

The additional overaging curves at 155-185°C, reported in Fig.4.19b, allowed to determine the maximum temperature that does not significantly affect the alloy strength. It can be noted that the hardness of the T83 alloy is almost maintained even after 24h of soaking time at 155°C; it can therefore be stated that no substantial microstructural evolution occurs at this temperature, and that the driving force for the diffusion processes is extremely low. The slight instability which occurs for short time of exposure at low temperature, barely detectable at 155°C, is most likely connected to the small coarsening of δ' precipitates, since the hardness variation is actually limited and the typical Al-Cu based precipitates (ϑ' and S) do not tend to coarsen at this low temperature. The hypothesis is in agreement with Lin et al. [152], who demonstrated that slight overaging occurred

even with prolonged time (96h) at 152°C, due to little coarsening of δ' precipitates. Recent TEM investigations by Deschamps et al. [159] underlined that microstructural changes might occur even during long-term aging at 85°C in case of high Li content (1.4 wt%), due to precipitation of additional δ' phases. Ortiz et al. [154] confirmed however that tensile properties remain substantially stable up to 1000h of exposure at 83°C and 135°C, while a relevant decrease of strength is detected when the alloy is exposed to 177°C, up to 1000h; the same observation is supported by Romios et al. [155] and Gao et al. [146], who considered the soaking at 180°C responsible for overaging.

A plateau of hardness, equal to about 70HB is reached when the 2099 alloy is maintained at temperatures equal to or higher than 260°C, as shown in Fig.4.19a. Due to its thermodynamically driven nature, the softening is faster at 290°C and 305°C, temperatures at which 24h is the required time to complete the microstructural evolution and to reduce the driving force for the coarsening of precipitates (Ostwald ripening).

In order to better evaluate the decrease of hardness as a function of temperature and time of exposure, the hardness data were modelled in Matlab® environment using the method of least-squares. In particular, Brinell data were suitably fitted using a quadratic function of temperatures, while a logarithmic function of 3rd order was adopted as regards the variation of hardness with time of exposure (Eq.4.3).

$$HB = 140.6543 + 0.4616\,T - 0.0020\,T^2 + 55.5398\ln(t) - 0.3911\,T\cdot\ln(t) + (5.7806e-04)\cdot\,T^2\ln(t) + 10.0125(\ln(t))^2 - 0.0996\,T\cdot(\ln(t))^2 + (2.2503e-04)\cdot\,T^2\cdot(\ln(t))^2 + 0.2925(\ln(t))^3 - 0.031\,T\cdot(\ln(t))^3 + (7.4126\,e-06)\cdot\,T^2\cdot(\ln(t))^3$$

Eq.4.3: Modelled residual hardness of AA2099 during overaging, as a function of temperature and time of exposure.

The validity of the model is confirmed by both Fig.4.20a, which reports experimental overaging curves compared to modelled ones, and Fig.4.20b, which gives evidence of the limited errors due to modelling. For most experimental values, the error is acceptable and well within the 5% margin.

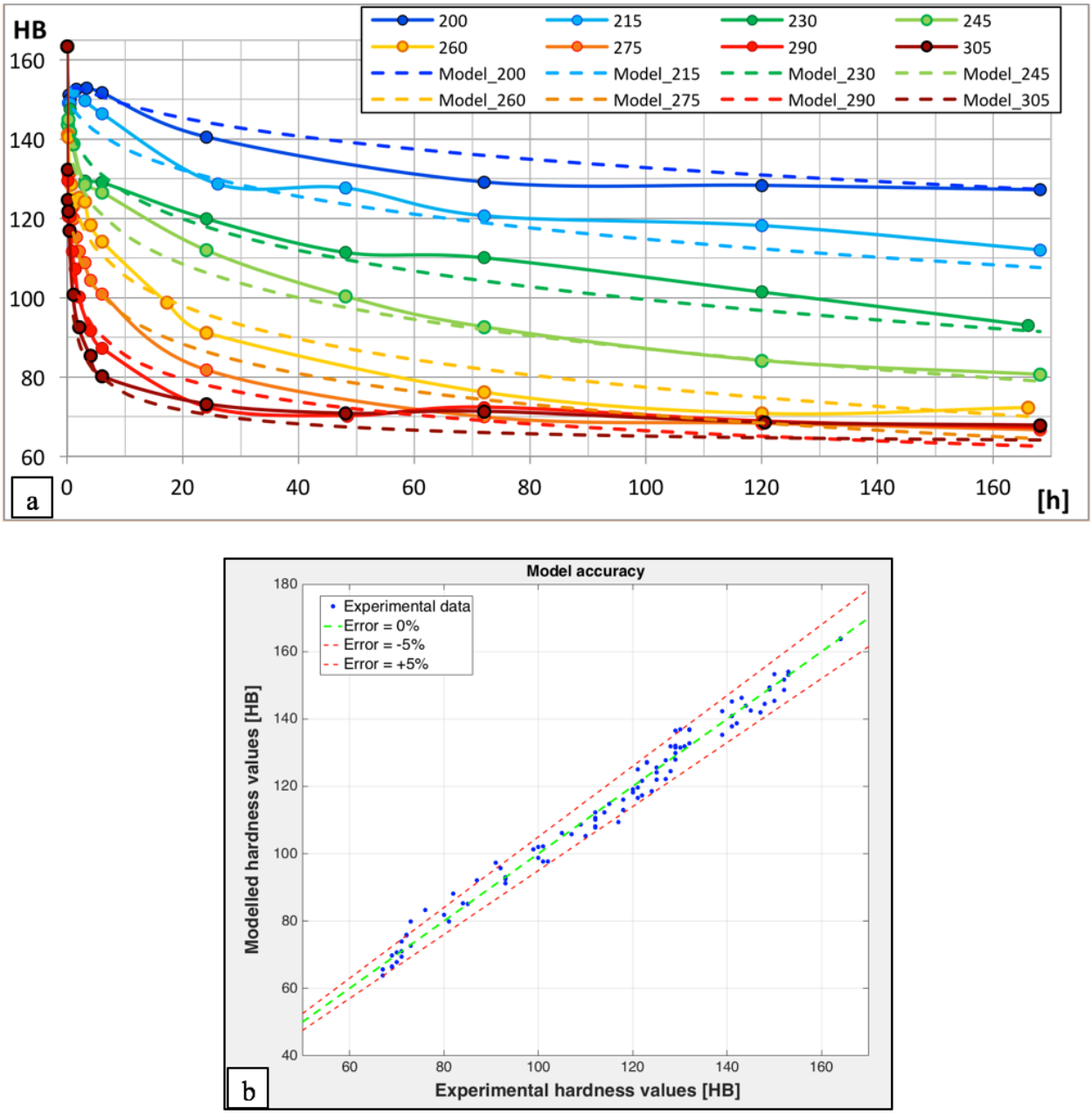

Fig.4.20: (a) Comparison between actual HTT curves of (solid lines) and modelled curves (dashed lines); (b) graph reporting experimental data compared to modelled ones, giving evidence that most of the modelled data are within the ±5% error band.

Additional SEM analyses carried out on the overaged samples are reported in Fig.4.21 and gave evidence of the microstructural evolution, which significantly depends on temperature and time of exposure. The consequences of Ostwald ripening are in fact clearly visible by comparing the SEM micrographs reported in Fig.4.18b and Fig.4.21a-b, obtained with the same magnification. Due to an increase in temperature (or time) of exposure, a network of coarse precipitates starts to decorate grain or sub-grain boundaries and finally it tends to cover the matrix itself.

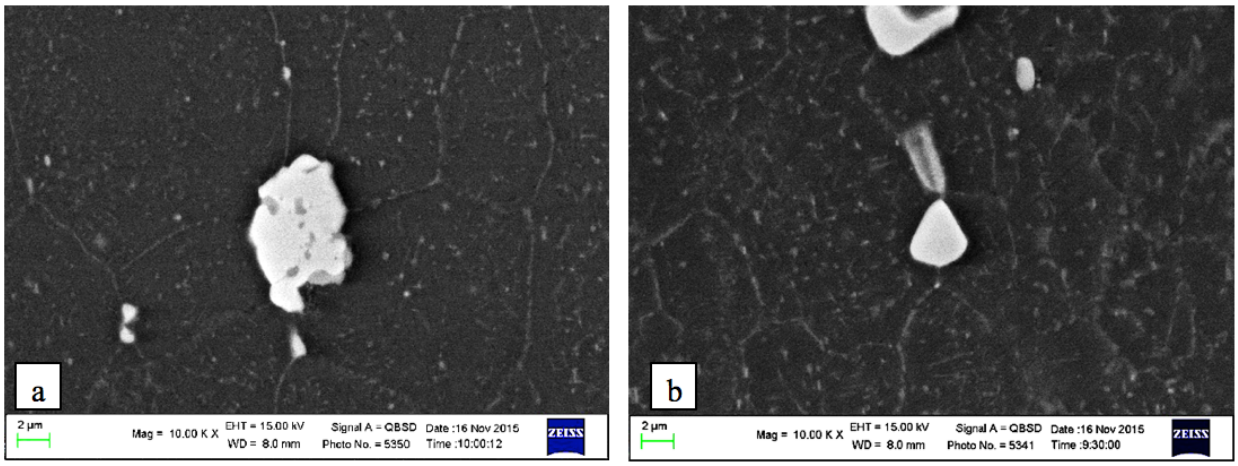

Fig.4.21: SEM micrographs of the overaged samples, after 24h soaking time at (a) 245°C and (b) 305°C, same magnification.

The coarsening of strengthening precipitates is unavoidable in heat treated aluminum alloys. However, in order to enlighten the potential of AA2099 in terms of thermal resistance, it is worth making a comparison with another high temperature resistant Al-Cu alloy, such as the AA2618:

- AA2099 contains Li, and its peculiarities are (i) the low density (2.63 g/cm^3) compared to the typical 2XXX Al-Cu alloys, and (ii) excellent mechanical properties at room temperature. The combination of the two aforementioned characteristics results in considerably high specific strength, which favors the applications of AA2099 alloy in the aerospace field.
- AA2618 contains significant amount of Ni and Fe, and it is specifically developed for high temperature applications in the automotive field.

By comparing the two alloys in the most overaged condition (exposure at 305°C for 168h), it is worth underlining that the residual hardness of the 2099 alloy (about 70HB) is still higher than that of the AA2618 (about 60HB, as reported by Ceschini et al. [30]). This result further strengthens the hypothesis that AA2099 can be suitable for automotive components running at high temperature, yet exhibiting a lower density.

Scanning Transmission Electron Microscopy analyses

Along with the T83 condition (164 HB), samples overaged for 24h at 245°C (residual hardness ≈ 110 HB) and 305°C (residual hardness ≈ 70 HB) were selected for STEM analysis, in order to study the peak-aged condition and the microstructural changes responsible of the slightly overaged and heavily overaged conditions. The decision process was driven by the results of the

overaging curves reported in Fig.4.19a, which show that the 3 selected samples are evenly spaced in the range of residual hardness investigated in this study. It should be underlined that the hardness plateau equal to 70HB is reached after just 24h at 305°C, and that hardness does not significantly change by further prolonging the time of exposure at 305°C. Since hardness and tensile properties are interrelated, and both strictly connected to microstructural changes, it can be inferred that the microstructural evolution responsible of overaging already occurred after 24h at 305°C. The latter condition was therefore considered as representative of the mostly overaged investigated condition. Fig.4.22 shows the collected STEM images. In the T83 condition, the ADF-STEM images (Fig.4.22a,d) show a fine, rich precipitate microstructure with Cu-containing phases (S [160], T_1 [161] and θ' phase [162]) appearing bright and the Li-containing δ phase [163] appearing dark, because the atomic weights of these elements are very different from that of Al. The phases were identified based on morphology, orientation relationship with the Al matrix and composition measured by EDS. Apart from T_1, all strengthening phases dissolve upon overaging at 245°C for 24h, while T_1 continues to exist and grows in thickness (Fig.4.22 b,e). According to Gao et al. [146], just prolonging the aging time at 200°C to 72h is sufficient to dissolve δ' and θ', while the T_1 and S phases still remain stable.

Even at the highest overaging temperature considered in the present investigation (305°C) a coarser distribution of T_1 particles is perceivable, as indicated in Fig.4.22c,f. This aspect confirms that the T_1 phase, which contains both Cu and Li, is the main responsible for the remarkable thermal stability of Al-Cu-Li alloys. The coarse and incoherent σ phase is formed at high temperatures (it is evident in the alloy overaged for 24h at 305°C, as highlighted in Fig.4.22c) and it does not significantly contribute to strengthening. In agreement with [164], the cubic structured σ phase is usually observed in overaged Al-Cu-Mg alloys, and it corresponds to the stoichiometric formula $Al_5Cu_6Mg_2$. It is however reported in literature [146,165] that cubic σ phase might also form in Al-Cu-Li alloys in different aging or overaging conditions.

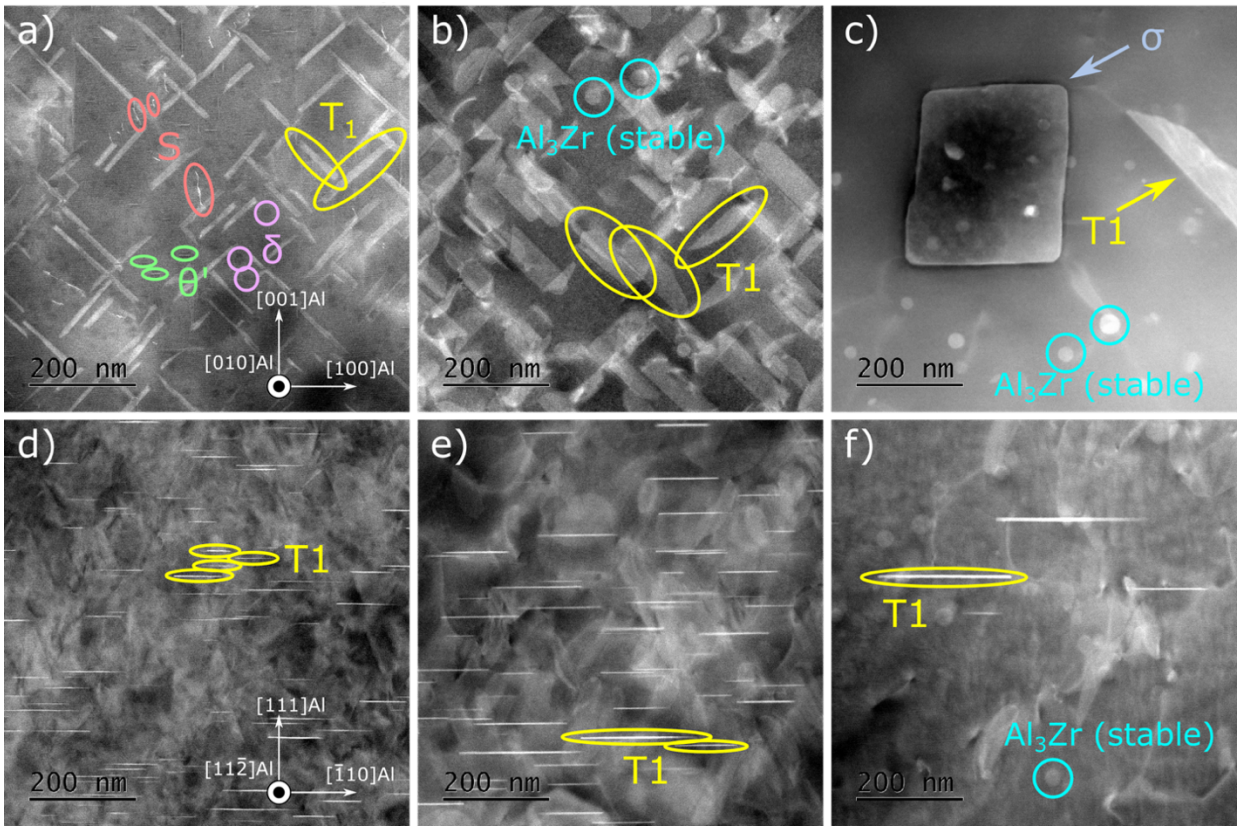

Fig.4.22: ADF-STEM images of the precipitate microstructure in (a),(d) the T83 condition, (b),(e) overaged at 245°C for 24h and (c),(f) overaged at 305°C for 24h. (a),(b),(c) are acquired along the <001>Al direction and (d),(e),(f) in the <112>Al direction.

EDS maps were also performed on the most overaged sample, as reported in Fig.4.23, in order to combine chemical and morphological analyses and to clearly define the phases still present after overaging. It is worth pointing out that the EDS maps reveal the presence of significant amount of Cu and Mg coupled with Zn in the cubic phase. The presence of Zn is in agreement with the theory proposed by Li et al. [165], aiming to explain the formation of σ phase in absence of Si or Ag: Zn is suspected to contribute to its nucleation. According to literature data [146,165], thermal exposure leads to overaging of all the strengthening precipitates characterizing the 2099 Al-Cu-Li alloy, with the exception of the σ phase. However, the coarse dimensions of the σ phase and its incoherency with the Al matrix prevent it from providing a significant strengthening effect.

Finally, Fig.4.24 shows ADF-STEM images of grain boundaries of the two extreme conditions from Fig.4.22. A small precipitate-free zone is evident in the T83 condition. Dislocations are able to move freely inside this zone, which makes all grain boundaries weak spots. The observations are in agreement with Lin et al. [152], whose TEM micrographs report the presence of continuous secondary phases and precipitate-free zone at grain boundaries. After over-aging at 305 °C for 24h,

the density of precipitates is much less, as earlier noted, and the strength difference between areas in the middle of grains and close to grain boundaries become negligible.

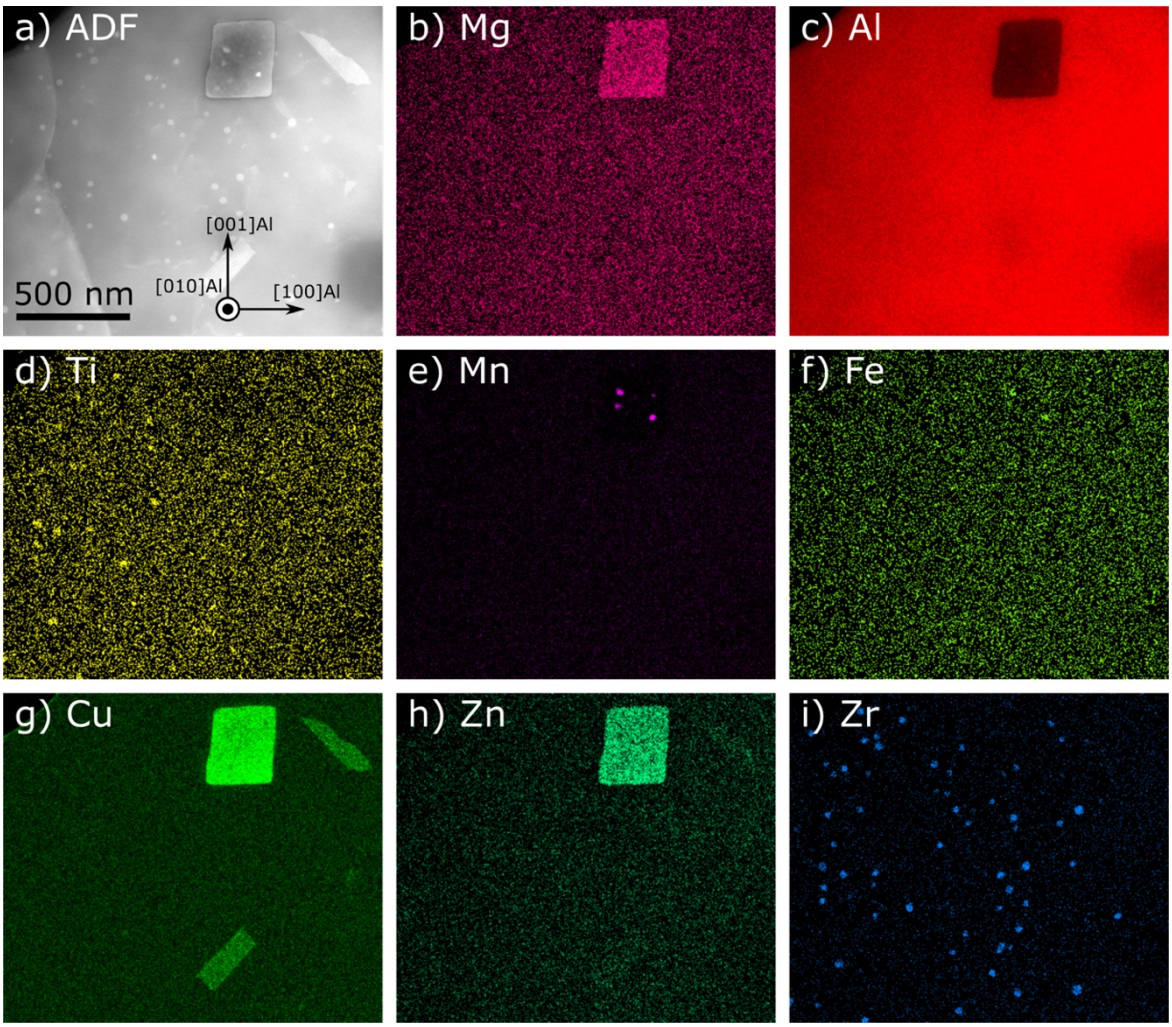

Fig.4.23: ADF-STEM image of the precipitate microstructure overaged at 305°C for 24h, acquired along the <001>Al direction (a), and corresponding EDS maps of Mg (b), Al (c), Ti (d), Mn (e), Fe (f), Cu (g), Zn (h), Zr (i).

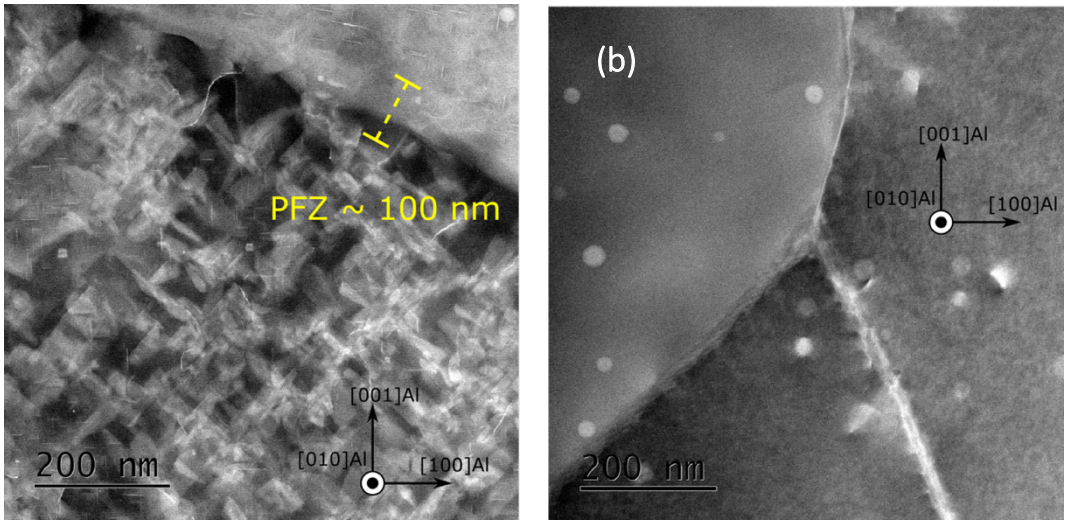

Fig.4.24: ADF-STEM image of the 2099 T83 alloy (a) and overaged at 305°C for 24h (b), acquired along the <001>Al direction, focusing on the grain boundaries.

Tensile tests

Based on the hardness interval determined by the overaging curves (roughly equal to 100HB, between the T83 condition and the minimum hardness value of 67HB, which is reached after 168h at 305°C), 6 hardness classes were defined for the tensile specimens: peak-aged (164HB), 147HB, 129HB, 112HB, 93HB, 73HB. Among the possible couples of time-temperature conditions to reach the targeted residual hardness values, the choice fell on the heat treatments that last enough to be accurate, but not extremely time-consuming. The actual residual hardness values were checked on the grips of tensile samples, after the completion of the tensile tests. The results of hardness and tensile tests on the specimens belonging to the different hardness sets are reported in Table 4.7. To better appreciate the mechanical properties of AA2099 after overaging, Table 4.8 was added, reporting the numerical results of tensile tests on overaged AA2618 specimens, carried out by Ceschini et al. in [30]. Even if AA2618 is specifically designed to resist thermal exposure [30,131,166], the tensile properties of AA2099 after overaging were always slightly superior than that of AA2618 [30], even at the lower residual hardness conditions. Again, this is a promising indication for high temperature applications.

Table 4.7: Classes of hardness for AA2099 tensile specimens, overaging treatments performed to reach the targeted hardness, actual Brinell hardness measured after tensile tests and results of tensile tests on the overaged samples (average and standard deviation).

Target [HB]	Overaging	Actual residual hardness [HB]	$R_{p0.2}$ [MPa] ±2σ	UTS [MPa] ±2σ	A_t[%] ±2σ
164 (T83)	No overaging	165	619 (±7.2)	635 (± 4.7)	9.3 (±1.3)
147	6h @ 215°C	150	457 (±1.3)	531 (± 5.1)	8.1 (±1.7)
129	24h @ 215°C	135	379 (±2.1)	447 (±2.0)	11 (±2.4)
112	24h @ 245°C	115	263 (±8.2)	388 (±3.3)	16.6 (±1.5)
93	72h @ 245°C	93	194 (±4.2)	329 (±3.1)	18.9 (±3.3)
73	24h @ 305°C	75	120 (±3.7)	266 (±9.2)	20.7 (±1.7)

Table 4.8: Classes of hardness for AA2618 tensile specimens, overaging treatments performed to reach the targeted hardness, actual Brinell hardness measured after tensile tests and results of tensile tests on the overaged samples [30].

Target [HB]	Overaging	Actual residual hardness [HB]	$R_{p0.2}$ [MPa]	UTS [MPa]	A_t[%]
142 (T6)	No overaging	142	365	423	4.1
125	24 @ 200°C	126	317	384	5.8
115	10h @ 230°C	116	267	353	6.6
105	120h @ 230°C	104	218	321	6.6
90	3.5h @ 290°C	90	166	279	7.8
80	9h @ 305°C	79	121	245	10.2
70	30h @ 305°C	71	107	231	10.7

The relationships between tensile properties and residual hardness values of the alloy are reported in Fig.4.25a. As can be noted in Table 4.7, negligible differences between targeted and actual hardness have been generally detected in the overaged samples. The actual residual Brinell hardness values were therefore taken into account in order to model the behavior of the 2099 alloy with residual hardness. As expected, a well-defined relationship exists between tensile properties and residual hardness, as also reported by Jabra et al. [156]. In particular, as shown in Fig.4.25a, UTS and $Rp_{0.2}$ exhibit an exponential decrease in the overaged alloy, while A_t% shows a logarithmic increase with prolonged overaging. It is worth to underline the different behavior of the AA2099 (Al-Cu-Li) alloy with respect to the AA2618 (Al-Cu-Mg-Ni-Fe) alloy [30], which display, respectively, an exponential and linear decrease of tensile properties with decreasing residual hardness.

Moreover, for each hardness class, the existing relationship of the average strength coefficient K and the average hardening coefficient n as a function of the residual material hardness is shown in Fig.4.25b. According to the experimental data, the strain hardening exponent is constantly growing for lower residual hardness, while the strengthening coefficient exhibits an opposite trend; both n and K follow a nearly linear function of residual hardness. The opposite trend of K and n as a function of residual hardness can be related to the microstructural modifications induced by the heat treatment conditions. Since the main contribution to strengthening in Al-Cu-Li alloys is provided by T_1 precipitates, their microstructural changes are the main responsible of the changes in mechanical properties. Attention has been therefore focused on the evolution of the interaction between dislocations and T_1 precipitates, as explained below.

- The very fine and coherent precipitates characterizing the T83 condition (clearly visible in Fig.4.22a) induce the maximum strengthening effect, which is directly translated into high values for the K coefficient). In agreement with recent researches by [146,167], T_1 precipitates in the peak aged condition consist of one or two unit cells only. Above the plastic threshold, the fine and coherent precipitates are sheared by dislocations according to the Ashby's model [128], as reported in [168]. However, these precipitates are not effective one step further the plastic field has been reached, since precipitate shearing prevents additional dislocation storage and strain hardening [168]. In case of the AA2099 alloy, given the almost total absence of secondary phases able to hinder the dislocations motion, deformation increases without appreciable strain hardening, and the strain hardening exponent is approximately null. This is confirmed by the almost horizontal trend

of the stress-strain curves referring to the T83 condition (reported as blue curves in Fig.4.26).

- On the contrary, the strengthening coefficient K progressively decreases for lower residual Brinell hardness, due to the coarsening of precipitates (whose evidences are reported in Fig.4.22b,c) At the same time, the strengthening exponent n is considerably increased due to the activation of the Orowan's mechanism [128]. As also confirmed by [168,169], when T_1 precipitates thicken and their spacing increases, it is reasonable the activation of by-passing mechanism. The interaction between coarser precipitates and dislocations is responsible for the growth of number of dislocations in the form of Orowan loop and their subsequent obstruction to slip.

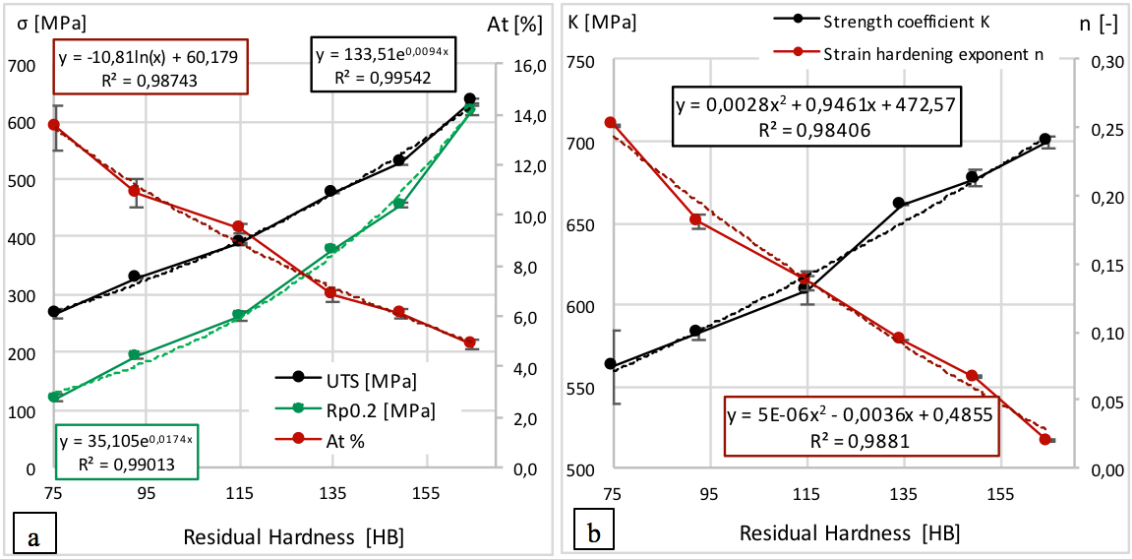

Fig.4.25:(a) Relationship between tensile properties (Proof Strength, Ultimate Tensile Strength, Elongation to failure) and residual hardness of AA2099; (b) relationship between strength coefficient K, strain hardening exponent n and residual hardness of the alloy. In both plots, each point is the average value of 3 tensile tests, while the error bars have been set as ±2σ.

Processing of the experimental data lead to the implementation of the following Eq.4.4, which is able to predict the true stress of the alloy in the plastic field, as a function of the residual alloy hardness:

$$\sigma_{Hollomon} = (0.0028HB^2 + 0.9461HB + 472.57) \cdot \varepsilon_{plastic}^{(5\cdot10^{-6}HB^2 - 0.0036HB + 0.4855)}$$

Eq.4.4: Stress-strain model of 2099 alloy in the plastic field, as a function of the alloy residual hardness. The model is based on Hollomon's law, the strengthening coefficient K and the strain hardening exponent n being determined from elaboration of tensile tests data.

The validity of the model is confirmed by the fact that experimental results (dashed line in Fig.4.26) appropriately match the curves generated by the model (solid line in Fig.4.26). Absolute and

relative errors were calculated for all hardness classes, as reported in Table 4.9. Due to the divergence of the modelled curves for high values of plastic deformation and in order to make an effective comparison between hardness classes, the experimental and modelled data were limited to $\varepsilon_{true} \leq 5\%$. It is possible to state that, with the exception of the peak aged condition, the maximum absolute error never reaches 30MPa. The relative error obviously tends to increase for the highly overaged conditions, due to the lower values of true stress. It is interesting to underline that the 93HB class exhibits a higher absolute error compared to 112HB and 73HB classes and it is also interesting to compare the table to Fig.4.25b: the higher error value is mainly linked to the interpolation error in modelling the strain hardening exponent n. At the same time, it can be also pointed out that errors in K values modelling are not considerably affecting the modelling results (the low error for 112HB class is obtained through a nearly perfect interpolation of n value, but poor modelling of K value).

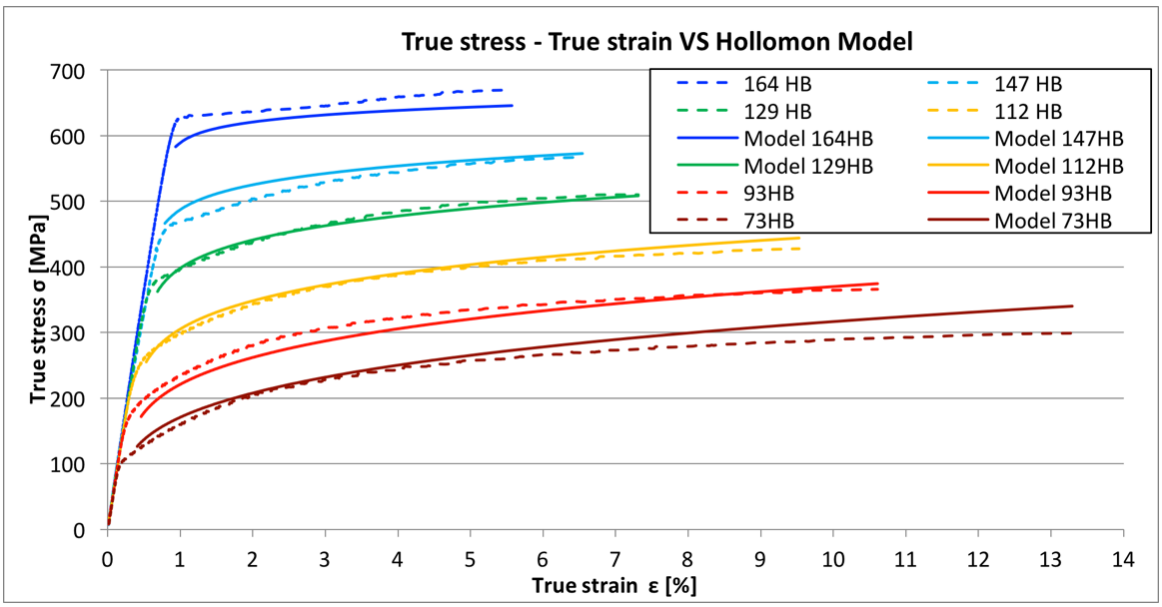

Fig.4.26: Actual true stress-true strain curves (dashed lines) compared to modelled curves (solid lines). The last ones have been calculated according to Hollomon's equation, therefore data are restricted to the plastic field. K and n parameters have been modelled as a function of residual hardness values, as reported in Fig.4.25b.

Table 4.9: Absolute and relative errors between true tensile data and the implemented Hollomon's model.

Error \ HB	164	147	129	112	93	73
Max absolute error [Mpa] $E_{abs} = \max(\lvert\sigma_{true\ i} - \sigma_{model\ i}\rvert)$	39	27	19	12	23	13
Corresponding relative error [%] $E_{rel} = \frac{\lvert\sigma_{true\ i} - \sigma_{model\ i}\rvert}{\sigma_{true\ i}}$	6,3%	5,7%	4,9%	4,5%	11,9%	9,0%

Finally, complementary SEM analyses of the fracture surfaces have been carried out on two tensile specimens, representative of the upper and lower residual hardness conditions: T83 and overaging for 24h at 305°C. The fracture surfaces of the tensile samples, reported in Fig.4.27, give evidence of microstructural changes affecting the alloy behavior at different residual hardness values. Low magnification SEM micrograph of the T83 sample (Fig.4.27a) highlights the presence of shear lips, confirming the not negligible elongation to fracture (about 9%) reported in Table 4.7. High magnification SEM micrographs of the same T83 sample (Fig.4.27c) reveal a mixture of intergranular fracture and presence of fine dimples. The fracture mode is consistent with the precipitate-free zones (PFZs) at grain boundaries, highlighted in our STEM investigations on the T83 sample (Fig.4.24), which act as stress concentration sites for crack initiation. The intergranular fracture mode in the peak-aged condition is also confirmed by others [40,140,152,157].

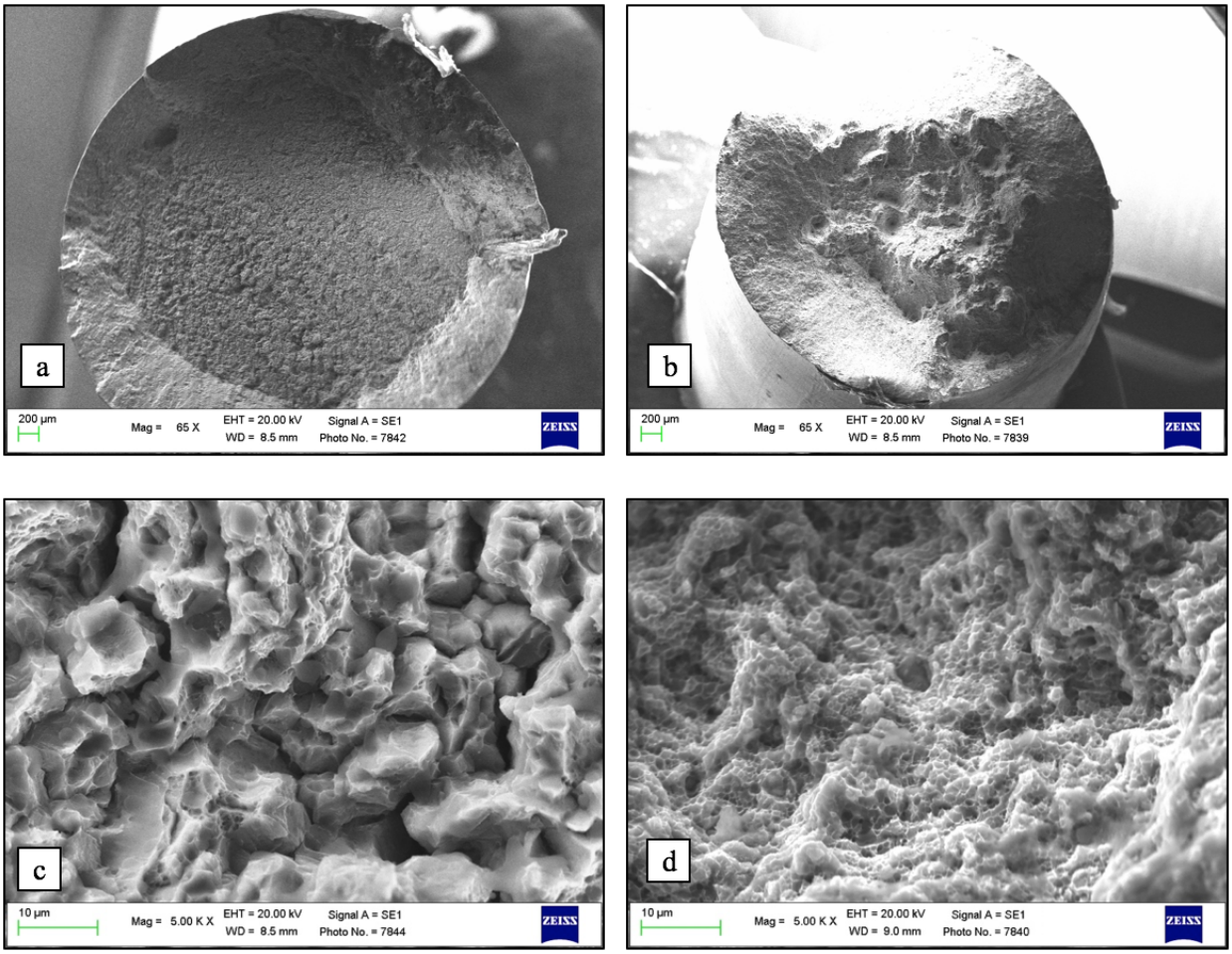

Fig.4.27: Low and high magnification micrographs of the fracture surfaces representative of (a), (c) the T83 condition, (b), (d) overaging to 75HB residual hardness; the significantly different fracture mechanisms is underlined.

Overaging induces significant changes in the fracture mode. The fracture surface appears considerably deformed even at low magnification (Fig.4.27b). The high magnification micrograph (Fig.4.27d) gives evidence of very fine dimples, which cover the entire surface and which make grain boundaries no more perceivable. It seems that at peak hardness, the weak points are the grain boundaries, while in the overaged conditions, the material is weak both at grain boundaries and in the interior of the grains because of the low density of precipitates. According to [152], also slight overaging (peak-aged condition with additional 48h at 152°C) results in coarsened, discontinuous, large-spaced grain boundary phases, which can therefore relieve stress concentration at grain boundaries, improving ductility. The observation is in agreement with our experimental data (Table 4.7), which highlight the nearly double elongation to fracture of the highly overaged condition, compared to the peak-aged condition.

4.3.4 Conclusions

With respect to other conventional Al alloys, AA2099 (Al-Cu-Li) exhibits a lower density and a higher elastic modulus, which provide an excellent specific stiffness at room temperature. The main strengthening mechanism of this alloy is precipitation hardening; however, similarly to other heat treatable Al alloys, also AA2099 undergoes coarsening of the strengthening precipitates during high temperature exposure, which can considerably reduce its performance. This study assessed the effect of overaging on the AA2099-T83, in the range 200-305°C, highlighting that:

- The lower the hardness, the lower the tensile strength of the alloy. To provide a useful instrument for the design process, the relation between residual hardness and tensile strength has been determined, according to Hollomon's equation in the plastic field.
- The lowest hardness and strength limit of AA2099 are reached after 24h at 305°C and it is maintained when the soaking time is further prolonged. This limit is comparable or even higher than that of Al alloys specifically designed for high temperature applications, which suggests that also AA2099 might be suitable for high temperature applications.
- After thermal exposure, the T_1 phases tend to thicken, but they do not dissolve unlike ϑ', δ and S phases, while the formation of the coarse and not strengthening σ phase is activated. T_1 precipitation has therefore to be enhanced in order to promote the thermal stability of the 2099 Al alloy.

Overaging curves and room temperature tensile tests of overaged samples are the basic step to evaluate the suitability of the alloy for high temperature applications. Since the Al-Cu-Li alloy AA2099 exhibited promising properties after overaging, even better than Al alloys specifically developed for high temperature applications, it is reasonable that also mechanical properties of AA2099 at high temperature would be encouraging.

4.4 Effects of overaging on microstructure and tensile properties of the 2055 Al-Cu-Li-Ag alloy

[The whole Sect. is taken from the published paper whose title is shown below. ©2017. This manuscript version is made available under the CC-BY-NC-ND 4.0 licence].

Materials Science & Engineering A 707 (2017) 221–231

Contents lists available at ScienceDirect

Materials Science & Engineering A

journal homepage: www.elsevier.com/locate/msea

Effects of overaging on microstructure and tensile properties of the 2055 Al-Cu-Li-Ag alloy

E. Balducci[a,*], L. Ceschini[b], S. Messieri[c], S. Wenner[d], R. Holmestad[d]

[a] Dept. of Industrial Engineering, Alma Mater Studiorum University of Bologna, via del Risorgimento 2, Bologna, Italy
[b] Dept. of Civil, Chemical, Environmental and Materials Engineering, Alma Mater Studiorum University of Bologna, via del Risorgimento 2, Bologna, Italy
[c] Ducati Motor Holding, Bologna, Italy
[d] Dept. of Physics, Norwegian University of Science and Technology, Høgskoleringen 5, Trondheim, Norway

Abstract

The lightweight, unconventional 2055 Al-Cu-Li-Ag alloy exhibits an excellent specific strength in the T83 state, but no literature reports the effects of overaging on this alloy. In the present work, the suitability of the alloy for lightweight components operating at high temperature is evaluated. Thermal exposure in the range 215 – 305 °C was investigated, highlighting its consequences on both microstructure and mechanical properties. In the most severe overaging state (24 h at 305 °C), the typical T_1 precipitates (Al_2CuLi) are dissolved, leading to the formation and coarsening of θ' and Ω phases. In all overaging conditions, the alloy performance was superior or at least comparable to that of another third generation Al-Li alloy, AA2099, which is characterised by a slightly lower density and encouraging mechanical properties for high temperature applications. Compared to AA2099, the AA2055 alloy provides a higher specific strength (the basic requirement for mass savings) both in the T83 and in the most severe overaging state (24 h at 305 °C). This work highlights that AA2055 is a promising candidate for lightweight components operating up to 305°C, and it lays the basis for high temperature tests of the alloy.

Keywords

Al-Cu-Li-Ag alloy; Thermal effect; Tensile test; Microstructure; STEM.

4.4.1 Introduction

Recently patented by Alcoa in 2012 [170], the AA2055 belongs to the 2xxx series of Al alloys, containing Cu as the major alloying element. It is an unconventional 2xxx alloy, since it contains a considerable amount of Li, Zn, Mg and Ag, which definitely makes it one of the most promising candidates of the third generation of Al-Li alloys. As widely reported in [36,143,171], the third generation of Al-Li alloys combines excellent mechanical properties, high stiffness, good corrosion resistance and fracture toughness with very low density, which successfully translates into a significantly high specific strength if compared to conventional 2xxx or 7xxx Al alloys. Li addition makes a key contribution in both density reduction (each 1 wt% of Li addition accounts for-0.079 g/cm^3 density reduction, according to Peet et al. [35]) and elastic modulus increase (1 wt% Li addition is expected to provide 6% increase in Young's elastic modulus [36]).

Generally speaking, the major strengthening effect in Al-Cu-Li alloys is provided by the T_1 (Al_2CuLi) phases, which precipitate along the {111} plane of the Al matrix [161,167,172,173] and tend to nucleate at grain or sub-grain boundaries. Aiming to discourage the incidence of precipitate free zones at the grain interior, cold stretching prior to aging is regularly adopted during the heat treatment of Al-Cu-Li alloys, since a dense network of dislocations provides for heterogeneous nucleation sites for T_1 [174–179]. Further, the more severe the pre-stretching (up to 15% according to Rodgers et al. [177]), the more the T_1 precipitation kinetics are accelerated, which leads to a higher volume fraction of precipitates, a finer T_1 size, and a lower coarsening rate during overaging.

Among the other strengthening precipitates, δ' (Al_3Li), ϑ' (Al_2Cu) and S' (Al_2CuMg) are commonly observed in the third generation of Al-Cu-Li alloys [36,146,164]. δ' precipitates were one of the main strengthening phases of the second generation of Al-Li alloys [36], generally containing more than 2wt% Li and therefore exhibiting an attractive low density. Several drawbacks were however attributed to the high content of Li, such as poor thermal stability, leading to low fracture toughness after thermal exposure, even at temperatures in the range 70-85°C [36,180].

Due to the presence of Li in both phases, δ' and T_1 are in competition and evidence confirms that higher Cu/Li ratio enhances T_1 precipitation [144,145]. The trend in the third generation of Al-Cu-

Li alloys is to maximize the volume fraction of T_1 at the expense of δ', due to the fact that the former is less sensitive to degradation after thermal exposure [36,37,144,159,176].

Since Al-Cu-Li alloys were specifically developed to satisfy the requirements of structural aerospace components, both lightweight and thermal stability at temperatures in the range 70-150°C were considered fundamental (due to aerodynamic heating). As a result, the effects of thermal exposure on Al-Cu-Li alloys have been commonly investigated below 200°C, aiming to study the decay of properties during the lifecycle of aerospace components. In particular, Davydov et al. [180] investigated the effects of exposure at 85°C and 95°C up to 1000h and 300h respectively, on both Al-Li-Mg-Sc-Zr and Al-Li-Cu-Sc-Zr alloys; similarly, Deschamps et al. [159] analysed the effects of long term aging at 85°C on Al-Cu-Li-Mg alloys, highlighting the superior thermal stability of T_1 precipitates compared to δ'. Long thermal exposure (over 7000 h) at temperature as high as 107 °C and 163°C was investigated by Mou et al. [181], while Kumar et. al [176] evaluated the effects of soaking at 160°C; both the studies revealed the presence of S' and T_1 in Al-Cu-Li-Ag alloys, yet substantially coarsened after prolonged overaging. Finally, Ortiz et al. [154] examined the effect of thermal exposure up to 177°C, highlighting a monotonous decrease in hardness and yield strength.

However, fuel efficiency and low weight are critical for aerospace as well as for automotive components, which makes it worth investigating the possibility to expand the employment of Al-Cu-Li alloys in the latter field. Even if high specific strength and stiffness are considerably attractive, automotive components are much more demanding than aerospace components in terms of high temperature resistance, which needs to be investigated up to 300°C. Jabra et al. [156] reported the consequences of overaging of Al-Cu-Li alloys at temperatures as high as 290°C, revealing a consistent decay of tensile properties. However, to the authors' best knowledge, there is a lack of research focused on the effects of thermal exposure at 200-300°C on the microstructure of Al-Cu-Li alloys. Such investigations are needed to fully understand the relationship between microstructural evolution and mechanical properties during overaging.

A previous study by the authors [37] showed the high potential of the lightweight AA2099 Al-Cu-Li alloy, whose response to overaging even at 305°C was found adequate for high temperature applications, and comparable to the heat resistant AA2618. The encouraging results of the AA2099 trigger the curiosity on the thermal resistance of a similar third generation alloy, AA2055, which is the main objective of this study. Despite the slightly higher density with respect to AA2099 (2.71 compared to 2.63g/cm^3 [182,183]), still the Al-Cu-Li-Ag AA2055 is lighter than the

conventional 2xxx or 7xxx Al alloys, and it shows interesting features which might be beneficial for reducing the negative effects of overaging underlined in [37]. First of all, compared to AA2099, the AA2055 contains a higher Cu and a lower Li amount, which increases the Cu/Li ratio and therefore leads to an expected higher volume fraction of T_1 (according to [144,145]). As stated before, T_1 phases are more thermally stable than δ' [37,176], demonstrated by the fact that T_1 continues to exist, though coarsened, even after overaging for 24h at 305°C [37]. Moreover, whereas AA2099 does not contain Ag, AA2055 contains up to 0.7wt% Ag, which is known to promote the formation of Ω phases in Al-Cu-Mg alloys (at the expenses of θ' [184,185]). The Ω phase (Al_2Cu) assumes the form of an othorhombic plate-like precipitate on the {111} planes of Al matrix, having the same chemical composition as θ' precipitates, but also exhibiting an evident segregation of Mg and Ag at the matrix/Ω interfaces. Hutchinson et al. [186] underlined the excellent coarsening resistance of Ω up to 200°C (the precipitates approximately maintained their original thickness after 1000h of exposure), and several researches have revealed the increased thermal stability, mechanical properties and creep resistance of Al-Cu-Mg alloys with Ag additions [184,187–191].

Besides the widely reported improvements of Al-Cu-Mg heat resistance, Ag additions are also reported to promote a higher volume fraction and a uniform nucleation of T_1 precipitates in Al-Cu-Li alloys, in particular when combined with Mg [192,193]. Both Ag and Mg also lessen the alloy stacking fault energy, reducing dislocation mobility and increasing the hot deformation activation energy [194]. All these aspects – the expected presence of Ω phases, the probable higher volume fraction of T_1, the lowered dislocation mobility if compared to AA2099 – sound promising in terms of the alloy response to overaging.

The present study aims to evaluate the effect of thermal exposure on the lightweight AA2055, and to compare the achieved results with the encouraging results from alloy AA2099 [37]. This work represents a preliminary, yet necessary step, to verify the suitability of the Al-Cu-Li-Ag alloy to operate at high temperature (up to 300°C), and to identify the most thermally stable precipitates, which must be enhanced by heat treatment in order to promote the thermal stability of the alloy.

4.4.2 Material and methods

The AA2055 Al-Cu-Li-Ag alloy was provided by Alcoa in the form of extruded bars with 120 mm diameter. The bars were received in the T83 condition, whose heat treatment consists of solution

treatment, quench, 3% stretching at room temperature followed by artificial aging. Table 4.10 reports the chemical composition limits of AA2055, as specified by Alcoa (the alloy supplier).

Table 4.10: Chemical composition limits [wt%] of AA2055.

Cu	Li	Zn	Ag	Mn	Mg	Ti	Zr	Fe	Others, each	Others, tot	Al
3.2-4.2	1.0-1.3	0.3-0.7	0.2-0.7	0.1-0.5	0.2-0.6	0.1	0.05-0.15	0.1	0.05	0.15	Bal.

The effects of thermal exposure on the alloy properties were assessed through room temperature tensile tests, performed both on peak-aged and overaged samples. To make an effective comparison with AA2099, the overaging conditions reported in [37] were reproduced on AA2055 before tensile testing, namely: (i) no overaging, (ii) 6h at 215°C; (iii) 24h at 215°C, (iv) 24h at 245°C, (v) 72h at 245°C, (vi) 24h at 305°C. During overaging, a K-type thermocouple assured a variation of the furnace temperature within ± 2°C.

At least two samples were subjected to tensile tests for each investigated condition. A tensile testing machine with screw grips was adopted and the strain rate was set equal to $3.3 \times 10^{-3}\ s^{-1}$. Sample geometry is reported in Fig.4.28. The calculation of proof strength ($Rp_{0.2}$), ultimate tensile strength (UTS) and elongation to failure (A_t%) were carried out according to EN ISO 6892-1: 2009 standard.

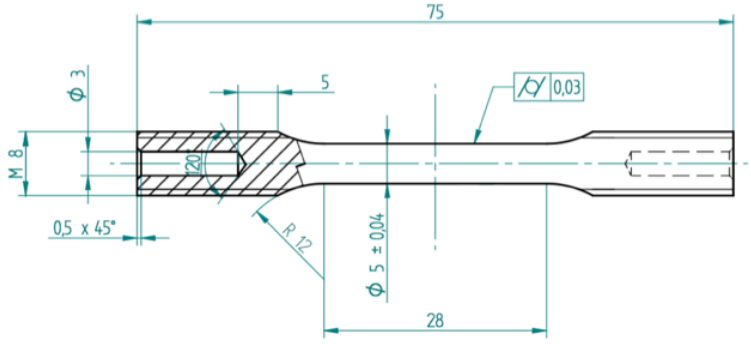

Fig.4.28: Geometry and dimensions [mm] of tensile specimens.

The effect of overaging was quantitatively evaluated by considering the variation of RT tensile properties with residual hardness. For this purpose, the residual hardness of each sample was measured after tensile tests, on its grip section. Brinell hardness tests were carried out according to the ASTM E 10-08 standard, using a hardened steel ball indenter with 2.5mm diameter, and an applied load equal to 62.5kg.

Tensile data were further analyzed in order to go deeper into the determination of overaging effects. Since the difference in precipitate size generally translates into different dislocation-

precipitate interaction (as widely reported in [168,169] with reference to T_1 precipitates), the determination of the strain hardening ability of the alloy in each overaged condition provided additional information on the precipitate strengthening mechanisms. The following Hollomon's Eq.4.5 was adopted to model the plastic behavior of the alloy:

$$\boldsymbol{\sigma = K\varepsilon^n}$$

Eq.4.5: Hollomon's law, representative of the behavior of the alloy in the plastic field, when deformation occurs at room temperature [127].

The strength coefficient K and the hardening coefficient n of the Hollomon's equation were evaluated according to ISO 10275:2007 standard, taking into account true stress-true strain data between 2% plastic strain and the percentage plastic extension at maximum force (A_g). K and n values have been modelled as a function of the residual hardness of the tensile samples to highlight the influence of overaging.

Scanning Electron Microscopy (SEM) analyses with secondary electrons were also performed on the fracture surfaces of the tensile samples, after degreasing with acetone, highlighting the variation of the fracture mechanisms with increased overaging.

The correct interpretation of tensile tests data was assured by in-depth microstructural investigations, conducted on overaged metallographic samples with the aim to precisely relate the changes in alloy performance to the microstructural evolution. For this purpose, the specimens were mechanically ground with SiC papers up to 4000 grit and finally polished with down to 0.05µm colloidal silica. Scanning Electron Microscopy and Energy Dispersive Spectroscopy (SEM-EDS) investigations provided a first overview of microstructural characteristics of samples representative of the T83, T83 + 24h at 245°C and T83 + 24h at 305°C conditions.

Annular dark-field scanning transmission electron microscopy (ADF-STEM) studies provided a deeper look into microstructural changes, allowing to evaluate how overaging affects the density, size and type of precipitates. Material in the same condition as for the SEM characterization was ground to 100 µm thick discs and electropolished with a Struers TenuPol-5. The electrolyte was a solution of 1/3 HNO_3 in 2/3 CH_3OH, cooled to −25°C and biased with 20V. This preparation leaves some Ag behind as nano-sized spheres on the sample surface, which must be taken into account when interpreting results from the analysis. ADF-STEM images and EDS maps were acquired with a JEOL JEM-2100F operated at 200kV. The ADF-STEM method was chosen as it gives contrast between light elements (e.g. Al) and heavy elements (e.g. Cu and Ag), and will thus give contrast

between the expected precipitates and the matrix. Precipitates were imaged with the electron beam parallel to $<001>_{Al}$ and $<112>_{Al}$ zone axes.

4.4.3 Results and discussion

Microstructural evolution during overaging: SEM-EDS and STEM-EDS analyses

Three conditions were selected for both SEM and STEM analyses: the T83 (no overaging) condition, and two overaging conditions (samples subjected to 245 °C and 305 °C for 24 h).
Low magnification SEM micrographs of the T83 material clearly reveal the typical extrusion texture, with secondary phases aligned along the extrusion direction (Fig.4.29a). Similarly to the AA2099 alloy [37,142], the majority of the secondary phases consists of coarse Al-Cu-Fe-Mn compounds (Fig.4.29c). Moreover, as reported in Fig.4.29b, several coarse Al-Cu compounds have been found in the present alloy (most probable primary Al_2Cu), whose size can reach up to 10µm. On the contrary, coarse Al-Cu particles were not observed in the AA2099 alloy [37], due to the lower amount of Cu.

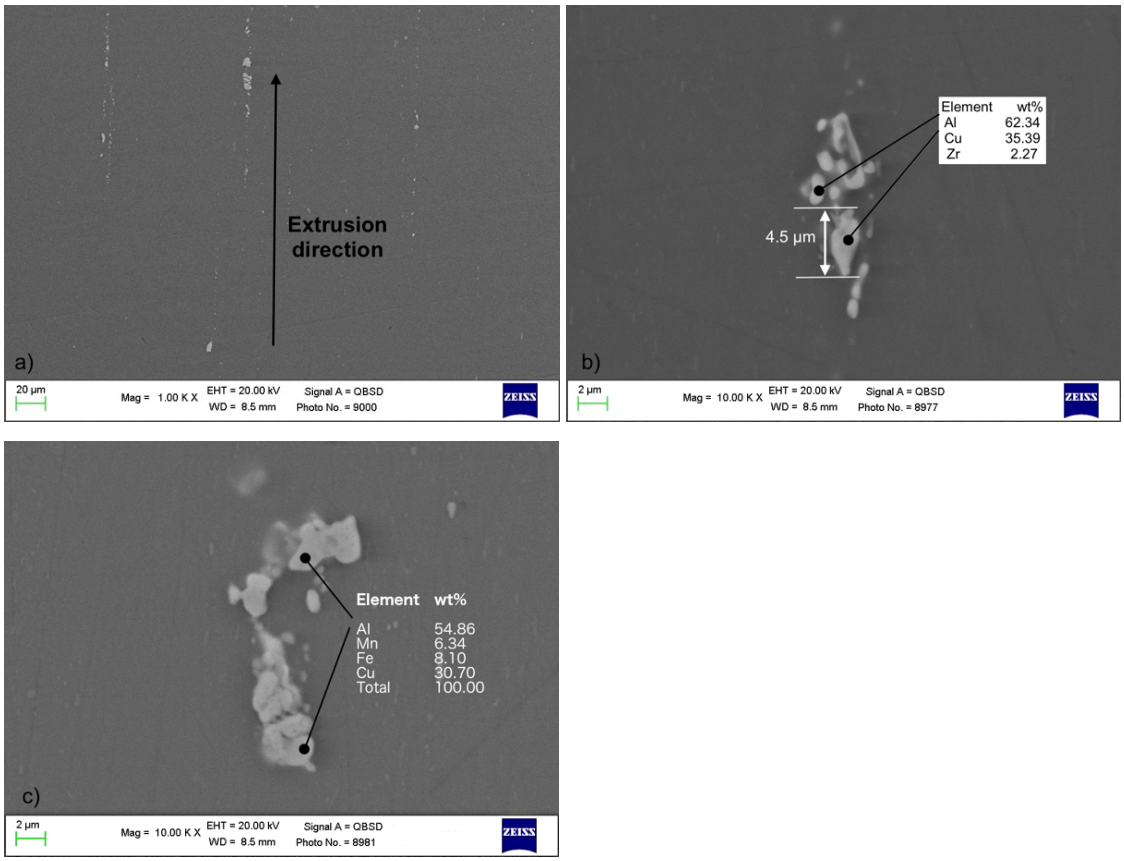

Fig.4.29: SEM investigations of T83 metallographic sample: (a) low magnification, (b), (c) higher magnification highlighting the secondary phases.

The SEM micrographs of overaged metallographic samples are reported in Fig.4.30. Even if microstructural changes cannot be detected at low magnification (Fig.4.30a,c), high magnification micrographs (Fig.4.30b,d) clearly reveal the substantial coarsening of strengthening precipitates compared to Fig.4.29b,c. In particular, coarsened precipitates form a network decorating grain or sub-grain boundaries in Fig.4.30d.

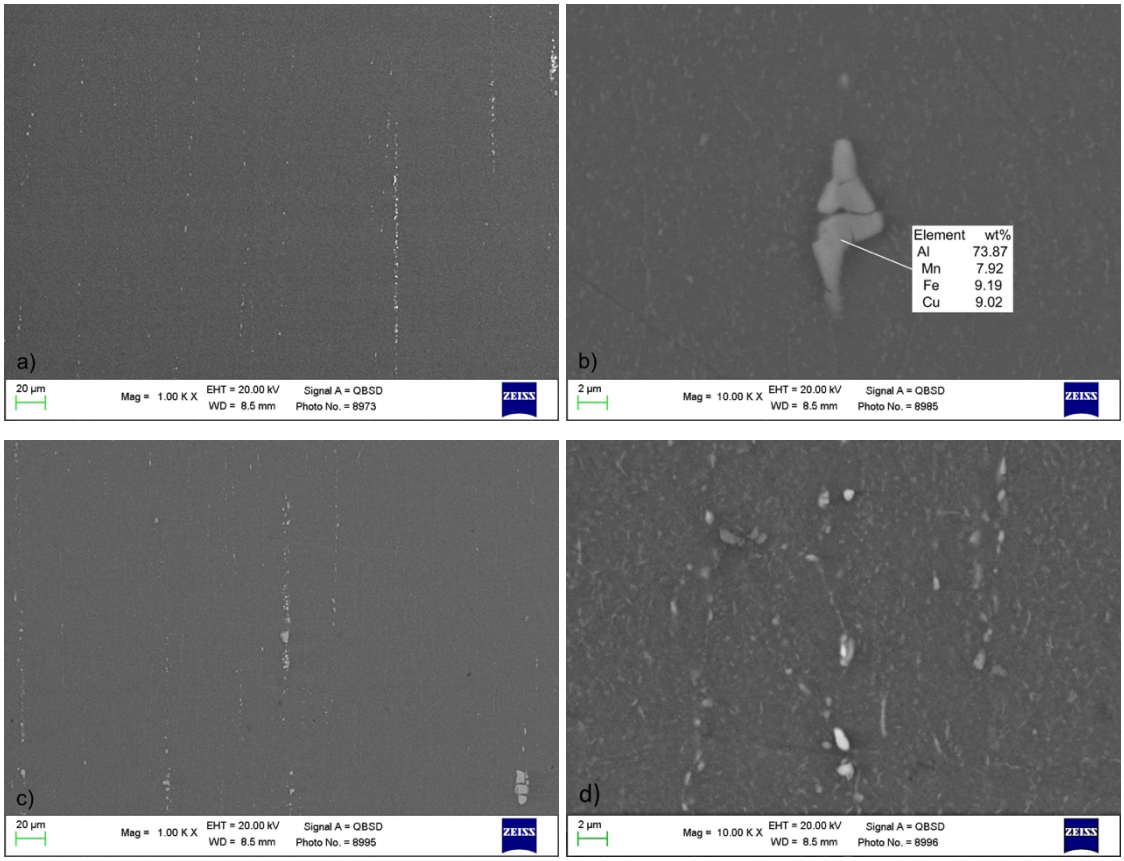

Fig.4.30: Low and high magnification SEM micrographs representative of: (a, b) T83 + 24h at 245°C condition; (c, d) T83 + 24h at 305°C condition.

Further details on the evolution of strengthening precipitates are offered by STEM investigations, focused on the same aforementioned conditions (no overaging, T83 + 24h at 245°C and T83 + 24h at 305°C). ADF-STEM images of each condition are displayed in Fig.4.31, where hardening precipitates are seen with bright contrast. Phases were identified based on morphology, orientation relationship with Al, and composition measured by EDS. The T83 condition contains mainly T_1 and ϑ' precipitates, which are coarsened by the overaging treatments. In agreement with both Kumar et al. [176] and Li et al. [145], who studied Al-Cu-Li alloys + 0.4wt% Ag, no evidence of Ω phases is detected at peak age. Moreover, no δ' precipitates were observed.

Even after prolonged exposure at high temperatures, the T_1 particles mostly keep their base thickness of about 1nm [37], which we see examples of after 24h of exposure at 245°C. The phase can however also thicken to multiple layers [172], but more commonly T_1 precipitates transform into Ω precipitates (which thickens more easily), as these two phases have very similar atomic structures [173]. After the 305°C heat treatment, all T_1 precipitates have disappeared, and a coarse microstructure of ϑ' and a few Ω precipitates remains. Some blob-like features are also visible in the images; these are agglomerates of Ag that stays behind on the sample surface while the sample is thinned by electropolishing.

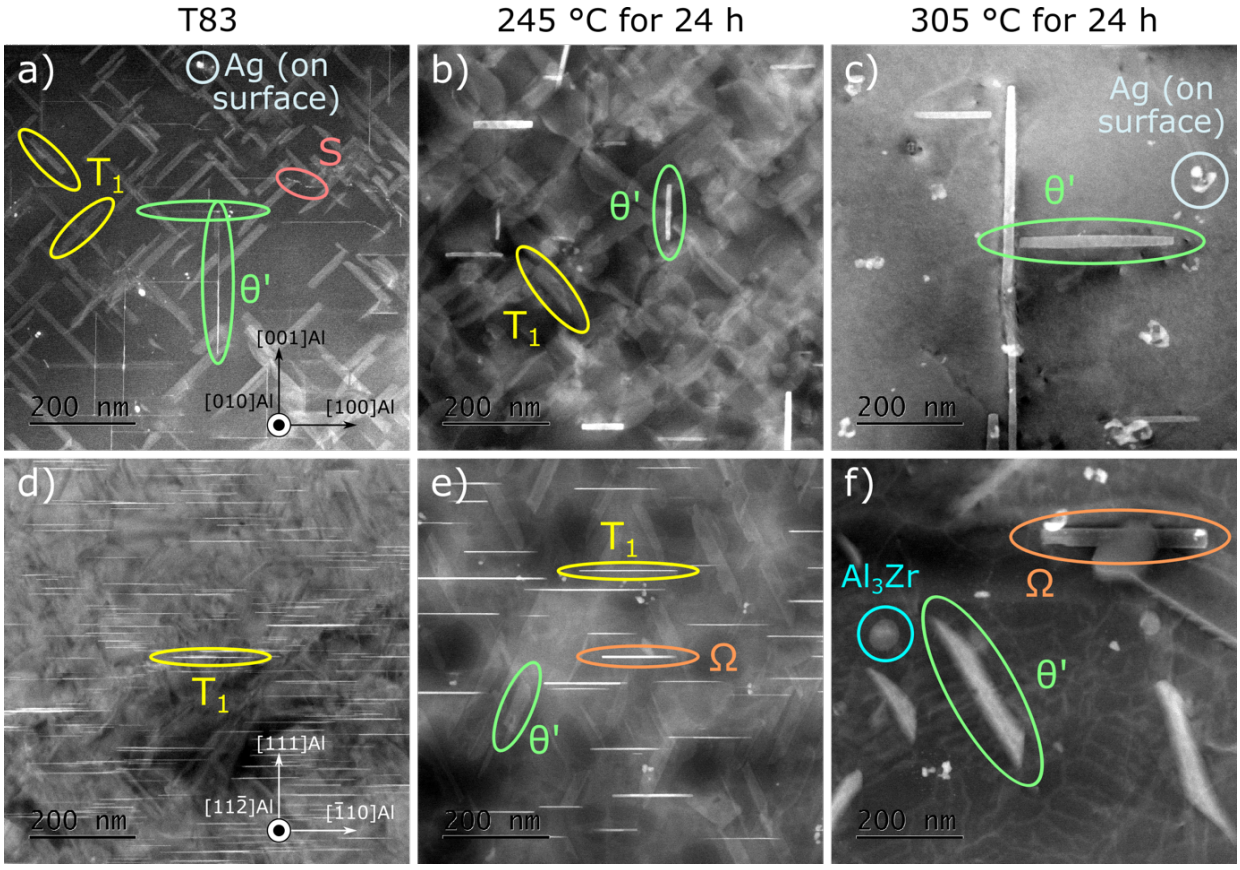

Fig.4.31: ADF-STEM images of alloy 2055 in three conditions: (a,d) T83, (b,e) T83 + 245°C for 24h, (c,f) T83 + 305°C for 24h. The samples are imaged in (a–c) the <001>$_{Al}$ zone axis and (d–f) the <112>$_{Al}$ zone axis. The different phases are highlighted with different colors (T_1 in yellow, ϑ' in green, S in red and Ω in orange.

The EDS map in Fig.4.32 supplements the STEM images by adding compositional information about the particles in the 24 h-305 °C condition. Starting from the top, Cu is found in a plethora of phases and is responsible for most of the contrast in the ADF-STEM images. The precipitates that only light up in the Cu map are almost certain to be of the ϑ' type, as the ϑ phase would be incoherent and very large. Some ϑ' particles are "tilted" and thus do not have the typical

$\{001\}_{\theta'}$ || $\{001\}_{Al}$ orientation relationship. This has been reported before in pure Al-Cu alloys [195]. The Ω phase contains Ag and Mg at their interfacial layers [196] and Zn has also been reported to segregate to these layers [197], as is visible in Fig.4.32(e-f). Further, Al_3Zr and Al-Cu-Mn-Fe dispersoids can be seen in Fig.4.32(g-i).

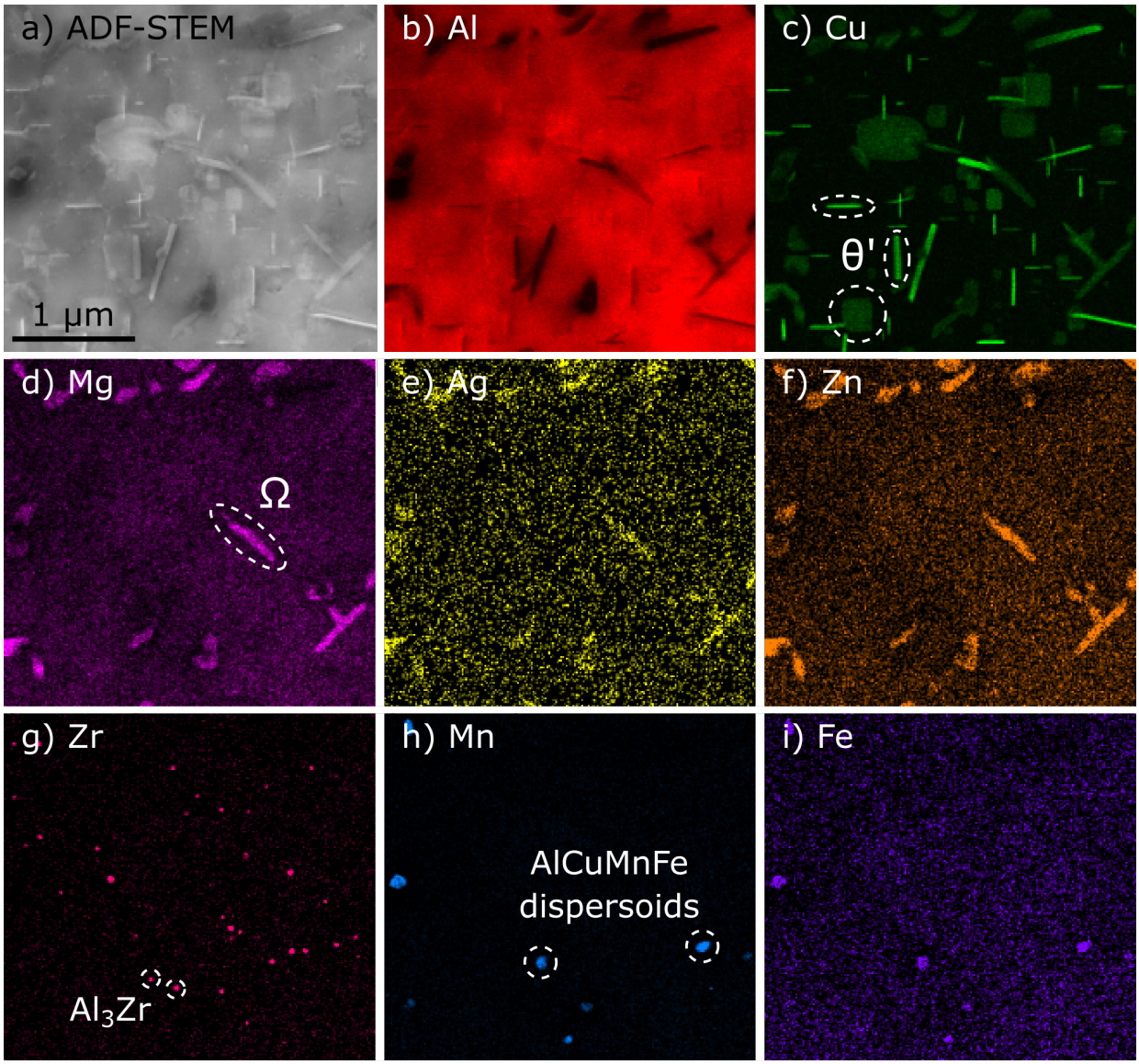

Fig.4.32: EDS maps of alloy 2055 subjected to T83 + overaging treatment at 305°C for 24h. Acquired in the <001>Al zone axis. (a) ADF-STEM image (b)-(i) characteristic X-ray peak (Kα) maps of all elements present in hardening precipitates and dispersoids.

Considering the microstructural evolution reported in [37] for AA2099, a solid comparison between AA2055 and AA2099 can be drawn. In the T83 condition, AA2055 exhibits a higher amount of both T_1 and ϑ' phases. A large amount of δ' precipitates was indeed observed in AA2099, sometimes as composite precipitates δ'-ϑ'-δ' (in agreement with [144,146,198]), which prevent ϑ' from rapid coarsening. After overaging for 24h at 245°C, the volume fraction of T_1

precipitates is almost maintained in AA2099, accompanied by the dissolution of the other strengthening phases such as S' and ϑ'. A completely different microstructural evolution occurs in AA2055, in which most of the T_1 precipitates undergo dissolution, favoring at the same time ϑ' coarsening and Ω precipitation. During overaging, the higher Cu/Li ratio of AA2055 makes ϑ' phase prevail against T_1 phase, while the reverse is true for AA2099.

Whereas the AA2055 alloy shows both ϑ' and Ω phases after 24h at 305°C, AA2099 microstructure after severe overaging is dominated by coarse and incoherent σ and T_1 phases.

Tensile tests

Representative stress-strain engineering curves for each investigated condition are reported in Fig.4.33 and provide an immediate overview of the overaging effects: the more severe the overaging conditions, the lower is the alloy performance. The average values of tensile parameters $R_{p0.2}$, UTS and total elongation to failure A_t% are shown in Table 4.11.

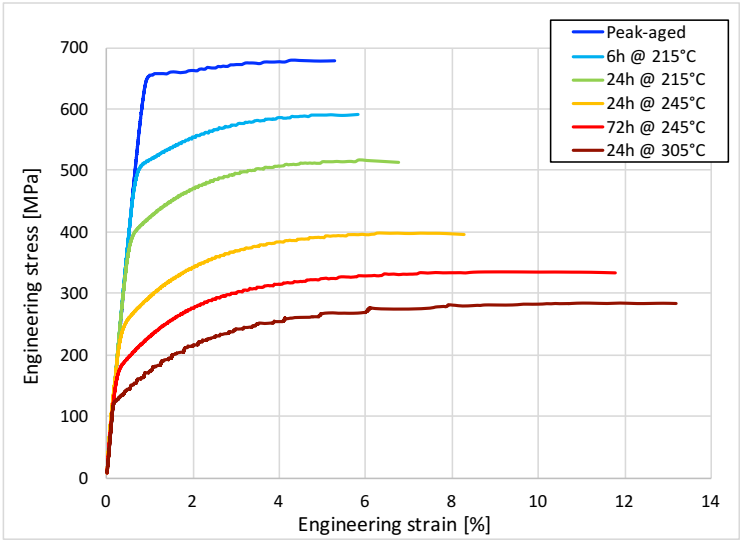

Fig.4.33: Stress-strain engineering curves representative of each investigated overaging condition.

Table 4.11: Overaging treatments performed on AA2055, residual hardness measured on tensile specimens and results of tensile tests (average ± 2 standard deviation).

Overaging	Residual hardness [HB]	$R_{p0.2}$ [MPa] ±2σ	$R_{p0.2}/\rho$ [MPa*cm^3/g]	UTS [MPa] ±2σ	A_t [%] ±2σ
No overaging	183 (T83)	653 (±6.8)	241.0	680 (± 0.3)	5.0 (±1.7)
6h @ 215°C	160	506 (±5.7)	186.7	590 (± 4.4)	5.5 (±1.2)
24h @ 215°C	145	404 (±6.3)	149.1	518 (±4.2)	5.8 (±0.8)
24h @ 245°C	112	260 (±6.3)	95.9	404 (±15.5)	7.7 (±0.4)
72h @ 245°C	93	189 (±7.6)	69.7	330 (±15.2)	11.6 (±0.7)
24h @ 305°C	85	135 (±1.0)	49.8	286 (±1.0)	12.8 (±0.2)

The average residual hardness and the average percentage reduction of tensile properties starting from the T83 condition are both markers of overaging and might be considered together. Fig.4.34a confirms that a continuous decay of mechanical properties occurs up to the 24h-305°C condition, consistently with the microstructural evolution highlighted in the previous section. Compared to the T83 condition, the most severely overaged samples experience a substantial reduction of R_m and $R_{p0.2}$ (-58% and-79% respectively), together with a considerable increase of elongation to failure (up to +150%). Fig.4.34b shows the actual values of R_m and $R_{p0.2}$ as a function of residual hardness for each tested sample. Both Fig.4.34a and Fig.4.34b reveal an extensive decrease of tensile properties while moving from the 24h – 215°C to the 24h – 245°C condition, the latter being encircled in red; such tensile data come along a significant decrease in the alloy residual hardness (-33HB). The softening is supported by the remarkable variation in microstructural features occurring after 24h at 245°C (Fig.4.31e), which mainly consists in a reduction of T_1 volume fraction. In agreement with Li et al. [145] and Deschamps et al. [159], T_1 precipitates contribute to the major strengthening effect compared to ϑ', S' or δ'.

It is also worth noticing that, in the T83 condition (characterized by 183 HB), the difference between ultimate tensile strength and yield strength is minimal (Fig.4.34b). By prolonging overaging, the degradation of $R_{p0.2}$ is always more pronounced with respect to R_m: this is a sign of the alloy tendency to strain hardening.

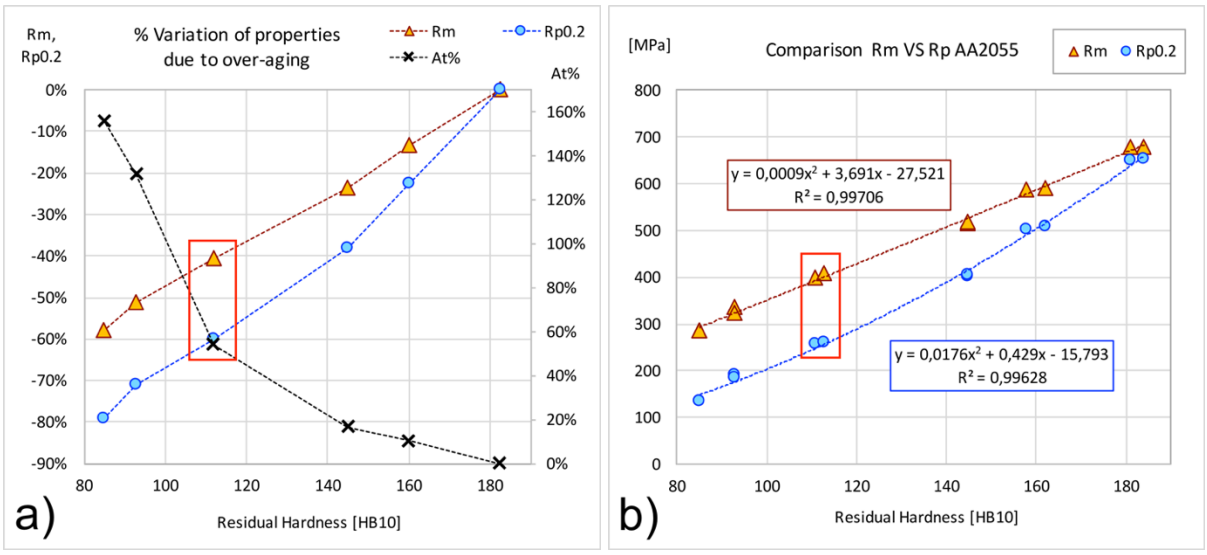

Fig.4.34: (a) Percentage variation of tensile properties, calculated as the average of 2 tensile tests for each condition. (b) Trend in Rm and Rp0.2 decrease with residual hardness, for each tested sample. Red boxes highlight the 24h-245°C condition in both (a) and (b).

In order to better highlight the strain hardening behavior of the alloy, the Hollomon's model [127] has been applied for each tested sample. The variation of Hollomon's strength coefficient K

and strain hardening exponent n with residual hardness has been investigated and polynomial functions have been chosen to correctly fit the experimental data, as reported in Fig.4.35. The following Hollomon's relationship was obtained (Eq.4.6), and the accuracy of K and n determination is demonstrated by the correct match between actual and modelled data reported in Fig.4.35b.

$$\sigma = (-0.0239\,HB^2 + 9.4479\,HB - 105.4) \cdot \varepsilon_{pl}^{\left(2\cdot 10^{-6}\,HB^2 - 0.0021\,HB + 0.3601\right)}$$

Eq.4.6: Predicted true stress as a function of true deformation and residual hardness in the plastic field, according to Hollomon's equation.

The trends of K and n are in good agreement with what reported in [37] and in [168], respectively with reference to AA2099 and AA2198. In the T83 state, the AA2055 microstructure (Fig.4.31a,d) is dominated by thin T_1 precipitates, which are sheared by dislocations during tensile tests. Their shareable nature [168,169] provides a negligible strain hardening exponent n. During overaging, however, the coarsening of precipitates (highlighted both in Fig.4.31 and Fig.4.32) induces a shift from Ashby to Orowan interaction between dislocations and precipitates. As reported in [168], precipitates by-passing produces the storage of dislocation in the form of Orowan loops, increasing the strain hardening capability of the alloy.

The analysis through Hollomon's equation highlights that a substantial decrease in the strength coefficient K occurs until 72h – 245°C (average residual hardness 92HB), which shows almost similar values compared to the 24h – 305°C conditions (average residual hardness 87HB); however, the strain hardening exponent n constantly grows up to the 24h – 305°C condition.

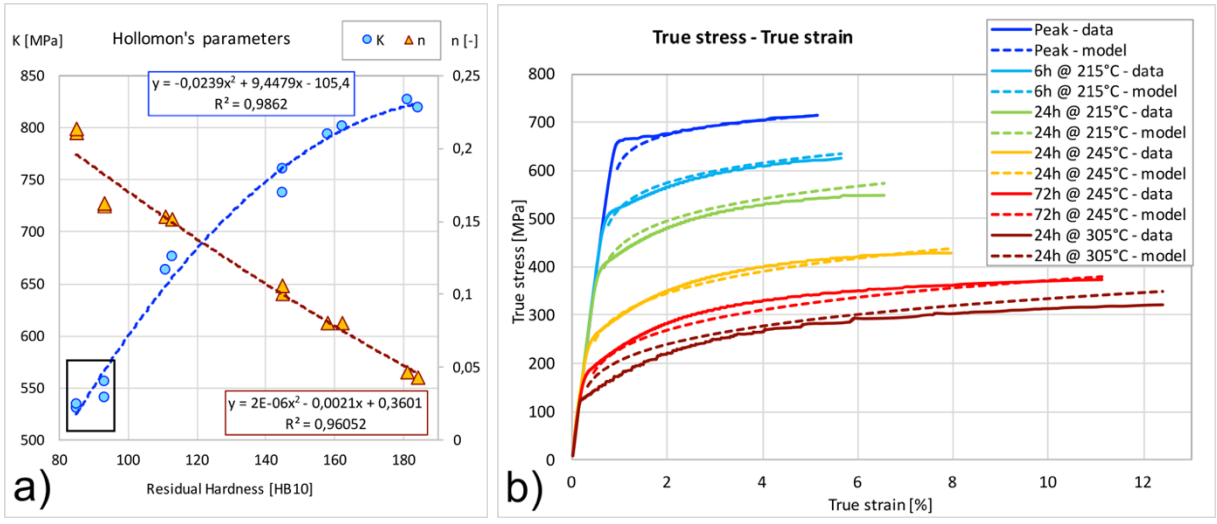

Fig.4.35: (a) Variation of Hollomon's parameters K and n with the residual hardness of the alloy, and polynomial fitting of data; the conditions T83 + 72 h at 245°C and T83 + 24h at 305°C are highlighted. (b) Actual true stress- true strain curves (solid line), compared to the modelled true stress true strain curves (dashed line), according to Hollomon's equation.

SEM investigations of the fracture surfaces (Fig.4.36) reveal a clear transition in the fracture mode due to overaging occurrence. In the T83 condition (Fig.4.36a), few fine dimples are clearly visible, but surrounded by faceted edges, without evident plastic deformation; in all probability, the latter areas marked the interface with the coarse secondary phases in the original sample (Fig.4.29b,c). The fracture surface is consistent with the limited elongation to fracture (5%) characterizing the peak-aged sample (Table 4.11). A slight change both in A_t% (5.8%), in the tensile properties and in the fracture surface (Fig.4.36b) is observable in the 24h – 215°C overaged sample: fine dimples in fact cover a wider portion, revealing an increased plasticity; moreover, the sharp contours are smoothed by plastic deformation burrs. The trend continues while moving towards the 24h – 245°C condition (Fig.4.36c), up to the most overaged 24h – 305°C (Fig.4.36d). In the latter, the dimples cover the whole surface and it is not possible to distinguish the original location of the secondary phases. It is evident that, due to prolonged overaging, the Al matrix becomes progressively weaker than the interface with the secondary phases, causing rupture inside the matrix itself.

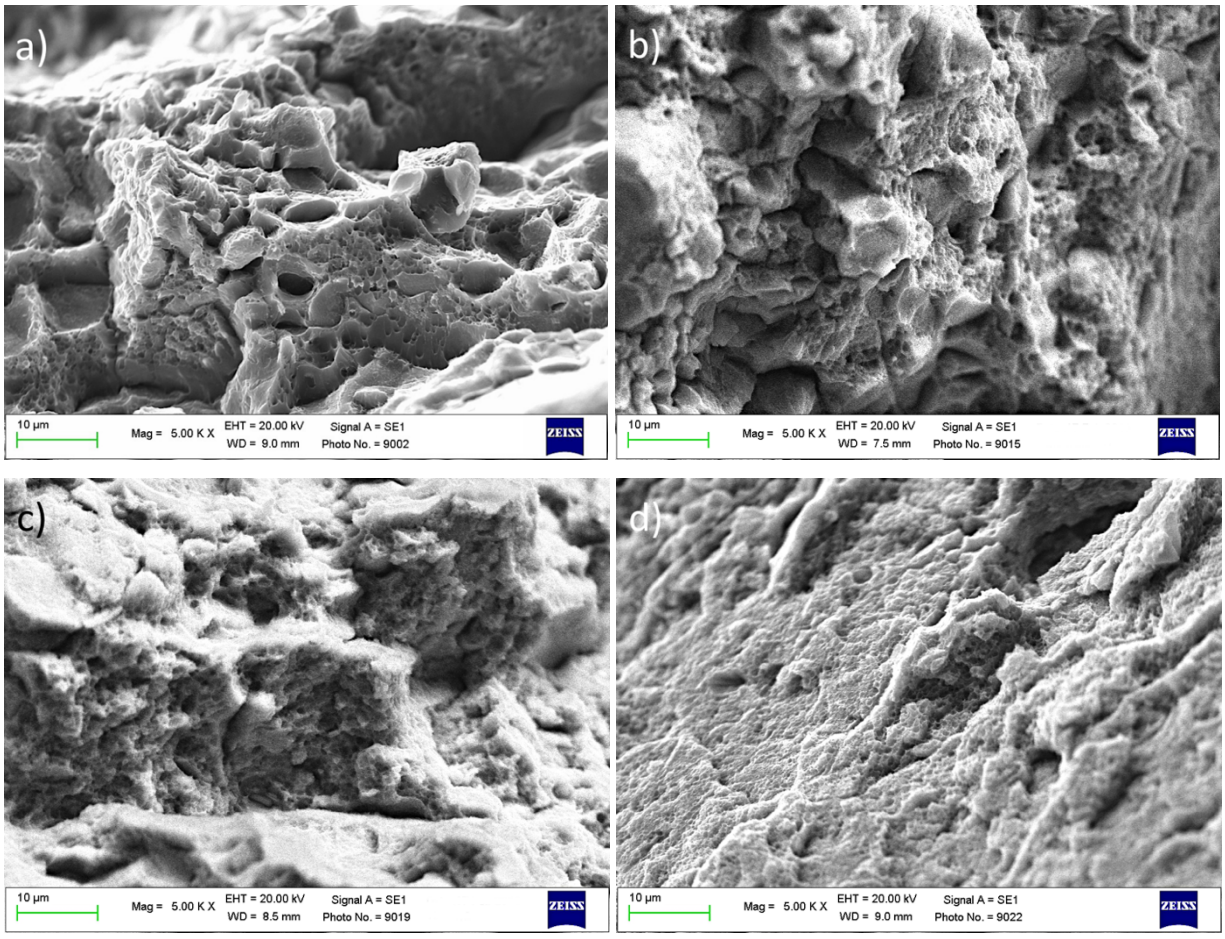

Fig.4.36: SEM micrographs of fracture surface of tensile samples, respectively in the: (a)T83; (b) T83 + 24h-215°C; (c) T83 + 24h-245°C; (d) T83 + 24h-305°C condition.

Fig.4.37 compares the tensile properties of AA2055 to those of AA2099, numerically reported in Table 4.12 and taken from [37]. In all overaging conditions, $R_{p0.2}$ and R_m characterizing AA2055 are higher or at least comparable to those of AA2099, which was however considered in [37] a viable alternative to the conventional AA2618 Al-Cu alloy, specifically developed for high temperature applications.

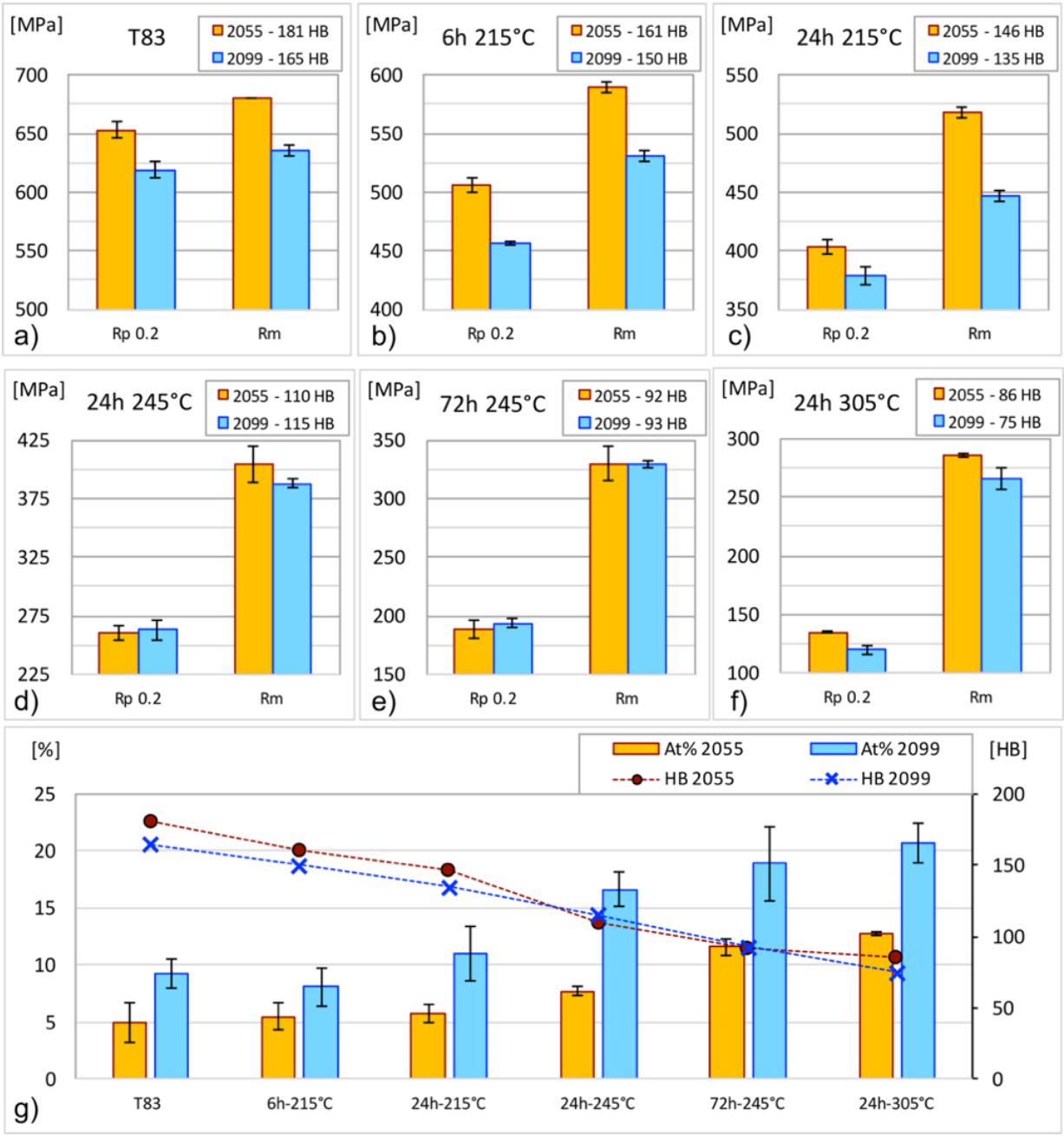

Fig.4.37: (a-f) Comparison between AA2055 and AA2099 tensile properties (the latter from [37]) in the investigated overaging conditions, respectively: (a) no overaging (T83), (b) T83 + 6h at 215°C, (c) T83 + 24h at 215°C, (d) T83 + 24h at 245°C, (e) T83 + 72h at 245°C, (f) T83 + 24h at 305°C. (g) Comparison between AA2055 and AA2099 elongation at fracture in each overaging condition, coupled with an overview on the alloys residual hardness.

Table 4. 12: Overaging treatments performed on AA2099, residual hardness measured on tensile specimens and results of tensile tests (average ± 2 standard deviation) from [37].

Overaging	Residual hardness [HB]	$R_{p0.2}$ [MPa] ±2σ	$R_{p0.2}/\rho$ [MPa*cm^3/g]	UTS [MPa] ±2σ	A_t [%] ±2σ
No overaging	165	619 (±7.2)	235.4	635 (± 4.7)	9.3 (±1.3)
6h @ 215°C	150	457 (±1.3)	173.8	531 (± 5.1)	8.1 (±1.7)
24h @ 215°C	135	379 (±2.1)	144.1	447 (±2.0)	11 (±2.4)
24h @ 245°C	115	263 (±8.2)	100.0	388 (±3.3)	16.6 (±1.5)
72h @ 245°C	93	194 (±4.2)	73.8	329 (±3.1)	18.9 (±3.3)
24h @ 305°C	75	120 (±3.7)	45.6	266 (±9.2)	20.7 (±1.7)

In the T83 condition (no overaging), AA2055 performance is superior with respect to AA2099; this characteristic might be attributed to the substantially higher amount of T_1 phases compared to AA2099, the latter being strengthened both by T_1 and δ' precipitates. In this state, considering the diverse densities, the specific strength of AA2055 (R/ρ) is however higher than that of AA2099.

In the initial stages of overaging (soaking at 215°C for 6h and 24h), the difference in the alloys performance is increased: this is probably due to the dissolution of δ' phases in AA2099, which are known to be extremely sensitive to thermal exposure [37,180].

The properties of the two alloys are indeed equivalent after a thermal exposure at 245°C for 24h or 72h (Fig.4.37d, e), exactly when the alloys are characterized by comparable residual hardness. After 24h at 245°C, AA2055 is strengthened by coarsened θ', Ω and T_1 precipitates (the latter being however considerably lowered in volume fraction with respect to the T83 state, favoring Ω formation), whereas AA2099 microstructure is dominated by T_1. The balance between these precipitates provide the same strengthening effects in both alloys. The tensile properties decrease to the same extent after soaking for 72 h at 245°C: the prolonged thermal exposure is expected to partially dissolve the T_1 phases in both alloys, preparing the formation of the σ phases in AA2099, whilst further enhancing Ω and θ' coarsening in AA2055.

In the T83 + 24h – 305°C condition, a slight difference between the alloys performance is perceivable (Fig.4.37f). The θ' and Ω phases, dominating the AA2055 overaged microstructure, better obstruct dislocation movements compared to the combination of the extremely coarsened T_1 and σ phases characterizing AA2099. The comparison between the high temperature resistant 2618 Al-Cu alloy and the lightweight 2099 Al-Cu-Li alloy, reported in [37], can be therefore further extended to the AA2055 Al-Cu-Li-Ag alloy, underlining that AA2055 exhibits the highest RT mechanical properties after 24h of aging at 305°C.

From Fig.4.37g, it is possible to state that AA2099 always shows a notably higher ductility, with a nearly double elongation to failure in all investigated conditions. This characteristic is consistent with the higher amount and coarser size of secondary phases in AA2055 compared to AA2099 [37]. During overaging, both alloys also show a similar transition from a mixture of brittle and ductile fracture mode in the T83 condition towards a completely ductile fracture surface in the severe overaging conditions. Consistently with the diverse elongation to failure, the fracture surfaces in the T83 condition are however visibly different, since a nearly intergranular fracture is observable in AA2099, while AA2055 fracture is evidently produced by a progressive rupture in correspondence of the interface with secondary phases (Fig.4.36a), which significantly lowers the total extension at fracture A_t.

4.4.4 Conclusions

The effects of overaging on the lightweight, non-conventional Al-Cu-Li-Ag AA2055 alloy, treated to the T83 condition, have been investigated through both hardness and tensile tests at room temperature (RT), aiming to preliminarily assess the thermal stability of the alloy. Moreover, the AA2055 behavior has been compared to a similar alloy belonging to the third generation Al-Li alloys, namely the AA2099, which is characterized by a higher amount of Li (lower density), a lower Cu/Li ratio and does not contain Ag, which is indeed known to increase the thermal resistance of Al-Cu alloys. The following conclusions can be drawn:

- In the T83 state, AA2055 is dominated by fine T_1, ϑ' and S precipitates, which provide extremely attractive tensile properties, superior to AA2099. In some circumstances, it can still be beneficial to use of the latter alloy for lightweight structural components, given its higher specific strength. The strain hardening capability of AA2055 is approximately zero, due to the shareable nature of strengthening precipitates.
- Prolonged thermal exposure causes a significant microstructural evolution in AA2055. As well as ϑ' precipitates, also T_1 slightly coarsen, but above all their substantially reduced volume fraction is thought to be the main responsible of the significant reduction of RT tensile properties. Part of the T_1 precipitates evolves into Ω phases, while S precipitates dissolve. The tensile properties of AA2055 and AA2099 tend to become similar upon

overaging. The strain hardening exponent of AA2055 alloy increases due to the coarsening of precipitates.

- In the most severe overaging condition currently investigated (T83 + 24h at 305°C), the alloy performance is considerably reduced compared to the peak hardness condition. The microstructure exhibits several coarse θ' and Ω precipitates, the latter formed and coarsened at the expenses of T_1. No T_1 phases were detected in this overaging state. In this condition, the RT tensile properties of AA2055 are higher than AA2099, providing a superior specific strength. In view of this, the alloy seems to be a promising candidate for high temperature applications requiring lightweight.
- The presence of up to 0.7wt% of Ag and the higher Cu/Li ratio of AA2055, compared to AA2099, have been proven to destabilize T_1 precipitates during overaging, enhancing at the same time the formation and coarsening of Ω and θ' precipitates. However, a major strengthening effect is provided by the interaction of Ω and θ' phases in AA2055 compared to the interaction of σ and T_1 in AA2099.

4.5 High temperature tensile tests of the lightweight 2099 and 2055 Al-Cu-Li alloy: a comparison

[The whole Sect. is taken from the published paper whose title is shown below, made available by Springer Nature License Number 4524860299577]. Most of the details about AA2099 and AA2055 discussed in the Introduction Sect. have been already reported in the previous Sect.4.3.1 and Sect.4.4.1.]

JOM
https://doi.org/10.1007/s11837-018-3006-x

ALUMINUM: NEW ALLOYS AND HEAT TREATMENT

High Temperature Tensile Tests of the Lightweight 2099 and 2055 Al-Cu-Li Alloy: A Comparison

E. BALDUCCI,[1,4] L. CESCHINI,[2] and S. MESSIERI[1,3]

1.—Department of Industrial Engineering, Alma Mater Studiorum University of Bologna, via del Risorgimento 2, Bologna, Italy. 2.—Department of Civil, Chemical, Environmental and Materials Engineering, Alma Mater Studiorum University of Bologna, via del Risorgimento 2, Bologna, Italy. 3.—Ducati Motor Holding, Bologna, Italy. 4.—e-mail: eleonora.balducci6@unibo.it

Abstract

The present study deals with the high temperature characterization of the unconventional, lightweight AA2099 and AA2055 Al-Cu-Li alloys (density equal to 2.63g/cm^3 and 2.71g/cm^3 respectively), which are widely employed for aerospace structural components thanks to their high specific strength at room temperature. The alloys have been characterized through tensile tests at 200°C and 250°C, after different overaging heat treatments, with the aim to simulate the variation of mechanical properties occurring in a component operating at high temperature. At 200°C, AA2099 alloy shows equivalent or superior performance compared to AA2055, therefore it exhibits advantages in terms of specific strength due to its lower density; T_1 precipitates, dominating AA2099 after overaging, are considered to provide effective strengthening. The reverse occurs at 250°C operating temperature, at which considerable improvements are offered by the combination of both Ω and θ' precipitates, which are present in AA2055 matrix in all overaged conditions.

Keywords

Al-Cu-Li alloy; High temperature; Overaging; Tensile test; Cu/Li ratio; Microstructure.

4.5.1 Introduction

AA2099 and AA2055 belong to the 3rd generation of Al-Li alloys and were patented by Alcoa respectively in 2003 and 2012 [36]. Thanks to Li addition, which is known to significantly reduce density while increasing Young's elastic modulus [35,36,171], these alloys exhibit low density (2.63g/cm^3 and 2.71g/cm^3 respectively [182,183]) combined with excellent mechanical properties, superior to any conventional Al alloy. This characteristic, together with the possibility to use standard production processes, makes them widely used for structural aerospace applications and considerably attractive in any field where resistance and lightweight are a requirement, such as in the automotive field where the race to boost fuel economy is getting extremely demanding [199].

As regards Al-Cu-Li alloys in general, Li is fundamental to provide a high specific strength. After solution, quenching and artificial aging, Al alloys with high Li content reveal a microstructure dominated by coherent δ' precipitates (Al_3Li), which however have been considered as the main responsible of the poor thermal stability of Al-Cu-Li in terms of fracture toughness [36,143,200]. Like Li, Cu additions provide both solid solution strengthening and precipitation strengthening, since Cu is involved in the formation of T_1 (Al_2CuLi) and θ' (Al_2Cu) precipitates. T_1 precipitates (Al_2CuLi), in particular, offer the major contribution to the alloy strengthening [36,143,146,168,201] and recent STEM investigations confirmed these precipitates are among the most thermally stable in Al-Cu-Li alloys when exposed at temperature higher than 200°C [37]. The formation of T_1 at the expenses of δ' precipitates (and θ' due to the lower Cu available) is known to be favored by a strain field [36,143–147,177,201] and high Cu/Li ratio [144,145], which makes both cold stretching prior to aging (typical T8 heat treatment) and balance of alloying elements two key issues to enhance Al-Cu-Li alloys performance. Moreover, specific amounts of alloying elements such as Zn, Mn, Zr, Mg, Ag can be added in order to tailor the alloy properties: Zn enhances corrosion resistance; Mn and Zr are added to control recrystallization during thermo-mechanical processing; both Mg and Ag provide solid solution and precipitation strengthening, and are also known to increase T_1 precipitation kinetics, segregating to the precipitates interface [36,148,192,193,201–203].

Several papers investigating Al-Cu-Li microstructural features after specific heat treatments or minor elements additions are available in literature [148,176,192,198,204–207]. Focusing in specific on AA2099 and AA2055 alloys, characterized respectively by low and high Cu/Li ratio, recent investigations by the authors [37,38] highlighted a few differences in the T83 state, namely the higher amount and density of both T_1 and ϑ' precipitates and the lack of δ' precipitates in AA2055 compared to AA2099. Both results are in agreement with Decreus et al. [144], who studied the effects of different Cu/Li ratio by comparing AA2198 and AA2196 alloys, chemically similar to AA2055 and AA2099 respectively: after artificial aging, no presence of δ' was found in the higher Cu/Li ratio alloy (AA2198); moreover, T_1 nucleation exhibits a lower incubation time in AA2198 alloy, providing a higher amount of T_1 precipitates compared to AA2196. This characteristic also turns into a slower coarsening rate and dissolution time of T_1 phases in AA2196 compared to AA2198 alloy during overaging (as highlighted in [38] for AA2099 and AA2055 respectively).
Data are further confirmed by Khan et al. [206], who focused the attention on two Al-Cu-Li alloys, plus Mg additions and Mg+Ag additions. The addition of the solely Mg (similarly to 2099) was found to retard the formation of GP zones and consequently ϑ' precipitates formation in the silver-free alloy, providing the presence of δ', T_1 and curved-shaped S' precipitates (Al_2CuMg) in the peak-aged condition. In the Al-Cu-Li alloy with Mg+Ag additions (similarly to 2055), however, the formation of Ag-Mg and Ag-Li co-clusters was favored, reducing the amount of Li and Mg available to trap vacancies, therefore favoring ϑ' formation with respect to T_1. Besides ϑ', T_1 and S' precipitates, hardly any δ' phases were visible, due to their dissolution in favor of T_1. The same is supported by Araullo-Peters et al. [203], whose atom probe analyses highlighted the presence of T_1, ϑ', S' precipitates, nucleating in proximity of dislocation loops, in the peak aged AA2198 alloy, chemically similar to AA2055; in this case, due to the high Cu/Li ratio, no δ' phases were observed, even in the early stage of the aging process.

To the best of the authors' knowledge, however, a very few studies deals with the effects of overaging on both microstructural evolution and degradation of mechanical properties of Al-Cu-Li, and most of them investigated the effects of thermal exposure below 200°C, which means that their results are hardly applicable in the study of automotive components operating at higher temperatures. A few of these researches are focused on the study/optimization of aging treatments, therefore often incur in overaging [146,152,155,176]; most of them, however, is focused on the effects of long term aging at low temperature [154,159,176,180,181,200], which occurs during the lifecycle of aerospace components due to aerodynamic heating. All of these

studies agree on the poor thermal stability of δ' precipitates. In particular, Katsikis et al. [200] investigated thermal exposure at 70°C up to 1000 h, Deschamps et al. [159] analyzed the effects of long term aging at 85°C up to 3000h, Davydov et al. [180] focused on the effects of soaking at 85°C and 95°C up to 1000h and 300h respectively, Mou et al. [181] analyzed the effects of prolonged (7000h) thermal exposure up to 163°C, finally Ortiz et al. [154] examined the effect of prolonged thermal exposure (1000h) up to 177°C, highlighting the significant reduction of tensile properties, but no attention has been given to microstructural features.
In addition to that, Jabra et al. [156] showed the consequences of overaging on Al-Cu-Li alloys at temperatures as high as 290°C, revealing a consistent decay of tensile properties, coupled with an increase of the elongation to failure. A brief inset on overaging of AA2198 alloy is also offered by Ovri et al. [208], who reported a substantial decay of properties and microstructural evolution after 10h at 370°C.

Only recently, however, the effects of overaging on both AA2099 and AA2055 in the range 200-300°C were systematically studied by the authors [37,38], through both SEM and STEM microstructural investigations and room temperature tensile tests after thermal exposure. The results of overaging tests seem promising, however mechanical testing at the operating temperature of interest is required to completely evaluate the possibility to expand the range of application of AA2099 and AA2055 at high temperature, or to determine if one of these alloys should be preferentially adopted at high temperature. The present paper aims to fill this gap and deals therefore with tensile tests at 200°C and 250°C of both AA2099 and AA2055 alloys. The results have been compared and discussed, with the aim to link the difference in mechanical properties to the difference in chemical compositions, or better to the presence of diverse precipitates. This is also considered an essential step to tailor the alloys chemical composition and heat treatment for specific applications at high temperature.

4.5.2 Material and methods

Both AA2099 and AA2055 Al-Cu-Li alloys were provided by Alcoa in the T83 condition (solution treatment, quenching, 3% stretching at room temperature, followed by artificial aging), in the form of extruded bars with 85 and 120mm diameter respectively. The chemical composition limits, provided by the supplier, are reported in Table 4.13; it can be noticed that the main

difference between the alloys is the dissimilar Cu/Li ratio and the relevant presence of Ag in the solely AA2055.

Table 4.13: Chemical composition limits [wt%] of AA2099 and AA2055; range of Cu/Li ratio AA2099 = 1.2-1.9, while AA2055 =2.5-4.2.

Alloy	Cu	Li	Zn	Mn	Mg	Ti	Zr	Fe	Ag	Al
2099	2.4-3.0	1.6-2.0	0.4-1.0	0.1-0.5	0.1-0.5	0.1	0.05-0.12	0.07	/	Bal.
2055	3.2-4.2	1.0-1.3	0.3-0.7	0.1-0.5	0.2-0.6	0.1	0.05-0.15	0.1	0.2-0.7	Bal.

Aiming to evaluate the suitability of these alloys for high temperature applications, tensile tests have been carried out at 200°C and 250°C, in slightly, middle and extremely overaged conditions. It is in fact widely known that heat treated Al alloys, when exposed at temperature above 200°C or more, undergo overaging. The phenomenon consists in a diffusion-controlled coarsening of strengthening precipitates, which finally lose their coherency with Al matrix, resulting in loss of strength both at room and high temperature. The variation of hardness during overaging treatments is able to keep track of these microstructural changes and to quantify their effects in terms of degradation of mechanical properties. In previous studies by the authors [37,38], a relationship between residual hardness and residual tensile properties at room temperature has been established for both AA2099 and AA2055. In addition to overaging, however, high temperature itself is responsible of lowered mechanical properties, since it induces a higher mobility of dislocations [209,210]. Testing the alloy at high temperature under different overaging conditions allows therefore to *fully* simulate the variation of mechanical properties in a component operating at high temperature.

For the purpose, before tensile tests, AA2099 and AA2055 samples were subjected to the following overaging heat treatments which are considered suitable to study the mechanical properties of a component operating up to 300°C: (i) 6h at 215°C, (ii) 24h at 215°C, (iii) 24h at 245°C, (iv) 72h at 245°C, (v) 24h at 305°C. Previous studies by the authors [37,38] confirm that these overaging conditions are able to produce classes of residual hardness evenly spaced between the typical T83 hardness and the minimum residual hardness detected at 305°C, and report the related variation of RT tensile properties.

In particular, at least 2 specimens were tested for each combination of alloy (2099-2055), test temperature (200°C-250°C), and overaging condition (from 6h@215°C, up to 24h@305°C). The tensile samples geometry is shown in Fig.4.38. During the overaging treatments, the samples temperature was controlled by a K-type thermocouple, allowing ± 2°C variation of the targeted

temperature. As for the tensile tests, a tensile testing machine with threaded grips, equipped with a resistance heated furnace, was adopted. In order to make sure that a homogeneous temperature field was reached in the sample, at least 2h of holding was required for each test; holding time was however adjusted for each test in order to reach the required test temperature at the specimen center, where a K type thermocouple was installed (as indicated in Fig.4.38). Finally, tensile test parameters were defined according to EN ISO 6892-2: 2009 standard, with a strain rate set equal to $3.3x10^{-3}$ s^{-1}; proof strength ($Rp_{0.2}$), ultimate tensile strength (UTS) were evaluated according to EN ISO 6892-1: 2009 standard.

For both alloys, data have been processed with the aim to accurately establish the relationship between the average values of UTS, $Rp_{0.2}$ and residual hardness, at the specific test temperature. Residual hardness was measured by micro-Vickers hardness tests, with 1kg load and 10s dwell time. For each tensile sample, 4 micro-Vickers indentations were performed on a section of the gauge length after testing, providing an average of 8 measurements for each combination of alloy, overaging condition and test temperature. The measured hardness values are the result of both overaging treatment and soaking at the specified temperature during tensile tests, therefore they are not directly comparable with hardness values reported in [37,38] after the solely overaging treatment.

Finally, tensile test data were considered together with STEM and SEM microstructural investigations presented in [37,38], in order to assess how the density, size and type of precipitates affect the alloys mechanical properties at high temperatures.

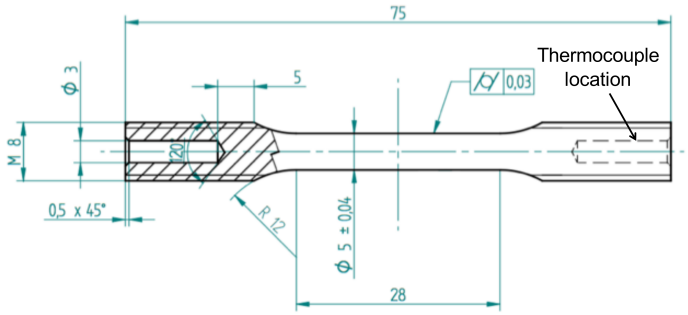

Fig.4.38: Geometry and dimensions [mm] of tensile specimens.

4.5.3 Results and discussion

For each overaging condition and each alloy, representative tensile curves at 200°C and 250°C are respectively reported in Fig.4.39a and Fig.4.39b. It is also fundamental to consider the

combination of tensile properties and residual hardness, as graphically reported in Fig.4.40, in order to better evaluate the alloys response at high temperature. In the following paragraphs, a separate discussion is reserved for the different test temperatures.

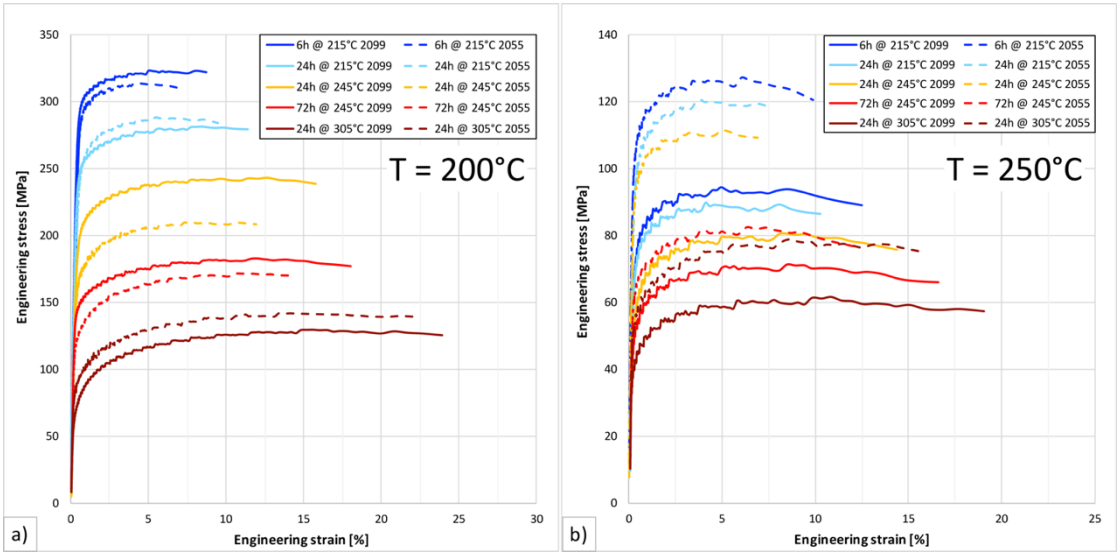

Fig.4.39: Comparison between engineering stress-strain curves of AA2099 and AA2055 Al-Cu-Li alloys at 200°C, previously subjected to different overaging conditions.

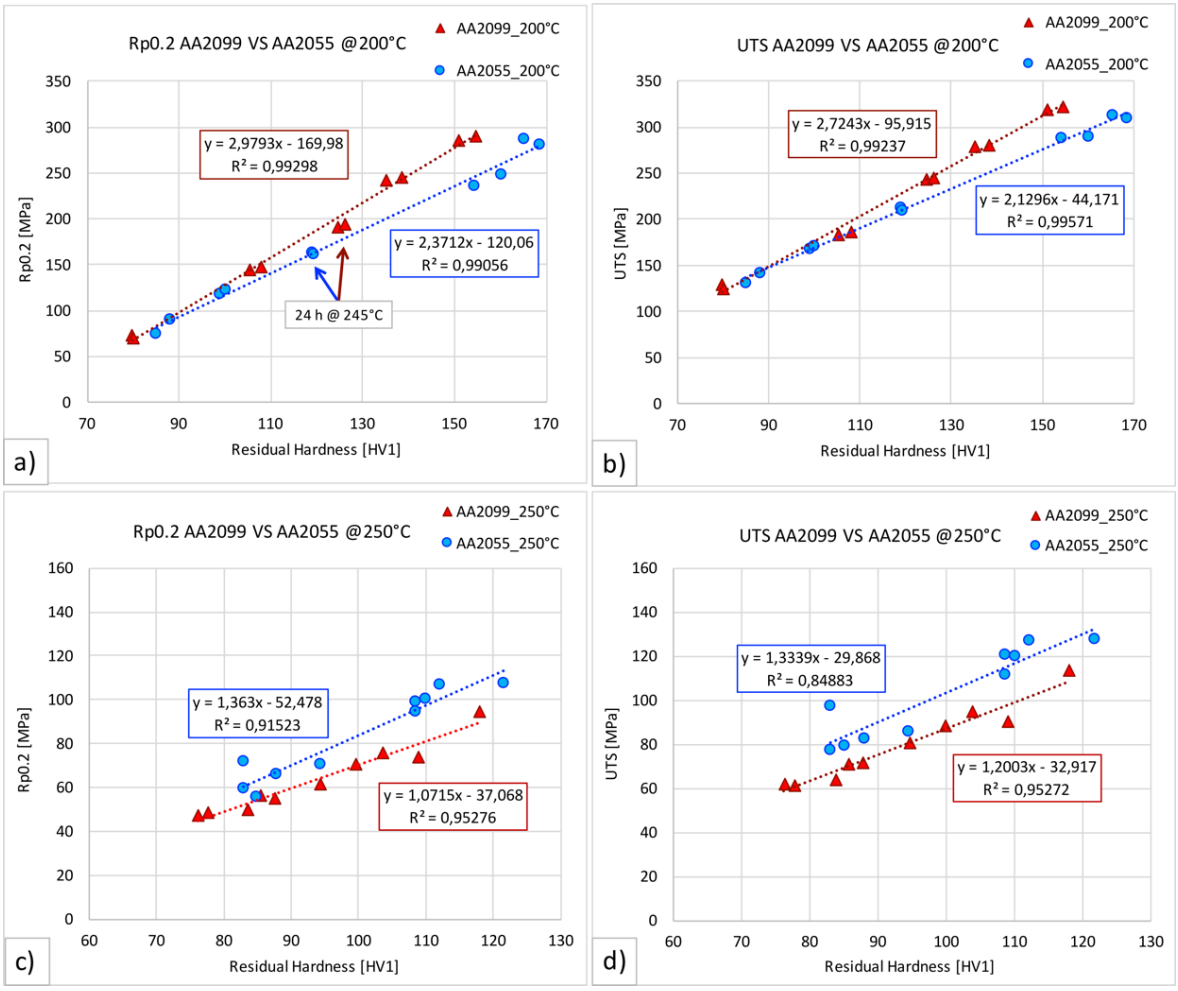

Fig.4.40: Comparison between tensile properties of AA2099 and AA2055 Al-Cu-Li alloys: (a), (b) at 200°C, (c), (d) at 250°C.

Tensile tests at 200°C

In the slightly overaged conditions investigated (6h and 24h at 215°C), it can be noticed that the tensile curves at 200°C seem overlapping in terms of yield strength, while the variation of tensile properties increases in the middle overaged condition (24h at 245°C), showing the benefits of AA2099 (solid line) compared to AA2055 (dashed line); finally, the difference tends to be reduced for prolonged overaging at 245°C (72h at 245°C), and even a reversal trend occurs when it comes to the fully overaged condition (24h at 305°C). This trend suggests the better performance of AA2055 under severely overaged conditions. Also, the lower elongation at fracture of AA2055 is perceivable in all the investigated conditions, due to the higher amount of coarse secondary phases (Al-Cu based particles in addition to Al-Cu-Fe-Mn dispersoids, as highlighted in [38]).

Slightly, middle and extremely overaged conditions are separately analyzed in the subsequent sections with reference to the relationship between residual hardness and tensile properties (Fig.4.40a,b), comparing AA2099 and AA2055 behavior and microstructural evolution.

6h and 24h at 215°C overaging + soaking for high temperature tensile tests

In the slightly overaged conditions, in agreement with [37,38] and with Fig.4.40 (a), (b), the AA2055 alloy shows considerably higher residual hardness, which is however not supported by considerably higher tensile properties at 200°C. This characteristic unequivocally shows the potentiality of a higher Li content (characterizing AA2099) in solid solution strengthening and above all of Li-based δ' and T_1 precipitates in enhancing both R_p and UTS, even at high temperature.

With reference to [37], in fact, AA2099 residual hardness falls in between the range characterizing T83 and T83 + 24h @245°C conditions, investigated through STEM analyses reported in Fig.4.22 (a), (d) and (b), (e) respectively. In this range of residual hardness, the microstructure evolves from the presence of fine T_1, δ', θ', co-precipitated δ'-θ'-δ' (also highlighted in [37,142,144,146]) and S precipitates, characterizing the T83 state, as highlighted in Fig.4.22 (a), (d), up to the presence of the solely T_1 phases, yet coarsened, characterizing the alloy overaged at 245°C for 24h, as reported in Fig.4.22 (b), (e). After soaking for 6h at 215°C, δ' phases are thought to be still present in the matrix, though coarsened, as well as θ', S and T_1 precipitates. After soaking for 24h at 215°C, δ' phases are in all probability starting their dissolution process, favoring T_1 coarsening: δ' and δ'-θ'-δ' composite precipitates are reported to completely vanish after 72h at 200°C [146], or 24h at 245°C [37], while T_1 phases still strengthen the matrix. Also S precipitates are supposed to evolve, however they are more coarsening resistant compared to δ' or δ'-θ'-δ'

and are reported to remain stable after 72h at 200°C [146]. S phases are therefore supposed to still be present in the matrix after 24h soaking at 215°C, contributing to AA2099 strengthening, besides moderately coarsened T_1 phases and a significantly reduced amount of δ' and δ'-ϑ'-δ' composite precipitates.

As regards AA2055 alloy, the references for microstructural evolution are STEM investigations on AA2055 alloy in the T83 – T83 +24h @245°C [38], reported in Fig.4.31 (a), (d) and (b), (e). Differently from T83 AA2099, which contains a huge amount of both δ', ϑ', S and T_1 phases, the AA2055 in the T83 condition is characterized by the presence of a high amount of finely dispersed T_1 phases, ϑ' streaks and tiny, curved S precipitates. It should be pointed out that no δ' phases are detected in AA2055 alloy even in the peak aged condition (in agreement with the results by Li et al. [145] for high Cu/Li ratio), therefore AA2055 properties do not take advantage of these fine and coherent precipitates as AA2099 does in the slightly overaged conditions. This characteristic explains the (moderately) superior performance of AA2099 at 200°C after 6h soaking at 215°C.

As pointed out by Fig.4.31 (b), (e), soaking at 245°C for 24h leads AA2055 microstructure to evolve towards a considerably reduced amount of coarsened T_1 phases, thicker ϑ' phases and an increasing amount of Ω phases. In agreement with Bai et al. [185], in Al-Cu-Mg-Ag alloys the competitive precipitation of Ω and ϑ' phase occurs, the former being characterized by weakest precipitation kinetics and being therefore disadvantaged. The semi-coherent Ω phase is however known to exhibit a greater strengthening ability compared to ϑ' phase [184,189]. Once the precipitation kinetics is activated, Ω phases tend to replace T_1 phases [173]. The substitution of Ω for T_1 is thought however to be at the very initial stages after 24h soaking at 215°C, so its effects are not clearly perceivable in terms of strengthening reduction: tensile properties of AA2055 and AA2099 alloys are therefore comparable, both of them being mainly strengthened by T_1 phases.

24h at 245°C overaging + soaking for high temperature tensile tests

Compared to AA2099, the hardness decrease is more rapid in AA2055 during exposure at 245°C (see arrows in Fig.4.40a), in agreement with [38]. The drop in hardness is accompanied by considerably lower tensile properties than those exhibited by AA2099 at the same overaging conditions. The different tensile properties are driven by the substantial difference in the alloys microstructure at the same overaging conditions, as highlighted by the STEM microstructural analyses reported in Fig.4.22 and Fig.4.31 (b), (e) (from [37,38]): AA2099 matrix is dominated by

numerous, though coarsened, T_1 phases; on the contrary, in AA2055, the density of T_1 precipitates is considerably reduced and substantially lower with respect to AA2099, even if this reduction is balanced by the formation of Ω precipitates. This aspect is in particular evidenced by micrographs imaged in the <112> Al zone axis (Fig.4.22e and Fig.4.31e): even if the remaining T_1 particles mostly keep their base thickness in AA2055, more commonly T_1 precipitates transform into Ω precipitates (which thickens more easily), as these two phases have very similar atomic structures [38,173,207]. It is interesting to underline that, under the same overaged condition, the difference in tensile properties is not perceivable at room temperature [38], as if the balance between ϑ', Ω and T_1 precipitates from one side (AA2055) and coarsened T_1 precipitates from the other side (AA2099) provides the same strengthening effect at room temperature. Instead, the substantial difference between AA2099 and AA2055 tensile properties at 200°C, after middle overaging, highlights the high potential of T_1 strengthening at high temperature. This aspect remarks the predominance of T_1 contribution to strengthening in Al-Cu-Li alloys, more valuable than Ω strengthening, even at 200°C.

72h at 245°C and 305°C overaging + soaking for high temperature tensile tests

In the extremely overaged conditions investigated, the gap between the alloys tensile properties at 200°C is reduced and almost disappeared. Under this condition, the strengthening effects of σ and T_1 phases, still present in AA2099, are almost comparable to ϑ' and Ω phases, which continue to strengthen AA2055 matrix. Considering the lower density of AA2099, advantages of AA2055 are negligible in terms of specific strength

Tensile tests at 250°C

The superior performance of AA2055 in all tested conditions is highlighted by Fig.4.39b. The significant drop in AA2099 properties at 250°C in the early stages of overaging (6h and 24h soaking at 215°C before tensile tests) is thought to be mainly related to the dissolution of the strengthening δ', δ'-ϑ'-δ' and S phases. As explained in the "Material and methods" Sect., at least 2h of soaking at high temperature was required for each tensile test to reach a homogeneous temperature field, equal to the test temperature in the sample center. The residual hardness of each AA2099 sample tested at 250°C appears lower than $120HV_1$, roughly characterizing the AA2099 samples overaged for 24h at 245°C and tested at 200°C (compare the red points highlighted by the arrows in Fig.4.40a to those characterized by the higher hardness in Fig.4.40b);

this aspect confirms that no δ', ϑ' and S phases are still present in all AA2099 samples tested at 250°C.

Moreover, considering together the residual hardness and tensile properties of both alloys (Fig.4.40), it is noteworthy that: (i) the plateau hardness of AA2055 is higher than that of AA2099 (further confirmed by [38]); (ii) AA2055 exhibits a superior performance, even at the same residual hardness of AA2099 specimens. This aspect highlight the better performance of Ω and ϑ' phases in obstructing dislocations movement at 250°C, compared to coarsened T_1 phases, respectively characterizing AA2055 and AA2099 alloys in the fully overaged condition. In agreement with [184,189], it is the semi-coherent Ω phase to exhibit a greater strengthening ability compared to the ϑ' phase.

It is also interesting, for the single alloy, to compare the different behavior at the same residual hardness but different test temperature (Fig.4.41), in order to point out the effect of an increased test temperature, under the same microstructural features. By considering the variation of AA2099 yield strength with overaging (Fig.4.41a), the trend at 200°C can be approximated by the steep linear regression reported in Fig.4.41a, (slope coefficient ≈ 2,98 MPa/HV_1); the linear regression slope is considerably reduced when the test temperature is increased up to 250°C (slope coefficient ≈ 1,07 MPa/HV_1), indicating that overaging plays a much minor role than what highlighted at 200°C, due to the higher mobility of dislocations. With reference to Fig.4.22, at 250°C the strengthening effect of evenly distributed though coarsened T_1 phases (Fig.4.22 b, e) is marginally different from that of coarse T_1 and σ phases, able to obstruct dislocations movement in the fully overaged condition (Fig.4.22 c, f).

A slightly different behavior is exhibited by the Al-Cu-Li-Ag alloy (Fig.4.41b): at 200°C, AA2055 specimens show a lower variation of tensile properties with residual hardness, as confirmed by the lower slope of linear regression (slope coefficient ≈ 2,37 MPa/HV_1); at the same time, when tested at 250°C, a certain slope is maintained (slope coefficient ≈ 1,36 MPa/HV_1), indicating that the interaction between dislocations and precipitates continues to change due to overaging. This aspect confirms that the combination of Ω and ϑ' precipitates (fully overaged AA2055, Fig.4.31 c, f) exhibits a higher strengthening effect at 250°C compared to T_1 and σ phases (fully overaged AA2099, Fig.4.22 c, f), since their coarsening affects the alloy strength.

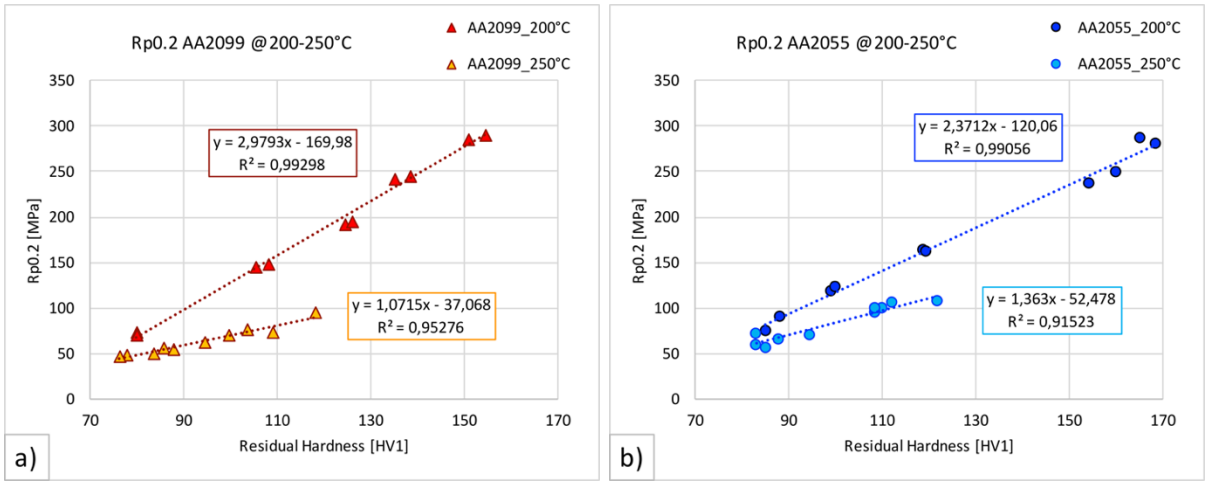

Fig.4.41: Comparison between high temperature tensile properties of (a) AA2099 and (b) AA2055 Al-Cu-Li alloys.

Given the difference in alloys density, in order to determine which alloy is the best candidate for specific high temperature applications, it is also necessary to evaluate the specific strength at the calculated operating temperature (Fig.4.42). Due to the lower density of AA2099, the advantages are further emphasized at 200°C; for applications at 250°C, AA2055 continues to offer benefits in all investigated overaging conditions.

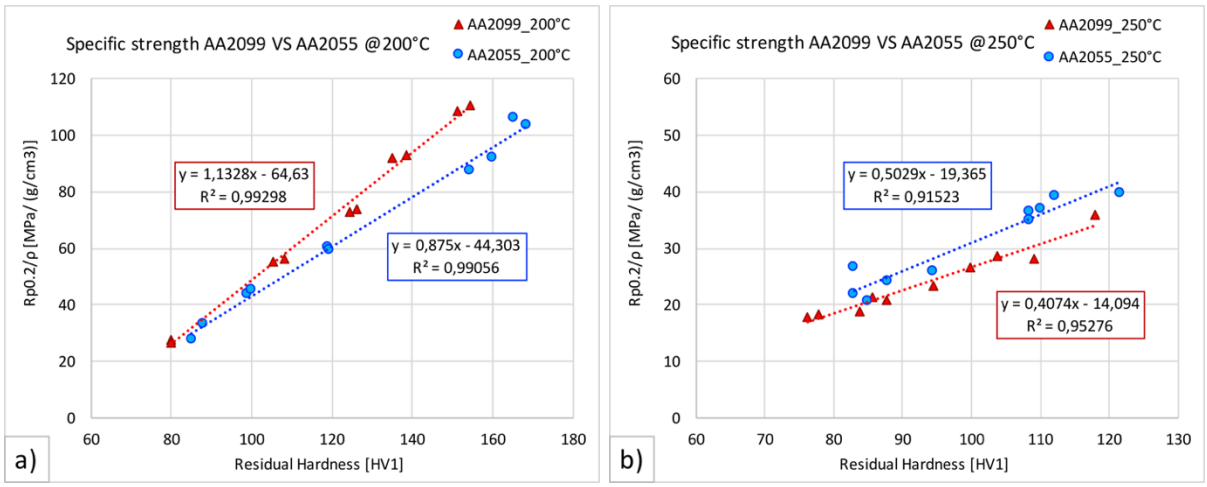

Fig.4.42: Comparison between specific strength of AA2099 and AA2055 Al-Cu-Li alloys at (a) 200°C and (b) 250°C.

4.5.4 Conclusions

In the present paper, the high temperature behavior of the lightweight AA2099 and AA2055 Al-Cu-Li(-Ag) alloys was assessed at 200°C and 250°C, under several overaging conditions, in order

to fully simulate the variation of mechanical properties occurring in a component operating at high temperature. The major results can be summed up as follows:

- At 200°C, the higher Li content characterizing AA2099 alloy considerably enhances specific strength, contributing to the superior (at least comparable) alloy performance in almost all overaging conditions with respect to AA2055. In the early stages of overaging, δ', δ'-θ'-δ' and S phases are still reinforcing AA2099 matrix besides T_1, and provide effective strengthening at 200°C. In the middle overaged condition, AA2099 microstructure is dominated by coarsened but uniformly distributed T_1 precipitates, which are therefore found effective in obstructing dislocation movements at 200°C, more than θ' and Ω phases characterizing AA2055. In the fully overaged conditions, the alloys performance is comparable at 200°C, showing a substantial equivalent strengthening effect of T_1 and σ phases from one side (AA2099) and Ω and θ' phases from the other.
- At 250°C, the reverse occurs. AA2099 is significantly softened by the combination of: (i) a complete dissolution (even at the initial stages of overaging) of δ', δ'-θ'-δ' and S phases, which were considered to still strengthen the matrix during tensile tests at 200°C; (ii) the substantial coarsening of T_1 precipitates, which become less effective. Even taking into account the higher density, AA2055 always shows a superior specific strength, highlighting the benefits of Ω and θ' combination compared to T_1 and σ phases, respectively strengthening AA2055 and AA2099 matrix in the fully overaged condition.

Part A - Results

Given the huge amount of experimental data collected in Part A, this section is aimed to briefly compare the numerical results of the most promising Al-Si and Al-Cu alloys investigated in the present dissertation.

Among Al-Si piston alloys, the eutectic AA4032 (density 2.68g/cm^3) was considered as a reference since it is massively used for both cast and forged automotive pistons. In addition to approximatively 12wt% Si, it contains up to 1wt% Ni, Cu, Mg and it is mainly strengthened by β-Mg_2Si, besides ϑ-Al_2Cu phases and Cu-Ni based aluminides.
Significant improvements in terms of residual hardness after thermal exposure were achieved thanks to a higher Cu content, up to 3.5wt%, in the abovementioned eutectic AA4032 alloy (whose density increases up to 2.77g/cm^3). Correspondingly, the tensile properties after overaging are supposed to be significantly enhanced, in agreement with many literature reviews reporting the effectiveness of Cu in increasing Al alloys resistance.
No beneficial effects have been indeed induced by 0.3wt% Mo additions to the Cu enriched AA4032 alloy: the overaging curves of base and Mo containing alloy were almost superimposed and therefore not reported in the comparison below. The negligible effect of Mo additions is well explained by the extremely high performance of the starting alloy, containing a huge amount of alloying elements and therefore not decisively influenced by the chemical modification. It should be also pointed out that Mo additions, even though limited, considerably increased the amount of casting defects, such as porosities or interdendritic shrinkage.

As regards Al-Cu alloys, one of the most diffused piston alloys in the current scenario is AA2618 (density = 2.77g/cm^3), which is today typically adopted in automotive pistons for racing applications. AA2618 contains approximatively 2.5wt% Cu, 1.5wt% Mg, 1wt% Ni and Fe and it takes advantage of both fine Cu-based precipitates (mainly the S-Al_2CuMg and ϑ-Al_2Cu phases) and of coarser thermally stable secondary phases with the stoichiometric formula Al_9FeNi (T-phase), which are known to significantly increase the high temperature resistance of the alloy. Compared to the eutectic Al-Si AA4032, the rate of the decay of residual hardness with time/temperature of

exposure is considerably lowered but almost comparable to that of AA4032+Cu, giving evidence of the superior coarsening resistance of Cu based precipitates.

Limited Zr additions to the more promising AA2618 (+0.14wt% Zr) were also tested, the upper limit of Zr content being set by the maximum amount which is retainable in solid solution during conventional casting, while avoiding the pro-peritectic precipitation of primary trialuminides. Regardless of the Zr content, the overaging curves of base AA2618 and AA2618+Zr were superimposed (thus only AA2618 overaging curves are reported in Fig.iv), and no positive results were achieved by the heat treatment adjustments, which were aimed to stimulate the homogeneous formation of fine Al_3Zr dispersoids. Nevertheless, the simple Zr addition in AA2618 alloy, at the same heat treatment industrially performed, showed beneficial effects in terms of alloy strength: the tensile tests performed at both RT and 250°C on specimens overaged for 48h at 250°C (residual hardness ≈ 100HB) revealed the superior performance of Zr enriched AA2618.

Finally, the unconventional Al-Cu-Li(-Ag) alloys AA2099 and AA2055 were investigated. These newly developed materials are characterized by considerably low density compared to AA2618, thanks to the not negligible Li content (up to 2wt% Li in AA2099, leading to density = 2.63g/cm^3; up to 1.3wt% Li in AA2055, leading to density = 2.71g/cm^3). In addition to the typical Cu based precipitates (ϑ-Al_2Cu, S-Al_2CuMg), these alloys in the peak-aged condition take advantage of T_1-Al_2CuLi, δ-Al_3Li and Al_3Zr phases.

In this case, the promising results in terms of overaging curves and RT tensile properties after thermal exposure are however not accompanied by equally promising tensile properties at 200°C and 250°C. The substantial drop in Al-Cu-Li alloys resistance is in particular experienced at 250°C.

The overaging curves of the most promising alloys, acquired at 245°C-250°C and 290°C-300°C, are reported in Fig.iv; here, the reference alloys for both mass production pistons (AA4032) and high performance pistons (AA2618) are highlighted. Due to negligible differences with respect to AA2032+Cu or AA2618, the overaging curves of AA4032+Cu+Mo nor AA2618+Zr are not reported.

As already mentioned, the trend of residual hardness of AA4032+Cu and AA2618 is similar and almost superimposed at 250°C, while a slight difference is observed between AA2618 and AA2099.

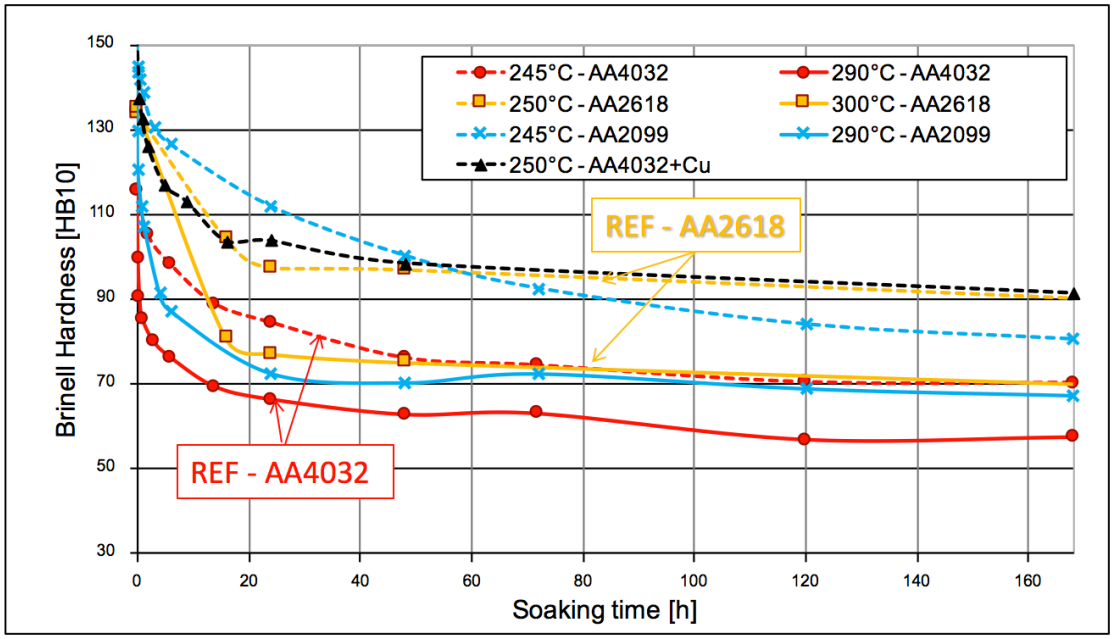

Fig.iv: Comparison between overaging curves of the investigated Al-Si and Al-Cu alloys, during thermal exposure at 245°C-250°C and 290°C-300°C.

The behavior of the most promising candidates in terms of increased strength-to-weight ratio at high temperature, AA2618+Zr and AA2099, is then evaluated by comparing the results of tensile tests at RT and 250°C (Fig.v). Unfortunately, the investigated overaging conditions are not totally comparable: 48h soaking at 250°C for AA2618+Zr and 24h soaking at 245°C for AA2099. Even if the benefits of the low density of AA2099 are evident at RT, it can be inferred that AA2618+Zr exhibits the most promising strength-to-weight ratio in case the operating temperature reaches 250°C. Additional tensile tests at intermediate temperatures have to be performed in order to determine the temperature range in which the innovative Al-Cu-Li alloy brings benefits.

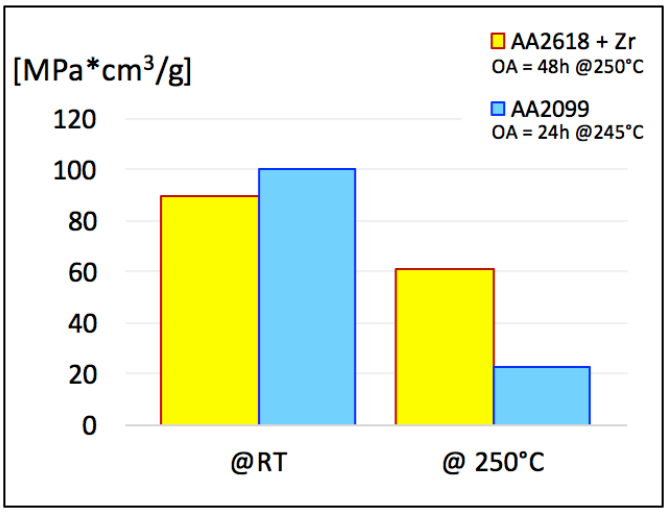

Fig.v: Comparison between tensile properties of AA2618+Zr and AA2099, at RT and 250°C. The specimens have been previously subjected to overaging treatment, respectively 48h at 250°C and 24h at 245°C.

Part A - Bibliography

[1] H. Yamagata, The science and technology of materials in automotive engines, Woodhead, 2005.

[2] E.A.A. European Aluminium Association, Applications - Power train - Pistons, in: Alum. Automot. Man., 2013.

[3] S. Mahle GmbH, ed., Pistons and Engine Testing, 2012.

[4] F.S. Silva, Fatigue on engine pistons - A compendium of case studies, Eng. Fail. Anal. 13 (2006) 480–492. doi:10.1016/j.engfailanal.2004.12.023.

[5] Bosch. https://www.youtube.com/watch?v=LjJSbHxIvnM.

[6] G. Minelli, Motori Endotermici Alternativi, 1984.

[7] G. Bocchi, Motori a quattro tempi, Ulrico Hoepli Editore, Milano, 1987.

[8] G. Ferrari, Motori a combustione interna, (2011).

[9] S. Pischinger, Lecture Notes: Internal Combustion Engines, Institute for Combustion Engines, Aachen, 2017.

[10] K. Kohashi, Y. Kimura, M. Murakami, Y. Drouvin, Analysis of Piston Friction in Internal Combustion Engine, SAE Int. (2013) 589–593. doi:10.4271/2013-01-2515.

[11] A. Panayi, H. Schock, B.-K. Chui, M. Ejakov, Parameterization and FEA Approach for the Assessment of Piston Characteristics, SAE Int. (2006).

[12] F. Migliore, Procedura di calcolo per pistone di motore motociclistico, Tesi di Laurea, Alma Mater Studiorum Università di Bologna, 2006.

[13] G. Cantore, M. Giacopini, R. Rosi, A. Strozzi, P. Pelloni, C. Forte, M. Achilluzzi, G.M. Bianchi, L. Ceschini, A. Morri, Validation of a combined CFD / FEM methodology for the evaluation of thermal load acting on aluminum alloy pistons through hardness measurements in internal combustion engines, Metall. Sci. Technol. 29 (2011).

[14] M. Warmuzek, Aluminium-Silicon Casting Alloys - Atlas of Microfractographs, ASM International, 2004.

[15] E. Sjölander, Heat treatment of Al-Si-Cu-Mg casting alloys, Ph.D. Thesis, Department of Mechanical Engineering School of Engineering, Jönköping University, 2011.

[16] C. Liao, J. Chen, Y. Li, H. Chen, C. Pan, Modification performance on 4032 Al alloy by using Al – 10Sr master alloys manufactured from different processes, Prog. Nat. Sci. Mater. Int. 24 (2014) 87–96. doi:10.1016/j.pnsc.2014.03.002.

[17] W. Kasprzak, D. Emadi, M. Sahoo, M. Aniolek, Development of Aluminium Alloys for High Temperature Applications in Diesel Engines, Mater. Sci. Forum. 618–619 (2009) 595–600. doi:10.4028/www.scientific.net/MSF.618-619.595.

[18] Y. Cho, D. Joo, C. Kim, H.-C. Lee, The Effect of Alloy Addition on the High Temperature

Properties of Over-aged Al-Si (CuNiMg) Cast Alloys, Mater. Sci. Forum. 519–521 (2006) 461–466. doi:10.4028/www.scientific.net/MSF.519-521.461.

[19] Y.-H. Cho, Y.-R. Im, S.-W. Kwon, H.-C. Lee, The Effect of Alloying Elements on the Microstructure and Mechanical Properties of Al-12Si Cast Alloys, Mater. Sci. Forum. 426–432 (2003) 339–344. doi:10.4028/www.scientific.net/MSF.426-432.339.

[20] Z. Asghar, G. Requena, F. Kubel, The role of Ni and Fe aluminides on the elevated temperature strength of an AlSi12 alloy, Mater. Sci. Eng. A. 527 (2010) 5691–5698. doi:10.1016/j.msea.2010.05.033.

[21] Z. Asghar, G. Requena, H.P. Degischer, P. Cloetens, Three-dimensional study of Ni aluminides in an AlSi12 alloy by means of light optical and synchrotron microtomography, Acta Mater. 57 (2009) 4125–4132. doi:10.1016/j.actamat.2009.05.010.

[22] C. Chen, A. Richter, R.C. Thomson, Mechanical properties of intermetallic phases in multi-component Al – Si alloys using nanoindentation, Intermetallics. 17 (2009) 634–641. doi:10.1016/j.intermet.2009.02.003.

[23] Y. Yang, K. Yu, Y. Li, D. Zhao, X. Liu, Evolution of nickel-rich phases in Al-Si-Cu-Ni-Mg piston alloys with different Cu additions, Mater. Des. 33 (2012) 220–225. doi:10.1016/j.matdes.2011.06.058.

[24] C. Chen, A. Richter, R.C. Thomson, Investigation of mechanical properties of intermetallic phases in multi-component Al–Si alloys using hot-stage nanoindentation, Intermetallics. 18 (2010) 499–508. doi:10.1016/j.intermet.2009.09.013.

[25] F. Stadler, H. Antrekowitsch, W. Fragner, H. Kaufmann, E.R. Pinatel, P.J. Uggowitzer, D. Chimica, The effect of main alloying elements on the physical properties of Al–Si foundry alloys, Mater. Sci. Eng. A. 560 (2013) 481–491. doi:10.1016/j.msea.2012.09.093.

[26] F. Stadler, H. Antrekowitsch, W. Fragner, H. Kaufmann, P.J. Uggowitzer, F. Stadler, H. Antrekowitsch, W. Fragner, H. Kaufmann, P.J. Uggowitzer, Effect of main alloying elements on strength of Al – Si foundry alloys at elevated temperatures, Int. J. Cast Met. Res. 25 (2012) 215–224. doi:10.1179/1743133612Y.0000000004.

[27] H. Fujii, T. Oka, Development of Lightweight Forged Piston Material by Optimizing Size of Needle-type Intermetallic Compound, SAE Int. (2008).

[28] M. Jayamathy, R. Vasanth, Aluminium Piston Alloy to Retard Age Softening Characteristics in Motorcycle Engines, SAE Int. (2006).

[29] R. Konečná, G. Nicoletto, L. Kunz, E. Riva, The role of elevated temperature exposure on structural evolution and fatigue strength of eutectic AlSi12 alloys, Int. J. Fatigue. 83 (2016) 24–35. doi:10.1016/j.ijfatigue.2015.05.007.

[30] L. Ceschini, A. Morri, A. Morri, M. Di Sabatino, Effect of thermal exposure on the residual hardness and tensile properties of the EN AW-2618A piston alloy, Mater. Sci. Eng. A. 639 (2015) 288–297. doi:10.1016/j.msea.2015.04.080.

[31] P. Shen, E.M. Elgallad, X. Chen, On the aging behavior of AA2618 DC cast alloy, Light Met. (2013) 373–377.

[32] E.M. Elgallad, P. Shen, Z. Zhang, X.-G. Chen, Effects of heat treatment on the microstructure and mechanical properties of AA2618 DC cast alloy, Mater. Des. 61 (2014) 133–140. doi:10.1016/S1005-8850(08)60281-9.

[33] K. Yu, W. Li, S. Li, J. Zhao, Mechanical properties and microstructure of aluminum alloy 2618 with Al3(Sc. Zr) phases, Mater. Sci. Eng. A. 368 (2004) 88–93. doi:10.1016/j.msea.2003.09.092.

[34] P. Naga Raju, K. Srinivasa Rao, G.M. Reddy, M. Kamaraj, K. Prasad Rao, Microstructure and high temperature stability of age hardenable AA2219 aluminium alloy modified by Sc, Mg and Zr additions, Mater. Sci. Eng. A. 464 (2007) 192–201. doi:10.1016/j.msea.2007.01.144.

[35] C.J. Peel, B. Evans, C.A. Baker, D.A. Bennet, P.J. Gregson, H.M. Flower, The development of aluminium-lithium alloys, in: T.H. Sanders, E.A. Starke (Eds.), Second Int. Conf. Alum. Alloy., 1984: pp. 363–392.

[36] R.J. Rioja, J. Liu, The evolution of Al-Li base products for aerospace and space applications, Metall. Mater. Trans. A Phys. Metall. Mater. Sci. 43 (2012) 3325–3337. doi:10.1007/s11661-012-1155-z.

[37] E. Balducci, L. Ceschini, S. Messieri, S. Wenner, R. Holmestad, Thermal stability of the lightweight 2099 Al-Cu-Li alloy: Tensile tests and microstructural investigations after overaging, Mater. Des. 119 (2017) 54–64. doi:10.1016/j.matdes.2017.01.058.

[38] E. Balducci, L. Ceschini, S. Messieri, S. Wenner, R. Holmestad, Effects of overaging on microstructure and tensile properties of the 2055 Al- Cu-Li-Ag alloy, Mater. Sci. Eng. A. 707 (2017) 221–231. doi:10.1016/j.msea.2017.09.051.

[39] E. Balducci, L. Ceschini, S. Messieri, High Temperature Tensile Tests of the Lightweight 2099 and 2055 Al-Cu-Li Alloy: A Comparison, JOM. (2018). doi:10.1007/s11837-018-3006-x.

[40] N.E. Prasad, A.A. Gokhale, P.R. Rao, Mechanical behaviour of aluminium – lithium alloys, Sadhana. 28 (2003) 209–246. doi:10.1007/BF02717134.

[41] Y. Ma, X. Zhou, G.E. Thompson, M. Curioni, P. Skeldon, X. Zhang, Z. Sun, C. Luo, Z. Tang, F. Lu, Anodic film growth on Al-Li-Cu alloy AA2099-T8, Electrochim. Acta. 80 (2012) 148–159. doi:10.1016/j.electacta.2012.06.126.

[42] E.A. Lindgren, L.P. Martin, M. Rosen, Characterization and Depth Profile of Lithium Depletion in Aluminum-Lithium Alloys By Ultrasound, Rev. Prog. Quant. Nondestruct. Eval. 17 (1998) 1435–1442.

[43] E.A. Starke, J.T. Staley, Application of modern aluminum alloys to aircraft, Prog. Aerosp. Sci. 32 (1996) 131–172. doi:10.1016/0376-0421(95)00004-6.

[44] W.X. Feng, E.S. Lin, E.A. Starke, The Effect of Minor Alloying Elements on the Mechanical Properties of Al-Cu-Li Alloys, Metall. Trans. A. 15 (1984) 1209–1220. doi:10.1007/BF02644715.

[45] Y. Wang, K. Brogan, S.C. Tung, Wear and scuffing characteristics of composite polymer and nickel/ceramic composite coated piston skirts against aluminum and cast iron cylinder bores, Wear. 250 (2001) 706–717.

[46] S.G. Pandian, S.P. Rengarajan, T.P. Bapu, V. Natarajan, H. Kanagasabesan, Thermal and Structural Analysis of Functionally Graded NiCrAlY/YSZ/Al2O3 Coated Piston, SAE Int. (2015) 578–585. doi:10.4271/2015-01-9081.

[47] W.D. Callister, D.G. Rethwisch, Materials Science and Engineering, 9th ed., John Wiley & Sons, 2011.

[48] ASM Handbook Vol. 4 Heat Treating, ASM International, 1995.

[49] J.P. Lyle, D.A. Granger, R.E. Sanders, Aluminum Alloys, Ullmann's Encycl. Ind. Chem. 1. (2000). doi:10.1002/14356007.a01_481.

[50] Heat Treatable Aluminium Alloys, Key to Met.

[51] E. Balducci, L. Ceschini, A. Morri, A. Morri, EN AW-4032 T6 Piston Alloy After High-Temperature Exposure : Residual Strength and Microstructural Features, J. Mater. Eng. Perform. 26 (2017) 3802–3812. doi:10.1007/s11665-017-2835-z.

[52] C.R. Brooks, Heat Treatment, Structure and Properties of Nonferrous Alloys, American Society for Metals, 1982.

[53] ASM Handbooks Online- Volume 4, Heat Treating, 2002.

[54] K.E. Knipling, D.C. Dunand, D.N. Seidman, Criteria for developing castable, creep-resistant aluminum-based alloys - A review, Int. J. Mater. Res. 97 (2006) 246–265. doi:10.3139/146.101249.

[55] I.M. Liftshitz, V. V. Slyozov,-, J. Phys. Chem. Solids. (1961) 35.

[56] C. Wagner,-, Elektrochemie. (1961) 581.

[57] E. Balducci, A. Morri, L. Ceschini, A. Morri, Effect of thermal exposure on mechanical properties of EN AW-2618 and EN AW-4032 piston alloys, La Metall. Ital. 6 (2016) 89–92.

[58] G.E. Totten, D.S. MacKenzie, Handbook of Aluminum - Volume 2: Alloy Production and Materials Manufacturing, 2003.

[59] S. Spigarelli, Il comportamento dei materiali ad alta temperatura, Dispense Corso Creep, Milano 18-19 Novembre 2015, Associazione Italiana di Metallurgia.

[60] Creep and Stress Rupture Failures, Failure Analysis and Prevention, in: ASM Handb., ASM Intern, 2002: pp. 728–737.

[61] F.C. Campbell, Fatigue and Fracture- Understanding the basics, ASM International, 2012.

[62] Francesco Iacoviello, Comportamento a temperatura elevata, Dispense, Università di Cassino.

[63] T. Balakrishna Bhat, V.S. Arunachalam, Strengthening mechanisms in alloys, Procedings Indian Acad. Sci. (Engg. Sci.). 3 (1980) 275–296.

[64] ASM Handbook Vol.2 Properties and Selection: Nonferrous Alloys and Special-Purpose Materials, ASM International, 1995.

[65] F.J. Humphreys, M. Hatherly, Recrystallization and Related Annealing Phenomena, Pergamon, 1996.

[66] H.C. Fang, K.H. Chen, X. Chen, L.P. Huang, G.S. Peng, B.Y. Huang, Effect of Zr, Cr and Pr additions on microstructures and properties of ultra-high strength Al-Zn-Mg-Cu alloys, Mater. Sci. Eng. A. 528 (2011) 7606–7615. doi:10.1016/j.msea.2011.06.018.

[67] H. a. Elhadari, H. a. Patel, D.L. Chen, W. Kasprzak, Tensile and fatigue properties of a cast aluminum alloy with Ti, Zr and V additions, Mater. Sci. Eng. A. 528 (2011) 8128–8138. doi:10.1016/j.msea.2011.07.018.

[68] W. Kasprzak, B. Shalchi, M. Niewczas, Structure and properties of cast Al – Si based alloy

with Zr–V–Ti additions and its evaluation of high temperature performance, J. Alloys Compd. 595 (2014) 67–79. doi:10.1016/j.jallcom.2013.11.209.

[69] J. Zhang, D. Ding, W. Zhang, S. Kang, Effect of Zr addition on microstructure and properties of Al − Mn − Si − Zn-based alloy, Trans. Nonferrous Met. Soc. China. 24 (2014) 3872–3878. doi:10.1016/S1003-6326(14)63545-7.

[70] S.P. Wen, K.Y. Gao, H. Huang, W. Wang, Z.R. Nie, Role of Yb and Si on the precipitation hardening and recrystallization of dilute Al – Zr alloys, J. Alloys Compd. 599 (2014) 65–70. doi:10.1016/j.jallcom.2014.02.065.

[71] S.K. Shaha, F. Czerwinski, W. Kasprzak, J. Friedman, D.L. Chen, Thermal stability of (AlSi)x(ZrVTi) intermetallic phases in the Al – Si – Cu – Mg cast alloy with additions of Ti , V , and Zr, Thermochim. Acta. 595 (2014) 11–16. doi:10.1016/j.tca.2014.08.037.

[72] S.K. Shaha, F. Czerwinski, W. Kasprzak, J. Friedman, D.L. Chen, Effect of Zr , V and Ti on hot compression behavior of the Al – Si cast alloy for powertrain applications, J. Alloys Compd. 615 (2014) 1019–1031. doi:10.1016/j.jallcom.2014.06.210.

[73] B.J. Rakhmonov, G. Timelli, F. Bonollo, The Effect of Transition Elements on High-Temperature Mechanical Properties of Al – Si Foundry Alloys – A Review, Adv. Eng. Mater. (2016) 1–10. doi:10.1002/adem.201500468.

[74] M.S. Zedalis, M.E. Fine, Precipitation and ostwald ripening in dilute AI Base-Zr-V alloys, Metall. Trans. A. 17 (1986) 2187–2198. doi:10.1007/BF02645917.

[75] K.E. Knipling, D.N. Seidman, D.C. Dunand, Ambient- and high-temperature mechanical properties of isochronally aged Al-0.06Sc, Al-0.06Zr and Al-0.06Sc-0.06Zr (at.%) alloys, Acta Mater. 59 (2011) 943–954. doi:10.1016/j.actamat.2010.10.017.

[76] K.E. Knipling, D.C. Dunand, D.N. Seidman, Nucleation and precipitation strengthening in dilute Al-Ti and Al-Zr alloys, Metall. Mater. Trans. A Phys. Metall. Mater. Sci. 38 (2007) 2552–2563. doi:10.1007/s11661-007-9283-6.

[77] K.M.C. Wong, a. R. Daud, A. Jalar, Microhardness and tensile properties of a 6XXX alloy through minor additions of Zr, J. Mater. Eng. Perform. 18 (2009) 62–65. doi:10.1007/s11665-008-9249-x.

[78] T. Ohashi, R. Ichikawa,-, Metallkd. 64 (1973) 517–521.

[79] S. Hori, S. Saji, A. Takehara,-, J Japan Inst Light Met. 31 (1981) 793–797.

[80] Y. Harada, D.C. Dunand, Microstructure of Al 3 Sc with ternary transition-metal additions, 331 (2002) 686–695.

[81] M.E. Van Dalen, D.N. Seidman, D.C. Dunand, Creep- and coarsening properties of Al – 0.06 at.% Sc – 0.06 at.% Ti at 300 – 450 ° C, 56 (2008) 4369–4377. doi:10.1016/j.actamat.2008.05.002.

[82] K.E. Knipling, R. a. Karnesky, C.P. Lee, D.C. Dunand, D.N. Seidman, Precipitation evolution in Al-0.1Sc, Al-0.1Zr and Al-0.1Sc-0.1Zr (at.%) alloys during isochronal aging, Acta Mater. 58 (2010) 5184–5195. doi:10.1016/j.actamat.2010.05.054.

[83] C. Xu, R. Du, X. Wang, S. Hanada, H. Yamagata, W. Wang, C. Ma, Effect of cooling rate on morphology of primary particles in Al − Sc − Zr master alloy, Trans. Nonferrous Met. Soc. China. 24 (2014) 2420–2426. doi:10.1016/S1003-6326(14)63366-5.

[84] A.M. Samuel, S.A. Alkahtani, H.W. Doty, F.H. Samuel, Role of Zr and Sc addition in controlling the microstructure and tensile properties of aluminum – copper based alloys, JMADE. 88 (2015) 1134–1144. doi:10.1016/j.matdes.2015.09.090.

[85] S. Mondol, T. Alam, R. Banerjee, S. Kumar, K. Chattopadhyay, Materials Science & Engineering A Development of a high temperature high strength Al alloy by addition of small amounts of Sc and Mg to 2219 alloy, Mater. Sci. Eng. A. 687 (2017) 221–231. doi:10.1016/j.msea.2017.01.037.

[86] Z. Jia, R. Jostein, J.K. Solberg, Q. Liu, Formation of precipitates and recrystallization resistance in Al–Sc–Zr alloys, Trans. Nonferrous Met. Soc. China. 22 (2012) 1866–1871. doi:10.1016/S1003-6326(11)61399-X.

[87] K.E. Knipling, D.C. Dunand, Creep resistance of cast and aged Al-0.1Zr and Al-0.1Zr-0.1Ti (at.%) alloys at 300-400 °C, Scr. Mater. 59 (2008) 387–390. doi:10.1016/j.scriptamat.2008.02.059.

[88] K.E. Knipling, D.C. Dunand, D.N. Seidman, Precipitation evolution in Al-Zr and Al-Zr-Ti alloys during aging at 450-600 °C, Acta Mater. 56 (2008) 1182–1195. doi:10.1016/j.actamat.2007.11.011.

[89] S.K. Shaha, F. Czerwinski, W. Kasprzak, J. Friedman, D.L. Chen, Monotonic and cyclic deformation behavior of the Al–Si–Cu–Mg cast alloy with micro-additions of Ti, V and Zr, Int. J. Fatigue. 70 (2015) 383–394. doi:10.1016/j.ijfatigue.2014.08.001.

[90] K.E. Knipling, D.C. Dunand, D.N. Seidman, Precipitation evolution in Al – Zr and Al – Zr – Ti alloys during isothermal aging at 375 – 425 ° C, 56 (2008) 114–127. doi:10.1016/j.actamat.2007.09.004.

[91] S. Zhang, J.P. Nic, D.E. Mikkola, New cubic phases formed by alloying Al3Ti with Mn and Cr, Scr. Metall. Mater. 24 (1990) 57–62.

[92] J.P. Nic, S. Zhang, D.E. Mikkola, Observations on the systematic alloying of Al3Ti with fourth period elements to yield cubic phases, Scr. Metall. Mater. 24 (1990) 1099–1104.

[93] D.D. Misko, J.B. Lumsden, W.O. Powers, J.A. Wert, No Title, Scr. Metall. Mater. 23 (1989) 1827–1830.

[94] N. Mabuchi, K. Hirukawa, H. Tsuda, Y. Nakayama, Scr. Metall. Mater. 24 (1990) 505–508.

[95] I.S. Virk, R.A. Varin, No Title, Scr. Metall. Mater. 1 (1991) 85–88.

[96] N.Q. Vo, D.C. Dunand, D.N. Seidman, Improving aging and creep resistance in a dilute Al–Sc alloy by microalloying with Si, Zr and Er, Acta Mater. 63 (2014) 73–85. doi:10.1016/j.actamat.2013.10.008.

[97] C. Booth-Morrison, D.C. Dunand, D.N. Seidman, Coarsening resistance at 400°C of precipitation-strengthened Al–Zr–Sc–Er alloys, Acta Mater. 59 (2011) 7029–7042. doi:10.1016/j.actamat.2011.07.057.

[98] M. Colombo, E. Gariboldi, A. Morri, Er addition to Al-Si-Mg-based casting alloy : Effects on microstructure , room and high temperature mechanical properties, J. Alloys Compd. 708 (2017) 1234–1244. doi:10.1016/j.jallcom.2017.03.076.

[99] M. Colombo, E. Gariboldi, A. Morri, Materials Science & Engineering A In fl uences of di ff erent Zr additions on the microstructure , room and high temperature mechanical

properties of an Al-7Si-0 . 4Mg alloy modi fi ed with, 713 (2018) 151–160. doi:10.1016/j.msea.2017.12.068.

[100] H. Hallem, Precipitation behaviour and recrystallisation resistance in aluminium alloys with additions of hafnium, scandium and zirconium An experimental investigation, The Norwegian University of Science and Technology, 2005.

[101] J. Robson, P. Prangnell, Dispersoid Precipitation and Process Modelling in Zirconium Containing Commercial Aluminium Alloys, Acta Mater. 49 (2001) 599–613.

[102] J.D. Robson, Optimizing the homogenization of zirconium containing commercial aluminium alloys using a novel process model, Mater. Sci. Eng. A. 338 (2002) 219–229. doi:10.1016/S0921-5093(02)00061-8.

[103] J.D. Robson, P.B. Prangnell, Modelling Al3Zr dispersoid precipitation in multicomponent aluminium alloys, Mater. Sci. Eng. A. 352 (2003) 240–250. doi:10.1016/S0921-5093(02)00894-8.

[104] M. Zhao, Y. Xing, Z. Jia, Q. Liu, X. Wu, Effects of heating rate on the hardness and microstructure of Al-Cu and Al-Cu-Zr-Ti-V alloys, J. Alloys Compd. 686 (2016) 312–317. doi:10.1016/j.jallcom.2016.06.063.

[105] A.R. Farkoosh, X.G. Chen, M. Pekguleryuz, Dispersoid strengthening of a high temperature Al–Si–Cu–Mg alloy via Mo addition, Mater. Sci. Eng. A. 620 (2015) 181–189. doi:10.1016/j.msea.2014.10.004.

[106] L.F. Mondolfo, Aluminium Alloys: Structure and Properties, Butterwort, London, 1976.

[107] A.R. Farkoosh, X.G. Chen, M. Pekguleryuz, Interaction between molybdenum and manganese to form effective dispersoids in an Al–Si–Cu–Mg alloy and their influence on creep resistance, Mater. Sci. Eng. A. 627 (2015) 127–138. doi:10.1016/j.msea.2014.12.115.

[108] J. Campbell, Complete Casting Handbook, Elsevier Ltd., 2011.

[109] M.G. Chu, G.J. Hildeman, Supersaturated aluminium alloy, EP 1 111 079 A1, 2001.

[110] A. Kula, L. Blaz, STRUCTURE AND PROPERTIES OF ALUMINUM ALLOYS WITH ADDITIONS OF TRANSITION METALS PRODUCED VIA COUPLED RAPID SOLIDIFICATION AND HOT EXTRUSION, in: Met. 2015- Brno- Czech Repub., 2015: pp. 1–6.

[111] A.B. Pandey, Dispersion strengthened L12 aluminium alloys, EP 2 112 240 A1, 2009.

[112] A. Tanihata, N. Sato, K. Katsumata, T. Shiraishi, Development of High-strength Piston Material with High Pressure Die Casting, SAE Int. (2006).

[113] M.E. Fine, E.A. Starke, Rapidly Solidified Powder Aluminium Alloys: A Symposium, 1986.

[114] D.J. Skinner, ELEVATED TEMPERATURE STRENGTH OF ALUMINUM BASED ALLOYS BY THE ADDITION OF RARE EARTH ELEMENTS, 5,284,532, 1994.

[115] J.W. Simon, K. Gorman, AGE HARDENABLE DISPERSION STRENGTHENED HIGH TEMPERATURE ALUMINUM ALLOY, 4,889,582, 1989.

[116] A.B. Pandey, High strength L12 aluminium alloys, EP 2 110 450 A1, 2009.

[117] A.B. Pandey, High strength aluminium alloys with L12 precipitates, US 7,879,162 B2, 2011.

[118] A.B. Pandey, High temperature aluminium alloys, EP 1 728 881 A2, 2006.

[119] D. Buono, E. Iarrobino, A. Senatore, U. Napoli, Optical Piston Temperature Measurement in an Internal Combustion Engine, 4 (2016). doi:10.4271/2011-01-0407.

[120] G. Nicoletto, E. Riva, A. Di Filippo, High Temperature Fatigue Behavior of Eutectic Al-Si-Alloys Used for Piston Production, Procedia Eng. 74 (2014) 157–160. doi:10.1016/j.proeng.2014.06.241.

[121] M. Rogante, V.T. Lebedev, F. Nicolaie, E. Retfalvi, L. Rosta, SANS study of the precipitates microstructural evolution in Al 4032 car engine pistons, 358 (2005) 224–231. doi:10.1016/j.physb.2005.01.240.

[122] E. Alonso, T.M. Lee, C. Bjelkengren, R. Roth, R.E. Kirchain, Evaluating the Potential for Secondary Mass Savings in Vehicle Lightweighting, (2012).

[123] T. Luedeke, M. Vielhaber, Holistic Approach for Secondary Weight Improvements, Procedia CIRP. 21 (2014) 218–223. doi:10.1016/j.procir.2014.03.139.

[124] G. Biroli, G. Caglioti, L. Martini, G. Riontino, Precipitation kinetics of AA4032 and AA6082: a comparison based on DSC and TEM, Scr. Mater. 39 (1998) 197–203.

[125] P. Krishnankutty, A. Kanjirathinkal, M.A. Joseph, M. Ravi, Effect of Aging Time on Mechanical Properties and Wear Characteristics of Near Eutectic Al – Si – Cu – Mg – Ni Piston Alloy, Trans. Indian Inst. Met. 68 (2015) 25–30. doi:10.1007/s12666-015-0584-y.

[126] F. Stadler, H. Antrekowitsch, W. Fragner, H. Kaufmann, P.J. Uggowitzer, The effect of Ni on the high-temperature strength of Al-Si cast alloys, Mater. Sci. Forum. 690 (2011) 274–277. doi:10.4028/www.scientific.net/MSF.690.274.

[127] J.H. Hollomon, Tensile Deformation, Trans. AIME. 162 (1945) 268–290.

[128] G.E. Dieter, Mechanical Metallurgy, McGraw-Hill, New York, 1986.

[129] R.E. Reed-Hill, Physical Metallurgy Principles, 1964.

[130] R. Konečná, G. Nicoletto, L. Kunz, M. Svoboda, A. Bača, Fatigue strength degradation of AlSi12cuNiMg alloy due to high temperature exposure: A structural investigation, Procedia Eng. 74 (2014) 43–46. doi:10.1016/j.proeng.2014.06.221.

[131] F. Nový, M. Janeček, R. Král, Microstructure changes in a 2618 aluminium alloy during ageing and creep, J. Alloys Compd. 487 (2009) 146–151. doi:10.1016/j.jallcom.2009.08.014.

[132] A.M.A. Mohamed, A.M. Samuel, F.H. Samuel, H.W. Doty, Influence of additives on the microstructure and tensile properties of near-eutectic Al-10.8%Si cast alloy, Mater. Des. 30 (2009) 3943–3957. doi:10.1016/j.matdes.2009.05.042.

[133] Y.H. Cho, Y.-R. Im, S.-W. Kwon, H.C. Lee, The Effect of Alloying Elements on the Microstructure and Mechanical Properties of Al-12Si Cast Alloys, Mater. Sci. Forum. 426–432 (2003) 339–344. doi:10.4028/www.scientific.net/MSF.426-432.339.

[134] S.K. Shaha, F. Czerwinski, W. Kasprzak, D.L. Chen, Tensile and compressive deformation behavior of the Al – Si – Cu – Mg cast alloy with additions of Zr , V and Ti, J. Mater. 59 (2014) 352–358. doi:10.1016/j.matdes.2014.02.060.

[135] F. Stadler, H. Antrekowitsch, W. Fragner, H. Kaufmann, E.R. Pinatel, P.J. Uggowitzer, The effect of main alloying elements on the physical properties of Al-Si foundry alloys, Mater. Sci. Eng. A. 560 (2013) 481–491. doi:10.1016/j.msea.2012.09.093.

[136] L. Ceschini, A. Morri, A. Morri, G. Pivetti, Predictive equations of the tensile properties based on alloy hardness and microstructure for an A356 gravity die cast cylinder head, Mater. Des. 32 (2011) 1367–1375. doi:10.1016/j.matdes.2010.09.014.

[137] I.N.A. Oguocha, S. Yannacopoulos, A calorimetric study of S and θ' precipitation in Al2O3 particle-reinforced AA2618, J. Mater. Sci. 34 (1999) 3335–3340.

[138] S. Toschi, E. Balducci, L. Ceschini, E.A. Mørtsell, A. Morri, M. Di Sabatino, Effect of Zr Addition on Overaging and Tensile Behavior of 2618 Aluminum Alloy, Metals (Basel). 9 (2019). doi:10.3390/met9020130.

[139] C. Giumarra, B. Thomas, R.J. Rioja, New Aluminium Lithium Alloys for Aerospace Applications, Proc. Light Met. Technol. Conf. 2007. (2007).

[140] W. Miller, J. White, D. Lloyd, The Physical Metallurgy of Aluminium-Lithium-Copper-Magnesium-Zirconium Alloys-8090 and 8091, J. Phys. Colloq. 48 (1987) 139–149.

[141] A. Smith, The Metallurgical Aspects of Aluminium-Lithium Alloys in Various Product Forms for Helicopter Structural Applications, J. Phys. Colloq. 48 (1987) 49–59. doi:10.1051/jphyscol:1987307.

[142] Y. Ma, X. Zhou, G.E. Thompson, T. Hashimoto, P. Thomson, M. Fowles, Distribution of intermetallics in an AA 2099-T8 aluminium alloy extrusion, Mater. Chem. Phys. 126 (2011) 46–53. doi:10.1016/j.matchemphys.2010.12.014.

[143] T. Warner, Recently-developed aluminium solutions for aerospace applictions, Mater. Sci. Forum. 519–521 (2006) 1271–1278. doi:10.4028/www.scientific.net/MSF.519-521.1271.

[144] B. Decreus, A. Deschamps, F. De Geuser, P. Donnadieu, C. Sigli, M. Weyland, The influence of Cu/Li ratio on precipitation in Al-Cu-Li-x alloys, Acta Mater. 61 (2013) 2207–2218. doi:10.1016/j.actamat.2012.12.041.

[145] J.F. Li, P.L. Liu, Y.L. Chen, X.H. Zhang, Z.Q. Zheng, Microstructure and mechanical properties of Mg, Ag and Zn multi-microalloyed Al-(3.2-3.8)Cu-(1.0-1.4)Li alloys, Trans. Nonferrous Met. Soc. China (English Ed. 25 (2015) 2103–2112. doi:10.1016/S1003-6326(15)63821-3.

[146] Z. Gao, J.H. Chen, S.Y. Duan, X.B. Yang, C.L. Wu, Complex precipitation sequences of Al-Cu-Li-(Mg) alloys characterized in relation to thermal ageing processes, Acta Metall. Sin. (English Lett. 29 (2016) 94–103. doi:10.1007/s40195-016-0366-5.

[147] C. Gao, Y. Luan, J.C. Yu, Y. Ma, Effect of thermo-mechanical treatment process on microstructure and mechanical properties of 2A97 Al-Li alloy, Trans. Nonferrous Met. Soc. China (English Ed. 24 (2014) 2196–2202. doi:10.1016/S1003-6326(14)63332-X.

[148] E. Gumbmann, W. Lefebvre, F. De Geuser, C. Sigli, A. Deschamps, The effect of minor solute additions on the precipitation path of an Al-Cu-Li alloy, Acta Mater. 115 (2016) 104–114. doi:10.1016/j.actamat.2016.05.050.

[149] M.H. Tosten, J.M. Galbraith, P.R. Howell, Nucleation of δ' (Al3Li) on β' (Al3Zr) in Al-Li-Zr and Al-Li-Cu-Zr alloys, J. Mater. Sci. Lett. 6 (1987) 51–53.

[150] D. Tsivoulas, P.B. Prangnell, The effect of Mn and Zr dispersoid-forming additions on recrystallization resistance in Al-Cu-Li AA2198 sheet, Acta Mater. 77 (2014) 1–16. doi:10.1016/j.actamat.2014.05.028.

[151] D. Tsivoulas, J.D. Robson, Heterogeneous Zr solute segregation and Al3Zr dispersoid

distributions in Al-Cu-Li alloys, Acta Mater. 93 (2015) 73–86. doi:10.1016/j.actamat.2015.03.057.

[152] Y. Lin, Z. Zheng, S. Li, X. Kong, Y. Han, Microstructures and properties of 2099 Al-Li alloy, Mater. Charact. 84 (2013) 88–99. doi:10.1016/j.matchar.2013.07.015.

[153] N. Brodusch, M. Trudeau, P. Michaud, L. Rodrigue, J. Boselli, R. Gauvin, Contribution of a New Generation Field-Emission Scanning Electron Microscope in the Understanding of a 2099 Al-Li Alloy, Microsc. Microanal. Off. J. Microsc. Soc. Am. Microbeam Anal. Soc. Microsc. Soc. Canada. (2012) 1. doi:10.1017/S143192761200150X.

[154] D. Ortiz, J. Brown, M. Abdelshehid, P. DeLeon, R. Dalton, L. Mendez, J. Soltero, M. Pereira, M. Hahn, E. Lee, J. Ogren, R. Clark, J. Foyos, O.S. Es-Said, The effects of prolonged thermal exposure on the mechanical properties and fracture toughness of C458 aluminum-lithium alloy, Eng. Fail. Anal. 13 (2006) 170–180. doi:10.1016/j.engfailanal.2004.10.008.

[155] M. Romios, R. Tiraschi, C. Parrish, H.W. Babel, J.R. Ogren, O.S. Es-Said, Design of Multistep Aging Treatments of 2099 (C458) Al-Li Alloy, J. Mater. Eng. Perform. 14 (2005) 641–646. doi:10.1361/105994905X64594.

[156] J. Jabra, M. Romios, J. Lai, E. Lee, M. Setiawan, E.W. Lee, J. Witters, N. Abourialy, J.R. Ogren, R. Clark, T. Oppenheim, W.E. Frazier, O.S. Es-Said, The Effect of Thermal Exposure on the Mechanical Properties of 2099-T6 Die Forgings, 2099-T83 Extrusions, 7075-T7651 Plate, 7085-T7452 Die Forgings, 7085-T7651 Plate, and 2397-T87 Plate Aluminum Alloys, J. Mater. Eng. Perform. 15 (2006) 601–607. doi:10.1361/105994906X136142.

[157] R. Doglione, Le leghe Alluminio-Litio, Metall. Ital. 97 (2005) 39–50.

[158] J. Chen, Ductile Tearing of AA2198 Aluminum-Lithium Sheets for Aeronautic Application, Ecole Nationale Supérieure des mines de Paris, 2011.

[159] A. Deschamps, M. Garcia, J. Chevy, B. Davo, F. De Geuser, Influence of Mg and Li content on the microstructure evolution of Al-Cu-Li alloys during long-term ageing, Acta Mater. 122 (2017) 32–46. doi:10.1016/j.actamat.2016.09.036.

[160] R. Kilaas, V. Radmilovic, Structure determination and structure refinement of Al2CuMg precipitates by quantitative high-resolution electron microscopy., Ultramicroscopy. 88 (2001) 63–72.

[161] C. Dwyer, M. Weyland, L.Y. Chang, B.C. Muddle, Combined electron beam imaging and ab initio modeling of T1 precipitates in Al-Li-Cu alloys, Appl. Phys. Lett. 98 (2011). doi:10.1063/1.3590171.

[162] L. Bourgeois, C. Dwyer, M. Weyland, J.F. Nie, B.C. Muddle, Structure and energetics of the coherent interface between the theta' precipitate phase and aluminium in Al-Cu, Acta Mater. 59 (2011) 7043–7050. doi:10.1016/j.actamat.2011.07.059.

[163] K. Mahalingam, B.P. Gu, G.I. Liedl, T.H. Sanders Jr, Coarsening of δ′ (Al3Li) precipitates in binary Al-Li alloys, Acta Metall. 35 (1987) 483–498.

[164] S.C. Wang, M.J. Starink, Precipitates and intermetallic phases in precipitation hardening Al–Cu–Mg–(Li) based alloys, Int. Mater. Rev. 50 (2005) 193–215. doi:10.1179/174328005X14357.

[165] H. Li, Y. Tang, Z. Zeng, Z. Zheng, F. Zheng, Effect of ageing time on strength and microstructures of an Al-Cu-Li-Zn-Mg-Mn-Zr alloy, Mater. Sci. Eng. A. 498 (2008) 314–320.

doi:10.1016/j.msea.2008.08.001.

[166] E. Balducci, L. Ceschini, A. Morri, A. Morri, M. Di Sabatino, L. Arnberg, Y. Li, High Temperature Behavior of the EN AW-2618A Piston Alloy Containing 0.12wt% Zr: Influence of Heat Treatment, in: Mater. Today Proc., Elsevier Ltd, 2015: pp. 5037–5044.

[167] T. Dorin, P. Donnadieu, J.M. Chaix, W. Lefebvre, F. De Geuser, A. Deschamps, Size distribution and volume fraction of T1 phase precipitates from TEM images: Direct measurements and related correction, Micron. 78 (2015) 19–27. doi:10.1016/j.micron.2015.06.002.

[168] T. Dorin, F. De Geuser, W. Lefebvre, C. Sigli, A. Deschamps, Strengthening mechanisms of T1 precipitates and their influence on the plasticity of an Al-Cu-Li alloy, Mater. Sci. Eng. A. 605 (2014) 119–126. doi:10.1016/j.msea.2014.03.024.

[169] T. Dorin, A. Deschamps, F. De Geuser, C. Sigli, Quantification and modelling of the microstructure/strength relationship by tailoring the morphological parameters of the T1 phase in an Al-Cu-Li alloy, Acta Mater. 75 (2014) 134–146. doi:10.1016/j.actamat.2014.04.046.

[170] E.L. Colvin, R.J. Rioja, L.A. Yocum, D.K. Denzer, T.K. Cogswell, G.H. Bray, R.R. Sawtell, A.L. Wilson, US 8,118,950 B2, US 8,118,950 B2, 2012.

[171] N.E. Prasad, A.A. Gokhale, R.J.H. Wanhill, Aluminium-Lithium Alloys: Processing, Properties, and applications, 2014. doi:http://dx.doi.org/10.1016/B978-0-12-401698-9.00018-5.

[172] P. Donnadieu, Y. Shao, F. De Geuser, G.A. Botton, S. Lazar, M. Cheynet, Atomic structure of T1 precipitates in Al – Li – Cu alloys revisited with HAADF-STEM imaging and small-angle X-ray scattering, Acta Mater. 59 (2011) 462–472. doi:10.1016/j.actamat.2010.09.044.

[173] S.J. Kang, T.-H. Kim, C.-W. Yang, J.I. Lee, E.S. Park, T.W. Noh, M. Kim, Atomic structure and growth mechanism of T1 precipitate in Al–Cu–Li–Mg–Ag alloy, Scr. Mater. 109 (2015) 68–71. doi:10.1016/j.scriptamat.2015.07.020.

[174] W.A. Cassada, G.J. Shiflet, E.A. Starke, The effect of plastic deformation on Al2CuLi (T1) precipitation, Metall. Trans. A. 22 (1991) 299–306. doi:10.1007/BF02656799.

[175] W. Cassada, G. Shiflet, E. Starke, Mechanism of Al2CuLi(T1) nucleation and growth, Metall. Trans. A. 22 (1991) 287–297. http://link.springer.com/article/10.1007/BF02656798.

[176] K.S. Kumar, S.A. Brown, J.R. Pickens, Microstructural evolution during aging of an Al-Cu-Li-Ag-Mg-Zr alloy, Acta Mater. 44 (1996) 1899–1915.

[177] B.I. Rodgers, P.B. Prangnell, Quantification of the influence of increased pre-stretching on microstructure-strength relationships in the Al-Cu-Li alloy AA2195, Acta Mater. 108 (2016) 55–67. doi:10.1016/j.actamat.2016.02.017.

[178] A.K. Khan, J.S. Robinson, Effect of cold compression on precipitation and conductivity of an Al-Li-Cu alloy, J. Microsc. 232 (2008) 534–538. doi:10.1111/j.1365-2818.2008.02116.x.

[179] B.M. Gable, A.W. Zhu, A.A. Csontos, E.A.J. Starke, The role of plastic deformation on the competitive microstructural evolution and mechanical properties of a novel Al-Cu-Li-X alloy, J. Light Met. 1 (2001) 1–14. doi:10.1016/S1471-5317(00)00002-X.

[180] V.G. Davydov, L.B. Ber, V.N. Ananiev, A.I. Orozov, M. V. Samarina, The heat treatment effect on thermal stability of Al-Li alloys at low temperatures, in: ICAA-6, 1998: pp. 985–990.

[181] Y. Mou, J.M. Howe, E.A. Starke, Grain-Boundary Precipitation and Fracture Behavior of an

Al-Cu-Li-Mg-Ag Alloy, Metall. Mater. Trans. A. 26 A (1995) 1591–1595.

[182] Arconic, Aluminum alloy 2055-T84 extrusions, 2016.

[183] Alcoa, ALLOY 2099-T83 AND 2099-T8E67 EXTRUSIONS, 2005. https://www.arconic.com/hard_alloy_extrusions/catalog/pdf/alloy2099techsheet.pdf.

[184] Y. Zhou, Z. Liu, S. Bai, P. Ying, L. Lin, Effect of Ag additions on the lengthening rate of Ω plates and formation of σ phase in Al-Cu-Mg alloys during thermal exposure, Mater. Charact. 123 (2017) 1–8. doi:10.1016/j.matchar.2016.11.008.

[185] S. Bai, P. Ying, Z. Liu, J. Wang, J. Li, Quantitative transmission electron microscopy and atom probe tomography study of Ag-dependent precipitation of Ω phase in Al-Cu-Mg alloys, Mater. Sci. Eng. A. 687 (2017) 8–16. doi:10.1016/j.msea.2017.01.045.

[186] C.R. Hutchinson, X. Fan, S.J. Pennycook, G.J. Shiflet, On the origin of the high coarsening resistance of Ω plates in Al-Cu-Mg-Ag alloys, Acta Mater. 49 (2001) 2827–2841.

[187] D. Bakavos, P.B. Prangnell, B. Bes, F. Eberl, The effect of silver on microstructural evolution in two 2xxx series Al-alloys with a high Cu:Mg ratio during ageing to a T8 temper, Mater. Sci. Eng. A. 491 (2008) 214–223. doi:10.1016/j.msea.2008.03.014.

[188] E. Gariboldi, P. Bassani, M. Albu, F. Hofer, Presence of silver in the strengthening particles of an Al-Cu-Mg-Si-Zr-Ti-Ag alloy during severe overaging and creep, Acta Mater. 125 (2017) 50–57. doi:10.1016/j.actamat.2016.11.056.

[189] H. Qi, X.Y. Liu, S.X. Liang, X.L. Zhang, H.X. Cui, L.Y. Zheng, F. Gao, Q.H. Chen, Mechanical properties and corrosion resistance of Al–Cu–Mg–Ag heat-resistant alloy modified by interrupted aging, J. Alloys Compd. 657 (2016) 318–324. doi:10.1016/j.jallcom.2015.10.094.

[190] J.B. Zhang, Y.A. Zhang, B.H. Zhu, R.Q. Liu, F. Wang, Q.M. Liang, Characterization of microstructure and mechanical properties of Al-Cu-Mg-Ag-(Mn/Zr) alloy with high Cu:Mg, Mater. Des. 49 (2013) 311–317. doi:10.1016/j.matdes.2013.01.044.

[191] X.Y. Liu, Q.L. Pan, X.L. Zhang, S.X. Liang, F. Gao, L.Y. Zheng, M.X. Li, Creep behavior and microstructural evolution of deformed Al-Cu-Mg-Ag heat resistant alloy, Mater. Sci. Eng. A. 599 (2014) 160–165. doi:10.1016/j.msea.2014.01.090.

[192] G. Itoh, Q. Cui, M. Kanno, Effects of a small addition of magnesium and silver on the precipitation of T1 phase in an Al-4%Cu-1.1%Li-0.2%Zr alloy, Mater. Sci. Eng. A. 211 (1996) 128–137. doi:10.1016/0921-5093(95)10157-8.

[193] B.-P. Huang, Z.-Q. Zheng, Independent and combined roles of trace Mg and Ag additions in properties precipitation process and precipitation kinetics of Al–Cu–Li–(Mg)–(Ag)–Zr–Ti alloys, Acta Mater. 46 (1998) 4381–4393. doi:10.1016/S1359-6454(98)00079-2.

[194] R. Zhu, Q. Liu, J. Li, S. Xiang, Y. Chen, X. Zhang, Dynamic restoration mechanism and physically based constitutive model of 2050 Al-Li alloy during hot compression, J. Alloys Compd. 650 (2015) 75–85. doi:10.1016/j.jallcom.2015.07.182.

[195] C. Laird, H.I. Aaroson, Crystallographic complexities in the Al-Cu system, Acta Metall. 15 (1967) 660–662. doi:https://doi.org/10.1016/0001-6160(67)90114-9.

[196] S.J. Kang, Y.W. Kim, M. Kim, J.M. Zuo, Determination of interfacial atomic structure, misfits and energetics of Ω phase in Al-Cu-Mg-Ag alloy, Acta Mater. 81 (2014) 501–511.

doi:10.1016/j.actamat.2014.07.074.

[197] S. Wenner, C.D. Marioara, S.J. Andersen, M. Ervik, R. Holmestad, A hybrid aluminium alloy and its zoo of interacting nano-precipitates, Mater. Charact. 106 (2015) 226–231. doi:10.1016/j.matchar.2015.06.002.

[198] S.Y. Duan, C.L. Wu, Z. Gao, L.M. Cha, T.W. Fan, J.H. Chen, Interfacial structure evolution of the growing composite precipitates in Al-Cu-Li alloys, Acta Mater. 129 (2017) 352–360. doi:10.1016/j.actamat.2017.03.018.

[199] European Commission - Climate Action, (n.d.). https://ec.europa.eu/clima/policies/transport/vehicles/proposal_en (accessed January 1, 2018).

[200] S. Katsikis, B. Noble, S.J. Harris, Microstructural stability during low temperature exposure of alloys within the Al-Li-Cu-Mg system, Mater. Sci. Eng. A. 485 (2008) 613–620. doi:10.1016/j.msea.2007.10.020.

[201] D. Tsivoulas, Heterogeneous Nucleation of the T1 Phase on Dispersoids in Al-Cu-Li Alloys, Metall. Mater. Trans. A Phys. Metall. Mater. Sci. 46 (2015) 2342–2346. doi:10.1007/s11661-015-2894-4.

[202] M. Murayama, K. Hono, Role of Ag and Mg on precipitation of T1 phase in an Al-Cu-Li-Mg-Ag alloy, 44 (2001) 701–706.

[203] V. Araullo-Peters, B. Gault, F. De Geuser, A. Deschamps, J.M. Cairney, Microstructural evolution during ageing of Al – Cu – Li – x alloys, Acta Mater. 66 (2014) 199–208. doi:10.1016/j.actamat.2013.12.001.

[204] N. Ott, Y. Yan, S. Ramamurthy, S. Kairy, N. Birbilis, Auger electron spectroscopy analysis of grain boundary microchemistry in an Al-Cu-Li alloy, Scr. Mater. 119 (2016) 17–20. doi:10.1016/j.scriptamat.2016.03.021.

[205] Q. LIU, R. hua ZHU, J. feng LI, Y. lai CHEN, X. hu ZHANG, L. ZHANG, Z. qiao ZHENG, Microstructural evolution of Mg, Ag and Zn micro-alloyed Al–Cu–Li alloy during homogenization, Trans. Nonferrous Met. Soc. China (English Ed. 26 (2016) 607–619. doi:10.1016/S1003-6326(16)64149-3.

[206] A.K. Khan, J.S. Robinson, Effect of silver on precipitation response of Al–Li–Cu–Mg alloys, Mater. Sci. Technol. 24 (2008) 1369–1377. doi:10.1179/174328408X262391.

[207] R. Yoshimura, T.J. Konno, E. Abe, K. Hiraga, Transmission electron microscopy study of the evolution of precipitates in aged Al–Li–Cu alloys: the Theta and T 1 phases, Acta Mater. 51 (2003) 4251–4266. doi:10.1016/S1359-6454(03)00253-2.

[208] H. Ovri, E.A. Jägle, A. Stark, E.T. Lilleodden, Microstructural influences on strengthening in a naturally aged and overaged Al-Cu-Li-Mg based alloy, Mater. Sci. Eng. A. 637 (2015) 162–169. doi:10.1016/j.msea.2015.04.039.

[209] G.E. Totten, D.S. MacKenzie, Volume 2: Alloy production and Materials Manufacturing, in: Handb. Alum., 2003: p. 731.

[210] W.D. Callister, D.G. Rethwisch, Materials Science and Engineering, John Wiley, 201

PART B
KNOCK DAMAGE ON AUTOMOTIVE PISTONS

The whole study of knocking damage on Al pistons is part of a wider project, carried out thanks to the cooperation among Ferrari Auto S.p.A. (Dept. of Powertrain Development), Fluid Machinery Research Group- Unibo and Metallurgy Research Group - Unibo, which is aimed at modelling and real-time controlling knock-induced damage on aluminium forged pistons. The final target is to develop an on-board spark advance controller, able to push the limits of engine calibration towards the maximum efficiency, while safeguarding components functionality. As mentioned in the General Introduction Sect., the context of this project is the never-ending research aimed to increase the efficiency of ICEs, due to the growing concerns on global environmental protection. Against this background, it is even more challenging the scenario for sports cars producers, who have to guarantee high performance against moderate fuel consumption.

Chapter 5 contains the theoretical background of Part B and it deeply explains the state of the art in terms of ICEs efficiency and the renewed interest in knock. The most promising strategies to reduce fuel consumption usually produce more favourable knocking conditions inside the combustion chamber. Knock has always been considered detrimental for engine life, however a distinction should be made between severe and light knocking combustions: the last do not compromise engine functionality and might be tolerated, up to a certain threshold, in order to gather higher engine efficiency.

Chapter 6 and Chapter 7 collect indeed the results of the experimental activities (bench tests) carried out at Unibo on Ferrari California T engine. In particular, each Chapter focuses on a specific step of knocking damages characterization:

- Chapter 6 aims to determine the main knocking effects on pistons, which are the most sensitive among the combustion chamber components, and the consequences of the damage on their functionality. The internship carried out in the Failure Analysis Area of Powertrain Development Dept. – Ferrari Auto S.p.A. was fundamental to both acquire data and provide a correct

interpretation for each damage. The mechanisms of knocking damage were also in-depth studied from a microstructural point of view.

- Chapter 7 aims to establish an experimental methodology able to objectively quantify knocking damage in terms of engine reduced functionality. Alongside this objective, equally crucial is to identify the relationship between engine calibration parameters and knocking damage, in order to eventually develop an on-board, real-time algorithm able to control the knocking intensity for a higher combustion efficiency compatible with a targeted piston life. This is an ambitious target whose optimizing is still ongoing.

THEORETICAL BACKGROUND

Chapter 5:

Engine efficiency and abnormal combustions

5.1 Engine efficiency

Generally speaking, the power P delivered by the engine is expressed by Eq.5.1: it is related to fuel conversion efficiency (η_{fuel}), volumetric efficiency (η_{vol}), lower heating value of the fuel (Q_{HV}), volume displaced by the single piston (V_d), number of cylinders (N_{cyl}), inlet air density ($\rho_{a,i}$), fuel/air ratio (F/A) and crankshaft rotational speed (rps [rotation/second]), divided by 2 revolutions per power stroke in four-stroke cycle engines:

$$P = \eta_{fuel} \cdot \eta_{vol} \cdot \frac{Q_{HV} \cdot V_d \cdot N_{cyl} \cdot \rho_{a,i} \cdot (F/A) \cdot rps}{2}$$

Eq.5.1: Formula for engine power P.

In order to achieve high power output and high performance, Eq.5.1 clearly shows the influence of:

- Fuel conversion efficiency (η_{fuel}), which directly affects fuel consumption, and thus represents the key parameter that has to be addressed to achieve the emission targets.
- Type of adopted fuel (Q_{HV}, F/A). Action on fuels is a feasible option just for racing engines, not for road vehicles, since the available fuel is imposed by gas stations. These parameters will not be discussed later on.
- Volumetric efficiency (η_{vol}), inlet air density ($\rho_{a,i}$), engine capacity (V_d, N_{cyl}), which contribute to the targeted engine performance. All of these factors have a substantial influence on engine power but do not affect fuel consumption, hence will not be further analysed. It is also worth mentioning that the today trend is to considerably favour an increase of η_{fuel} at the expenses of η_{vol}., as confirmed by the renewed interest in Miller cycle [1].

Due to its importance, the fuel conversion efficiency η_{fuel} deserves a more in-depth analysis. This single parameter indeed consists of different efficiency factors:

- Thermodynamic efficiency of the ideal combustion cycle representative of spark-ignition engines
- Cycle efficiency related to spark timing and finite combustion speed
- Efficiency related to pumping losses
- Chemical efficiency, intended as 100% in case of complete combustion
- Efficiency related to thermal heat exchange, intended as 100% in the ideal case of the adiabatic combustion chamber.

Thermodynamic efficiency

The formula of thermodynamic efficiency can be determined from a thermodynamic analysis of the indicating engine cycle, under the assumption that the spark-ignition combustion process can be represented by the well known Otto cycle, considering the compression and expansion strokes as isoentropic processes, and the heat addition cycle as a constant volume process [2–4]. The work per cycle W_c is obtained as the sum of compression and expansion stroke work per cycle, while the inducted energy is represented by the chemical energy provided by the mass of fuel inducted per cycle (m_f). With reference to Fig.5.1, indicating as r_c the compression ratio = $V_5/V_4 = V_2/V_3$, and indicating as $\gamma = C_p/C_v$ the ratio between heat capacity at constant pressure and heat capacity at constant volume, the thermodynamic efficiency η_{th} is given by Eq.5.2. This distinctly highlights that η_{th} strictly depends on the compression ratio.

$$\eta_{th} = \frac{W_c}{m_f \cdot Q_{HV}} = \frac{m \cdot c_v(T_2 - T_3) + m \cdot c_v \cdot (T_4 - T_5)}{m_f \cdot Q_{HV}} =$$

$$= \frac{m \cdot c_v \cdot (T_2 - T_3) + m \cdot c_v \cdot (T_4 - T_5)}{m \cdot c_v \cdot (T_4 - T_3)} = 1 - \frac{T_5 - T_2}{T_4 - T_3} =$$

$$= 1 - \frac{T_5\,(1 - T_2/T_5)}{r_c{}^{\gamma-1} \cdot T_5 \; - r_c{}^{\gamma-1} \cdot T_2} = 1 - \frac{1}{r_c{}^{(\gamma-1)}}$$

Eq.5.2: Formula for engine thermodynamic efficiency.

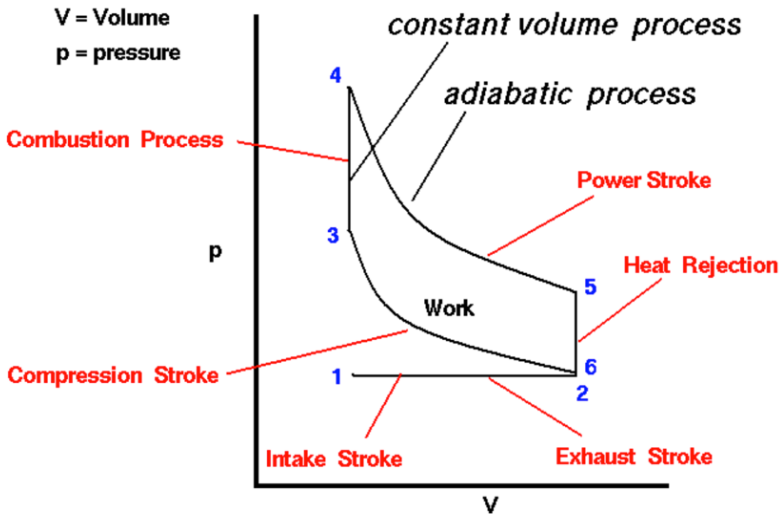

Fig.5.1: Schematic of Otto cycle, which is usually considered as a reference for internal combustion engines [5].

Cycle efficiency related to spark timing and finite combustion speed

Spark timing is a key operating variable affecting the performance of spark-ignition engines, their efficiency and emissions at any given load and speed, since the trigger of combustion determines the combustion centre of gravity and, as a consequence, the peak cylinder pressure. If spark timing is too much advanced, combustion starts considerably before piston top dead centre (TDC). Even if peak pressure might be increased compared to lower spark advanced cycles (Fig.5.2a, blue line VS red line), the dissipation of energy due to the compression work spent up to the TDC is not balanced by the higher expansion stroke, therefore the work achieved by the overall indicated pressure cycle is reduced (see lower η_{timing} associated to blue line VS η_{timing} associated to red line in Fig.5.2b). In contrast, if combustion start is too much retarded (see green, black or pink lines in Fig.5.2a), the lower peak pressure is the main responsible of lower η_{timing} (Fig.5.2b). At any fixed rpm, there exists a specific spark timing which gives the maximum engine torque under the same operating conditions.

In addition to that, also the combustion duration affects the cycle efficiency, as reported in Fig.5.2 (c), (d): under the same engine parameters (spark advance, inducted energy, rpm), the cycle efficiency is lower at lower combustion speed due to the reduced expansion ratio.

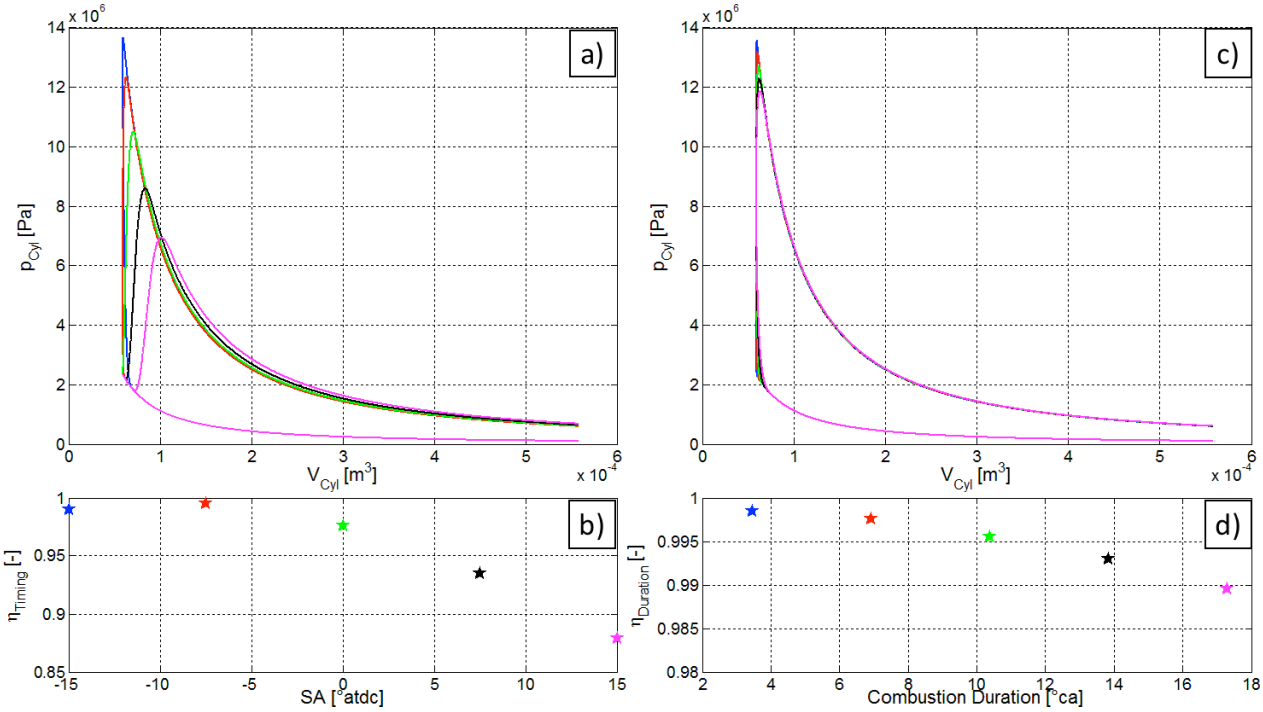

Fig.5.2: Combustion cycle efficiency related to spark timing (a, b) and finite combustion speed (c, d).

Efficiency related to pumping losses, chemical efficiency, heat exchange

Pumping losses are of course undesirable, since they produce a negative work of the indicating cycle. The chemical efficiency is related to the fuel complete combustion and it is enhanced by fuel homogeneous distribution inside the combustion chamber and fuel/air ratio equal to the stoichiometric ratio. Heat exchange from the combustion chamber towards pistons, engine crankshaft, engine head and engine coolant is unavoidable and necessary to both components structural strength and to avoid abnormal combustions, but it penalises engine efficiency.

Given these premises, the today main strategies aiming to boost fuel economy, while achieving the targeted power output, focus on:

1. Higher compression ratio* [6–8], which allows a higher thermodynamic efficiency as previously mentioned.
2. Optimisation of indicating cycle efficiency through advanced spark timing* [9] and increased combustion speed, with the aim to reach the maximum expansion ratio.
3. Direct injection [10–17], which allows to optimise the injection strategy in terms of charge stratification, fuel/air mixing and spark timing over the whole operating range. Powering

through fuel injection modulation and splitting leads to significant emissions reduction (especially soot) and to higher indicated mean effective pressure (IMEP) and combustion efficiency.

4. Engine downsizing*. By reducing the capacity of engine, the time of operation at higher loads is extended, and the results are lower pumping losses in part load operations thanks to a wider open throttle [17]. The re-introduction of turbochargers is needed in order to maintain adequate vehicle acceleration and top speed [13,17,18].

**(under knock limitations)*

The strategies highlighted by the superscript *, however, are implemented under knock limitations. All of these, in fact, lead to higher pressure and temperatures in the combustion chamber, conditions which make the engine more susceptible to abnormal combustion modes, like engine knock, mega-knock and pre-ignition. The possibility to incur in abnormal combustions is therefore the main limitation to engine efficiency.

5.2 Abnormal combustions: literature review

Since the very first development of internal combustion engines, abnormal combustions have been considered of concern because, when severe, they can cause detrimental engine damage. The traditional philosophy that *all* abnormal combustions are damaging has caused engine manufacturers and calibration engineers to operate with extremely large safety margins [19]. The today aim is, in fact, to attain the maximum thermal efficiency while *absolutely* avoiding knock [8]. A distinction should be made, however, between two completely different types of abnormal combustions, namely knock and pre-ignition, which are visually reported in Fig.5.3.

The characteristics of these abnormal combustions are separately described in Sect.5.2.1 and Sect.5.2.2, while their related damages are reported in Sect.5.2.3.

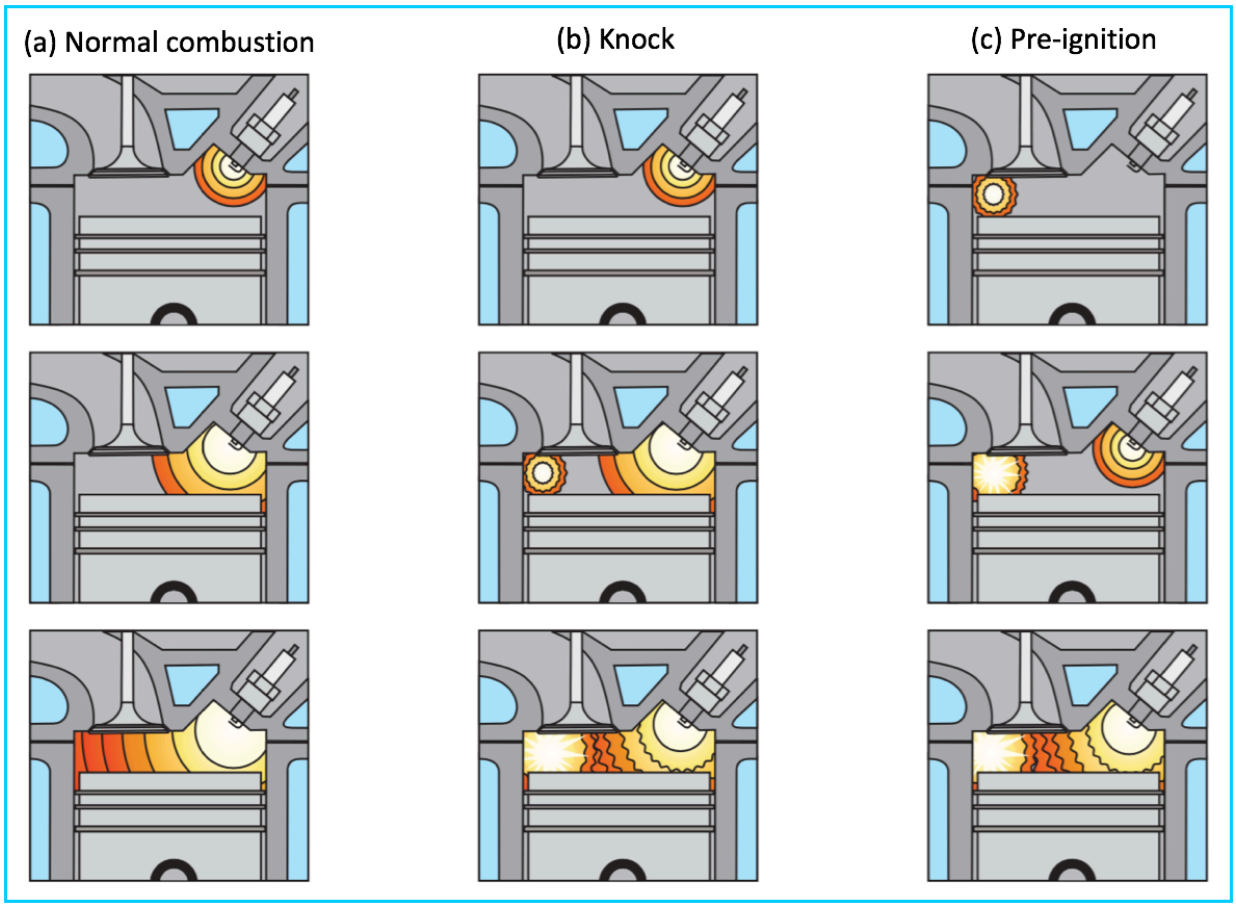

Fig.5.3: Difference between a normal combustion process (a), a knocking combustion (b) and a pre-ignition (c) [20].

5.2.1 Knocking combustions

Knock characteristics

The normal combustion shown in Fig.5.3 is a smooth turbulent flame propagation, with flame trajectory almost linear [21]. Knock consists indeed of the spontaneous ignition of one or more local regions within the end-gas (fuel, air, residual gas, mixture), ahead of the propagating flame [2]. When this abnormal combustion process takes place, the flame surface wrinkles and increases, leading to a more intense burning rate [2,21]: the result is an extremely rapid release of much of the chemical energy in the end gas, causing very high local pressure and the propagation of pressure waves of substantial amplitude across the combustion chamber, which make the engine structure vibrating at its natural frequencies [2,18]. This provides the classical knock noise.

Due to this knock peculiarity, one of the most sensitive indexes for knock detection is the Maximum Amplitude Pressure Oscillation (MAPO), which computes the maximum absolute value of the band-pass filtered pressure signal, as reported in Eq.5.3 [9]. A comparison between in-

chamber pressure signals during normal and knocking combustion cycles is offered by Fig.5.4. It should be pointed out that MAPO is defined within a single combustion cycle. Due to the cycle-to-cycle variation and due to the stochastic nature of the knocking combustion, a statistical approach is needed to determine the severity of knock during a test. MAPO index is thus usually evaluated in terms of percentiles (MAPO n^{th}%) inside a moving buffer of cycles, and the resulting signal is commonly averaged.

It is MAPO itself to be substantially limited during engine calibration. In fact, knock pressure oscillations (whose maximum is described by MAPO) simultaneously cause both mechanical and thermal stresses, since they significantly increase local peak pressure and substantially enhance the heat transfer [18,22] towards combustion chamber components. The increased heat flux, in particular, results from the fact that pressure waves disturb the insulating quench zone at the surfaces of the combustion chamber. It should be also pointed out that, as highlighted in Part A of this Ph.D. thesis, high temperature further intensifies the consequences of mechanical stresses, in particular on Al components, due to material softening and overaging.

$$MAPO = max\left(\left|P_{cyl\_filt}\right|\right)_{\vartheta_i}^{\vartheta_f}$$

Eq.5.3: Formula for MAPO parameter, which is usually adopted to define the severity of knock [9].

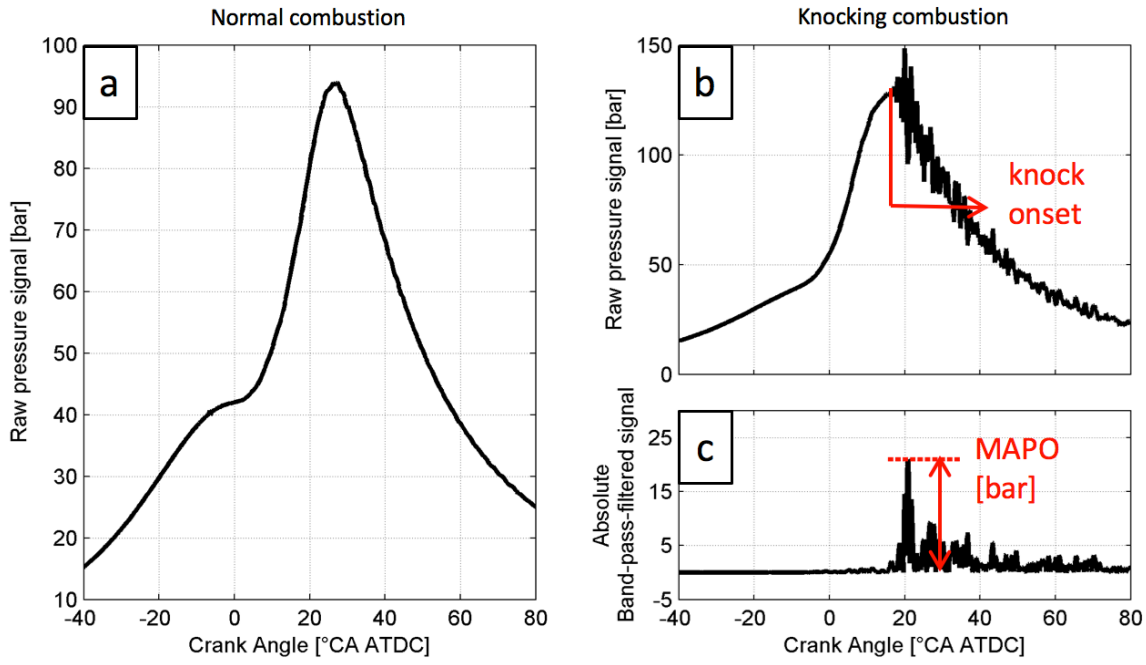

Fig.5. 4: In-chamber pressure signals VS crank angle during (a) Normal combustion, (b) knocking combustion. (c) Visual explanation of the band-pass filtered pressure signal and determination of MAPO, according to Eq.5.3.

Knock causes

It can be inferred that conventional knock usually occurs because the spark-triggered flame propagation compresses the end unburned gas to auto-ignition. Several recent studies [8,13,16,21], many of which with high speed direct photography and pressure acquisition, confirm in fact the theory of auto-ignition of the end-gas as the trigger for knock, and underline the substantial impact of the initial conditions (pressure and temperature) on knocking development. In particular, pressure at spark timing plays a key role, determining almost entirely the temperature and pressure conditions in the end gas regions at the onset of knock and thus controlling the chemical reactivity of the mixture; compression ratio has a lower influence.

Towards light knock acceptance

As highlighted in Sect.5.1, knock is an inherent constraint on engine performance and efficiency, because it limits the today main strategies aimed to boost fuel economy. Since the term "knock" is still deeply related to unfavourable consequences, the current guideline in engine calibration is that knock must be totally and carefully avoided [11], even if the strategies to prevent knock (namely to decrease the compression ratio, to retard the spark timing, to use cooled Exhaust Gas Recirculation [8,11,16]) strongly penalise engine efficiency. This trend clearly explain why several recent research activities are indeed focused on the signals and methodologies able to precisely detect the knocking combustion modes (such as in-cylinder pressure analysis [9,11], optical investigations [6,7,11,17], engine block vibration [11], exhaust gas temperature [11]), rather than deeply understanding the mechanisms of knock damage.

However, as already hypothesized by Nates et al. in the '90s [8,19,23–25], *only when exceeding a certain threshold* knock compromises engine functionality, and the threshold depends both on: (i) the severity of thermo-mechanical knock induced stresses; (ii) material properties. Light knock might be not harmful and even beneficial in terms of both engine efficiency and low emissions: if light knock is accepted, in fact, the engine operating point can be shifted towards the maximum efficiency conditions. This aspect is graphically highlighted in Fig.5.5:

- the green line shows the safety threshold today adopted, which is known not to produce engine damage. This threshold lead to both higher fuel consumption and less knocking phenomena

- the orange line represents a potential new operating point for the engine, which guarantees a considerably reduced fuel consumption, at the expenses of increased knock probability. Its consequences on engine durability are however unexplored.

The rising questions are therefore: "How much knock is in fact damaging?" and "What is the relationship between knock intensity and knock damage?" [9,19,23,25,26]. This forward-looking issue was at first raised by Fitton and Nates in 1996 [19] but it still remains open.

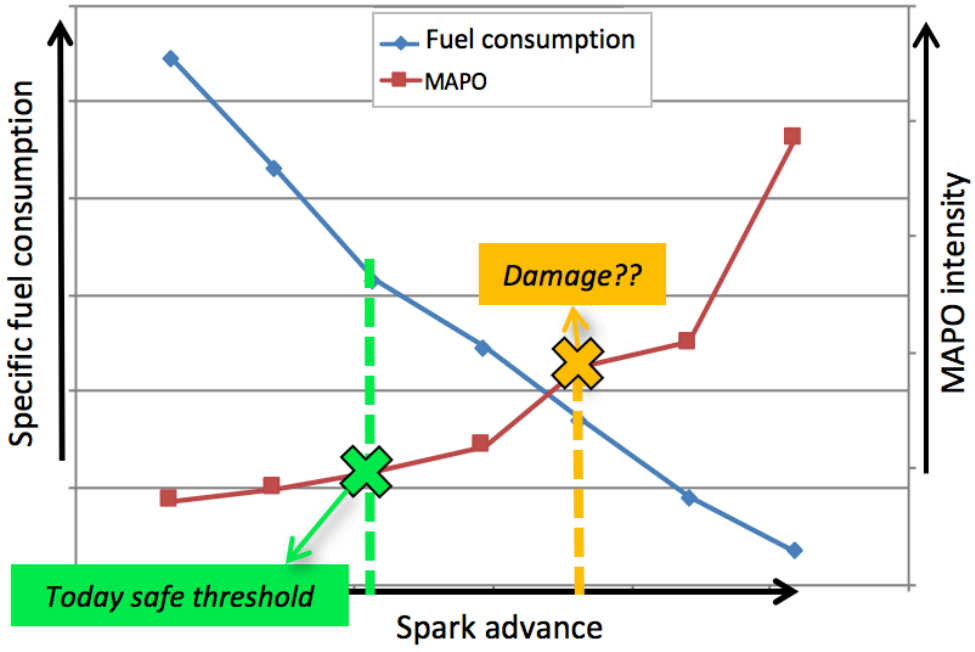

Fig.5.5: Graphical explanation of the effects of increased spark advance on both fuel consumption and knock tendency: the green line shows the today safety threshold, which lead to both higher fuel consumption and less knocking phenomena; the orange line represents a potential new operating point for the engine, which guarantees a considerably reduced fuel consumption, at the expenses of increased knock probability. Numerical values are not reported due to data confidentiality.

Aiming to partially tolerate knocking combustions, an additional critical aspect should be considered: knock is an "autocatalytic" phenomenon which, unless rapidly extinguished, might grow in intensity, as confirmed by the actual experimental points reported in Fig.5.5: the red line indicating MAPO intensity shows a steep increase over a certain level. The consequence is a potential into pre-ignition: as explained in [27], this abnormal combustion can occur in case of knocking operation near thermal limit conditions. The detrimental consequences of pre-ignition have been also experienced by our Research Group during knock bench tests at Unibo, as reported in [28]: here, pre-ignition occurs after a relatively short sequence of consecutive heavy knocking cycles, and the operation rapidly migrates toward a self-sustaining condition which led to engine failure.

In view of this, the today most challenging task in engine calibration is the setting of knock threshold levels which are able to both prevent damages and maximize engine performance [9].

5.2.2 Pre-ignition

Pre-ignition characteristics

As highlighted in Fig.5.3, the start of combustion occurs before spark timing [2,16] during pre-ignition. Due to this earlier triggering, pre-ignition is characterised by a more vigorous peak firing pressure compared to normal combustions, which results in exceptionally high thermo-mechanical stresses on combustion chamber components. Every pre-ignition overheats the hot surface due to the early combustion, resulting in a higher pre-ignition probability for the next cycle; the result is a self-sustaining, thus detrimental, operation. Among abnormal combustions, pre-ignition is potentially the most damaging.

Pre-ignition causes

Pre-ignition is usually triggered by a hot spot on the combustion chamber walls [2]. The "hot-spots" should be high surface-to-volume ratio zones of the chamber, such as the spark-plug electrodes or ceramic insulator, exhaust valves, piston valve reliefs, which showed noticeable evidence of melting at the end of the operation. The angular position is stochastic and therefore variable.

5.2.3 Damages related to abnormal combustions

It is common knowledge that even a few cycles of pre-ignition are deleterious in terms of engine life [16]. Among the typical pre-ignition damages there are [16,29]:

- Rupture of spark-plug electrode or ceramic insulator due to thermal shock (Fig.5.6). In this case, usually spark leaks can be observed, indicating reduced spark plug functionality. Aluminum deposits coming from pistons are usually observed, while melting of the electrodes and ceramic insulator is perceivable in the severest abnormal combustions, due to higher thermal loads. It often happens that spark-plug rupture and exhaust valve melting (Fig.5.7) are simultaneously observed: this is due to the fact that debris from broken spark plug might be

jammed between the valve seat (cylinder head) and the valve body during the exhaust stroke; as a consequence, an anomalous passage of exhaust gases from combustion chamber to the upper part of valve stem is produced, finally leading to valve melting.

- Consistent wear of piston ring groove, formation of blow-by channels, breakage of piston lands, ring gap closure (Fig.5.8). These damages usually occur at non-thrust side of the piston, due to the relatively large clearance near combustion TDC.
- Piston seizure (Fig.5.8) and cylinder liners damage, consequence of piston seizure. The insufficient clearance between the matching surfaces and the resulting friction further intensify the heat-induced expansion, finally resulting in complete piston seizure. Such destructive effects are reported in (Fig.5.9): several seizure marks are visible on cylinder liner, together with transferred Al material. It is interesting to point out that also melting of the liner is visible at the TDC, beneath the location of piston valve relief, which is supposed to be the hot spot triggering knocking and pre-ignition combustions.

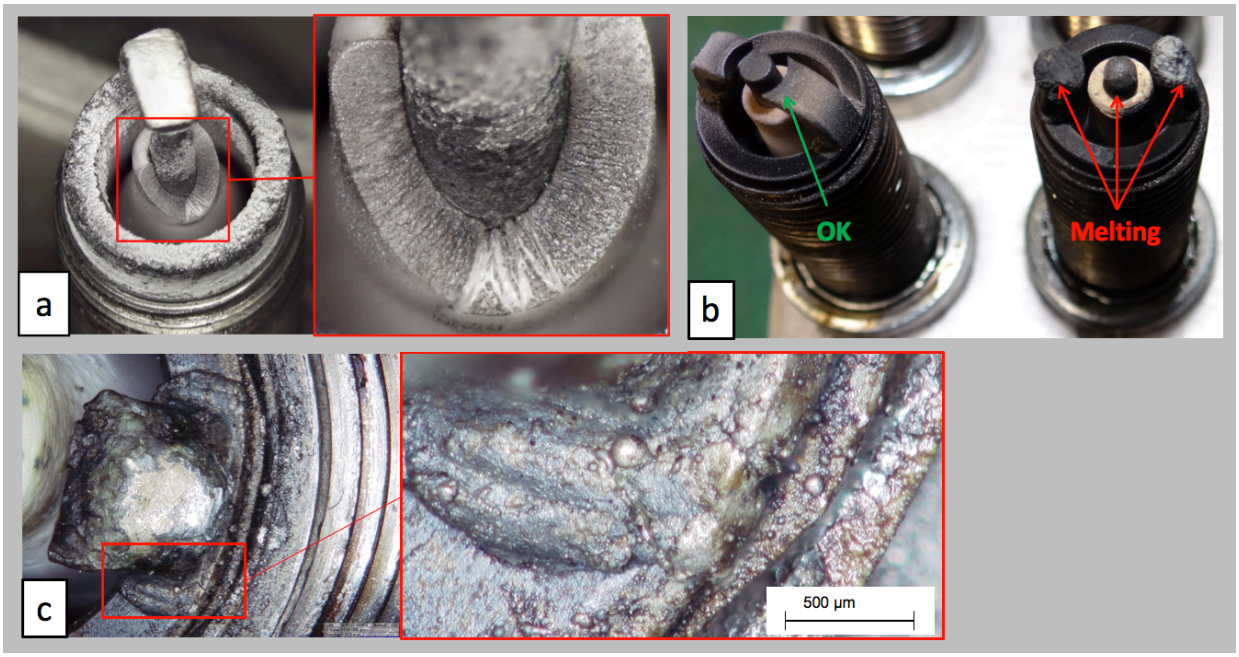

Fig.5.6: Spark-plug failure caused by pre-ignition or heavy knock. (a) Breakage of ceramic insulator and spark leaks, from [29]. *(b) Electrodes melting, from* [29]. *(c) 3D micrographs highlighting spark-plug failure due to pre-ignition; the high magnification of the enclosed area confirms melted drops on spark-plug metal body; images collected after the controlled knock/pre-ignition bench tests reported in* [28].

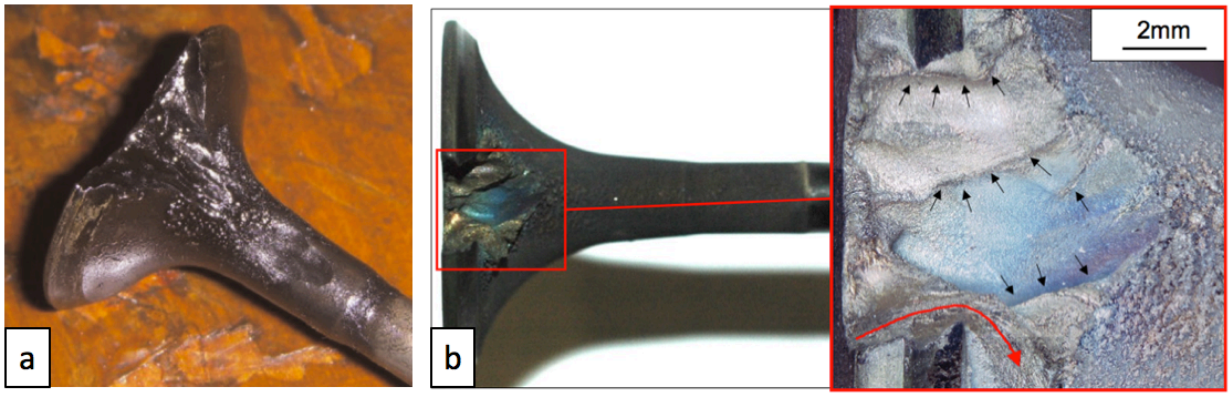

Fig.5. 7: (a) Exhaust valve melt caused by super-knock [16]. *(b) Similar damage of exhaust valve during knock/pre-ignition tests at Unibo. In both cases, an anomalous extended area of valve stem is covered by carbon de deposits, due to the abnormal passage of exhaust gases from combustion chamber to the upper part of valve stem, once valve failure has occurred. An additional higher magnification of exhaust valve damaged area is reported in b). Partially smoothed edges, indicated by arrows, reveal exhaust gas flow. A thin, adhering oxide skin (its colour ranging from yellow, straw to light blue) is formed during gas flow, due to the highly oxidising atmosphere.*

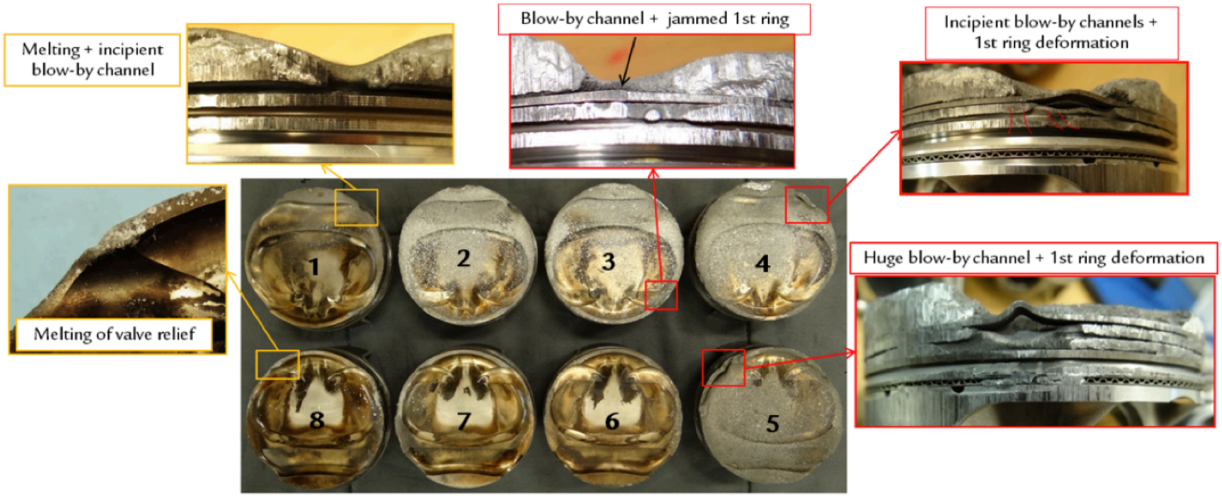

Fig.5.8: Effects of severe knocking combustions + pre-ignition on pistons.

Fig.5.9: Macrographs reporting piston and corresponding cylinder liner damage. (a) Evident piston seizure. (b) Heavy seizure marks due pre-ignition; in addition, transfer of Al and partial melting under valve relief location are observed.

It is also reported in literature that knock can significantly damage the engine components which form the combustion chamber, such as cylinder heads, cylinder liners, and above all pistons

[19,20,23–25]. According to Nates et al. [25], possible damages on pistons partially include those aforementioned:

- Surface erosion at piston top land and crown (Fig.5.10), in particular in the end-gas region (farthest from the spark-plug), which are more prone to auto-ignition; moreover, the damage is more evident at piston top land crevices, where local pressure conditions during knock occurrence are supposed to be far more severe than in the bulk of the combustion chamber [19]. This damage is reported to be rarely observed in old cast iron pistons [25].
- In some cases, also erosion at cylinder head is observed [11] (Fig.5.11).
- Lands fracture, blow-by channel with subsequent power loss, piston seizure and jammed or broken rings in the most severe cases [23]. Nates et al. [25] thought this damage to be related to knock increased heat flux, which might lead to localised thermal expansion of both piston and rings. Damage more likely related to pre-ignition.

Even if the last catastrophic failures are traditionally attributed to knock, these are not merely caused by knock itself, but are rather the result of repeated, persistent knocking combustions, which grow in intensity, finally turning into mega-knock or pre-ignition [28]. On the contrary, the erosion surface damage highlighted in Fig.5.10 and Fig.5.11 is typical of knock pressure oscillations.

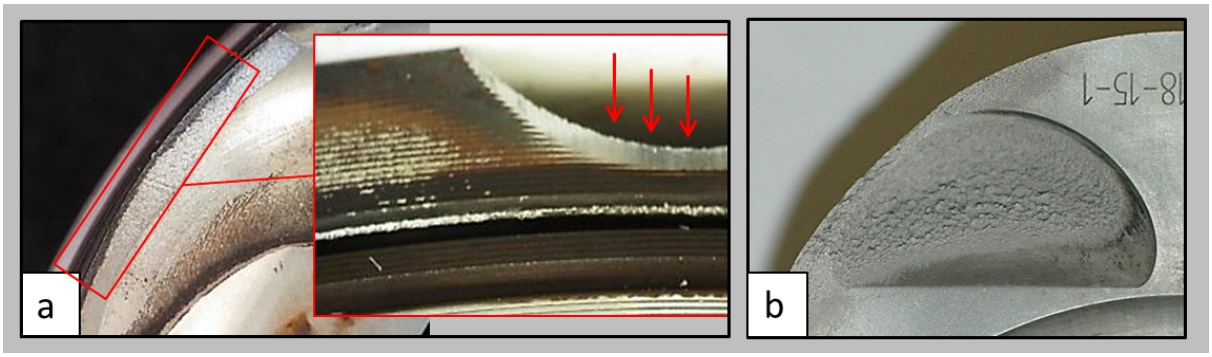

Fig.5.10: (a) Stereo-microscopy images at the intake valve relief, medium knocking erosion and tiny ring groove closure. (b) Macrograph at the exhaust valve relief, heavier knocking conditions: erosion is more pronounced [29].

Fig.5.11: Macrographs reporting erosion at cylinder heads, V8 turbocharged engines.

EXPERIMENTAL ACTIVITIES

Chapter 6:

Consequences of knock on Al pistons

Among all combustion chamber components, pistons are the most sensitive to knock damages and thus deserve an in-depth study. Chapter 6 is dedicated to this issue and it is divided as follows:

- Sect.6.1 describes in details the whole experimental set up which allows to carry out up to 10 bench tests under different engine operating points and to investigate the consequences of each single engine parameter variation. It also reports the characteristics of Al pistons investigated and the main techniques which were implemented to characterize the knock damage.
- Sect.6.2 collects the main results in terms of pistons damage characterization. The whole Sect. is an extract from the published paper "Knock induced erosion on Al pistons: examination of damage morphology and its causes", E.Balducci, L.Ceschini, N.Rojo, N.Cavina, R. Cevolani, M. Barichello, *Engineering Failure Analysis*, vol. 92, 2018, 12-31.
- Sect.6.3 shows the key role of pressure at knock onset in setting the upper limit of MAPO values, providing clearer understanding of the damage distribution in the knock intensity – thermal load domain. Most of the data and conclusions here collected have been also reported in the published paper "Investigation of Knock Damage Mechanisms on a GDI TC Engine", N.Cavina, N.Rojo, L.Ceschini, E.Balducci, L.Poggio, L.Calogero, R.Cevolani, *SAE Technical Papers*, vol. Sept, 2017.

6.1 Material and methods

6.1.1 Engine equipment and bench tests parameters

Supplied engine

All bench tests have been carried out on the 3.855 litre bi-turbo V8 GDI turbocharged engine of the Ferrari California T model, whose main features are reported in Fig.6.1. During the tests, every cylinder was equipped with a 6045A Kistler in-cylinder pressure transducer, whose signal was sampled at 200 kHz. The engine is also equipped with ION (ionization current) sensing system as standard production apparatus. Both in-cylinder pressure and ION signal have been recorded, aiming to develop, in a later stage of the project, an on-board controller based on ION signal.

Max power	412 kW/ 560 Hp at 7500 rpm
Max torque	755 Nm at 4750 rpm
Stroke	82 mm
Bore	86,5
Compression Ratio	9,4: 1
Spark plug	Centrally located
Displacement	3855 cc, 8 cylinder

Fig.6.1: Characteristics of the V8 turbocharged Ferrari California T engine adopted for bench tests.

Strategies for bench tests control

Due to the high power output of the engine, for brake cooling reasons, just one cylinder bank per time was subjected to knock test (apart from test #1 which was carried out in Ferrari

S.p.A. as later mentioned). In order to define and catalogue the damage caused by various knocking intensities and frequencies, during bench tests at Unibo the spark advance of *each* single cylinder was separately controlled by a rapid control prototyping system (Miracle® by Alma Automotive), replacing Eldor ECU. For the majority of the tests, the desired knocking levels have been defined in terms of target percentile values for MAPO parameter (Eq.5.3) and achieved thanks to a Proportional-Integral-Derivative (PID) controller. In specific, a real-time indicating system (OBI, On-Board Indicating® by Alma Automotive) communicates via CAN-bus (Controller Area Network) the knock index value (KI) of every combustion to the spark advance controller, which calculates the resulting knocking level and spark advance correction (ΔSA). Such information is transmitted, via CAN-bus again, to the ECU, which will apply the calculated correction to the subsequent combustion, for the given cylinder. Fig.6.2 [28] shows this very fast communication infrastructure that allows, for every cylinder, cycle-by-cycle spark advance control. As it is very difficult to instantaneously control a desired knock level due to the stochastic nature of the phenomenon, SA corrections are small and relatively unaggressive, typical of a PID control logic. In this way, the target level is reached, and the engine knock response (distribution of knock intensity) is practically equivalent to "regular" constant spark advance operation.

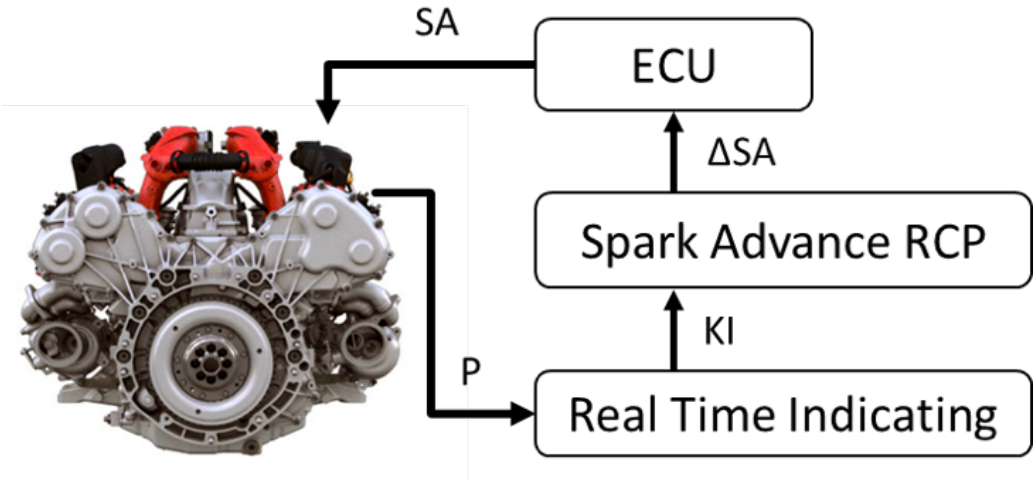

Fig.6.2: Knock controller layout during the experimental tests.

During the final step of the experimental activities, when a deeper knowledge of knocking phenomena was reached, bench tests have been controlled by an on-board implementable, real-time control strategy proposed by N.Rojo in his Ph.D. thesis, under the supervision of the Fluid Machinery Research Group (further details in his Ph.D. thesis). The last tests ultimately validate the knocking damage model discussed in the next Sect.

Summary of bench tests: aim of each test and knock target

Thanks to the flexible controller, the imposed knock target considerably changed for all cylinders and from one set to another. The engine operating points of 4500 and 6000rpm under WOT load have been investigated. Single bench tests conditions are following reported:

- Bench test #1 was the pilot bench test, carried out at Ferrari Auto S.p.A. under severe knocking conditions. The entire engine speed range was covered by the test (up to 7500 rpm), while only full load conditions were considered since they represent the most critical conditions in terms of knocking combustions.

  The aim of this preliminary test was to generate high knocking damage and to preliminary determine suitable techniques to detect damage. The output of this activity has been reported in ref. [26], and will not be further mentioned in this dissertation.
- Bench tests #2-#3-#4-#6 have been conducted at Unibo. The engine operating point of 4500rpm WOT was investigated, the intake manifold pressure being equal to 2200mbar and the normalized air-to-fuel ratio λ equal to 0.79. Different knocking combustions frequencies were also tested (namely MAPO 98% and MAPO 99.5%).

  These bench tests at first allowed to gain a broader understanding of knocking damage on pistons, highlighting that also the temporal distance between knocking combustions should be considered in the damage model. These results have been included in [30] and reported in Sect.6.2 since they are the most valuable in terms of knocking damage characterization.
- Bench test #5 was carried out at Unibo and produced pre-ignition as a consequence of the severe and persistent knocking conditions imposed at 4500rpm. This bench test offered the opportunity to investigate on the relationship between heavy knocking combustions, the related overheating of the combustion chamber components and the triggered pre-ignition combustions. The results of this activity have been collected in ref. [28].
- Bench tests #7-#8-#9 have been conducted at Unibo. The engine operating point of 6000 rpm WOT was investigated, the intake manifold pressure being equal to 2300 mbar and the normalized air-to-fuel ratio λ equal to 0.73. In order to further investigate on the relationship between knocking damage – knock intensity (MAPO) – pressure at knock onset, fuels with different knock resistance (RON number respectively equal to 95-91-100) have been employed.

The aim of these bench tests was to investigate on the effects of knocking events occurring under different p_max90% levels. The results of bench tests #7-#8 are reported in [31] and in Sect.6.3.

- Bench test #10-#11 have been carried out at Unibo at 6000 rpm WOT, the intake manifold pressure being equal to 2200 mbar and the normalized air-to-fuel ratio λ equal to 0.79. During these last bench tests, the damage model implemented by the Fluid Machinery Dept. was validated: a specific damage rate was imposed during the test and the subsequent pistons analysis led to few adjustments, confirming the robustness of the model.

6.1.2 Starting material

Pistons macro-characteristics

Ferrari California T engine is equipped with forged pistons provided by Mahle. Pistons are made of the near eutectic Al-Si-Cu-Ni-Mg alloy (Mahle M142P). The chemical composition was checked on pistons crown, through Glow Discharge Optical Emission Spectroscopy (GD-OES) analysis, with a sputtered burnt spot of 4mm diameter (Table 6.1).

Table 6. 1: Results of GD-OES chemical analysis on piston crown (average of 3 measurements).

Element	Si	Cu	Mg	Ni	Fe	Mn	Ti	Zn	Zr	V	Al
[wt%]	11.87	2.93	0.76	2.25	0.24	0.08	0.05	0.05	0.01	0.01	Bal.

The alloy has been widely described in Sect.1.2 and subjected to heat treatment optimization and chemical modifications during Ph.D. activities as reported in Sect.3.2.

The starting material was characterised by an average hardness equal to 120 HB. The heat treatment parameters have not been shared by pistons supplier; however, given the starting hardness values, it can be inferred that the typical T7 heat treatment was carried out, consisting of: solution treatment, quench and artificial aging prolonged over the peak aging condition (to provide better alloy stability). As can be observed from an illustrative macrograph of an as-received piston, before engine bench test (Fig.6.3), all pistons exhibit:

- an anodized layer, starting from the lowest part of the top land up to the relief groove below the 1st ring groove, as clearly indicated in blue both in Fig.6.3a and Fig.6.3b. Given its intrinsic hardness and chemical incompatibility with steel rings, the anodized layer is fundamental to avoid the 1st ring groove sticking and aluminum wear [32,33];

- a graphitic layer on piston skirt, shown by the yellow arrow in Fig.6.3a. This layer is aimed to improve boundary lubrication and reduce friction loss during piston alternating motion [33].

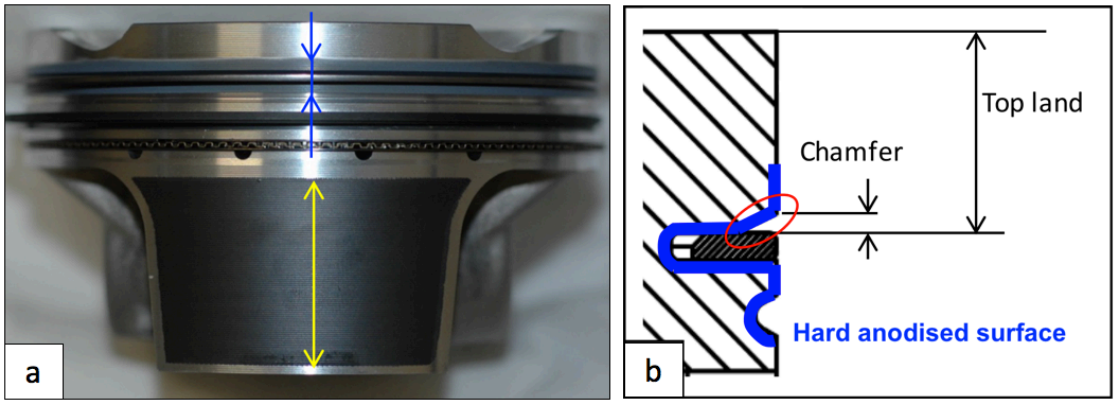

Fig.6. 3: Macrograph of an as-received new piston, lateral view from the intake side; blue arrows highlight the piston anodized layer, yellow arrow indicates the graphitic layer on piston skirt. (b) Schematic of piston section with focus on the 1st ring groove: the extension of the anodized layer is highlighted in blue; the chamfer area (most sensitive to knocking damage, as reported in the next paragraphs) is encircled in red (from [30]*).*

Hardness-Time-Temperature curves of Al piston alloy

Piston alloy thermal resistance was assessed through hardness-time-temperature curves, investigating the temperature range 175÷300 °C, since such temperatures are usually experienced by petrol engine pistons [34]. For the purpose, specific samples were machined from pistons and dedicated to overaging tests. Both Brinell hardness tests (with 2.5mm diameter indenter and 62.5kgf load, according to ASTM E 10-08 standard, adopting *Galileo Mod.A 00 durometer*) and micro-Vickers hardness tests (1kgf load and 10s dwell time, adopting *Galileo ISOSCAN AC micro-durometer*) were carried out on overaged specimens, in order to get equivalent HTT curves in two hardness scales. Each data point of the overaging curves (namely each time-temperature combination) represents the average of 6 Brinell hardness measurements or 6 micro-Vickers hardness measurements.

The overaging curves are reported in Fig.6.4a in HB scale. It is worth highlighting that prolonged exposure at temperatures higher than 250°C lead to the same plateau of residual hardness (67÷65 HB). Both Brinell hardness and micro-Vickers hardness tests were performed on samples after overaging, in order to estimate a correlation between the two hardness scales, as reported in Fig.6.4b. These experimental data allowed to determine the average operating temperature of pistons after bench tests.

In order to have a continuous relationship of hardness-time-temperature, the experimental data were modelled in Matlab® environment through the least squares method. The following Eq.6.1

was found to be appropriate to fit the experimental data, where HB is the residual Brinell hardness value after exposure at the temperature T [°C] for the soaking time t [h]. The accuracy of the model is highlighted in Fig.6.5. It is possible to state that the model error is always lower than 5%, except from a single experimental point.

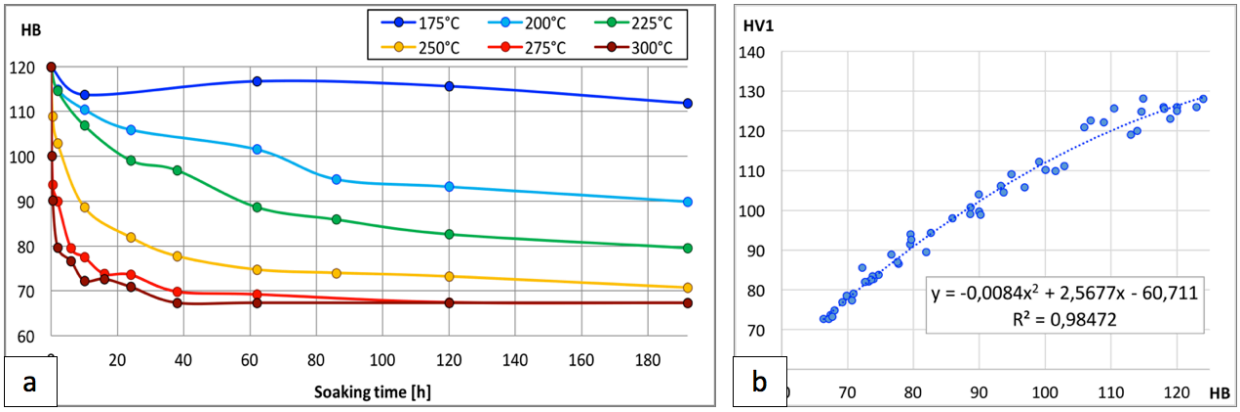

Fig.6. 4: Overaging curves (Brinell hardness) of Al-Si-Cu-Ni-Mg alloy, overaged in the range 175÷300°C up to 192h; (b) Relationship between Brinell and Micro-Vickers hardness values in the range of interest (from [30]*).*

$$HB = 219{,}6516 - 0{,}5473T + 0{,}0003T^2 + 81{,}1580\ln(t) - 0{,}626318\,T\ln(t) + 0{,}001106\,T^2\ln(t) - 5{,}827299\,(\ln(t))^2 + 0{,}031715\,T\,(\ln(t))^2 - 3{,}474714e-05\,T^2\,(\ln(t))^2 - 0{,}398005\,(\ln(t))^3 + 0{,}002514\,T\,(\ln(t))^3 - 3{,}567775e-06\,T^2\,(\ln(t))^3$$

Eq.6. 1: Model for hardness variation during overaging (at specific temperature T and time t of exposure) for piston alloy Al-Si-Cu-Ni-Mg, T7 heat treated (from [30]*).*

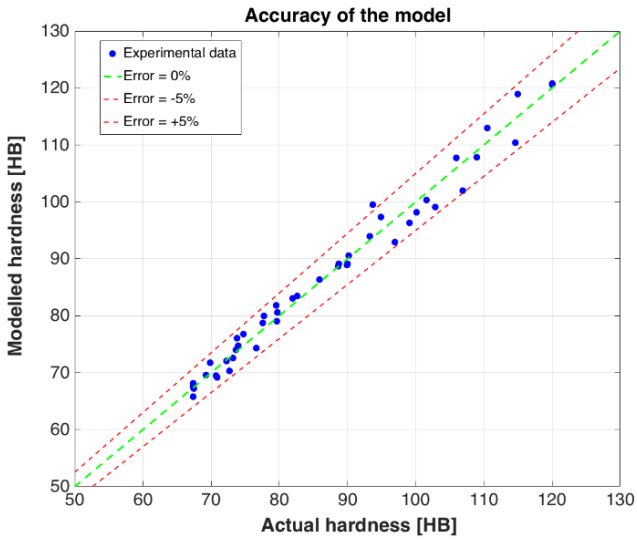

Fig.6.5: Accuracy of the model able to determine hardness-time-temperature relationship (from [30]*).*

6.1.3 Pistons characterization

In order to precisely establish the damage produced by knocking combustions, pistons have been carefully analysed both before and after bench tests, adopting the typical failure analysis techniques as following explained.

Characterization before bench test

The main methodologies of investigation before bench tests consisted of:

- Macrographs through *Nikon D40* digital camera, acquired both on pistons crown and on 4 angular positions of piston lands: intake, exhaust and pin axis side (Fig.6.6). The low magnification images allowed to have a complete overview of pistons and to record the details before bench test.
- 3D digital micrographs through *Hirox KH-7700* equipment. The higher magnification images were collected in particular at valve reliefs and anodized layer of the top land, aiming to record the surface finish of the as received components. Examples of these are reported in Fig.6.7.
- Brinell hardness measurements (2.5mm indenter diameter, 62.5kg load), carried out at the bottom of each piston before bench test in 4 different position (Fig.6.8a), adopting *Galileo Mod.A 00 durometer*. Piston crown was not touched in order not to compromise the combustion chamber; a few tests have been also carried out both at piston crown and bottom, showing a very slight variation (in the range of 1-2HB). Brinell hardness values can be therefore considered as representative of the as received state of the piston. It should be pointed out that a high variation in terms of starting hardness was detected on pistons (Fig.6.8b), and the difference was taken into account for the correct interpretation of the knock increased heat flux. This is particularly relevant for short bench tests (≤10h), due to the shape of overaging curves .
- Roughness tests, carried out using a HommelWerke profilometer, equipped with a TK300 stylus (tip radius 5µm). In particular, roughness tests were carried out in the anodized area above the 1st ring groove, aiming to detect erosion in this area. A measurement length of 1mm was selected, the cut-off being equal to 0.025mm (according to DIN 4768).
- Size of 1st ring groove, measured through Johnson gauge blocks (Fig.6.9). The dimensional tolerance indicated in the drawing for piston ring groove is in fact large, so that it is

necessary to characterize the state of the as received piston in order to detect limited plastic deformations after bench tests.

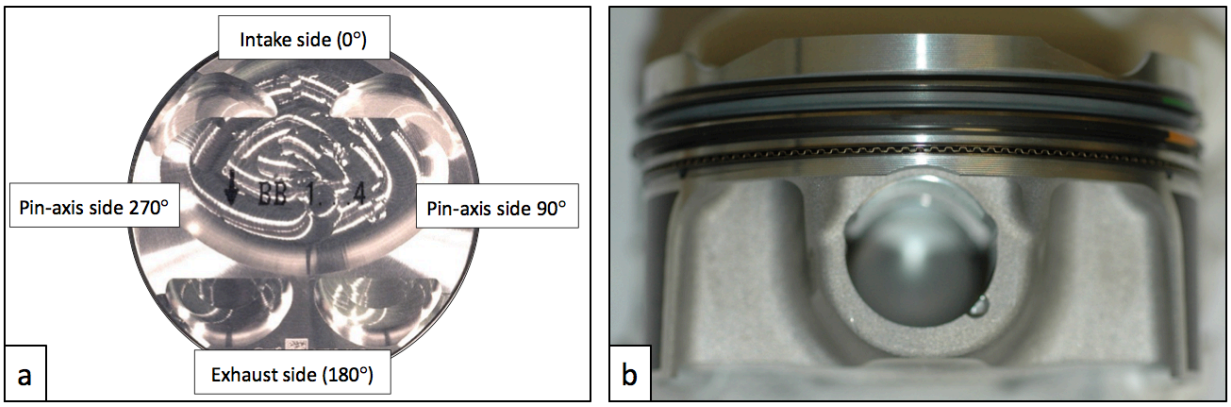

Fig.6.6: (a) Macrograph of piston crown before bench tests, with the indication of the 4 lateral areas of interest. (b) Illustrative macrograph of pin-axis side 90°.

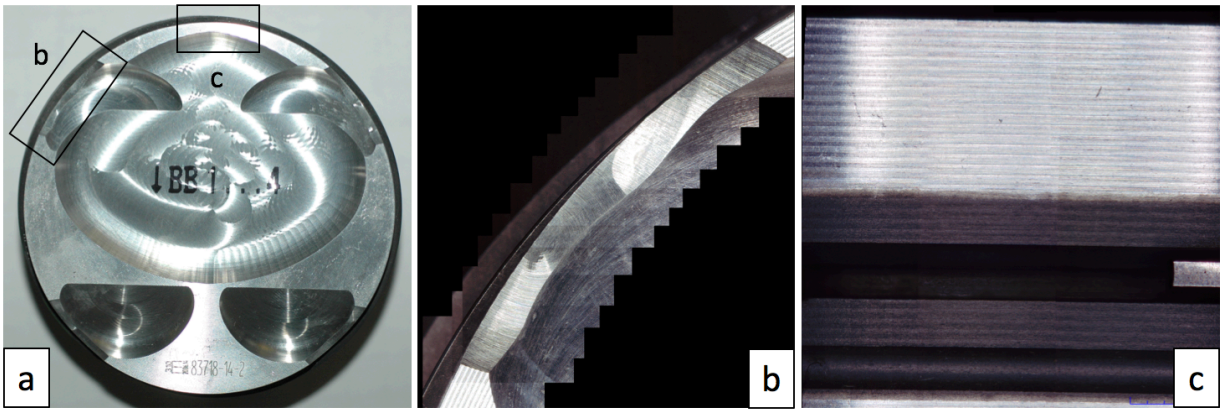

Fig.6.7: (a) Macrograph of piston crown before bench test, highlighting the areas investigated through Hirox micrographs: (b) intake valve relief and (c) top land and 1st ring groove, intake side.

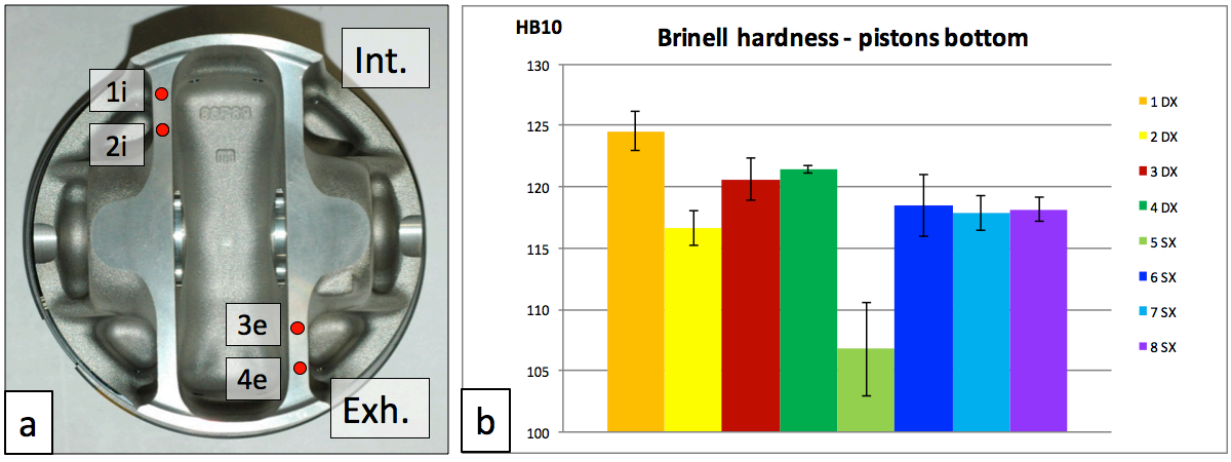

Fig.6. 8: (a) Points of measurement of Brinell hardness on pistons before bench tests. (b) Example of Brinell hardness variability on as-received pistons, to be taken into account in case of short bench tests.

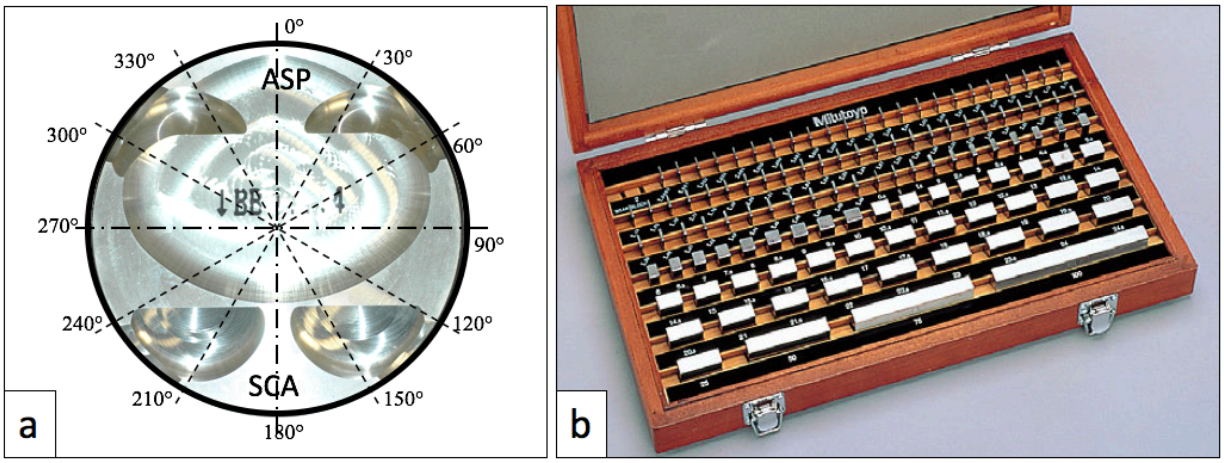

Fig.6.9: (a) Areas of measurement of piston 1st ring groove size. (b) Johnson gauge blocks adopted.

Characterization after bench test

The aforementioned steps for pistons characterization before bench test are all repeated after bench test, and in-depth analyses have been also added. In chronological sequence:

- Macrographs were acquired on pistons after bench test, before any washing procedure. These allow to collect information from carbon residues.
- Pistons were subjected to cleaning procedure, which consisted of 4h soaking in a neutral degreaser (UVEOL DET7) and gentle brushing, and final washing with acetone.
- Macrographs were once again taken after the degreasing step, to highlight the most damaged areas to be further examined.
- Visual analysis through 3D digital microscope was carried out in specific damaged areas, detected both by naked eye and macrographs. In particular intake and exhaust valve reliefs were investigated for all pistons, while analyses of the top land and 1st ring groove were carried out just in specific cases in which damage occurred. Piston valve reliefs were observed from the top, while piston top land from the lateral side, without any further preparation.

  The 1st ring groove was indeed observed after cutting pistons in correspondence of the 2nd ring groove and subsequently lathe machining up to the lower side of the 1st ring groove (as schematically explained in Fig.6.10a,b). This area was observed in the upper side (area highlighted in light blue in Fig.6.10b), which was found to be more sensitive to knock damage. By disclosing the upper side of the 1st ring groove, it was possible to observe and evaluate the wear (in particular the erosion) of the anodised layer inside the ring groove, which represents the actual and most important functional layer.

- Micro-Vickers hardness tests were performed on pistons crown after bench tests, in the exhaust and intake side (Fig.6.11). For the purpose, pistons were degreased and grinded up to 4000 grit size on their crown. The applied load was set equal to 1 kgf, and the dwell time equal to 10 s, adopting *Galileo ISOSCAN AC micro-durometer*. The choice of micro-Vickers rather than Brinell hardness tests was due to the need of acquiring information about local hardness variation (appreciable only at relatively low load); moreover, the limited thickness of piston crown in the intake side made it impossible to carry out Brinell tests according to ASTM E 10-08 standard. Micro-Vickers hardness tests on pistons were selected as an indicator of the average, local, in-service temperature.
- Roughness tests on the 1st ring groove anodized layer and piston valve reliefs, to detect (and possibly quantify) erosion. At least 3 measurements were performed for each area and the average of these was considered as representative.
- Measurements of piston 1st ring groove through gauge blocks, in order to evaluate the amount of plastic deformation produced by knock extreme thermo-mechanical stresses. Heavy abnormal combustions (i.e. knock, mega-knock or pre-ignition), might lead to crack formations and/or plastic deformation, which are detectable thanks to metrological tests
- Further visual analyses at the highest magnification were carried out through OM and SEM. OM analyses were carried out on metallographic section of the most damaged valve reliefs, aiming to underline the development of erosion in piston crown at valve reliefs and in the 1st ring groove; an *Optical Microscope Zeiss Axio® Image Analizer* was adopted.

  SEM analyses did not require any specific sample preparation, except for an accurate degreasing and subsequent cleaning with acetone; a *Scanning Electron Microscope Zeiss EVO® MA 50* was adopted.

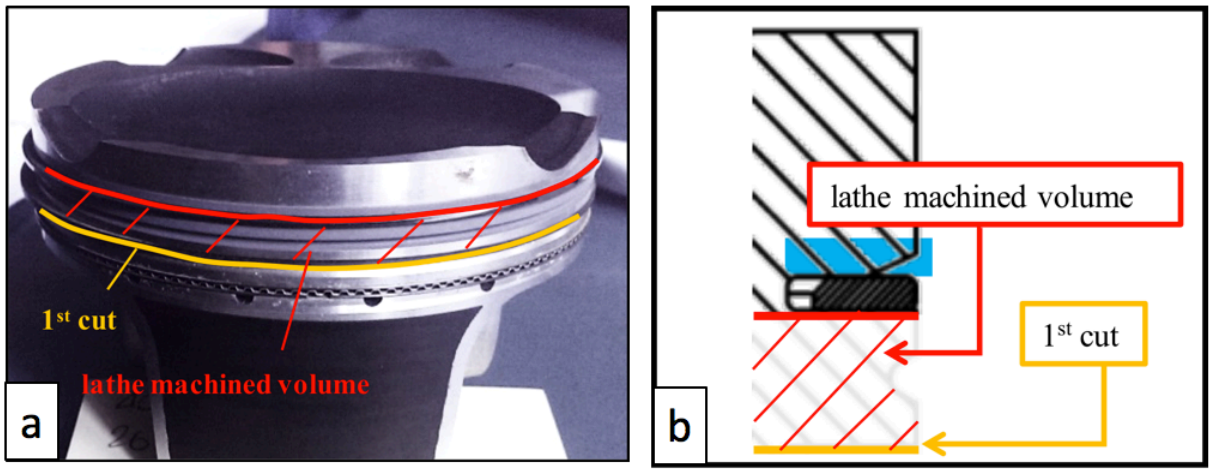

Fig.6. 10: Points of interest for micro-Vickers tests, 1-5 in the intake side (orange circles), 6-10 in the exhaust side (red circles).

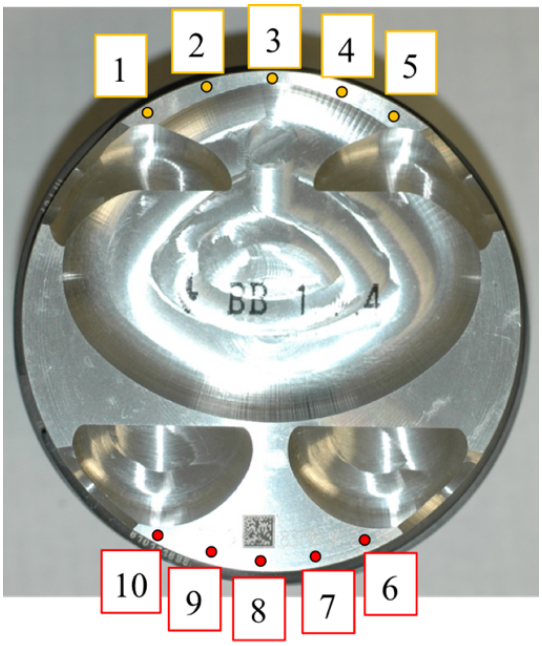

Fig.6. 11: Points of interest for micro-Vickers tests, 1-5 in the intake side (orange circles), 6-10 in the exhaust side (red circles).

6.2 Knock induced erosion on Al pistons: examination of damage morphology and its causes

[This Sect. contains an extract from the published paper whose title is shown below. The Introduction and Materials and Methods paragraphs have not been reported, since all information in this regard is respectively available in Sect.5.2 and Sect.6.1 of the present dissertation. ©2018. This manuscript version is made available under the CC-BY-NC-ND 4.0 licence].

Engineering Failure Analysis 92 (2018) 12–31

Contents lists available at ScienceDirect

Engineering Failure Analysis

journal homepage: www.elsevier.com/locate/engfailanal

Knock induced erosion on Al pistons: Examination of damage morphology and its causes

E. Balducci[a,c,*], L. Ceschini[b], N. Rojo[a], N. Cavina[a], R. Cevolani[c], M. Barichello[c]

[a] Dept. of Industrial Engineering, Alma Mater Studiorum Univ. of Bologna, Viale Risorgimento 4, Bologna, Italy
[b] Dept. of Civil, Chemical Environmental and Materials Engineering, Alma Mater Studiorum Univ. of Bologna, Viale Risorgimento 2, Bologna, Italy
[c] Ferrari Auto SpA, Via Abetone Inferiore 4, 41053 Maranello, MO, Italy

Abstract

In the present study, a systematic and deep examination of knocking damage on Al pistons is carried out, highlighting that only when exceeding a certain threshold knock compromises engine functionality. Controlled knocking combustions were induced during bench tests, by varying the spark advance for each cylinder. Several knock intensities and frequencies were investigated, with the aim to evaluate the possible knocking damages and to understand their influence on piston functionality. All the observed damages have been separately described and studied through failure analysis techniques, in particular optical and scanning electron microscopy and 3D digital microscopy, providing explanations of their occurrence. Among them, the erosion damage was predominantly observed and therefore fully evaluated. Preliminary attempts to relate engine parameters to knock damage were also made.

This study is part of a wider project, whose aim is to increase knocking limits from the "safe calibration area" up to the limits which produce acceptable damages on pistons, in order to enhance engine efficiency.

6.2.1 Results and discussion

Engine bench tests

MAPO index (Eq.5.3) was adopted to define and control knocking intensity. In all cases, with the exception of piston 4 and 11, knocking combustions have been generated by adjusting spark advance, through a PID controller, in order to achieve the targeted MAPO 98th 99.5th percentile. The overall targeted values, indicated as MAPO 98% and 99.5% in Table 6.2, are normalised with respect to their maximum value, for confidentiality reasons.

Unlike the other pistons, piston 4 is representative of the knock safe condition, while piston 11 was controlled "in frequency", aiming to produce a single knocking cycle (characterised by MAPO > 85.7%) every 50 cycles. By imposing the typical PID controller (pistons #1÷10 and #12), it is not possible to control the "temporal distance" of knocking events. For example, a targeted value of MAPO 98% equal to X bar (controlled in 600 cycles buffer as the authors did) can be obtained, in principle, by two extremely different situations: isolated knocking combustions, evenly distributed in 600 cycles (1 event over X bar each 50 cycles), or 12 consecutive events over X bar each 600 cycles. In order to better investigate the influence of "temporal distance" of knocking events, for piston 11 a significant increase of the spark advance (inducing high probability of generating cycles with MAPO > 85.7%) was actuated until reaching the desired knock frequency, under the constraint of 2 max number of consecutive cycles controlled with high spark advance.

Table 6.2: Targeted MAPO % values for each set (normalized wrt the max value); the PID control was imposed on a 600 cycles buffer, respectively on 99.5%, 98.5% and a mixture of both in set #1,2,3; an exception was made for piston 11, controlled "in frequency".

# set	[h] test	Piston #	Target MAPO 99.5% [%]	Target MAPO 98% [%]	"in frequency" control
1	15	1	64.3	/	/
		2	85.7	/	
		3	64.3	/	/
		4	Knock limit	/	/
2	3	5	/	64.3	/
		6	/	64.3	/
		7	/	42.9	/
		8	/	32.1	/
3	15	9		42.9	/
		10		42.9	/
		11	/	/	1cycle/50 MAPO>85.7
		12	100		/

The actual output of engine bench tests is reported in Table 6.3. Both MAPO 99.5th and 98th percentile (MAPO 99.5% and MAPO 98%) have been calculated for each cylinder, as well as the maximum pressure value 90th percentile (p_max90%), after analysing the recorded pressure signals. These are indeed the parameters commonly used to identify knocking intensity and the thermo-mechanical stresses on combustion chamber components. A slight difference between the targeted MAPO % (Table 6.2) and the achieved results (Table 6.3) can be noticed; this is mainly linked to the complexity of PID control. MAPO% values have been normalised to the maximum targeted value, while p_max90% values have been normalised to the actual maximum value detected.

While PID-controlled distributions of both MAPO and p_max can be very similar to the natural response of the engine controlled with constant spark-advance, the distribution of MAPO and p_max intensities in cylinder 11 is considerably different, and the superscript "*" is aimed to remind that these values are not directly comparable with the others.

Table 6.3: Actual output of bench tests, determined after processing of pressure signal data.

#set	Test [h]	# piston	MAPO 99.5% [%]	MAPO 98% [%]	p_max 90% [%]
1	15	1	64.3	45.7	94.1
		2	75.0	52.1	94.2
		3	66.4	44.3	93.8
		4	28.6	20.0	88.0
2	3	5	89.3	57.9	98.4
		6	82.1	55.7	100
		7	55.7	37.1	97.6
		8	38.6	27.9	93.5
3	15	9	75.0	49.3	91.9
		10	69.3	47.9	93.8
		11	130.7*	52.9*	74.0*
		12	97.1	62.9	95.6

Preliminary visual analysis of pistons

Visual naked-eye inspection of pistons after bench tests represents the very first but essential level of analysis. Macrographs allow a complete overview of pistons, saving the

information connected to carbon deposits distribution and highlighting the most damaged areas to be further examined, at the same time keeping track of the macro-damages location.
It is worth pointing out the importance of tracing the presence of carbon deposits before polishing with neutral degreaser. After bench tests, pistons are in fact still covered by carbon residues, which need to be removed in order to further analyse the surface damage. The amount of compact carbon residues on pistons crown mainly depends on the air-fuel equivalent ratio (λ), on the adoption of direct injection (DI) or port fuel injection (PFI) systems, on the injection timing and on the geometry of the combustion chamber, which might enhance the accumulation of deposits in specific areas. Few papers in literature report that there might be a connection between the presence of carbon deposits and the trigger of abnormal combustions, since carbon residues might act as hot spots in the combustion chamber; the local heat release triggers the flame front and the flame propagates from the hot-spot to the rest of the mixture [14,16].

By considering the results of the bench tests objective of this study (which were carried out keeping constant all the variables affecting carbon deposits, namely λ, the engine geometry and injection system and timing), it is possible to state that the presence of a compact and homogeneous layer of carbon deposits on the whole piston head underlines the absence of remarkable abnormal combustion events. It is indeed the removal of these deposits in specific areas to be considered as a marker, in agreement with Nates et al. [23] who stated that the extent of erosion might vary from light cleaning of deposits to progressive amounts of erosion of piston material. In Fig.6.12, a representative comparison between pistons tested under knock-safe and more severe knocking conditions is reported. The peripheral area of pistons appears cleaner when bench tests involved heavier knocking combustions. Since the spark-plug is centrally located, the end-gases responsible of knocking occurrence exactly cover the annular region around piston edge.

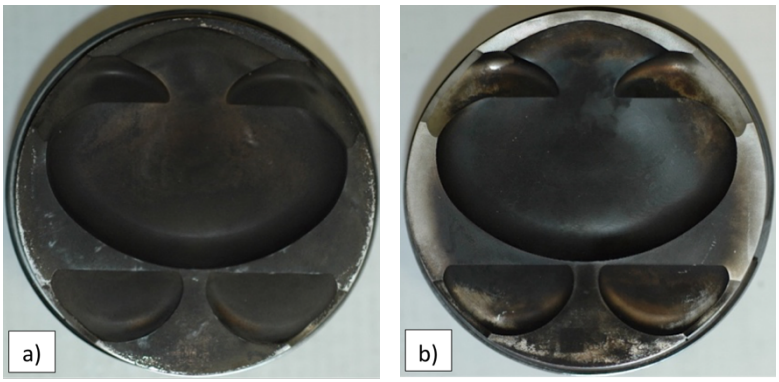

Fig.6.12: Macrographs of pistons head after bench tests, respectively operating (a) under knock limit (piston 4), (b) in knocking conditions (piston 6).

The same "cleaning effect" is observed in Fig.6.13, which reports two representative macrographs of piston 5 top land, taken from different sides. It is evident that the anti-thrust area (Fig.6.13a) is eroded and therefore free from carbon residues, while a compact layer of deposits tends to cover the top land of the whole thrust side (Fig.6.13b). Again, in the specific area where knock occurs most violently, piston surface is not covered by carbon residues. The interaction between pressure waves due to knock is thought to be the main responsible of piston crown cleaning.

Once the most damaged sites were detected in the macro-scale, through visual observation and macrographs, 3D optical micrographs, Optical Microscope (OM) and/or Scanning Electron Microscope (SEM) allowed to better evaluate the damage morphology.

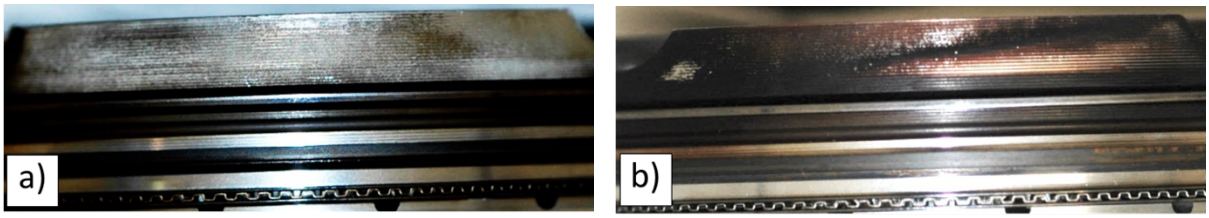

Fig.6. 13: Comparison between macrographs of piston 5 top land, respectively belonging to the (a) anti-thrust side, (b) thrust side; the absence of carbon residues in the anti-thrust side of piston top land is due to knocking erosion.

Knocking damage in valve relief

The considerable amount of data collected on 12 pistons allows to state that valve reliefs are the piston areas most susceptible to knocking damage: in all pistons but piston 4, in fact, damage in at least one valve relief has been detected. The main observed damage mechanisms in this area are erosion and polishing of valve edge, both in the intake and exhaust side, which also means both in the thrust and anti-thrust side, without any preferential location (at least at the tested engine operating point of 4500 rpm).

Under moderate knocking conditions (Fig.6.14a,b,c), the occurrence of sliding contact between cylinder and piston valve relief is underlined by the polished area at the top; just a slight erosion is perceivable, due to the jagged edge.

Erosion becomes much more visible under heavier knocking conditions as shown in Fig.6.14d,e,f, which offer an overview of the damage occurred in piston 12 and piston 5 valve reliefs. Fig. 11f, in particular, reports an overview from the top of piston 5 valve relief and it reveals the severe erosion

which seems to initiate from the right corner (red arrow) and to propagate to the left and to the centre of piston crown (blue arrows).

When knock intensity further grows up, polishing is completely replaced (or its marks completely deleted) by erosion damage, as reported in Fig.6.14g,h. Under one of the most severe knocking intensity investigated (piston 11, controlled "in frequency", with a calculated MAPO 99.5% equal to 130.7%, as reported in Table 6.3), valve relief is entirely worn out.

The high sensitivity of piston valve relief, and in particular of its most protruding edge (red arrow in Fig.6.14f), to knocking combustions is in agreement with Wang et al. [16], who stated that a protrusion in the combustion chamber surface may become a hot spot, finally inducing knock or pre-ignition. The phenomenon is mainly connected to the fact that abnormal combustions exasperate the heat exchange due to an increase in gas turbulence [18,22]. In the typical pistons geometry, valve reliefs are characterised by an unfavourably high surface-to-volume ratio, which makes valve reliefs more sensitive to heat exchange and also prevents the material from optimal heat dissipation through conduction. Taking into account that valve reliefs are also the farthest point from the centrally located spark-plug, it clearly emerges that valve reliefs are one of the most suitable trigger point for knocking combustions.

It has to be pointed out that the two evidenced damage mechanisms (erosion and polishing) might occur separately, as can be clearly seen by comparing Fig.6.14c and Fig.6.14g. To fully understand the underlying causes of valve relief damage, two indexes were provided for each piston to quantify the damage, separately evaluating polishing and erosion. The most damaged valve reliefs, respectively in terms of polishing and erosion, were taken into account for each piston to determine the polishing and erosion indexes.

The polishing damage for each piston was quantified by measuring the maximum width of the polished area (Fig.6.15). The erosion damage was indeed qualitatively evaluated, by comparing the most eroded valve relief of each piston; an erosion index within the range 0÷5 was imposed, where the level 5 corresponds to the highest experienced erosion level, as reported in Fig.6.16. The quantitative results of the visual analyses in valve reliefs are reported in Table 4. The damage quantification is the basis for further considerations on the influence of engine calibration parameters on piston damage. The two main mechanisms of damage are separately considered in the following paragraphs, to better investigate on their respective causes.

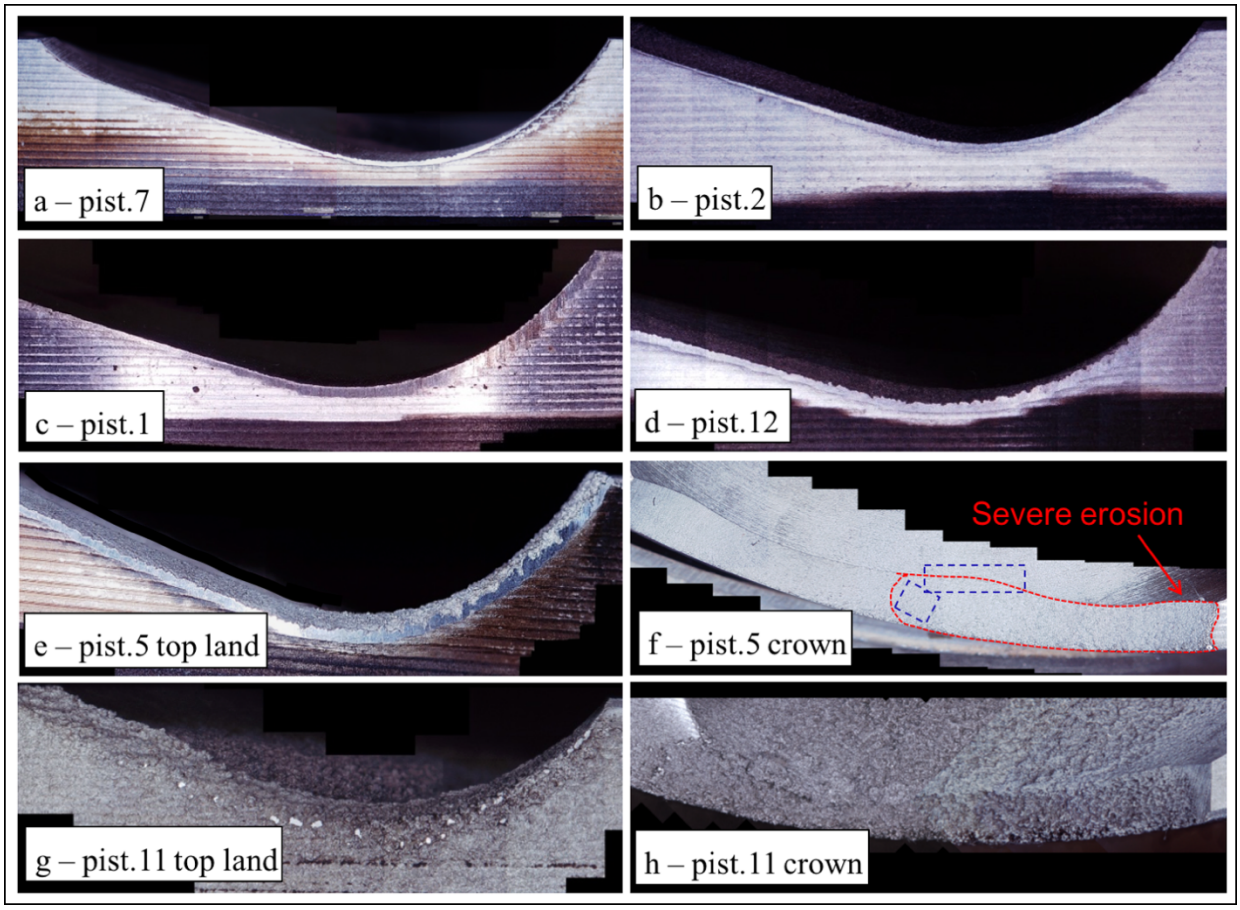

Fig.6.14: Hirox 3D micrographs of piston valve reliefs respectively highlighting (a), (b), (c) the polishing effect in piston top land; (d), (e) the combined presence of polishing and erosion in piston top land; (g) the prevalence of erosion in piston top land; (f), (h) the significant eroded area, clearly visible by observing piston valve relief from piston crown.

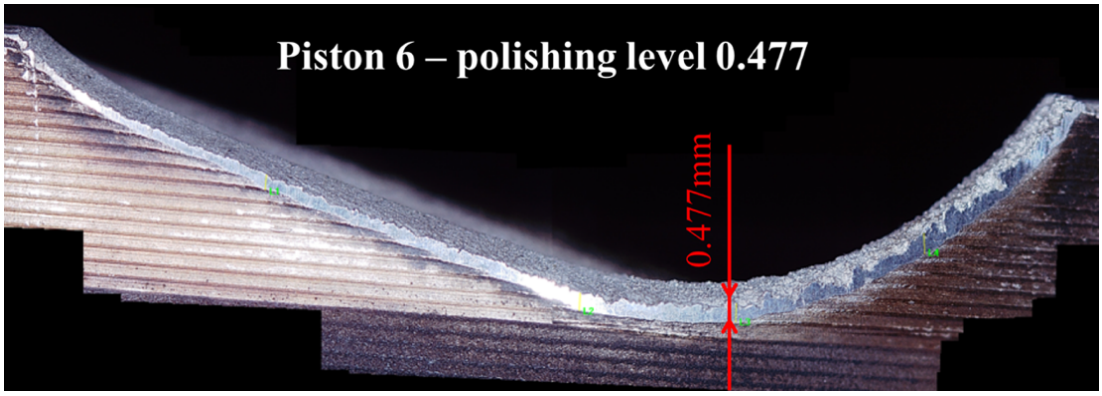

Fig.6. 15: Procedure for the measurement of the polished area in valve reliefs, after bench tests.

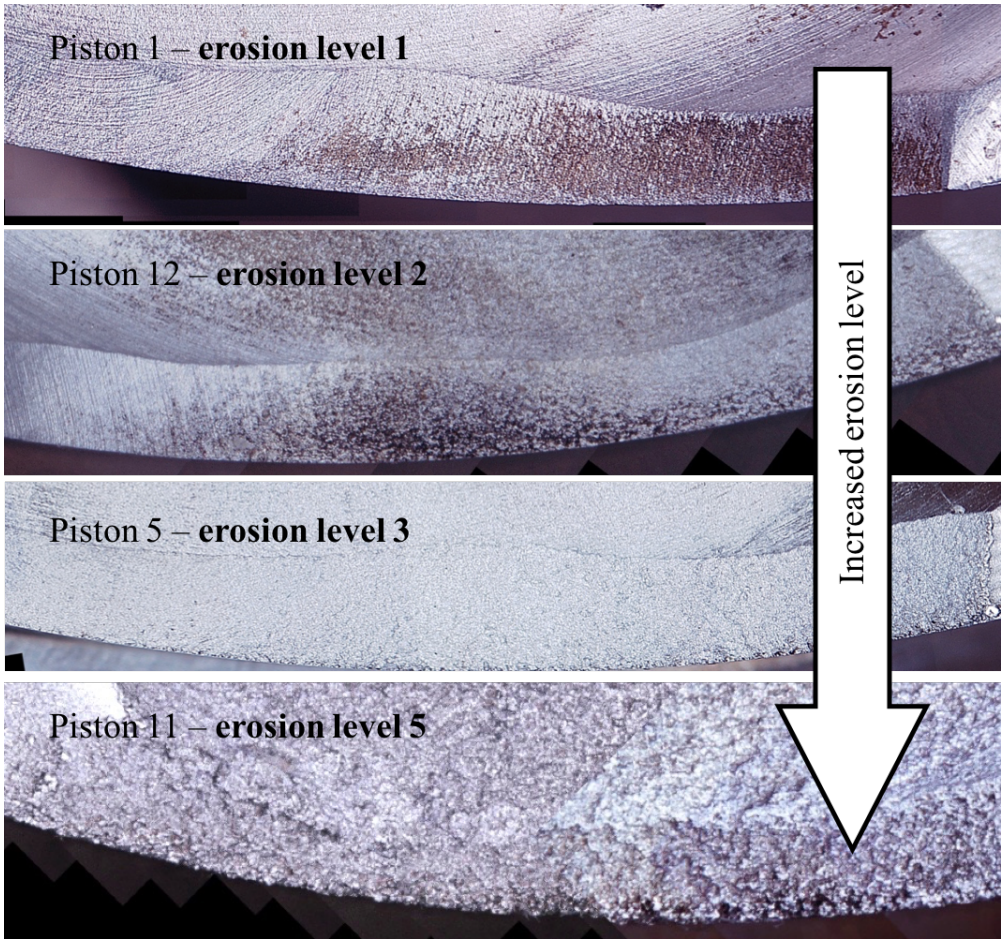

Fig.6. 16: Determination of the erosion level of valve reliefs, based on visual observation and comparisons between pistons after bench tests.

Table 6. 4: Polishing and erosion indexes (referred to damage in valve reliefs) for all pistons after bench test; operating conditions for all pistons have been reported as a reminder from Table 6.3.

Pist. #	Polishing index [mm]	Erosion index (qualitative 0÷5)	Pmax90%	MAPO 99.5% / 98%
1	0.456	1	94.1	64.3 / 45.7
2	0.383	1.5	94.2	75.0 / 52.1
3	0.556	1.5	93.8	66.4 / 44.3
4	0	0	88.0	28.6 / 20.0
5	0.378	3	98.4	89.3 / 57.9
6	0.477	3	100	82.1 / 55.7
7	0.195	1.2	97.6	55.7 / 37.1
8	0.03	0	93.5	38.6 / 27.9
9	0.377	1.5	91.9	75.0 / 49.3
10	0.395	0.8	93.8	69.3 / 47.9
11	0.09	5	74.0*	130.7 / 52.9
12	0.535	2	95.6	97.1 / 62.9

Polishing damage in valve relief

Even if the polishing of valve relief edge is an inoffensive damage, which does not compromise piston function, it is worth further analysing its causes since it is frequently observed. This damage clearly arises from the sliding contact between cylinder and piston valve relief and it is most likely connected to a localised thermal expansion, which is thought to be produced by *constantly higher temperatures* compared to the other parts of piston top land. The hypothesis is supported by the following considerations:

- As stated above, valve reliefs are characterized by a high surface-to-volume ratio and are therefore disadvantaged in heat dissipation; this is especially true for valve reliefs *edge*. It is therefore reasonable to assume that a constantly higher temperature is maintained at the edge, compared to other piston areas.
- Polishing, at different extent, characterizes at least one valve relief for each piston, even if piston working conditions were not extremely severe; just piston 4 was unaffected. It is well known that the average piston temperature mainly depends on the *pressure* inside the combustion chamber [28]. It is worth underlining that all pistons, except for pistons 4 and 11, experienced a p_max90% above 90%.
- P_max90% cannot be considered the solely parameter affecting the temperature inside the combustion chamber, since *knocking combustions* are known to significantly increase the instantaneous heat flux [2,18,22]. However, single and localized pressure peaks are thought to have a limited influence on the average temperature field, so that the effect of MAPO 99.5% can be neglected. This is confirmed by the fact that piston 11 is characterized by the highest level of MAPO 99.5% but at the same time it exhibits a negligible polished area. From the other side, MAPO 98% is representative of the intensity of a higher number of knocking events, and it is better related to an increase of temperature and to the polishing damage.

The aforementioned considerations reveal the dependence of polishing from both p_max90% and MAPO98%, which has been further investigated. Due to the different order of magnitude of p_max90% (~10^2) and MAPO 98% (~10), both parameters have been normalised as previously reported. This procedure was aimed to roughly give the same weight to both parameters, before understanding their respective influence on polishing extension. The maximum pressure (p_max)

and its high frequency oscillations (MAPO) are thought to produce a combined effect, so the parameters have been summed up and the result of the simple sum is shown in Fig.6.17.

Time was not considered in the relationship: since the stationary operating point of 4500 rpm has been investigated for all pistons, the average temperature field established during operations was not affected by time but only by pressure and knocking events inside the combustion chamber. Since the temperature field is kept constant, also the thermal expansion does not increase during time.

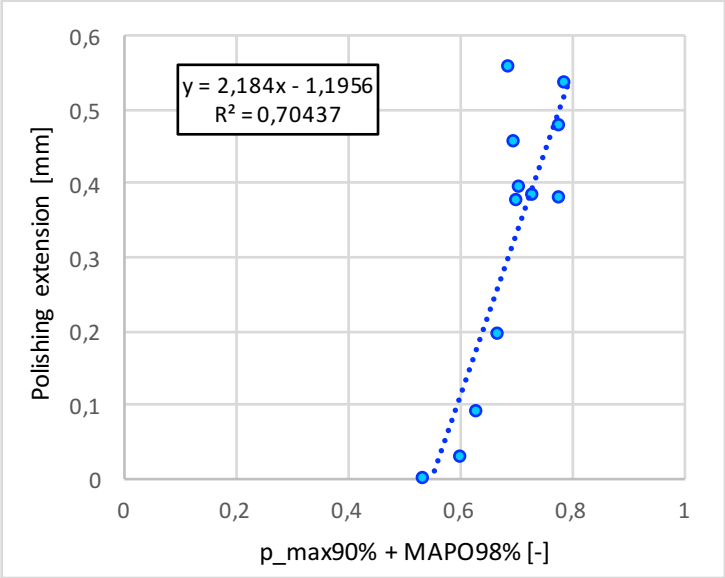

$$Pol. = 2.184(pmax90 + MAPO98) - 1.1956$$

Fig.6. 17: Relationship between polishing index (Pol.) and pressure parameters pmax90% and MAPO98%.

Erosion damage in valve relief

Like polishing, also the erosion of piston valve reliefs, to some extent, does not compromise piston function. However, erosion produces debris inside the combustion chamber, which might be damaging to: (i) several engine components which are part of the combustion chamber itself (like pistons, cylinders and engine head) but also to (ii) other components such as the turbocharger or catalyst, which are likely to be affected by debris. Erosion is evident in pistons 5-6-11-12 (some of them reported in Fig.6.14d, e-f, g-h), which were subjected to the 3 highest values of MAPO 99.5% during engine operation.

Among them, erosion damage was heaviest in piston 11, which experienced the most severe MAPO 99.5% and which is therefore taken into consideration to understand the main cause of erosion. In the worst condition, the “in frequency” control of piston 11 produced a maximum

number of 2 sequential knocking combustions (respectively characterised by MAPO values beneath and above the targeted threshold of 85.7%) each 50 cycles, whose global results are:

- A single but severe knocking event, confirmed by the extremely high value of MAPO 99.5% and by a "low" value of MAPO 98% (Table 6.3), at least lower if compared to the other pistons 5-6-12 characterized by evident erosion. Since MAPO 98% indicates the threshold exceeded by the 2% of combustions, this parameter is mainly representative of an average pressure oscillation, and at the same time it is less sensitive to single pressure peaks. The fact that high values of MAPO 99.5%, rather than MAPO 98%, seem better related to erosion damage means that most of the erosion damage is produced by intense, even localized knocking events, rather than by "low-intensity", even frequent knocking combustions.
- A considerably low p_max90%, compared to the other pistons. This means that the average temperature (mainly connected to p_max90%) has a minor influence on erosion damage in case of severe knocking events.

It can be therefore inferred that, among the considered engine parameters, erosion damage mainly depends on the intensity of single knocking combustions (evaluated by MAPO 99.5%), therefore on both knock induced mechanical stresses (pressure waves) and on its sudden heat release (thermal strain and stresses).

The relationship between erosion level and MAPO 99.5% clearly results also from Fig.6.18.

As well as the polishing damage, the erosion damage revealed to be not time-dependent. This characteristic is reasonable, since the level of erosion was evaluated by considering the surface morphology: the duration of bench tests is thought to affect the amount of removed material rather than the surface morphology. Unfortunately, the substantial difficulties in accurately removing carbon residues after bench tests prevents from precisely evaluating the limited weight loss due to erosion.

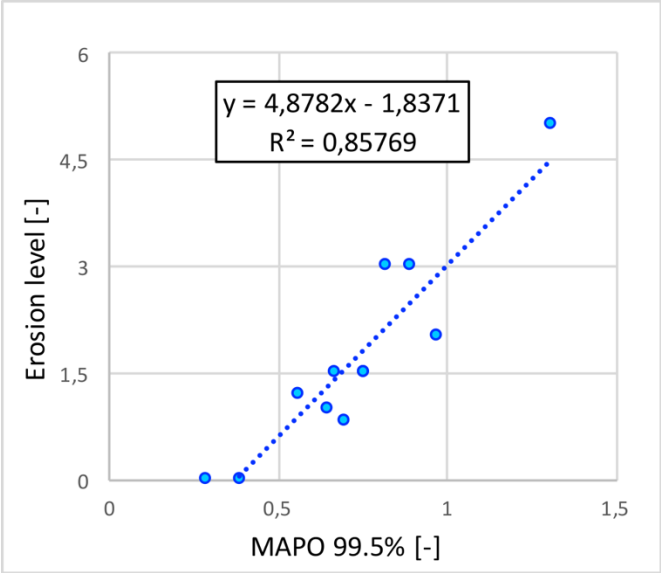

$$Erosion = 4.8782\ MAPO99.5\% - 1.8371$$

Fig.6.18: Relationship between erosion index (Erosion) and normalised pressure oscillations MAPO99.5%. Erosion level is qualitatively evaluated as explained in Fig.6.16 and the numerical values for each piston are reported in Table 6.4.

From one side, the direct cause of polishing has been easily found as a consequence of a sliding contact between piston and cylinder, while the cause of erosion is thought to be multifaceted. OM and SEM analyses proved to be consistent in better explaining the development of erosion. Once again, piston 11 was taken into account, being the most representative in terms of erosion.

The main results of OM analyses are reported in Fig.6.19. A metallographic section was radially extracted from piston 11 crown, as reported in Fig.6.19a, with the aim to accurately investigate the erosion damage produced at the edge of piston valve pocket. The produced damage is highlighted in Fig.6.19b-c: visible deep cracks tend to propagate in the soft α-Al matrix, at the interface with Cu-Ni based intermetallics and Si particles. This is a preferential site for cracks initiation, since (i) α-Al matrix is softer than both intermetallics and eutectic/primary Si particles, (ii) interfaces are known to be weaker. Plastic deformation marks are not visible in the metallographic sections, since a preferential orientation of intermetallics is not discernible. Cracks initiation in correspondence of Si particles was also observed in the same piston alloy after thermo-mechanical fatigue tests by Humbertjean et al. [35], while Floweday et al. [36] observed the same failure in high performance automotive diesel pistons. The damage can be therefore clearly attributed to thermo-mechanical fatigue. In agreement with Fitton et al. [19], no dendrites or molten zones have been observed, which means that the heat flux during heavy knock was not

such emphasised to produce melting. Melting was however observed by the authors in the same automotive pistons after pre-ignition combustions [28].

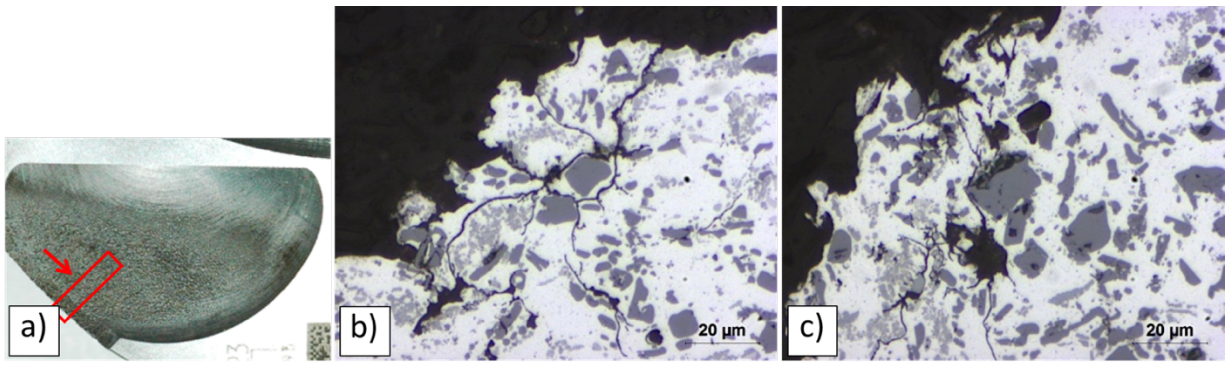

Fig.6. 19: OM analyses on exhaust valve relief of piston 11, pin axis side 270°. (a) Macrograph indicating the selected section for OM on metallographic samples, observed from the direction indicated by the arrow; (b), (c) OM micrographs revealing the effect of erosion in the transversal section.

Additional SEM analyses allowed a deeper comprehension of the damage morphology. Two different areas of piston 11 valve relief 270° were considered, as clearly indicated in Fig.6.20a:

- The valve edge itself (enclosed in yellow), which exhibited the heaviest erosion damage;
- The upper part of the valve relief (enclosed in blue), which includes both slightly up to heavily eroded areas, moving from piston crown to valve edge. This area was analyzed in order to get information about the different stages of erosion and its evolution.

Low magnification micrographs highlight the significantly pitted aspect of valve pocket edge (Fig.6.20b) compared to its upper part (Fig.6.20c), which is the result of the different knocking intensity experienced. It is reasonable to assume that the abnormal combustion started in all its intensity at valve edge (piston *periphery*, therefore more prone to knock), where the maximum damage is in fact produced, but its pressure oscillations and heat release also affected the whole valve pocket area before reducing the knocking energy. This hypothesis is further confirmed by solely observing Fig.6.20c: the transition from light to heavier knocking damage is evident when moving down to valve edge, since machining grooves start to be partially smoothed by erosion and are finally completely torn out. Plastic deformation also highlights the direction of knocking pressure waves and heat release, as highlighted by blue arrows in Fig.6.20c, as a clear sign of knocking propagation from the periphery to the centre of piston crown.

Fig.6.20d shows a higher magnification micrograph of piston valve edge: deep erosion is evident, the surface being covered by dimples, but it also worth highlighting the presence of wide hollows, which are thought to be the result of large intermetallics or Si crystals detachment. The hypothesis is confirmed by the evident deep cracks which encircle secondary phases in OM sections

(Fig.6.19b-c). The higher magnification reported in Fig.6.20e underlines the plastic flow produced by knocking combustions, highlighted by the arrows. Once again, it is possible to observe the fine dimples produced by gas auto-ignition.

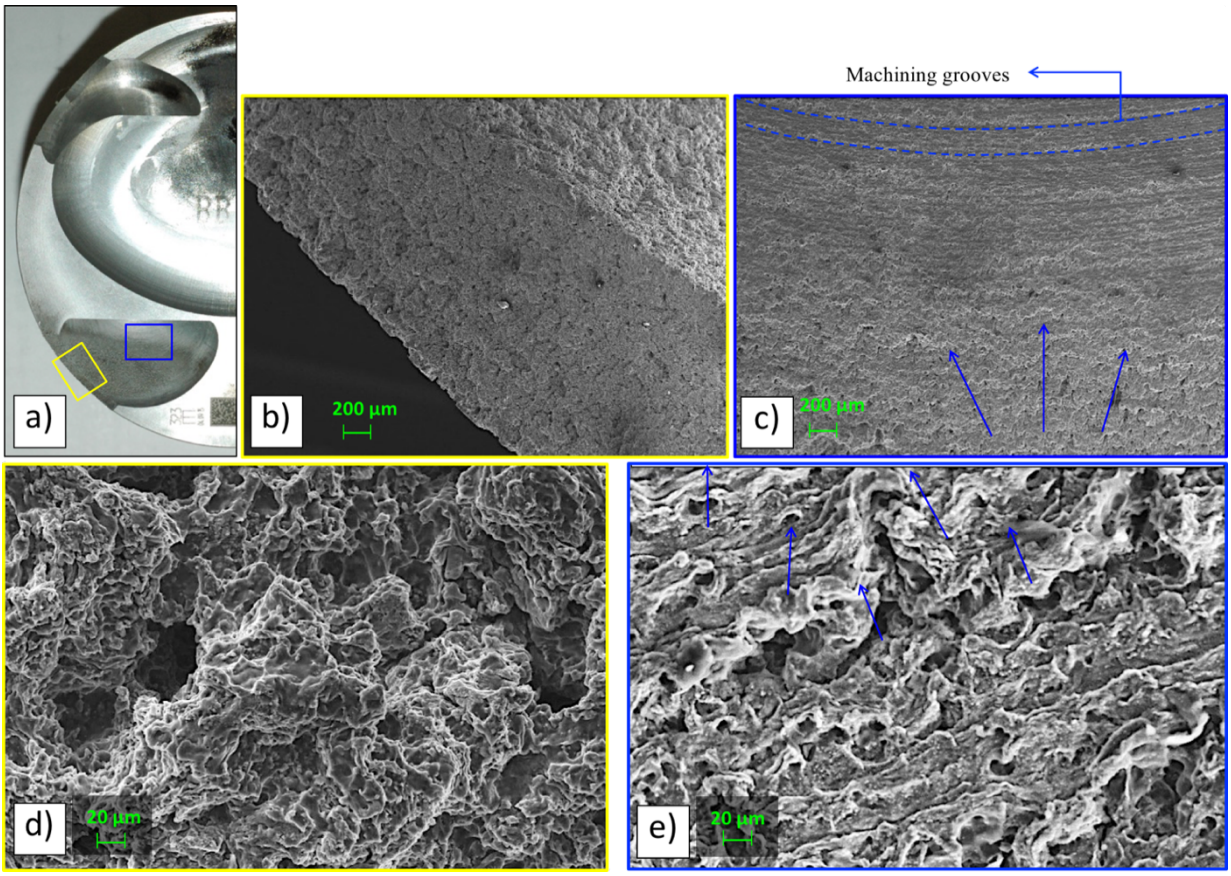

Fig.6. 20: SEM analyses on exhaust valve relief of piston 11, pin axis side 270°. (a) Macrograph indicating the selected areas. (b), (c) Low magnification SEM micrograph respectively showing the morphology of valve relief edge (enclosed in yellow) and central area (enclosed in blue). (d), (e) High magnification SEM micrograph respectively focusing on valve relief edge (enclosed in yellow) and central area (enclosed in blue).

Knocking erosion in the 1st ring groove

Pistons #5, #6 and #11 also showed erosion spots in the anodised area of the 1st ring groove, which was clearly visible, even at naked eye, in tilted pistons. The 1st ring groove collects the end-gases farthest from the central spark-plug, and it is therefore one of the potential triggering sites of knock. Moreover, this is a crevice area, which might be extremely susceptible of knocking damage: as stated by Fitton et al. [19], knocking erosion in crevices might be strengthened by cracks propagation caused by extreme pressure differences. Nevertheless, the 1st ring groove is usually cooler compared to piston head, as can be noticed considering several studies on pistons temperature field [32,33]. In fact, normal combustion starts with a spherical flame front from the spark plug and hits at first piston head; here, the combustion gases lose part of their thermal energy while piston crown increases its temperature. The 1st ring groove is mainly

reached by the heat dissipated by piston crown and top land, and it is usually cooled down thanks to heat conduction through the 1st ring (and cylinder). Its cooler temperature is one of the main reasons explaining why knock erosion in the 1st ring groove occurs more rarely (just 3 pistons were affected among the 12 investigated) than knock erosion in piston valve relieves (evidence noticed in 10 pistons).

The damage in this area was investigated through both 3D Hirox analyses and SEM micrographs, after cutting all pistons, as reported in Fig. 6.10. Both pistons 5 and 6 exhibited an extended eroded zone, which roughly covered the whole area in between the two intake valve pockets, while erosion in piston 11 ring groove was confined between the exhaust valve pockets.

Fig.6.21a shows the upper side of the 1st ring groove belonging to piston 5, in particular the area enclosed between the intake side 0° and lateral side 90°, as indicated by the white box and arrow on piston macrograph. Fig.6.21a is also representative of the 1st ring groove from the intake up to the lateral side 270°, since the damage appeared roughly symmetrical with respect to the intake side 0°. Fig.6.21b is aimed to precisely locate the damage of the anodised area: reference points with respect to valve relief geometry were created by combining the observation of the top land and of the 1st ring groove in correspondence of the valve relief, as indicated by the dotted lines in Fig.6.21a-b.

The heavy erosion, which produces a brighter area, is mainly localised in correspondence of the intake side 0° (area encircled in green in Fig.6.21a), while erosion extent tends to decrease moving towards the intake valve relief 90° (as well as 270°). As can be noticed from Fig.6.21a, in fact, the lateral side 90° of the 1st ring groove exhibited a dark grey colour, typical of the anodised layer, with a few white spots due to erosion. The 1st ring groove of piston 6 is not reported, since it is similar to piston 5. Focusing the attention on Fig.6.21a, erosion mainly seems to affect the peripheral area of the 1st ring groove, namely the chamfer area indicated in red in Fig.6.21a).

The whiter colour of the eroded areas characterising the anodised 1st ring groove is due to the different reflection of light on the eroded surface. OM and SEM analyses were carried out in order to precisely investigate the damage morphology in the anodised layer of the 1st ring groove.

Fig.6.22a-b shows OM analyses on metallographic sections of the 1st ring groove belonging to piston 5, respectively taken from the intake and exhaust side; both the micrographs are focused on the chamfer area, which is found to be more prone to knocking damage as also mentioned in the above paragraph. By comparing Fig.6.22a-b, it is clearly visible that the anodised layer covering the chamfer in the intake side of the 1st ring groove is completely worn out, while the anodised

layer is perfectly intact in the exhaust side, as shown by Hirox analyses (Fig.6.21a). OM analyses therefore confirm that knocking combustions are able to significantly damage the anodised layer.

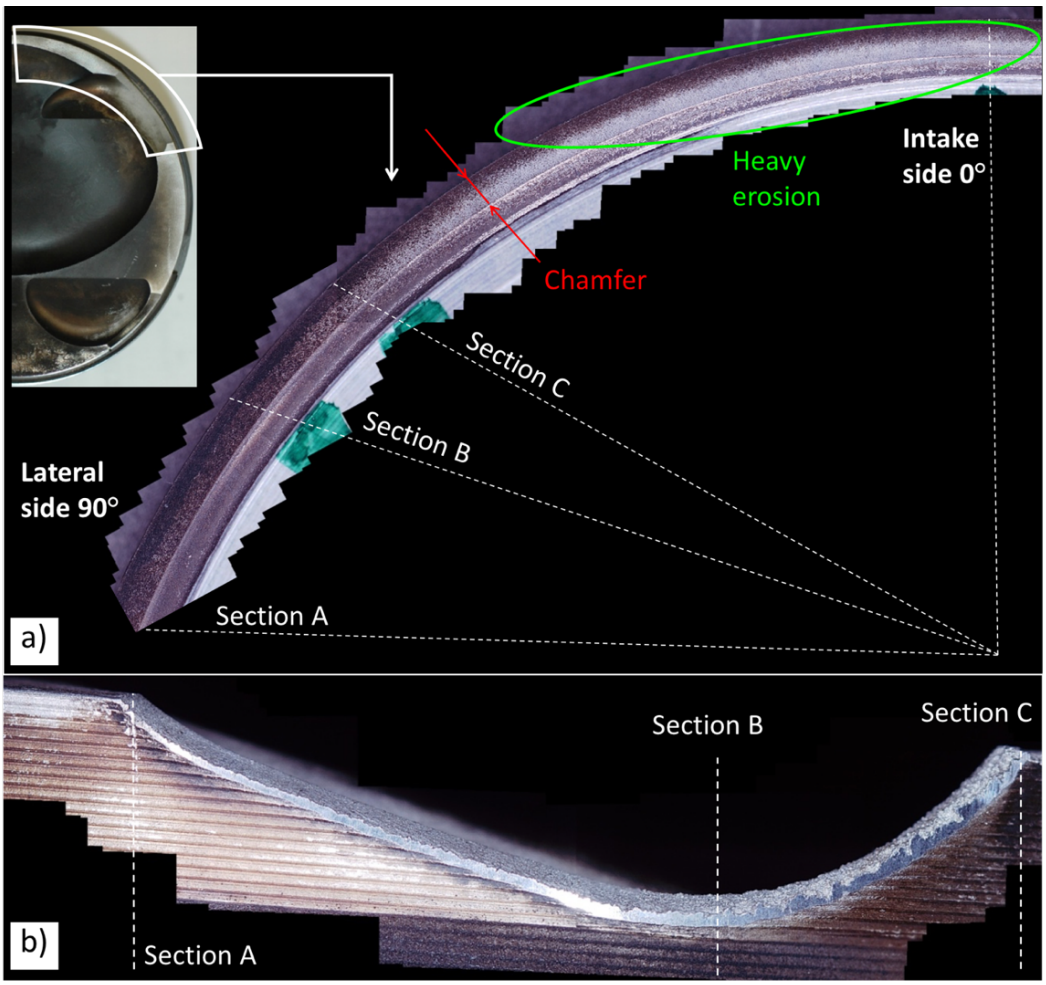

Fig.6. 21: (a) 3D Hirox micrograph reporting an overview of the upper part of the 1st ring groove - piston 5. White box and arrow on piston macrograph enclose the analyzed area, green circle underline the heavy eroded area of the anodized layer, dashed lines are aimed to precisely locate the damage in the angular directions, with respect to the intake side and valve relief geometry. (b) 3D Hirox micrograph showing the reference sections with respect to valve relief geometry.

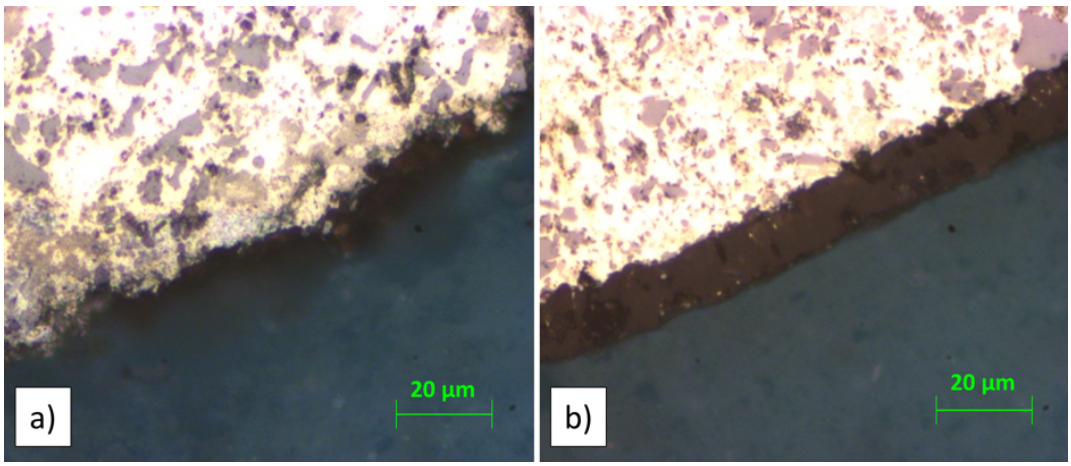

Fig.6. 22: OM micrographs of the 1st ring groove belonging to piston 5, respectively taken from (a) the intake and (b) the exhaust side. Both micrographs are focused on the chamfer area (clearly indicated in Fig.6.3b).

SEM analyses of the 1st ring groove belonging to piston 5, intake side, are reported in Fig.6.23a-b-c, where low magnification micrographs (Fig.6.23a-b) allow to have an overview of the interesting sites, while the higher magnification micrograph (Fig.6.23c) clearly shows the damage morphology. Lower magnification micrographs always referring to the 1st ring groove of piston 5, but exhaust side, are also reported in Fig.6.24a-b (same magnification of Fig.6.23a-b). Visual analyses on piston 5 exhaust side did not reveal any damage, therefore this area might be considered representative of pistons undergone normal combustions, therefore worn due to normal contact with piston ring. Simultaneously observing Fig.6.23 and Fig.6.24 respectively allows to compare the status of the anodised layer of the 1st ring groove: (i) severely affected by local knocking combustions, (ii) influenced by normal bench test; the comparison is therefore helpful in correctly evaluating the knocking damage. The low magnification micrograph of the 1st ring groove intake side (Fig.6.23a) clearly reveals the presence of 3 areas, characterised by different morphological aspects. On the contrary, just 2 areas are identified in the exhaust side of the same piston (Fig.6.24a), which are characterised by a totally comparable aspect but are indeed separated by the chamfer edge of the 1st ring groove (indicated by arrows). The damage caused by knock is separately considered for each zone, as follows:

- Zone 1 is the very inner area of the 1st ring groove, therefore it is supposed to be less susceptible to knock damage. Fig.6.23b-Zone1 shows the presence of a compact anodized layer (light grey-white color), combined with the presence of a less compact oxide layer (dark grey) covering the surface. The difference in color is due to the different electrical conductivity of these areas, related to the different thickness of the oxide layer. This aspect is better appreciated at higher magnification, by observing Fig.6.23c. Here also the typical defect of anodization on Al-Si alloys [37] can be observed: the anodized layer grows thanks to Al passivation, therefore it hardly covers eutectic Si or Si primary crystals, which usually tend to remain exposed (as indicated by the arrow). Since the anodized layer is usually not uniform in thickness, it is not possible to immediately link the alternation of whiter/darker areas to knocking damage. However, by comparing the same Zone 1 in Fig.6.23b and Fig.6.24b, it can be inferred that the intake side is in fact more eroded than the same area in the exhaust side, confirming that knocking erosion might even affect the internal part of the 1st ring groove.
- Zone 2 is a transition zone to the more damaged area. At low magnification (Fig.6.23a), this area in the intake side of piston 5 seems similar to Zone 1, but both Fig.6.23b-c clearly show

the higher intensity of erosion experienced by Zone 2. In particular, Fig.6.23c reveal that the anodized layer in Zone 2 is clearly damaged and fragmented. If compared to both Zone 1 and 2 belonging to the exhaust side of piston 5 (Fig.6.24a-b), the damage is further emphasized.

- Zone 3 is totally absent in the exhaust side (Fig.6.24a-b). Since this aspect is identified just in the intake side of the 1st ring groove belonging to piston 5, it can be considered a pure product of abnormal combustions. The white color is due to the oxidation process of the surface, in all probability connected to the very high temperature produced by knock in this area. The anodized layer is completely disappeared, as confirmed by the flattened and deformed surface (Fig.6.23c). The area was probably flattened due to the high-pressure contact with the 1st ring.

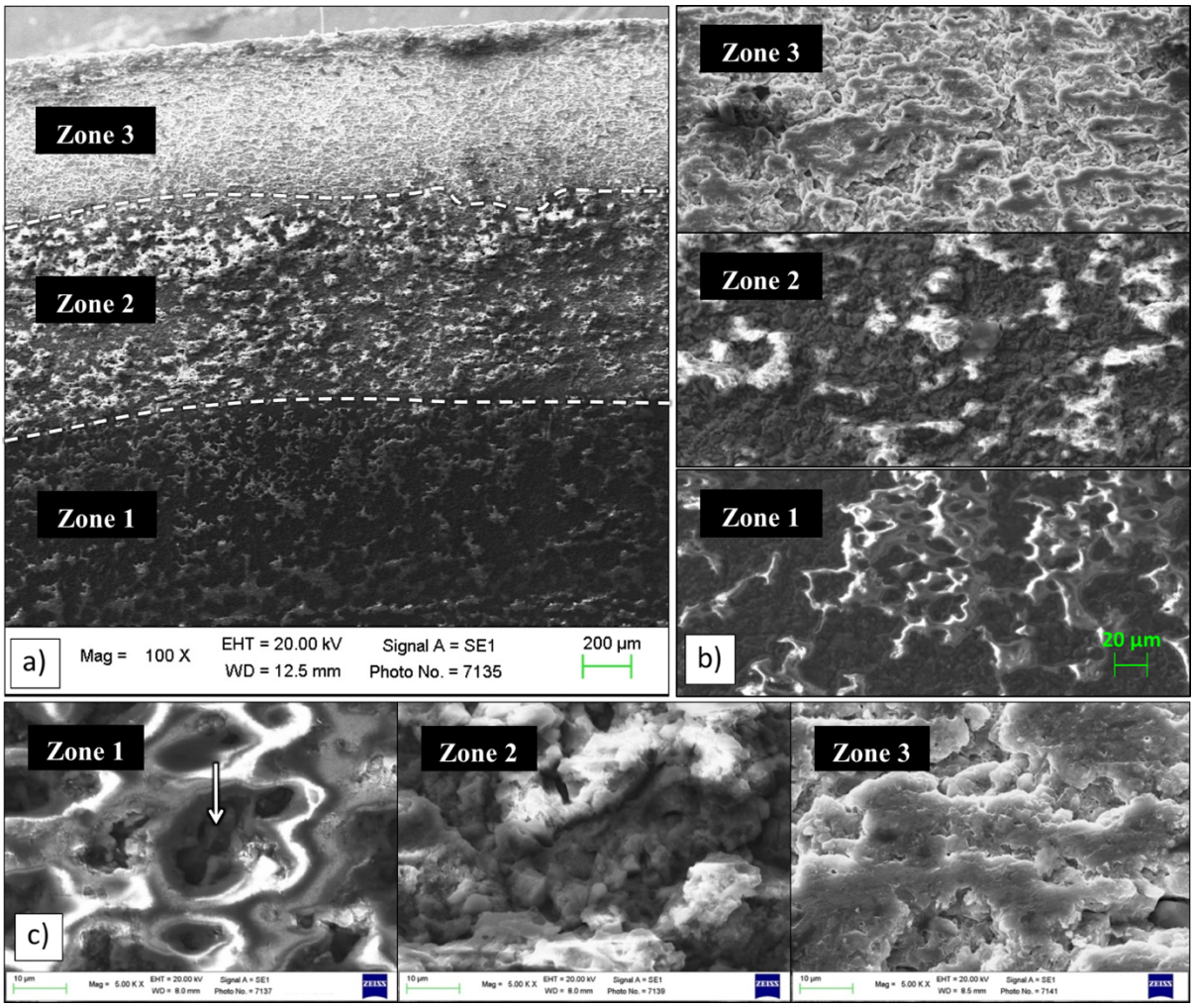

Fig.6. 23: SEM micrographs of the 1st ring groove, intake side, belonging to piston 5. (a) Low magnification micrograph (100 X), showing the clear presence of 3 different zones in the anodised layer, separated by dashed lines in order to make it clear; (b),(c) higher magnification micrographs (respectively 1000 X and 5000X) of the 3 different zones.

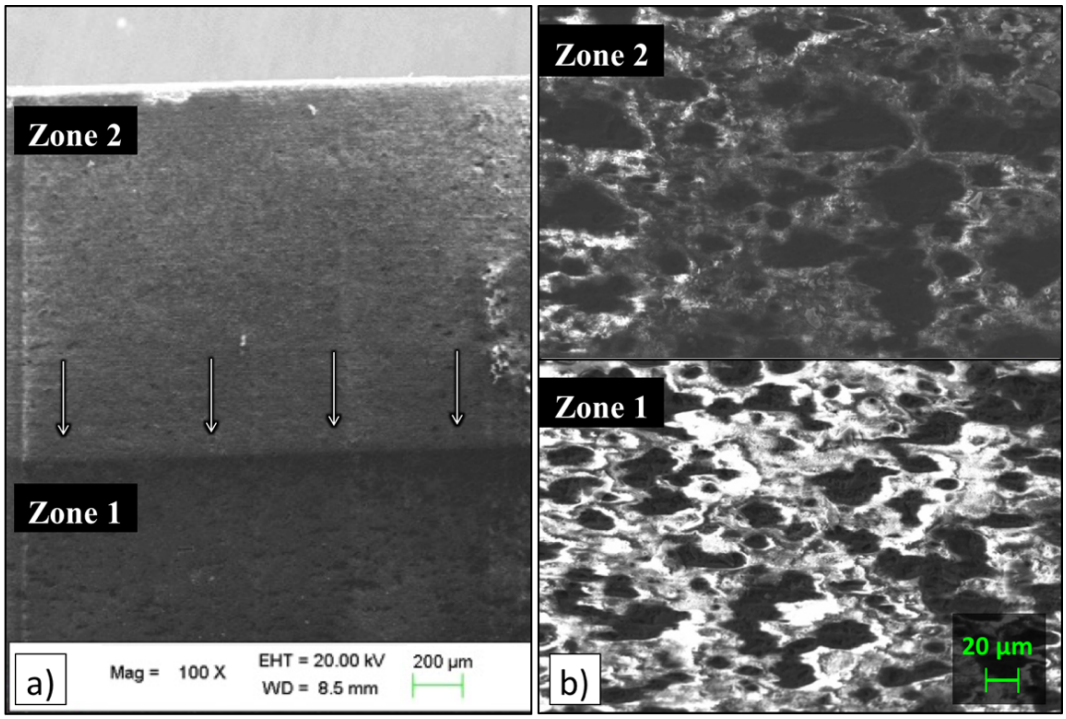

Fig.6. 24: SEM micrographs of the 1st ring groove, exhaust side, belonging to piston 5. (a) Low magnification micrograph (100 X), showing the presence of 2 different zones in the anodised layer; the separation line is offered by chamfer edge, pointed out by arrows. (b) Higher magnification micrographs (1000 X) of the 2 different zones.

Since the anodised layer is a functional layer, its wear might prevent the 1st ring from correctly working inside the groove and might totally compromise piston functionality, causing 1st ring sticking. Abnormal wear of the anodised layer wear is therefore not tolerable.

Due to the limited number of pistons affected by wear inside the 1st ring groove, it was not possible to properly evaluate which parameters control its onset. The high pressure inside the combustion chamber is thought to partially shift the knock triggering area from valve reliefs to the 1st ring groove, however other bench tests are needed to confirm this hypothesis. Nevertheless, piston sections and optical micrographs have been found suitable to accurately determine the wear level in the anodised area (Fig.6.22), the disadvantage being the destructive nature of these analyses.

Knocking erosion in piston top land and piston crown

In a few cases, also erosion in pistons crown and top land has been found and it was characterised through 3D digital microscope analyses. Damages in piston crown and top land usually do not occur individually, but are rather linked to other erosion sites. In other words, they represent the extension of erosion propagating from valve relief edge or from the 1st ring groove.

An example is given by piston 5 (Fig.6.25): piston crown is in fact damaged both in the central area 0° (intake side) and at valve edge 90°, respectively encircled in solid and dashed line, and indicated as 1 and 2 in Fig.6.25a. It can be inferred that the erosion in piston crown at 0° (1 in Fig.6.25a) is the result of erosion propagating from piston top land (reported in Fig.6.25b), which in turn is due to the high intensity knocking combustion in correspondence of the 1st ring groove: it is in fact clearly visible that heavier erosion affects the lower part of piston top land, next to the 1st ring groove, while moving up to piston crown erosion marks are slighlty smoothed.

Also erosion in piston crown next to valve relief is connected ot other knocking sites: Fig.6.25c clearly highlights in fact that valve relief is significantly worn out (indicated by the arrow), while small spots of erosion are covering piston crown. The Hirox analyses carried out in the anodised area and valve relief of piston 5, reported in Fig.6.21a, visibly confirm that the main knocking site (in terms of knocking intensity and therefore damage) are the 1st ring groove and valve relief themselves; starting from here, knocking effects are propagating at lower intensity towards piston crown.

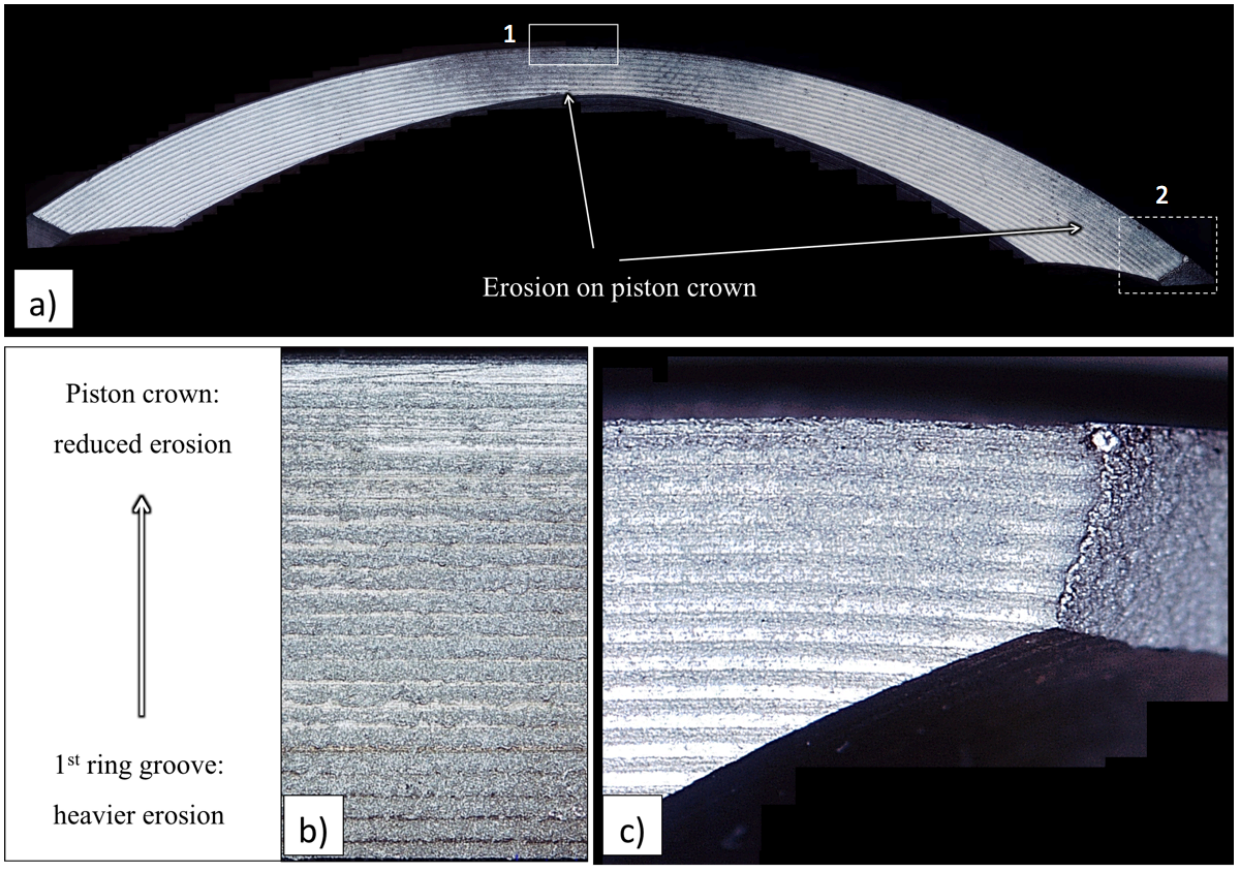

Fig.6.25: Eroded areas in piston 5 crown: (a) overview of piston crown intake side, where the interesting sites are pointed out by arrows, encircled and numbered as 1 and 2; (b) eroded top land in intake side 0°, responsible of erosion site 1 in piston crown; (c) erosion on intake valve edge 90°, responsible of erosion site 2 in piston crown.

Hardness tests on pistons crown

Micro-Vickers hardness tests have been carried out on pistons crown after bench tests, in the intake and exhaust side (as shown in Sect.6.1- Fig.6.11) and the results are presented in Fig.6.26 (normalised with respect to the maximum value detected). It is commonly accepted that heat flux is emphasised during knocking and anomalous combustions in general [2,18,22], as also determined by the authors in [28]. Due to the overaging affecting heat-treated Al alloys exposed at high temperature, hardness tests on pistons were selected as an indicator of the average in-service temperature [32,38], which was thought to be related to knocking intensity.

One of the most striking but evident result from Fig.6.26 is that, regardless of knocking severity, the average hardness in the intake side was lower than that in the exhaust side for all pistons. Since the intake side is cooled down by fresh air at each combustion cycle, this area was expected to experience a lower temperature with respect to the exhaust side, which for heat-treated Al alloys also means higher residual hardness. However, the precise opposite systematically occurred, in all probability due to the higher surface-to-volume ratio of the intake side. Once again, as for valve relief, it is evident that piston geometry significantly affects the temperature field and therefore it might enhance the formation of hot spots able to trigger knocking combustions.

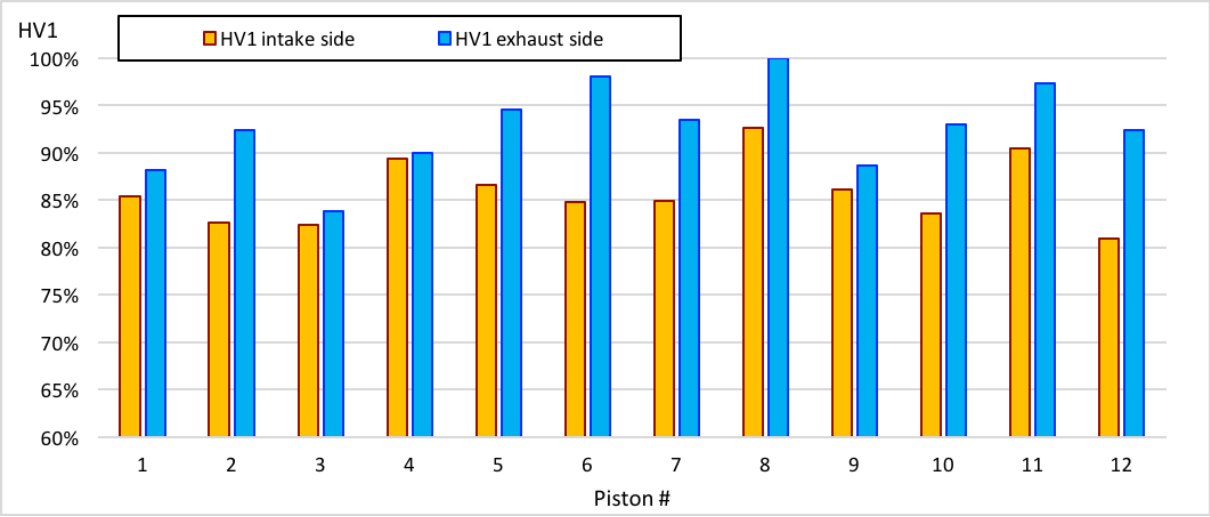

Fig.6. 26: Average piston hardness respectively in the intake (orange bars) and exhaust (blue bars) side; each bar represents the average of 5 measurements (see details in Sect.6.1 and Fig.6.11.).

Focusing on the effects of knocking on pistons residual hardness, it is worth highlighting that knock did not always cause erosion in the intake side, but also in the exhaust side: an example is piston 11, which nevertheless exhibits a higher residual hardness in the exhaust side. No direct correlation can be therefore found between piston area damaged by knock and the residual

hardness in the same area: knocking events are not lasting enough to produce a substantial overaging, even if the instantaneous heat flux is known to be enhanced. It is reasonable to assume that a localised and isolated knocking event produces an instantaneous increase of temperature in piston skin, but the material is not able to keep track of this in terms of residual hardness. The hardness decrease is, in fact, related to overaging, which is a diffusion-controlled phenomenon and therefore it requires *time* at a certain *temperature* to produce its effects.

It is however fundamental to point out that Al alloys, overaged or not, exhibit a considerable decrease in mechanical strength at high temperature (an example being shown in [38,39] as regards the high performance AA2618 piston alloy): even if an instantaneous increase of temperature is not able to produce a perceivable overaging, it instantaneously decreases the yield and ultimate strength of the alloy, which becomes more prone to plastic deformation and final failure. In view of this, the main thermal effect of knock is assumed to be a significant instantaneous alloy softening, which strengthens the effects of knock pressure oscillation and therefore further locally intensifies the erosion damage: the knock-induced higher temperatures therefore act as an intensification factor for the knock-induced mechanical stresses.

Finally, micro-Vickers tests further confirm what can be defined as a "tip-effect": in all pistons, in fact, the lower hardness values have been found in the measurement points 1 and 5 (with reference to Fig.6.11), where the surface-to-volume ratio is higher, close to the intake valve reliefs. Pistons #2 and #11, subjected to the same duration of bench test (15h), were selected to illustrate this trend in the thermal field. Thanks to the overaging curves and HB-HV_1 correlation reported in Sect.6.1- Fig.6.4b, it was possible to calculate the average temperature experienced by all pistons in each measurement point; Table 5 and Table 6 reports both residual hardness and temperature data normalised to the maximum value experienced, due to confidentiality reasons. The average temperature in the extremal points 1 and 5 of pistons #2 and #11 was respectively found up to 5% and 7% higher, compared to the other points of interest 2-3-4 in the intake side.

Taking into account the residual hardness/temperature values reported in Table 6.5 and Table 6.6, moreover, the marginal effect of knock on the average temperature field, compared to p_max90%, can be noticed and further confirmed. While working at the same operating point and for the same bench test duration, piston 11 in fact exhibits considerably higher residual hardness (and therefore lower temperatures) compared to piston 2, even if it was subjected to a more severe knocking regime (Table 6.3); the reason was found in the lower p_max90%, which is the main responsible of the average temperature inside the combustion chamber.

Since many variables affect pistons residual hardness, it is generally complicated to gain useful information on knocking intensity by simply considering these data.

Table 6. 5: Micro-Vickers hardness values in piston #2 (the points of interests for measures 1-10 are indicated in Fig.6.11). The lower hardness values are underlined and highlighted in bold; the average temperature experienced by point 8 cannot be calculated due to negligible hardness decrease.

Piston #2										
Measure #	1	2	3	4	5	6	7	8	9	10
HV_1 norm.	78%	83%	85%	85%	80%	84%	95%	99%	94%	87%
T norm.	100%	97%	95%	96%	98%	96%	86%	N/A	89%	94%

Table 6. 6: Micro-Vickers hardness values in piston #11 (the points of interests for measures 1-10 are indicated in Fig. 5). The lower hardness values are underlined and highlighted in bold; the average temperature experienced by points 8 and 9 cannot be calculated due to negligible or null hardness decrease.

Piston #11										
Measure #	1	2	3	4	5	6	7	8	9	10
HV_1 norm.	87%	92%	94%	91%	85%	95%	97%	100%	99%	93%
T norm.	94%	91%	88%	91%	95%	86%	81%	N/A	N/A	90%

6.2.2 Conclusions

In the present work, controlled knocking combustions were induced in a turbocharged engine at 4500rpm during bench tests. The corresponding main mechanisms of damage on Al-Si pistons were investigated in order to determine the influence of knocking intensity and frequency on the resulting damage. The main results can be summarised as follow:

- The pressure oscillations due to knock have a cleaning effect on carbon residues. The visual analysis on pistons before degreasing is therefore fundamental, since the distribution of carbon residues provides useful information on knocking preferential sites.
- Valve reliefs are extremely sensitive to knocking damage, due to their high surface-to-volume ratio which significantly enhances the local temperature. Knock in valve reliefs acts in two ways, through polishing and erosion. Polishing is an inoffensive damage, frequently observed, and mainly related to localized thermal expansion that induces a localized sliding contact between piston valve relief and cylinder. Erosion damage is more severe and compromising, since it produces debris inside the combustion chamber. OM and SEM analyses show that erosion is due to cracks nucleation in the softer Al matrix, at the

interface with Si particles or secondary phases, and following propagation. Erosion is most pronounced under severe (even isolated) knocking combustions, and its level is well related to MAPO99.5%.

- In a few cases, usually related to high maximum pressure inside the combustion chamber, severe erosion in the 1st ring groove was detected. Knock in this area is deleterious since it is able to completely wear out the anodized layer, compromising the functionality of the 1st ring and the combustion gases sealing. The high-pressure contact between the steel ring and the bare aluminum in the 1st ring groove might lead, in fact, to ring sticking and significant wear of the Al piston. The damage can also develop in lands rupture and blow-by channels formation.
- Evidence of erosion was also found in piston crown and top land. Both these damages are generally consequences of knock trigger in other sites, such as piston valve reliefs or 1st ring groove.
- Hardness measurements on pistons after bench tests cannot be directly related to knocking intensity: piston thermal field is, in fact, strictly related to piston geometry and to the maximum pressure inside the combustion chamber, which usually masks the temperature increase due to knock. The instantaneous higher temperatures induced by knock are assumed not to produce substantial overaging in the alloy, due to the limited time of exposure, but rather to produce a correspondingly instantaneous alloy softening, which acts as an intensification factor for knock-induced mechanical stresses.

6.3 Combination of (MAPO, p_max) to produce knocking damage: synergetic effect of mechanical and thermal load

[The data reported in this Sect. consist of an extract from the published paper whose title is shown below, but reviewed from a "metallurgical" point of view, stressing the relevance of engine parameters in affecting material behaviour. The paper was also further integrated with the results of recent bench tests. Both Introduction and Material and Methods paragraphs have been considerably shortened with respect to the published version, since most of the information in this regard is respectively available in Sect.5.2 and Sect.6.1 of the present dissertation].

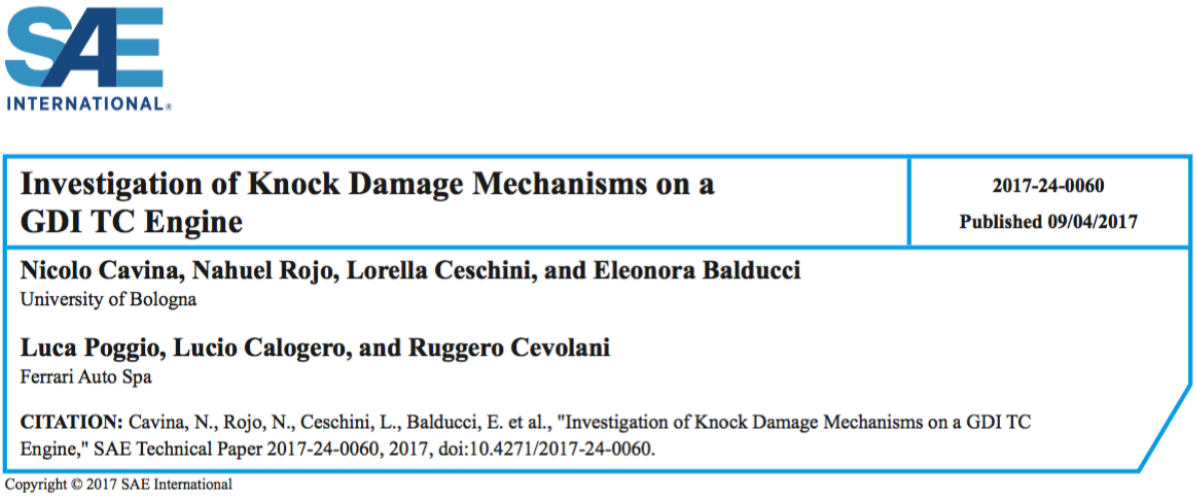

Investigation of Knock Damage Mechanisms on a GDI TC Engine

2017-24-0060
Published 09/04/2017

Nicolo Cavina, Nahuel Rojo, Lorella Ceschini, and Eleonora Balducci
University of Bologna

Luca Poggio, Lucio Calogero, and Ruggero Cevolani
Ferrari Auto Spa

CITATION: Cavina, N., Rojo, N., Ceschini, L., Balducci, E. et al., "Investigation of Knock Damage Mechanisms on a GDI TC Engine," SAE Technical Paper 2017-24-0060, 2017, doi:10.4271/2017-24-0060.

Abstract

The paper focuses on understanding the knocking damage mechanisms and which among engine parameters mainly influence material properties and therefore pistons failure during abnormal combustions. Aiming to underline the synergetic effects of *thermal* and *mechanical* loads, the paper reports an attempt to separately control p_max-MAPO: steady-state tests have been in fact conducted at different and constant levels of knock intensity (i.e. pressure waves oscillation amplitude, defined by MAPO) and pressure levels inside the combustion chamber (which mainly govern average temperature). Since these parameters are strictly interrelated for a given engine operating condition and for a given fuel, fuels with different knock resistance (i.e., RON number) have been employed. This Sect. provides a clearer understanding of the damage distribution in the knock intensity-thermal load domain.

6.3.1. Introduction

Knocking operation is supposed to induce damage through two different mechanisms: (i) *mechanical damage*, due to the action of pressure waves on piston surface, possibly coupled with differential thermal expansion of the material; (ii) *thermal damage* (material strength decay), caused by higher temperatures due to heat transfer increase during abnormal combustions [2,18,19,22,24,25,40].

For given operating conditions, and at fixed air and fuel quantities, wall thermal load (i.e. heat flowing through the walls) depends on spark advance: the higher the spark advance, the higher the in-cylinder pressure, temperature and nominal heat transferred to the walls (disregarding of knock). Considering this, maximum pressure p_max will be used in this Sect. as a reliable and convenient raw indicator for the wall thermal load; p_max is defined as the maximum value of the low-pass filtered pressure signal, see Fig.6.27. Knocking operation, however, is supposed to amplify the thermal load and to add a contribution towards further heating the combustion chamber walls [22,40], even if the heating is instantaneous and cannot be efficaciously traced by hardness measurements on pistons head, as reported in the previous Sect.6.2 [30]. Knock intensity is defined by the common index MAPO (as reported in Eq.5.3 and graphically explained in Fig.6.27).

Both p_max and knock therefore contribute in defining the thermal effects on combustion chamber components and it is difficult to isolate knock effect since advancing the spark advance generated both increased p_max and MAPO.

By using different RON number fuels (with a different tendency to auto-ignite), it is possible to introduce a second degree of freedom, in addition to the spark advance, to control piston boundary conditions. It is in fact possible to:

- obtain the same p_max level but different knocking intensity, by applying the same spark advance to different RON number fuels (lower RON number fuels show a stronger tendency to auto-ignite and therefore cause a higher MAPO under the same conditions);
- to induce the same knocking intensity but different p_max levels, by differentiating spark advance for different RON number fuels.

The weight of each factor in determining the detected knock damage should be therefore identified.

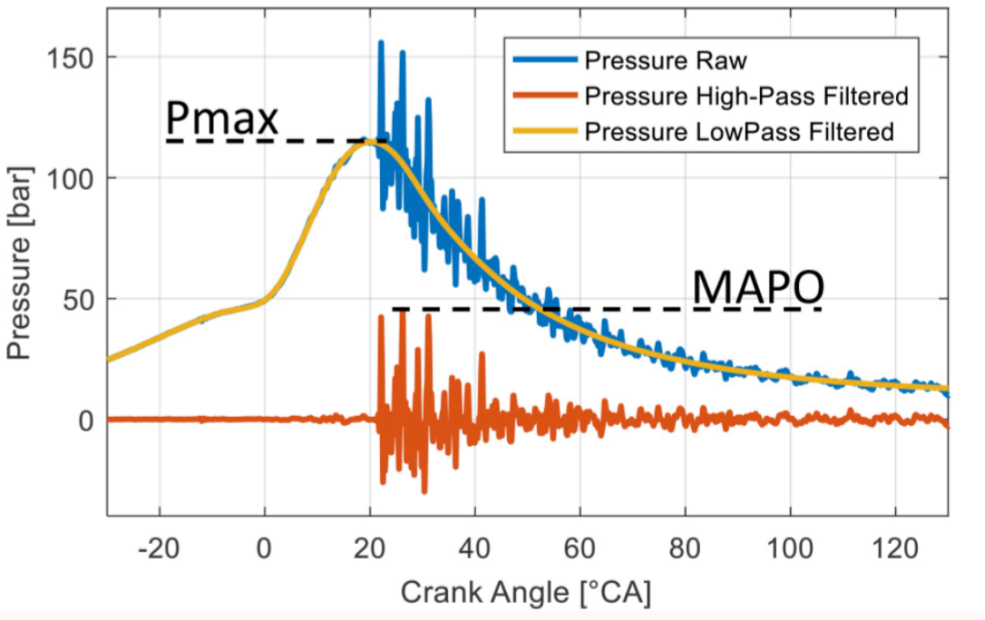

Fig.6. 27: Typical in-cylinder pressure signal for a knocking cycle. P_max is defined as the maximum value of the in-cylinder low-pass filtered pressure signal, while MAPO is defined as the maximum of the absolute value of the high-pass filtered pressure signal.

6.3.2. Materials and methods

Experimental tests have been conducted on a V8 turbocharged Gasoline Direct Injection (GDI) engine at constant 6000rpm, λ = 0.73, load equal to 2300mbar intake pressure. Fuels with 3 different knock resistance levels (RON) have been used, in specific RON 91, RON 95, RON 100, for a total duration respectively of 7.5h, 10h, 6.1h. Spark Advance (SA) is controlled, for every cylinder, in closed loop, targeting a predefined, individual knock level. The tests were conducted on only one active bank (so it is de facto an inline 4-cylinder engine) and generated a total amount of 12 pistons to be analyzed.

Examination of the in-cylinder pressure history has been conducted, coupled with the analysis of knock induced damage on pistons, with the aim of modelling a pressure-based knock damage model. In-cylinder pressure analysis is focused on knock intensity measurement, and the time-based pressure signal is also used to estimate piston temperature through heat exchange modelling.

Instead, the objective of piston analysis is to characterize and quantitatively evaluate the induced knock damage.

6.3.3. Results and discussion

During all tests with RON 91, RON 95 and RON 100, different knock levels were controlled in the 4 cylinders, one of which (cylinder 5 in RON 91 and RON 100 test, cylinder 1 in RON 95 test) always in non-knocking mode under constant spark advance. The target was set in terms of MAPO99.5% and achieved through a PID controller. Data ate normalized with reference to the max p_max and MAPO values achieved during bench tests, as reported in Table 6.7.

Table 6. 7: Operating conditions and duration for each test.

RON 91 test – 7.8h				
Cylinder	5	6	7	8
MAPO 99.5% measured [%]	16.0	57.5	75.0	100.0
P_max 90% [%]	65.1	71.6	73.2	72.9
RON 95 test – 10h				
Cylinder	1	2	3	4
MAPO 99.5% measured [%]	20.5	43.5	50.0	67.0
P_max 90%	80.1	85.7	86.6	87.7
RON 100 test – 6.1h				
Cylinder	5	6	7	8
MAPO 99.5% measured [%]	15.5	35.5	50.0	64.5
P_max 90%	80.7	95.7	98.7	100.0

In all (damaged) pistons, the most damaged area was found to be the exhaust valve relief, area which is mainly affected by knock due to its high surface/volume ratio, as reported in Sect.6.2 and [30]) Among the most damaged pistons there are, in order of decreasing seriousness, piston #8 – RON91 test, piston #4 – RON95 test, piston #8 – RON100 test. The macrographs of these pistons are reported in Fig.6.28, and clearly show a difference in terms of extension of the eroded area.

Knocking damage was qualitatively evaluated by considering both the severity of erosion at valve reliefs and ring groove plastic deformation. The two aspects are interconnected, since knocking combustions produce a substantial increase of thermo-mechanical loads and when localized over piston valve reliefs tend to produce a consistent ring groove closure. In-depth Hirox analyses of pistons valve reliefs in the same position helped to precisely rank pistons in terms of erosion index

(E). An example of that is offered by Fig.6.29, which collects micrographs of the most damaged piston valve reliefs after the tests with different RON number fuels.

The summary of the qualitative erosion indexes for all pistons is reported in Table 6.8; data clearly highlight the aforementioned relationship between erosion index E and 1st ring groove size, also showing that ring groove closure is observed only when exceeding E≥3.

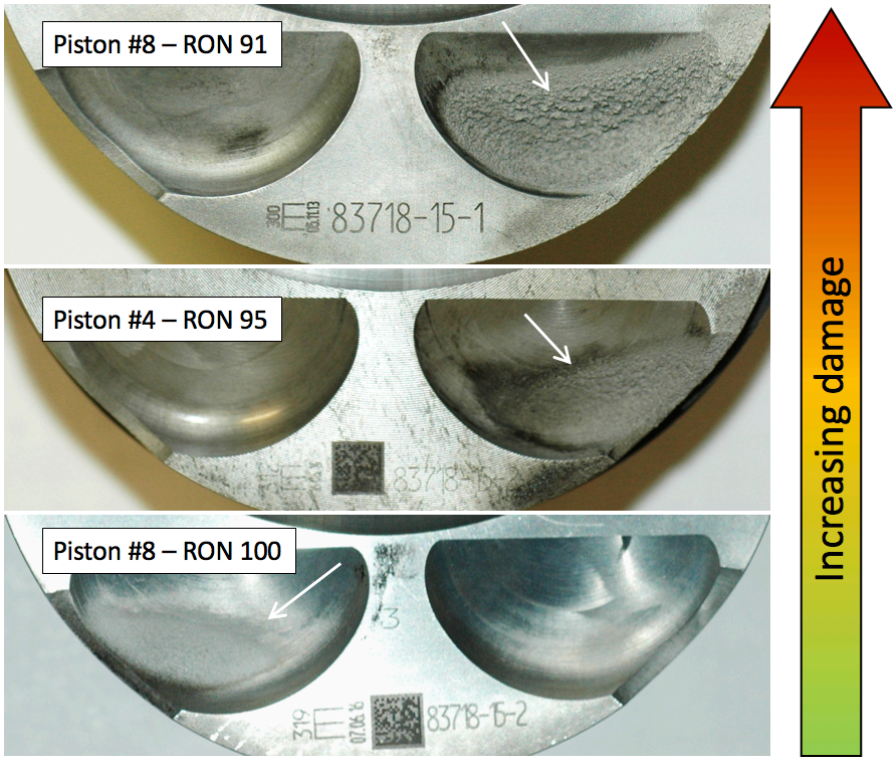

Fig.6. 28: Macrographs of pistons showing the maximum damage during tests with RON 91, RON 95 and RON 100 fuels.

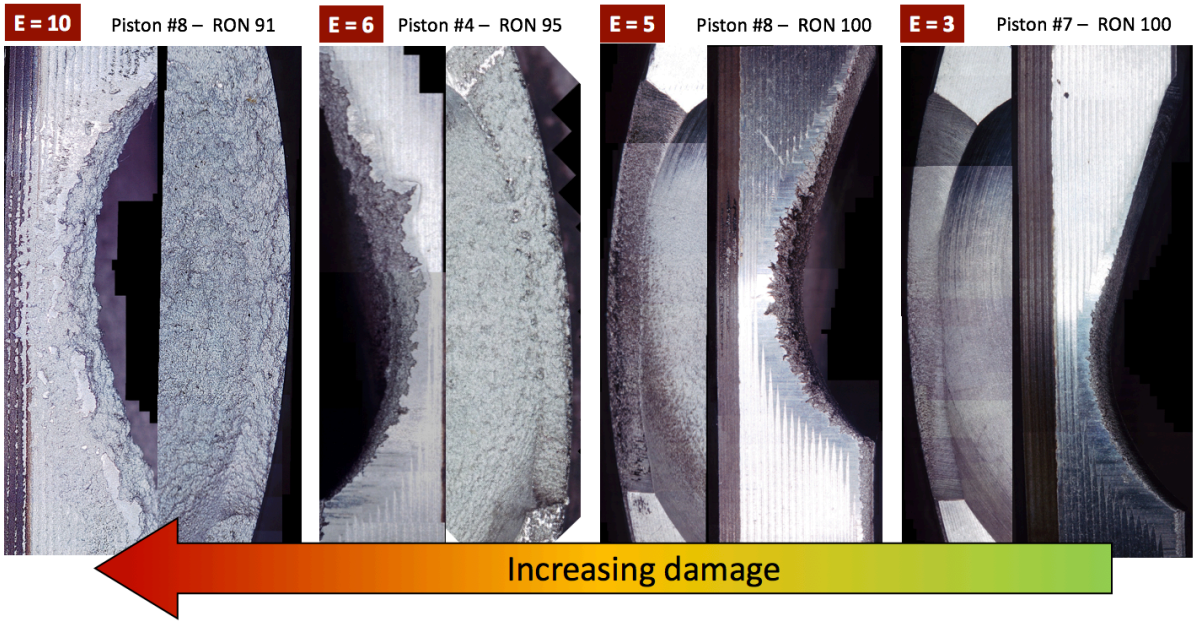

Fig.6. 29: Hirox micrographs of the most damaged pistons valve reliefs, in order of damage severity, during tests with different RON fuels number.

Table 6.8: Erosion indexes E for each piston and size of 1st ring groove.

RON	Piston #	Most damaged valve	Erosion index E	1st groove size
91	5	None	0	100%
	6	None	1.2	100%
	7	Exhaust, 270°	2	100%
	8	Exhaust, 90°	10	98%
95	1	none	0	100%
	2	Exhaust, 90°	0	100%
	3	Exhaust, 90°	1.5	100%
	4	Exhaust, 90°	6	98%
100	5	None	0	100%
	6	None	0	100%
	7	Exhaust, 270°	3	98%
	8	Exhaust, 90° - 270°	5	97%

By measuring residual hardness on pistons crown (in the positions highlighted inby Fig.6.11) and considering the hardness-temperature-time curves for the alloy (Fig.6.4), it was possible to evaluate an equivalent mean piston temperature for each piston, and to plot them as a function of p_max90%, as shown in Fig.6.30. Data confirm the almost linear relation between in-chamber pressure and temperature: as expected, it can be inferred that higher p_max90% values correspond to higher average temperatures at pistons head (and combustion chamber components in general).

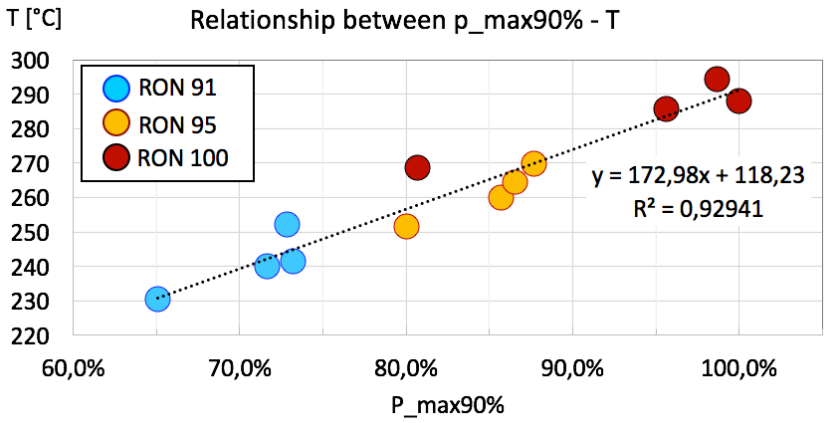

Fig.6.30: Relationship between p_max90% and average piston temperature in the exhaust side, evaluated thanks to hardness-temperature-time curves and hardness tests at piston crown. P_max90% data are normalized due to confidentiality reasons.

Moreover, as predicted and desired, operating with different RON fuels allowed to investigate the effects of knock induced stresses at different average temperature (or p_max90%, since these parameters are almost interchangeable). The experimental points in terms of MAPO-p_max90% and MAPO-average T are highlighted in Fig.6.31a-b.

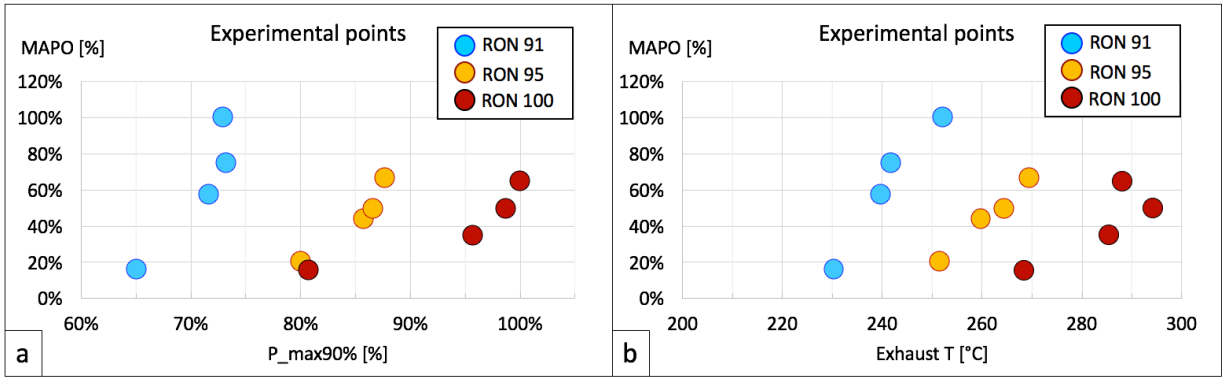

Fig.6. 31: Experimental points, plotted in the field MAPO-p_max90% (a) and MAPO-exhaust T (b).

By matching the measured temperature-MAPO values with the erosion indexes (Fig.6.32) it is possible to state that the safe area without any erosion and/or plastic deformation does not solely depend on MAPO level but also on the experienced in-chamber temperature (well related to p_max90% as highlighted in Fig.6.30): the higher the in-chamber temperature (the higher the p_max90%), the lower the MAPO intensity which can be tolerated without any damage. For the purpose, in order to precisely compare experimental points reached through tests with different duration (7.8h, 10h, 6.1h respectively for RON 91, RON 95, RON 100), the erosion index E has been normalized with respect to the operation time, assuming the hypothesis that damage accumulation is linearly time-dependent.

The effect of piston temperature on the induced damage is evident if pistons #6 – RON91, #3 – RON95, #7 – RON100 are considered: these pistons approximately operated under the same knocking level (57.5%, 50.0%, 50.0% respectively), but different erosion levels are achieved, equal to 1.2, 1.5, 3 (which turn into 1.5, 1.5, 4.9 if normalized to the operating time). Evidently, the different impact of knock depends on the different piston temperature and therefore on the different material sensitivity to mechanical stresses.

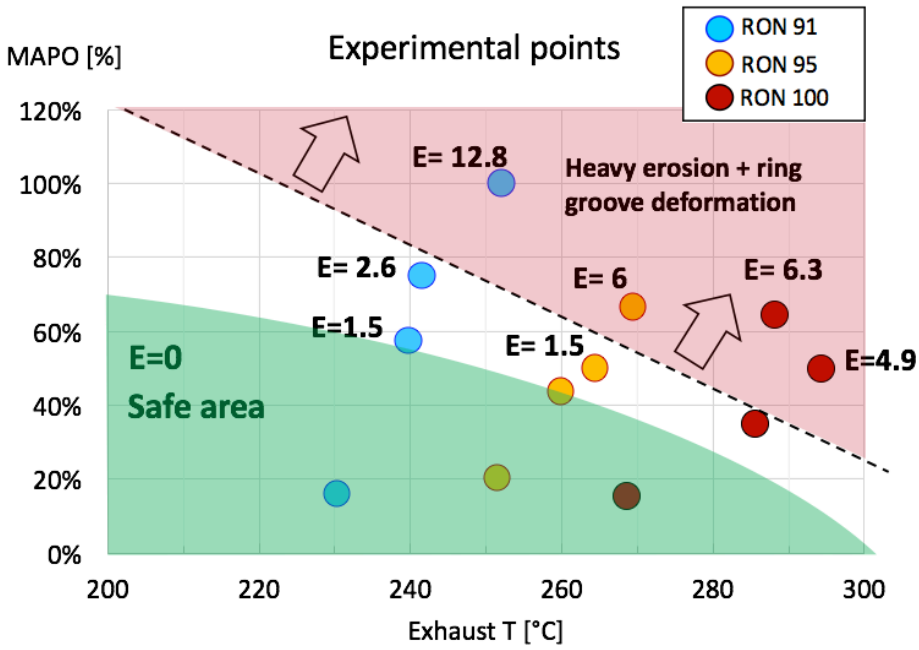

Fig.6. 32: Relationship between knock intensity (MAPO), in-chamber temperature (represented here by the average temperature at piston exhaust side) and knocking damage (erosion index E). It is highlighted that the "safe" area (in green) tolerates higher MAPO values for lower temperatures.

6.3.4 Conclusions

The experiments with different RON number fuels give evidence that the higher the specific power is (and so the piston temperature), the lower the knock level to be considered "safe" for Al pistons damage. P_max is considered particularly relevant in determining knock damage, since it has a substantial contribution to the chamber surfaces temperature, and it is known that temperature strongly influences instantaneous material properties (especially for Al alloys), in addition to leaving an imprint on residual properties (hardness and strength). P_max (or high temperature) therefore acts increasing material sensitivity to knock pressure oscillation.

It can be ultimately inferred that the actual knock-safe thresholds should mainly depend on p_max, or better on piston temperature. This is an important element, to be considered in modelling knock damage, and in general to be taken into account for engine calibration.

Chapter 7:

Modelling knocking damage

In the final step of the Ph.D. activities, all the elements needed to model piston knock damage, with a control-oriented approach, were available: the main knocking damage mechanisms were identified, as well as the main engine parameters to be considered in determining the effects of each single knocking cycle. Still, a precise experimental methodology able to objectively quantify knocking damage in terms of engine reduced functionality was missing. Chapter 7 aims to fill this gap:

- Sect.7.1 separately takes into account all the aforementioned methodologies employed for knocking damage characterization and discusses their pros and cons in determining an objective index able to effectively quantify the reduced piston functionality.
- Sect.7.2 briefly shows the skeleton of the knock damage controlled, implemented on-board during the last bench tests and validated by the observations on pistons.

7.1 Objective characterization of knocking damage

7.1.1 Methods to quantify knocking erosion at piston valve reliefs

All the tested methods are reported below. The main limit of each method is the scarcely accuracy in correctly determining the volume of eroded material. To now, still visual analysis is employed to correctly rank pistons damage at valve reliefs.

Macrographs

Even if usually underestimated, macrographs acquired on pistons after bench test and before any washing procedure are considered fundamental in order to precisely evaluate which areas are mainly affected by knock and have to be further investigated. This is due to the cleaning effect on carbon residues typically exerted by anomalous combustions.

Just in case of heavy erosion (such as piston #8 – RON 91 reported in Fig.6.28, macrographs are able to give quantitative information about the damage, through a precise determination of the extension of the eroded area. Aiming to develop an automatized algorithm, macrographs of all analysed have been always collected in the same position and at the same, comparable distance from piston head. An example of digital image filtering is reported in Fig.7.1.

However, due to the fact that heavy eroded pistons are not of interest, further development of this characterization were not considered.

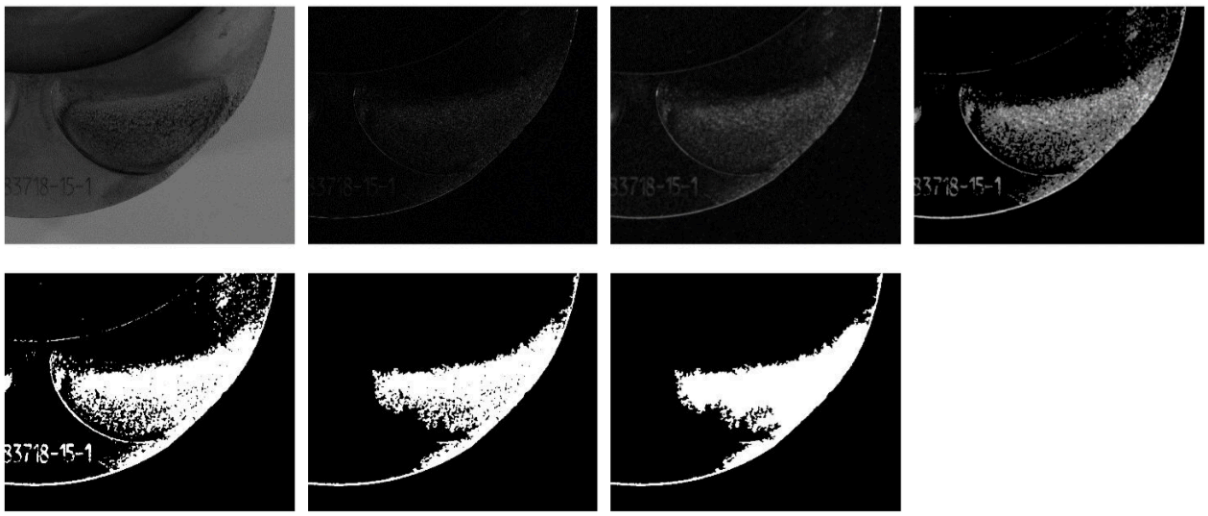

Fig.7.1: Example of consecutive digital image filtering, used to estimate the eroded area. In the top-left picture, the original picture, in the bottom-right the final image highlighting the eroded surface. Some disturbances (such as piston production numbers and matrix) required the contribution of the user.

Hirox

In-depth images through Hirox 3D digital microscope were fundamental for knock erosion characterization, in particular at valve reliefs. As highlighted both in Sect.6.2 and Sect.6.3, however, these visual analyses simply allow to subjectively establish a rank of the most eroded pistons valve reliefs. The limit of this approach is the not negligible influence of the operator in the numerical value of the erosion index E such determined.

Roughness and profilometer tests

In addition to Hirox analyses, several roughness and profilometer tests have been carried out with the aim to precisely and objectively quantify erosion; below reported the most significant attempts.

- A few bench tests show the presence of erosion at piston top land, so that roughness measurements were able to detect a change in roughness values between eroded and untouched pistons. In particular, the anodized layer of the top land above the 1st ring groove was extremely sensitive to erosion: due to its brittleness, the anodic oxide fil hardly resists to knock pressure oscillations.

  An example of these measurements is reported in Fig.7.2, which refers to pistons from set #4 (4500rpm WOT, intake manifold pressure equal to 2200mbar and the normalized air-to-fuel ratio λ equal to 0.79). In this case, the targeted knock level decreased from piston #5 to piston #8, and so did also the roughness values. The mean roughness depth RzD was selected to quantitatively evaluate the erosion damage, since it was found to be both able to discriminate between different erosion levels and not overly affected by a single discontinuity (as Rt does). According to DIN-4768 standard, RzD is in fact calculated by determining the average maximum peak-to-valley distance within 5 successive sampling lengths. The arithmetical mean deviation Ra was indeed found to be not sufficiently sensitive to erosion intensity.

  However, erosion at piston top land was rarely observed; moreover, it characterized the most severely eroded pistons, which are not of scientific interest since such damage cannot be accepted. Further developments in this approach were not carried out.

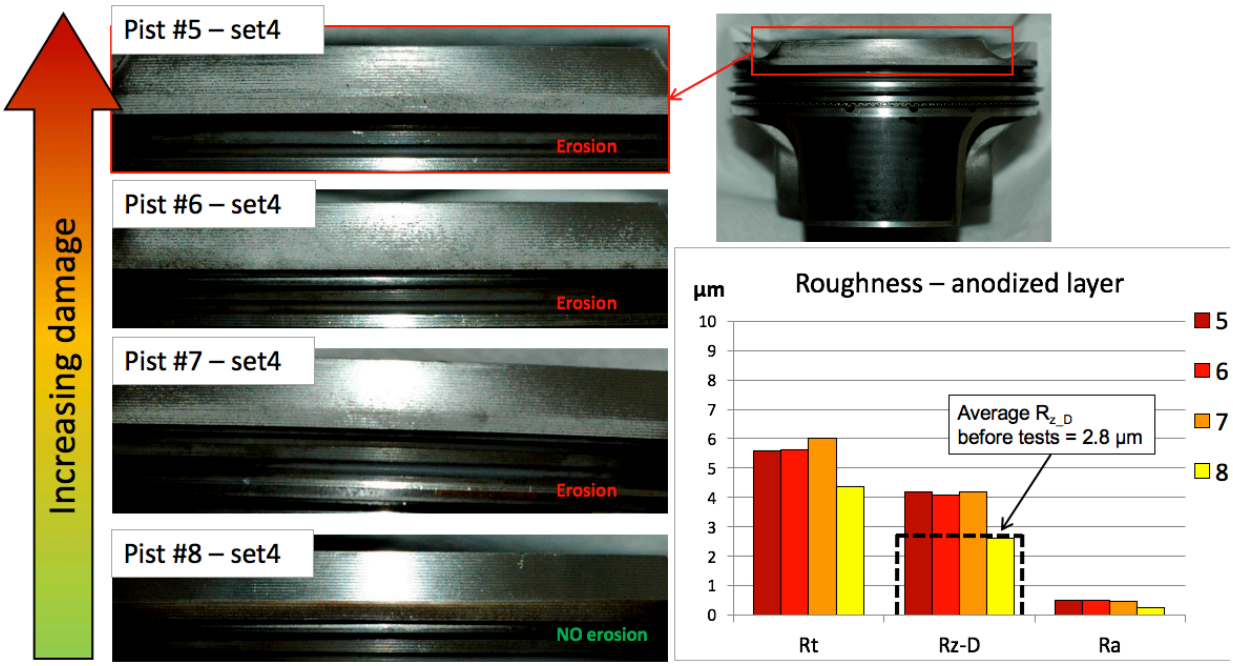

Fig.7. 2: Example of erosion damage detected at pistons top land (set4) and attempts to objectively quantify the damage through roughness measurements.

- Erosion at valve reliefs was indeed observed in all investigated cases were damage occurs. A few attempts to quantify erosion were carried out at Unibo through HommelWerke profilometer, equipped with a TK300 stylus (tip radius 5 µm). The first data in this regards are also reported in [31]. A measurement length of 1.5mm was selected and two profiles were acquired for each valve relief (both 90° and 270°) within 1mm distance from each other, as indicated by the blue and red lines/ellipses in Fig.7.3. Due to the curvature of the valve reliefs it was not possible to directly use the difference between min-max values to quantify the erosion depth. Analogously to the previous attempts, raw data were filtered to obtain roughness parameters and the mean roughness depth RzD was selected to quantitatively evaluate the erosion damage, since it was found to be sensitive to increased erosion level and in line with the visual ranking through Hirox images.
- Additional attempts in these terms have been carried out at Ferrari Dept. of Powertrain Development, through Mitutoyo Contracer CV-2100 series – contour measuring system. The adopted procedure is shown in Fig.7.4: in order to be as much accurate as possible to precisely compare piston profiles at valve reliefs before and after bench tests, (a) pistons positioning in the vise was guided by square set equipment, then (b) the lines of interest were precisely drawn on pistons and (c) stylus profilometer was imposed to exactly follow

these lines. The achieved results are shown in (d), where for defined intervals the dimension of the eroded material was found. The weakness of the method was due to the fact that the equipment was not dedicated and in several attempts, it was not possible to precisely superimpose the acquired profiles. In particular, in case of low erosion damage, the accuracy of the method is extremely low. A slight deviation is also encircled in red in Fig.7.4d.

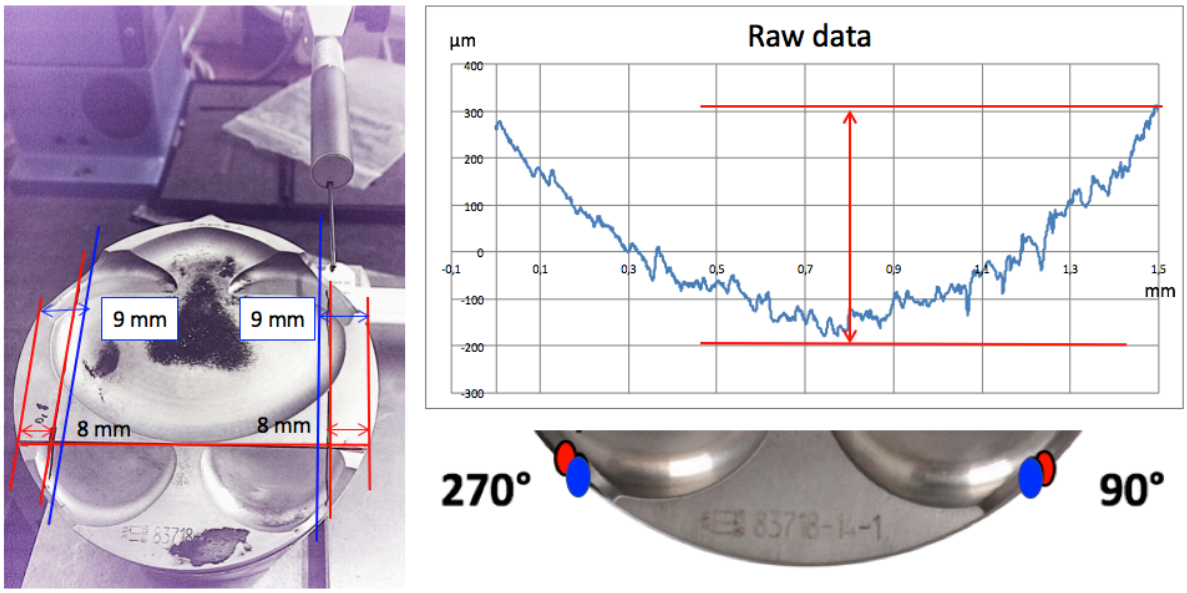

Fig.7. 3: Attempts to quantify erosion through roughness measurements in valve reliefs, at Unibo Dept. of Metallurgy.

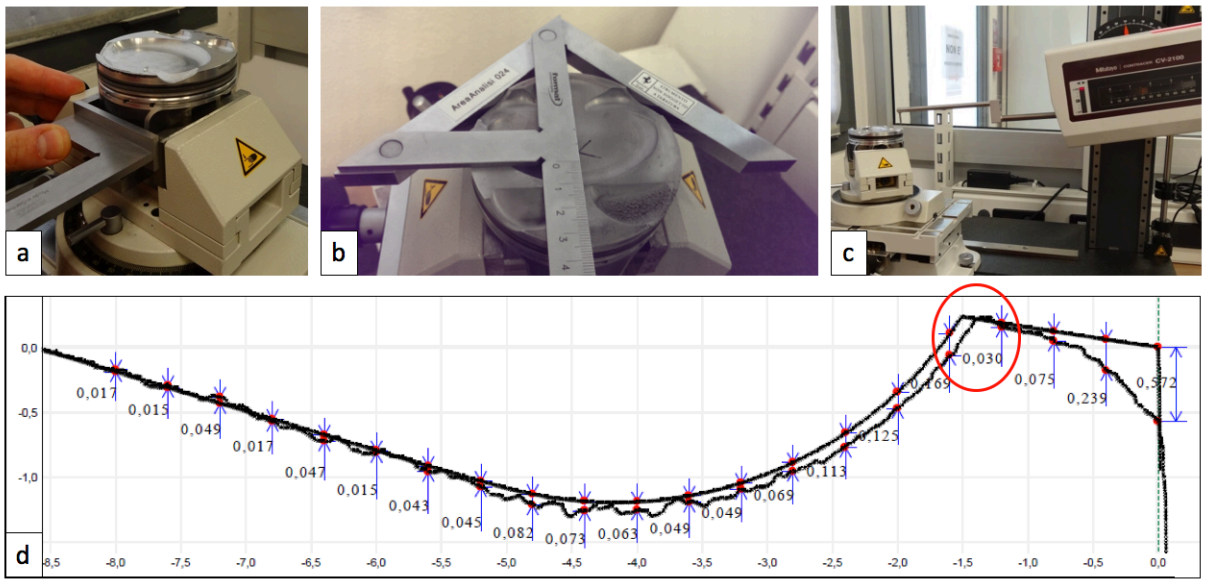

Fig.7. 4: Attempts to quantify erosion through profilometer measurements in valve reliefs, at Ferrari Dept. of Powertrain Testing. (a) Piston precise positioning in the vise, with the help of a set square; (b) equipment to find piston center and trace the diameters of interest at precise angular position; (c) ongoing measurement; (d) Superimposed profiles, before and after bench tests.

- A final attempt has been made through 3D laser scan, through Faro Edge ScanArm®, at Ferrari Dept. of Powertrain Development. The idea was to compare the acquired cloud of points to the 3D CAD geometry, in order to determine the eroded volume. For the purpose, piston #7 form set8 was selected, due to its low level of erosion (E=2 according to the ranking based on Hirox images). In this case, the resolution of the instrument was not high enough to detect erosion damage, and significant scattering of the data/noise was detected, compromising the possibility to correctly evaluate erosion.

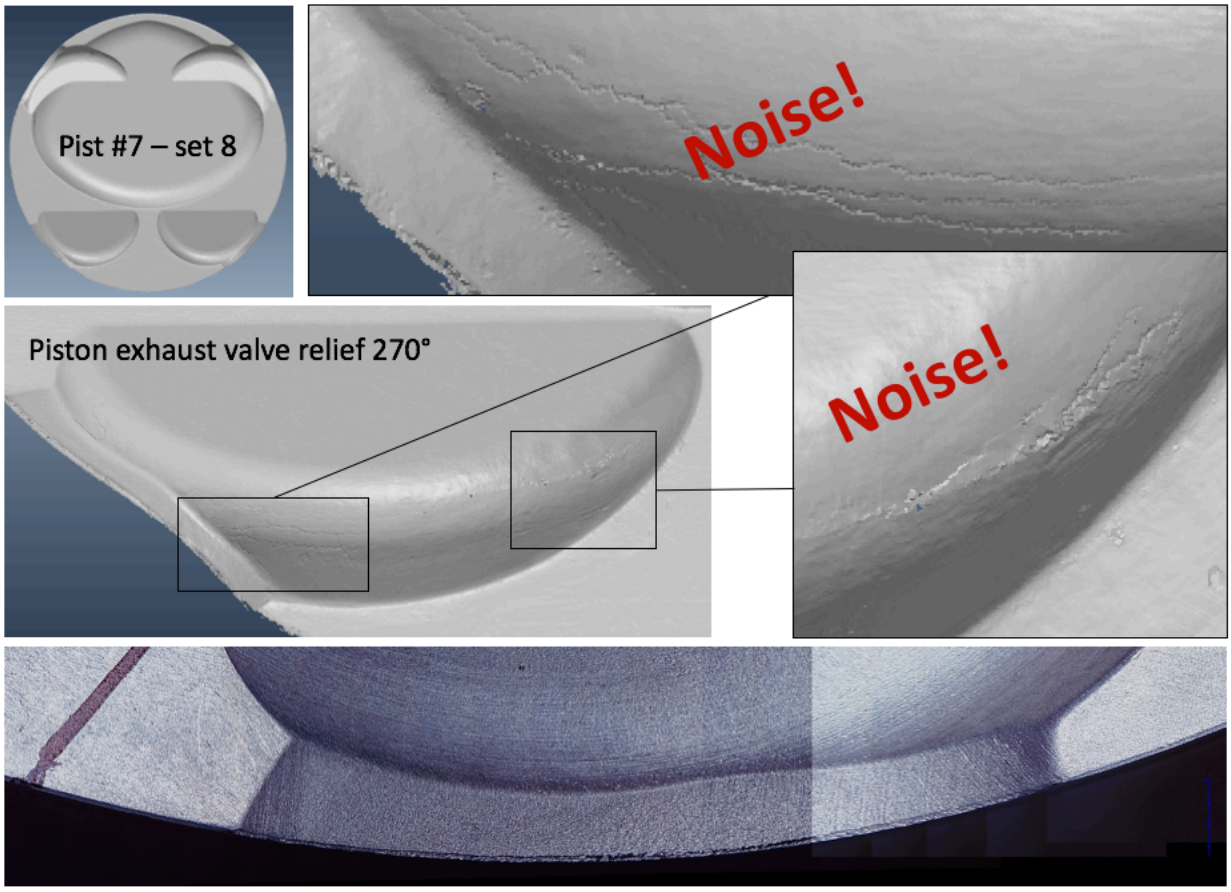

Fig.7. 5: Attempt to quantify erosion through 3D laser measurements.

7.1.2 Methods to quantify knocking damage at 1st ring groove

Another relevant damage detected was the damage at 1st ring groove. This can manifest in 2 different ways:

- Reduction of the 1st ring groove size, in case knocking combustions are localized above valve reliefs.

- Erosion and consistent wear of the anodized layer inside the 1st ring groove (see Sect.6.2 and Figs.6.21-22-23); this damage is more seldom encountered and related to abnormal combustions occurring inside the 1st ring groove.

In both cases, damage can be objectively and quantitatively evaluated through the adoption of Johnson gauge blocks (Fig.6.9) which are able to determine the 1st ring groove dimension in close-spaced angular sections: in the first case, the plastic deformation of the 1st ring groove usually translate in reduced dimensions, while in the last case, gauge blocks reveal the exact opposite due to anomalous wear.

As reported in Sect.6.2, during Ph.D. activities the wear of the anodized layer was also evaluated through OM micrographs on specific metallographic sections. These activities helped in understanding the damage mechanism but had important drawbacks: (i) they consist of destructive analyses; (ii) they were conducted in a few localized angular position of pistons; (iii) they were extremely time-consuming in case a mapping of ring groove dimension was aimed, as highlighted in Fig.6.9a.

7.1.3 Methods to evaluate the degradation of material properties

As already mentioned in Sect.6.1, micro-Vickers hardness tests were performed on pistons crown after bench tests, in the exhaust and intake side (Fig.6.11). As collected, raw data already represent quantitative and objective indexes, and allow to:

- acquire information about local average temperatures, which were found to be precious information in order to study the knocking damage mechanism;
- determine the alloy residual hardness, which can be directly translated into residual alloy mechanical properties (such as tensile and fatigue strength) at specific temperature. Part A of the present dissertation clearly shows that Al alloys residual hardness usually has a linear dependence with mechanical properties both at room and high temperature, so that a reduction of residual hardness means an alongside reduction of mechanical properties.

7.1.4 Damages weighted in terms of residual piston functionality

Most of the aforementioned damages, namely erosion at valve reliefs, variation of the size of piston 1st ring groove and substantial wear of the anodized layer covering the 1st ring groove are

thought to affect residual piston functionality, in particular as regards the amount of blow-by (passage of combustion gases from the combustion chamber towards engine crankcase, which results in power loss) and oil consumption.

Erosion at valve reliefs, if prolonged, might in fact lead to the formation of blow-by channels, which significantly interfere with the correct operation of piston 1st ring. The same can be inferred, of course, as regards the aforementioned damages at 1st ring groove, which penalize the 1st ring functionality, leading to 1st ring jamming or adhesion in the groove.

A decrease in residual hardness is thought to accelerate the 3 aforementioned damages: the lower the material residual mechanical properties, the lower will be its resistance to mechanical stresses, which will cause erosion and plastic deformation; at the same time, the lower hardness means a lower support to anodized layer, which is thought to exhibit a consequent higher wear rate.

Even if quantitative measurements in terms of these damages have been collected (as reported in the previous paragraphs), though their influence on pistons functionality has not still been assessed. A few additional bench tests are scheduled in Ferrari S.p.A. for the next months with the aim to:

- Precisely collect information about oil consumption and blow-by throughout the tests
- Determine the influence of material properties reduction on the aforementioned damages. For the purpose, an engine bank has been equipped with overaged pistons at the hardness plateau (≈65 HB, see Fig.6.4b), while the other bank consists of the typical, as received T7 pistons. The same (MAPO, p_max90%) levels will be tested on each bank, aiming to underline the influence caused by the solely starting material properties.

The precise translation of erosion index into reduction of piston residual functionality is therefore still ongoing.

7.2 Knocking damage control

Since the details of the on-board strategies are not the focus of the present dissertation, this Sect. is a brief introduction to the recently developed damage model implemented by Fluid Machinery Research Group in the ECU dedicated to ignition strategies and knock control (Miracle® by Alma Automotive); this knocking controller was used and validated during the last bench tests. For any additional information in this regard, refer to the Ph.D. thesis by N. Rojo.

The reasoning behind the control is shown in Fig.7.6: knock intensity (expressed by MAPO) might have an elastic (not permanent) or plastic (permanent) damage on pistons, depending on material properties at the specific local temperature. This is what clearly emerged from the bench tests with different RON fuels, whose results have been collected in Sect.6.3.

In particular, the permanent damage would have an amplitude substantially determined by the distance from the threshold, so that the model is implemented exactly as a typical material flow stress curve (Fig.7.6a). Since the threshold is also based on the local temperature, the map threshold-temperature (Fig.7.6b) is also contained in the ECU and it determines the shape of the "knock damage curves" at each specific temperature.

Both the shape of the "knock damage curves" indicating knock damage and the dependence of the threshold from the temperature is based on piston material properties; it automatically follows that, in case of change of piston material (such as from Al alloy to steel) both the pendency of the "knock damage curves" and the relationship between "safe" threshold and temperature should be recalibrated.

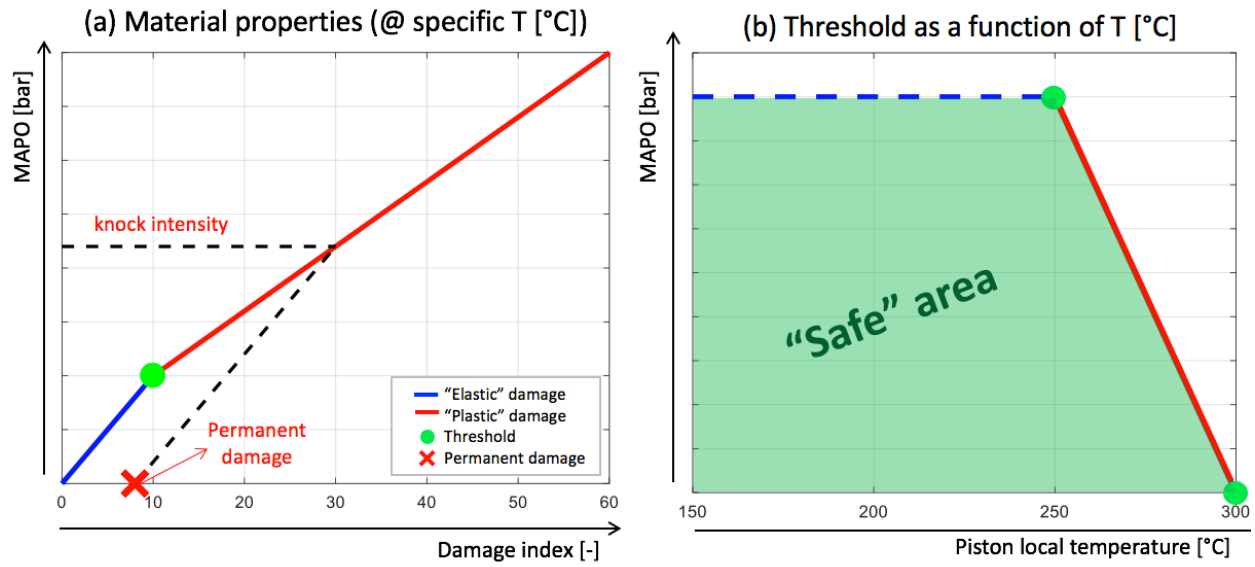

Fig.7. 6: Knocking effects on Al pistons: (a) effects at constant temperature; (b) variation of "Safe" threshold as a function of piston temperature.

In addition to that, also the local temperature of pistons was modelled in the ECU, as a function of received combustion heat (dependent on p_max90%, knock intensity and engine operating point), heat subtracted by cooling oil, distance from oil jets, as shown in Fig.7.7a. The final Simulink control blocks are indeed schematically reported in Fig.7.7b.

The so obtained cycle damage is summed for each cycle and it determines the final piston damage.

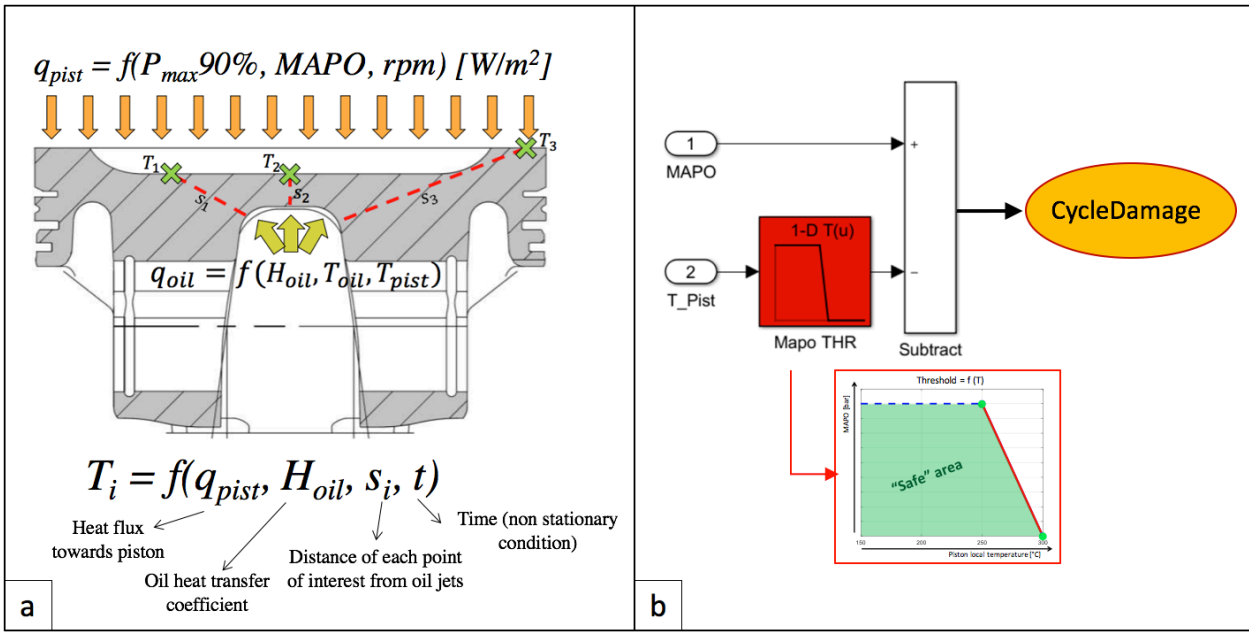

Fig.7. 7: (a) Parameters affecting piston local temperature; (b) final damage-based control

Part B - Bibliography

[1] H. Wei, A. Shao, J. Hua, L. Zhou, D. Feng, Effects of applying a Miller cycle with split injection on engine performance and knock resistance in a downsized gasoline engine, Fuel. 214 (2018) 98–107. doi:10.1016/j.fuel.2017.11.006.

[2] J.B. Heywood, Internal Combustion Engine Fundamentals, McGraw-Hill, New York, 1988.

[3] G. Minelli, Motori Endotermici Alternativi, 1984.

[4] R. Stone, Introduction to Internal Combustion Engines, 4th ed., 2012.

[5] Ideal Otto Cycle, (n.d.). https://www.grc.nasa.gov/www/k-12/airplane/otto.html.

[6] G. Töpfer, J. Reissing, H. Weimar, U. Spicher, Optical Investigation of Knocking Location on S.I.-Engines with Direct-Injection, Sae Tech. Pap. Ser. (2000).

[7] M. Kowada, I. Azumagakito, T. Nagai, N. Iwai, R. Hiraoka, Study of Knocking Damage Indexing Based on Optical Measurement, SAE Int. J. Engines. (2015). doi:10.4271/2015-01-0762.Copyright.

[8] D. Bradley, G.T. Kalghatgi, Influence of autoignition delay time characteristics of different fuels on pressure waves and knock in reciprocating engines, Combust. Flame. 156 (2009) 2307–2318. doi:10.1016/j.combustflame.2009.08.003.

[9] N. Cavina, E. Corti, G. Minelli, D. Moro, L. Solieri, Knock Indexes Normalization Methodologies, SAE Int. J. Engines. (2006). doi:10.4271/2006-01-2998.

[10] Z. Wang, Y. Qi, X. He, J. Wang, S. Shuai, C.K. Law, Analysis of pre-ignition to super-knock: Hotspot-induced deflagration to detonation, Fuel. 144 (2015) 222–227. doi:10.1016/j.fuel.2014.12.061.

[11] X. Zhen, Y. Wang, S. Xu, Y. Zhu, C. Tao, T. Xu, M. Song, The engine knock analysis- An overview, Appl. Energy. 92 (2012) 628–636. doi:10.1016/j.apenergy.2011.11.079.

[12] N. Giovannoni, S. Breda, S. Paltrinieri, A.D. Adamo, S. Fontanesi, F. Pulvirenti, CFD Analysis of the Effects of Fuel Composition and Injection Strategy on Mixture Preparation and Fuel Deposit Formation in a GDI Engine, SAE Tech. Pap. 2015-24-2408. (2016). doi:10.4271/2015-24-2408.Copyright.

[13] Y. Qi, Z. Wang, J. Wang, X. He, Effects of thermodynamic conditions on the end gas combustion mode associated with engine knock, Combust. Flame. 162 (2014) 4119–4128. doi:10.1016/j.combustflame.2015.08.016.

[14] M. Costa, P. Sementa, U. Sorge, F. Catapano, G. Marseglia, B.M. Vaglieco, Split Injection in a GDI Engine Under Knock Conditions : An Experimental and Numerical Investigation, SAE Int. J. Engines. (2015). doi:10.4271/2015-24-2432.Copyright.

[15] H. Yu, Z. Chen, End-gas autoignition and detonation development in a closed chamber, Combust. Flame. 162 (2015) 4102–4111. doi:10.1016/j.combustflame.2015.08.018.

[16] Z. Wang, H. Liu, T. Song, Y. Qi, X. He, S. Shuai, J. Wang, Relationship between super-knock and pre-ignition, Int. J. Engine Res. (2014) 166–180. doi:10.1177/1468087414530388.

[17] H. Vafamehr, A. Cairns, O. Sampson, M.M. Koupaie, The competing chemical and physical effects of transient fuel enrichment on heavy knock in an optical spark ignition engine, Appl. Energy. 179 (2016) 687–697. doi:10.1016/j.apenergy.2016.07.038.

[18] J. Mutzke, B. Scott, R. Stone, J. Williams, The Effect of Combustion Knock on the Instantaneous Heat Flux in Spark Ignition Engines, SAE Int. (2016). doi:10.4271/2016-01-0700.Copyright.

[19] J. Fitton, R. Nates, Knock Erosion in Spark-Ignition Engines, SAE Tech. Pap. (1996) 11. doi:10.4271/962102.

[20] B. Waldhauer, U. Schilling, S. Schnaibel, J. Szopa, Piston damages - Recognising and rectifying, MSI Motor Service International, 2004.

[21] H. Wei, D. Gao, L. Zhou, D. Feng, R. Chen, Different combustion modes caused by flame-shock interactions in a confined chamber with a perforated plate, Combust. Flame. 178 (2017) 277–285. doi:10.1016/j.combustflame.2017.01.011.

[22] B. Grandin, I. Denbratt, The Effect of Knock on Heat Transfer in SI Engines, Sae Tech. Pap. Ser. 2002-01-0238. (2002). doi:10.4271/2002-01-0238.

[23] R.J. Nates, A.D.B. Yates, Knock Damage Mechanisms in Spark-Ignition Engines, SAE Int. (1994). doi:10.4271/942064.

[24] R.J. Nates, Knock Damage in Spark-Ignition Engines, University of Cape Town, 1995.

[25] J.C. Fitton, R.J. Nates, Investigation into the relationship between knock intensity and piston Seizure, N&O J. (1992).

[26] L. Ceschini, A. Morri, E. Balducci, N. Cavina, N. Rojo, L. Calogero, L. Poggio, Experimental observations of engine piston damage induced by knocking combustion, Mater. Des. 114 (2017) 312–325. doi:10.1016/j.matdes.2016.11.015.

[27] E. Winklhofer, A. Hirsch, P. Kapus, M. Kortschak, H. Philipp, TC GDI Engines at Very High Power Density — Irregular Combustion and Thermal Risk, in: SAE Tech. Pap., Consiglio Nazionale delle Ricerche, 2009. doi:10.4271/2009-24-0056.

[28] N. Cavina, N. Rojo, A. Businaro, L. Ceschini, E. Balducci, A. Cerofolini, Analysis of Pre-ignition Combustions Triggered by Heavy Knocking Events in a Turbocharged GDI Engine, Energy Procedia. 101 (2016) 893–900. doi:10.1016/j.egypro.2016.11.113.

[29] E. Balducci, S. Parisi, F. Boccia, M. Barichello, L. Ceschini, Knock (and pre-ignition) damage on engine components: case studies, La Metall. Ital. in press (2018).

[30] E. Balducci, L. Ceschini, N. Rojo, N. Cavina, R. Cevolani, M. Barichello, Knock induced erosion on Al pistons: Examination of damage morphology and its causes, Eng. Fail. Anal. 92 (2018). doi:10.1016/j.engfailanal.2018.05.002.

[31] N. Cavina, N. Rojo, L. Ceschini, E. Balducci, L. Poggio, L. Calogero, R. Cevolani, Investigation of Knock Damage Mechanisms on a GDI TC Engine, SAE Int. (2017). doi:10.4271/2017-24-0060.Copyright.

[32] H. Yamagata, The science and technology of materials in automotive engines, Woodhead, 2005.

[33] S. Mahle GmbH, ed., Pistons and Engine Testing, 2012.

[34] G. Cantore, M. Giacopini, R. Rosi, A. Strozzi, P. Pelloni, C. Forte, M. Achilluzzi, G.M. Bianchi, L. Ceschini, A. Morri, Validation of a combined CFD / FEM methodology for the evaluation of thermal load acting on aluminum alloy pistons through hardness measurements in internal combustion engines, Metall. Sci. Technol. 29 (2011).

[35] A. Humbertjean, T. Beck, Effect of the casting process on microstructure and lifetime of the Al-piston-alloy AlSi12Cu4Ni3 under thermo-mechanical fatigue with superimposed high-cycle fatigue loading, Int. J. Fatigue. 53 (2013) 67–74. doi:10.1016/j.ijfatigue.2011.09.017.

[36] G. Floweday, S. Petrov, R.B. Tait, J. Press, Thermo-mechanical fatigue damage and failure of modern high performance diesel pistons, Eng. Fail. Anal. 18 (2011) 1664–1674. doi:10.1016/j.engfailanal.2011.02.002.

[37] L.E. Fratila-Apachitei, F.D. Tichelaar, G.E. Thompson, H. Terryn, P. Skeldon, J. Duszczyk, L. Katgerman, A transmission electron microscopy study of hard anodic oxide layers on AlSi(Cu) alloys, Electrochim. Acta. 49 (2004) 3169–3177. doi:10.1016/j.electacta.2004.02.030.

[38] L. Ceschini, A. Morri, A. Morri, M. Di Sabatino, Effect of thermal exposure on the residual hardness and tensile properties of the EN AW-2618A piston alloy, Mater. Sci. Eng. A. 639 (2015) 288–297. doi:10.1016/j.msea.2015.04.080.

[39] E. Balducci, L. Ceschini, A. Morri, A. Morri, M. Di Sabatino, L. Arnberg, Y. Li, High Temperature Behavior of the EN AW-2618A Piston Alloy Containing 0.12wt% Zr: Influence of Heat Treatment, in: Mater. Today Proc., Elsevier Ltd, 2015: pp. 5037–5044.

[40] R.J. Nates, Thermal Stresses Induced by Knocking Combustion in Spark-Ignition Engines, Sae Tech. Pap. Ser. (2000). doi:10.4271/2000-01-1238.

Conclusions

Aiming to boost the efficiency of internal combustion engines, in addition to hybridization, the automotive industry is considerably investing on materials research with high strength-to-weight ratio for engine components. In this context, it is particularly crucial the role of Al alloys for pistons, which form the core of the combustion chamber and have to withstand considerably high thermo-mechanical stresses. Al alloys exhibit many desirable characteristics for piston materials, such as a high thermal conductivity and a low density, the latter favoring secondary mass savings of con-rods and crankshaft and therefore vehicle lightweighting. Nevertheless, Al alloys typically suffer from overaging and softening at high temperature, which substantially limit the in-chamber temperature and pressure, directly related to the combustion efficiency.

On this basis, the experimental activities of Part A of this Ph.D. thesis collect a critical analysis on Al-Si and Al-Cu piston alloys, both for the mass production and for the racing field. Besides the variation of mechanical properties with thermal exposure (examined through overaging curves and tensile tests), the microstructural features were deeply investigated, with the aim to determine the most effective combination of suitable alloying elements and heat treatment to enhance high temperature resistance. In the most promising cases, tensile tests at high temperature (200°C and/or 250°C) were carried out on overaged specimens, in order to fully simulate the variation of mechanical properties undergone by Al pistons; these tests have been always accompanied by STEM/TEM investigations, with the aim to trace the precipitates evolution which mainly governs the Al alloys resistance at high temperature.

The first part is dedicated to outline the state of the art of Al alloys for automotive pistons and it focuses on the two common Al-Si AA4032 and Al-Cu AA2618 alloys. Starting from samples machined from hot forged pistons, the effects of thermal exposure in the range of interest for pistons operating temperature (200-300°C) have been considered, highlighting a substantial decay of alloys resistance. For both alloys, a linear relationship was drawn between residual hardness and RT tensile properties and the tensile behavior in the plastic field was also modelled according to Hollomon's law, with the aim to better underline the interaction between overaged precipitates and dislocations. A higher performance of Al-Cu AA2618 was highlighted in all overaging conditions, due to the lower coarsening rate of Cu-based precipitates θ (Al_2Cu) and S (Al_2CuMg)

compared to β (Mg_2Si), and due to the presence of thermal resistant Al-Fe-Ni secondary phases strengthening AA2618.

The influence of higher amounts of Cu to the base AA4032 alloy was also evaluated, highlighting a consistent improvement in terms of residual hardness after overaging. Correspondingly, the RT tensile properties after overaging are supposed to be significantly enhanced This high performance eutectic Al-Si alloy is then referred to as AlSi12CuNiMg alloy.

The two most promising piston alloys developed to date in the automotive scenario, namely Al-Cu AA2618 and AlSi12CuNiMg, have been more deeply studied, aiming to further enhance their high temperature properties and resistance to overaging. According to the literature data, transition elements were added to stimulate the formation of fine and homogeneously distributed, thermally stable dispersoids, able to effectively hinder dislocation motion at high temperature. Since a research directly applicable to the industrial field is the target of this Ph.D. thesis, only conventional casting routes have been considered, thus the amount of transition elements which can be added to these alloys is considerably limited because of primary precipitation.

Up to 0.3wt% Mo additions were tested in the eutectic AlSi12CuNi alloy, in order to stimulate the formation of heat resistant Al-(Fe-Mo)-Si dispersoids; the effects of 0.25wt% Zr in the Al-Cu AA2618 alloy were indeed evaluated, aiming to take advantage of the coarsening resistant Al_3Zr. In both cases, an optimized heat treatment was developed, since the transition elements have a sluggish diffusivity in Al matrix and they typically form at the higher solution temperatures; besides, the base industrial heat treatment on both base and modified alloys was considered as a reference.

While no beneficial effects have been induced by Mo additions (actually responsible of an increased amount of casting defects), positive results were achieved for AA2618 enriched in Zr and heat treated according to the base industrial heat treatment. Even if the advantages of Zr additions are not immediately perceivable in terms of residual hardness after thermal exposure, improvements of tensile properties at 250°C were observed on overaged specimens. The experimental results are confirmed by TEM microstructural investigations of the most overaged samples (192h at 300°C): the higher Zr amount seems to produce both a more uniform distribution and a higher coarsening resistance of S-Al_2CuMg precipitates, which are of course surrounded by an increased number of nanometric Al_3Zr dispersoids.

Finally, two innovative Al-Cu-Li(-Ag) alloys, namely AA2099 and AA2055, were in-depth characterized, aiming to determine their potential in terms of high temperature applications. In addition to the typical Cu based precipitates (ϑ-Al_2Cu, S-Al_2CuMg), these alloys in the peak-aged condition take advantage of T_1-Al_2CuLi, δ-Al_3Li and Al_3Zr phases, which provide extremely high strength-to-weight ratio at room temperature. Thanks to this characteristic, extremely appreciated also for automotive components, these alloys are nowadays typically employed for structural aerospace applications. The effects of overaging on the room and high temperature tensile properties of the alloys were assessed in the range 200-300°C; the mechanical characterization was also coupled with STEM microstructural investigations, aiming to highlight the most coarsening resistant precipitates. As encountered in the conventional Al alloys, also these precipitates (with the exception of Al_3Zr dispersoids) are prone to coarsening at T>200°C. When overaged at 300°C, AA2099 alloy is still strengthened by coarsened T_1-Al_2CuLi and newly formed blocky σ-AlCuMg phases, while AA2055 is reinforced by coarsened Ω and ϑ-Al_2Cu phases.
It is worth pointing out that RT tensile properties of AA2099 and AA2055 are superior than that of AA2618 alloy in all overaging conditions, providing a not negligible increase in terms of strength-to-weight ratio at RT, even after thermal exposure. Nevertheless, tensile tests at 200°C and 250°C show a substantial drop in Al-Cu-Li alloys resistance, in particular experienced at 250°C. Even if the overaging conditions are not totally comparable between AA2099/AA2055 and AA2618 tensile specimens, it can be inferred that AA2618 exhibits the most promising strength-to-weight ratio in case the component operating temperature reaches 250°C. Additional tensile tests of AA2618 at intermediate temperature, under comparable overaging conditions with respect to AA2099 and AA2055 alloys, should be however performed to completely confirm the trend.

The second part of the dissertation (Part B) is indeed focused on another relevant aspect which is today deeply investigated in the automotive scenario and might mark a step forward towards the reduction of fuel consumption: knocking combustions under a certain threshold should be partially accepted, allowing the engine to operate with higher efficiency. However, these abnormal combustions produce pressure oscillations which significantly increase the thermo-mechanical stresses of all components forming the combustion chamber, in particular pistons, further underlining the need of heat resistant Al alloys.
Since the increase in engine efficiency heavily depends on the numerical value of the tolerated knocking threshold (approximately, the higher the threshold, the higher the efficiency), systematic

experimental activities have been carried out in order to determine the acceptable knocking level (and correspondingly the acceptable knocking damage) which does not compromise engine functionality. No data addressing this issue are available in literature.

Several bench tests have been thus performed under controlled knocking conditions, in cooperation with Ferrari Auto S.p.A. and Fluid Machinery Research Group. The main damage mechanisms produced by knock were investigated, as well as their effects in terms of reduced piston functionality and their relationship with engine calibration parameters.

It can be inferred that the instantaneous higher temperature induced by knock does not produce substantial overaging in the alloy, due to the limited time of exposure, but it is rather responsible of an instantaneous alloy softening, which acts as an intensification factor for knock-induced mechanical stresses. Piston valve reliefs (and any "edge" in the combustion chamber in general) are therefore extremely sensitive to knock damage, due to their high surface-to-volume ratio which significantly enhances the local temperature and might also trigger knocking combustions. The intensity of erosion damage of piston valve reliefs appears well related to the severity of single knocking cycles (adequately represented by the engine parameter MAPO 99.5%). In the most severe cases, knock pressure oscillations were found to considerably damage the anodized layer of piston first ring groove and/or to locally produce a plastic deformation of the ring groove, compromising the functionality of the first ring.

In depth investigations also revealed that the in-chamber temperature at knock onset (well represented by the in-chamber pressure) significantly affects the damage produced by comparable events in terms of knock intensity (MAPO).

The experimental activities highlighted that the today calibrations adopt extremely large "safety" margins and that the tolerable knocking threshold might be significantly increased (producing acceptable damages) in order to gain a higher engine efficiency. Bench tests aimed to precisely link the piston damage to the reduction of engine functionality (power loss, increased blow-by or oil consumption) are still ongoing.

Ringraziamenti

Si concludono così tre anni di Dottorato, anni di impegno, di tenacia nel perseguire i risultati della ricerca e di entusiasmo nel vederne i frutti. Ma anche anni di sacrifici, soprattutto l'ultimo anno e mezzo, in cui ho dovuto affrontare la sfida di un nuovo lavoro, in un ambiente stimolante quanto competitivo, e parallelamente portare a conclusione questo ambizioso percorso.

Un grazie di cuore a tutti quelli che mi hanno supportato (e sopportato!) in questi tre anni, a partire dal mio fidanzato Andrea e dai miei genitori Anna e Luigi: voi avete sempre creduto in me, anche quando il raggiungimento del traguardo mi sembrava impossibile, anche quando la stanchezza che provavo mi sembrava troppa per una persona sola. Voi mi avete sempre dato la carica per affrontare le difficoltà di questo percorso e soprattutto mi avete aperto gli occhi per cogliere il buono e il bello di tutto ciò che ho affrontato. Grazie a mia cugina Giulia, che pur nella sua lontananza per il lavoro è sempre stata accanto a me, che mi mostra ogni volta di avere bisogno di me quanto io ne ho di lei, che mi ha insegnato a non perdermi d'animo ma piuttosto rimboccarmi le maniche per ogni nuova avventura della mia vita.

Grazie alla Professoressa Ceschini che ha reso possibile tutto questo, che mi ha trasmesso la passione per i materiali e mi ha resa parte del Dipartimento di Metallurgia, permettendomi di lavorare accanto a lei e fianco a fianco con persone preparate e meravigliose: grazie Andrea per avermi guidata in tante attività; grazie Stefania e Valerio per le tante risate insieme e per aver reso felice l'ambiente di lavoro di tutti i giorni; grazie Lavinia per la bella persona che sei e per la forza che mi hai dimostrato e che infondi a chi ti sta accanto; grazie Chiara per il tuo supporto in ogni momento di bisogno e per la tua ironia e autoironia contagiosa; grazie Carla e Alessandro per i preziosi consigli; grazie Iuri e Fabrizio per le innumerevoli ore al SEM!

Un grazie enorme anche al Professor Cavina, che mi ha coinvolta in uno dei progetti più interessanti che potessi mai sperare e che con il suo entusiasmo nella ricerca mi ha fatto scoprire una passione per i motori che non pensavo fosse nelle mie corde! E grazie dei feedback costanti, delle critiche costruttive, della guida nell'ottenere ogni singolo risultato del progetto. Grazie a Nahuel per il confronto continuo, per le idee brillanti, per l'energia contagiosa impiegata ogni giorno nel progetto.

Infine, grazie, grazie e ancora grazie a tutte le persone che mi hanno accolta in Ferrari, prima aiutandomi nel mio progetto di Dottorato e poi rendendomi a tutti gli effetti parte del loro

team. Grazie Seba per la tua competenza e la condivisione totale con tutti noi, grazie per la tua presenza ed il tuo aiuto tecnico ogni volta che ne abbiamo la necessità. Grazie Mike e Fabio per le battute che smorzano la tensione nel lavoro quotidiano (e che mi ricaricano per l'intera giornata!). Grazie Beppe, che tra una presa in giro e l'altra mi tieni accanto a te per insegnarmi la praticità che deve avere un ingegnere meccanico. Grazie a voi che rendete il mio ambiente di lavoro migliore e che, inconsapevolmente, mi avete aiutata a portare a termine questo percorso.